



Provided by the author(s) and University of Galway in accordance with publisher policies. Please cite the published version when available.

Title	Investigation of Biomass Combustion in Grate Furnaces using CFD
Author(s)	Duffy, Neil
Publication Date	2012-12-12
Item record	http://hdl.handle.net/10379/3823

Downloaded 2024-04-16T06:53:19Z

Some rights reserved. For more information, please see the item record link above.



Investigation of Biomass Combustion in Grate Furnaces using CFD

Neil Duffy

B.E. National University of Ireland, Galway, 2007



A thesis submitted to the National University of Ireland as fulfilment of the
requirements for the Degree of Doctor of Philosophy

Department of Mechanical and Biomedical Engineering
National University of Ireland, Galway

December 2012

Supervisor of Research: Dr. John Eaton

ABSTRACT

Channelling is an undesirable phenomenon in the fixed-bed combustion of biomass. It is characterised by an uneven air distribution, and thus fuel conversion, throughout the fuel bed. Attempts to mitigate the channelling effect using redesigned grates have resulted in an increase in grate wear. Computational fluid dynamics can provide an insight into these issues. To this end, an unsteady, 2D numerical model for predicting solid fuel combustion under fixed-bed conditions is designed and developed. The commercial CFD code Fluent is used as the basis.

The model is then validated using different existing data for ignition rates and species profiles through a biomass fuel bed.

The model is applied to investigate factors that influence channelling in a randomly packed bed of biomass. These factors include: resistance to flow through the grate, the bed height, flue gas recirculation, and the initial moisture content of the fuel. A high value of grate resistance is confirmed as a key factor to reducing channelling.

The 2D model is extended to three dimensions to capture 3D features within the fuel bed and grate. To reduce the simulation run times, the 3D model is parallelised to run on high performance computers or clusters.

The complete 3D model is employed to examine measures to reduce grate wear. The influences of the shape of the grate, the inlet air flux, and the thickness of the ash layer are investigated. Results indicate that small passages are beneficial, but that low grate porosity and/or large spacing between passages may lead to excessive temperatures of the grate material or potentially carburising conditions at the surface of the grate.

ACKNOWLEDGMENTS

First of all, I would like to thank my supervisor, Dr. John Eaton, for his continued guidance over the years, from start to finish of this project. I would like to thank IRCSET for awarding me a scholarship, without them this study simply would not have been possible. I would like to thank the university and its staff for providing the tools necessary to carry out my research, in particular, Jane and Sharon, our departmental secretaries who have been very helpful over the years. I would like to thank all of the lecturers in the mechanical engineering department, most of whom have acted as a sounding board at some stage in my study, in particular, Dr. Rory Monaghan, and the members of my GRC committee, Dr. Nathan Quinlan, and Prof. Sean Leen. I would also like to thank ICHEC for providing the high performance computing facilities necessary to complete this work, and its staff, all of whom have been very helpful whenever issues arose. Similarly, to the support crew at Ansys, for both CFX and Fluent, while there are too many to name, I have received a huge amount of feedback from them over the years. Further afield, Dr. Sven Hermansson was instrumental, he provided me with a lot of key advice whenever I contacted him, and also gave me a sample of his own code, which laid the foundation for a significant section of my own work, he is gratefully acknowledged. Prof. Hallett in Ottawa University kindly sent me some data, which enabled me to validate my model. Thank you to Dr. Bryden, and Prof. Fredlund, who sent me copies of their own thesis, to Prof. Williams, Dr. Mehrabian, Dr. Yang, Dr. Kaer, and Prof. Di Blasi, who kindly answered my questions when I contacted them. Closer to home, I would like to thank my friends and fellow postgrad students, for sounding out problems or just for a laugh when it was needed. Finally, to my parents, my sisters Pauline and Suzanne, and my girlfriend Nikki – let's just say there wouldn't be much point doing this without them.

TABLE OF CONTENTS

1. INTRODUCTION	1
1.1 Objective and Thesis Overview	1
1.2 Energy Consumption.....	3
1.2.1 Global energy consumption	3
1.2.2 Irish energy consumption	5
1.3 Biomass as a Renewable Source of Energy.....	6
1.3.1 Describing biomass fuel: wood as basis.....	6
1.3.2 Logistics.....	8
1.4 Overview of the Thermochemical Conversion of Biomass	9
1.5 Thermochemical Conversion Technologies	12
1.5.1 Overview of conversion methods.....	12
1.5.1.1 Fixed-bed (grate) conversion.....	12
1.5.1.2 Fluidised-bed conversion (FBC).....	14
1.5.1.3 Pulverised fuel conversion.....	15
1.5.2 Fixed-bed conversion.....	15
1.5.3 Grate-firing – key issues.....	18
1.5.3.1 Pollutant emissions	18
1.5.3.2 Deposit formation and corrosion (fouling)	19
1.5.3.3 Fuel bed specific issues.....	19
1.6 Modelling Combustion in a Grate Furnace	20
1.6.1 Freeboard modelling	20
1.6.2 Fuel bed modelling	21
1.7 Scope of this Thesis.....	21
2. REVIEW OF PREVIOUS WORK.....	23
2.1 Review of Thermochemical Conversion Models.....	23
2.1.1 Drying.....	23

2.1.1.1	Constant temperature drying model.....	24
2.1.1.2	Kinetic method	25
2.1.1.3	Algebraic drying model	26
2.1.1.4	Transport drying model.....	26
2.1.1.5	Discussion of drying models	28
2.1.2	Pyrolysis (devolatilisation)	29
2.1.2.1	Model classification	30
2.1.2.2	Single-step model.....	30
2.1.2.3	Single-stage, multi-reaction models	32
2.1.2.3.1	Competing rates model.....	32
2.1.2.3.2	Parallel step model – based on product distribution.....	33
2.1.2.3.3	Parallel step model – based on fuel composition	33
2.1.2.4	Two-stage, semi-global models.....	34
2.1.2.4.1	Tar cracking	34
2.1.2.4.2	Tar cracking and repolymerisation	35
2.1.2.5	Distributed activation energy models (DAEM).....	35
2.1.2.6	Network models for pyrolysis	37
2.1.2.7	Discussion of pyrolysis models.....	40
2.1.2.7.1	Heat of reaction	40
2.1.2.7.2	Conclusion	41
2.1.3	Heterogeneous reaction models.....	41
2.1.3.1	Global reaction models.....	44
2.1.3.2	Intrinsic reactivity models	47
2.1.3.2.1	Intrinsic reactivity model – Smith.....	47
2.1.3.2.2	Extended reaction model	50
2.1.3.3	Discussion of heterogeneous reactions	50
2.1.3.3.1	Products from char combustion.....	50

2.1.3.3.2	Char structure.....	51
2.1.3.3.3	Char composition.....	51
2.1.3.3.4	Heat of reaction.....	51
2.1.3.3.5	Conclusion of heterogeneous submodels.....	52
2.1.4	Discussion on thermochemical conversion models.....	52
2.2	Review of Fixed-Bed Modelling.....	54
2.2.1	Fixed-bed simulation methods.....	54
2.2.2	Implementation approach.....	57
2.2.2.1	Eulerian-Eulerian (porous medium) approach.....	58
2.2.2.2	Eulerian-Eulerian (granular) approach.....	59
2.2.2.3	Eulerian-Lagrangian approach.....	59
2.2.3	One-dimensional (1D) bed models.....	60
2.2.4	Two-dimensional (2D) bed models.....	62
2.2.5	Three-dimensional (3D) bed models.....	63
2.2.6	Particle models.....	64
2.2.7	Particle mixing models.....	66
2.2.8	Randomly-packed bed models.....	67
2.2.9	Discussion.....	68
3.	MODEL DESCRIPTION.....	69
3.1	Overview.....	69
3.2	Gas Phase.....	71
3.2.1	Thermal and mass dispersion.....	73
3.2.2	Resistance to gas flow.....	73
3.2.3	Turbulence.....	74
3.2.4	Homogeneous reactions.....	74
3.3	Fuel Phase.....	75
3.3.1	Heat and mass transfer.....	76
3.3.2	Thermally-thin assumption.....	77
3.3.3	Drying.....	78

3.3.4	Pyrolysis	79
3.3.5	Char oxidation and char gasification	80
3.3.6	Thermal conductivity	82
3.3.7	Specific heat capacity	83
3.3.8	Particle shrinkage	83
3.3.9	Density of the solid phase within the cell	85
3.3.10	Volatile gas composition	85
3.3.11	Energy released	86
3.4	Ignition Mechanisms	87
3.5	Bed Shrinkage	88
3.5.1	Description of shrinkage submodel	90
3.5.2	Node identification	92
3.5.2.1	Shrinkage implementation in the 2D modelling case	92
3.5.2.2	Shrinkage implementation in the 3D modelling case	94
3.5.3	Implementation	96
3.5.3.1	Collapse filter	96
3.5.3.2	Node manipulation	96
3.6	Solution Procedure	97
3.7	Summary	98
4.	VALIDATION	101
4.1	Mesh Resolution	101
4.2	Ignition Rates	103
4.2.1	Model calibration	103
4.2.2	Final results	104
4.3	Species Profiles	105
4.4	Summary and Discussion	107
5.	2D INVESTIGATION OF CHANNELLING IN FIXED-BED COMBUSTION ..	109
5.1	Objective and Overview	109
5.2	Initial Bed Porosity	110

5.3	Parameters Investigated.....	112
5.4	Results.....	116
5.4.1	Grate resistance	116
5.4.2	Flue gas recirculation (FGR)	125
5.4.3	Moisture content	128
5.5	Discussion	130
6.	3D MODEL OF CHANNELLING IN FIXED-BED COMBUSTION	132
6.1	Objective and Overview.....	132
6.2	Initial Bed Porosity.....	133
6.3	Parameters Investigated.....	138
6.4	Results.....	138
6.4.1	Circular passage	139
6.4.2	Rectangular passage	144
6.5	Discussion	149
7.	3D INVESTIGATION OF MEASURES TO REDUCE GRATE WEAR	151
7.1	Objective.....	151
7.2	Background.....	151
7.3	Overview	153
7.4	Parameters Investigated.....	154
7.5	Model Description	157
7.5.1	CO ₂ gasification.....	157
7.5.2	Particle properties	159
7.5.2.1	Geometry.....	159
7.5.2.2	Density and shrinkage.....	160
7.5.3	Heat and mass transfer with ash build-up	161
7.5.4	Heat transfer to the grate	162
7.6	Validation.....	165
7.7	Results.....	167
7.7.1	Temperature.....	167
7.7.1.1	Bare grate – no ash layer	167

7.7.1.2	Grate covered by 2 mm initial ash layer	175
7.7.2	Carburisation	179
7.7.2.1	Bare grate – no ash layer	179
7.7.2.2	The effects of a thin ash layer	181
7.8	Discussion	184
8.	CONCLUSIONS AND RECOMMENDATIONS.....	187
8.1	Conclusions Regarding Channelling in Grate Furnaces	187
8.1.1	2D model developed.....	187
8.1.2	Model validation	187
8.1.3	2D investigation of channelling	187
8.1.4	3D model developed.....	188
8.1.5	3D model parallelised.....	188
8.1.6	3D investigation of channelling	188
8.2	Conclusions Regarding Grate Design	188
8.2.1	Size of the grate passages.....	188
8.2.2	Grate porosity/spacing between passages.....	189
8.2.3	Inlet air flux.....	189
8.2.4	Ash layer.....	189
8.2.5	Recommendations for grate design.....	189
9.	RECOMMENDATIONS FOR FUTURE WORK.....	191
9.1	Applying the Current Model.....	191
9.1.1	Fully-coupled fuel bed and freeboard simulation.....	191
9.1.2	Separate fuel bed and freeboard simulation	191
9.1.3	Length of the grate	192
9.1.4	Detailed grate shape	193
9.2	Model Extensions	193
9.2.1	NO_x emissions.....	193
9.2.2	Walking column approach.....	193
9.2.3	Conduction between the fuel particles and the grate	194

9.2.4	Corrosion.....	194
9.2.5	Deposition.....	194
Appendix A	PARALLELISATION.....	196
A.1	Overview.....	196
A.1.1	Internal and external cells.....	197
A.1.2	Cell access.....	198
A.1.3	Generating an array using values from multiple compute nodes.....	198
A.2	User-Defined Memory (UDM) Values.....	201
A.2.1	Initialisation.....	201
A.2.2	Updating values.....	201
A.3	Mesh Deformation (Bed Shrinkage).....	201
A.3.1	Issues with parallel mesh deformation.....	202
A.3.2	Solution overview.....	204
A.3.3	Identifying outlying cells.....	206
A.3.4	Moving nodes in outlying cells.....	209
A.4	Parallel Verification.....	212
Appendix B	MESH SPACING PLOTS.....	215
Appendix C	COLLATED EQUATIONS.....	219
Appendix D	LIST OF UDFS AND FUNCTIONS.....	230

LIST OF FIGURES

<i>Figure 1.1</i>	Image of industrial grate furnace	1
<i>Figure 1.2</i>	Evolution from 1971 to 2010 of world total primary energy supply	4
<i>Figure 1.3</i>	2010 fuel share of world TPES.....	4
<i>Figure 1.4</i>	Predicted fuel shares of world TPES in 2030.....	5
<i>Figure 1.5</i>	2009 share of Ireland’s renewable sources	6
<i>Figure 1.6</i>	Separate stages of the thermal degradation of a wood particle.	9
<i>Figure 1.7</i>	Schematic diagram of the thermal degradation process within a thermally thick particle	11
<i>Figure 1.8</i>	Major chemical and physical mechanisms during solid fuel combustion.	12
<i>Figure 1.9</i>	Principal combustion technologies for biomass	13
<i>Figure 1.10</i>	Fluidising velocity of air for various bed systems	14
<i>Figure 1.11</i>	Fuel/air feed configurations in a fixed bed.....	16
<i>Figure 1.12</i>	Schematic of a fixed-bed furnace with a moving grate	17
<i>Figure 1.13</i>	Types of moving grate.....	18
<i>Figure 2.1</i>	Illustrations of a devolatilising coal particle	39
<i>Figure 2.2</i>	Schematic diagram of a porous material	43
<i>Figure 2.3</i>	Schematic of different reaction zones (for a spherical particle).....	43
<i>Figure 2.4</i>	Schematic of fixed-bed furnace	54
<i>Figure 2.5</i>	Eulerian – Eulerian approach.....	55
<i>Figure 2.6</i>	Eulerian-Lagrangian approach	56
<i>Figure 2.7</i>	Neighbouring layer approach.....	56

<i>Figure 2.8</i>	Cascading reactor model.....	57
<i>Figure 3.1</i>	Computational cell and surrounding nodes	70
<i>Figure 3.2</i>	Sequence of particle-scale processes.	76
<i>Figure 3.3</i>	Combustion behaviour in a cross-current flow unit.....	88
<i>Figure 3.4</i>	Overview of bed shrinkage	89
<i>Figure 3.5</i>	User-defined coordinate system applied to every cell	90
<i>Figure 3.6</i>	Fuel bed shrinkage processes	91
<i>Figure 3.7</i>	Node moved in 2D.....	93
<i>Figure 3.8</i>	NUDM storage of node position relative to the surrounding cells	94
<i>Figure 3.9</i>	Node moved in 3D.....	95
<i>Figure 3.10</i>	Implementation of deformation routine.....	99
<i>Figure 3.11</i>	Equation interaction and solution procedure	100
<i>Figure 4.1</i>	Comparing mole fraction of CO_2 for different grid sizes	102
<i>Figure 4.2</i>	Comparing gas phase temperature for different grid sizes	102
<i>Figure 4.3</i>	Steady-state ignition rate for different air flow rates after 900 s	105
<i>Figure 4.4</i>	Comparison of measured and predicted species profiles through the bed at $t = 1200$ s	107
<i>Figure 5.1</i>	Simulated domain showing shape of fuel bed surface after time t	110
<i>Figure 5.2</i>	Fuel bed porosity – initial distribution and corresponding variations of average over vertical traverses.....	112
<i>Figure 5.3</i>	Position-dependent shape function: (a) initial shape; (b) multiplier used to modify the existing random porosity and create a relatively porous passage	113
<i>Figure 5.4</i>	Effects of grate resistance on distribution of flow speed: $t = 600$ s, $h_0 = 100$ mm.	118

<i>Figure 5.5</i> Effects of grate resistance on distribution of flow speed: $t = 600$ s, $h_0 = 200$ mm	119
<i>Figure 5.6</i> Effects of grate resistance on distribution of flow speed: $t = 600$ s, $h_0 = 300$ mm	120
<i>Figure 5.7</i> Variation of standard deviation of outlet gas speed with different grate resistances as a function of the relative resistance of the grate	122
<i>Figure 5.8</i> Variation of standard deviation of outlet gas speed with different grate resistances as a function of the log of the relative the fuel bed	123
<i>Figure 5.9</i> Variation of standard deviation of outlet gas speed with different grate resistances as a function of the initial height of the fuel bed	123
<i>Figure 5.10</i> Gas pathlines demonstrating the capture area of a 50 mm passage after 600 s for the 200 mm bed with $\beta_{gt} = 10^5$	124
<i>Figure 5.11</i> Effects of flue gas recirculation on distribution of flow speed: $h_0 = 200$ mm, $\beta_{gt} = 10^6$	126
<i>Figure 5.12</i> Effects of flue gas recirculation on the centreline temperatures ($x = 100$ mm) for the gas and solid phases	127
<i>Figure 5.13</i> Variation of mean and standard deviation of outlet gas speed with flue gas recirculation	128
<i>Figure 5.14</i> Effects of initial fuel moisture content on distribution of flow speed: $h_0 = 200$ mm, $\beta_{gt} = 10^6$	129
<i>Figure 5.15</i> Variation of mean and standard deviation of outlet gas speed with initial moisture content	130
<i>Figure 6.1</i> Schematic diagram of a grate furnace showing the simulated domain	133
<i>Figure 6.2</i> Simulated 3D domain showing shape of fuel bed surface after time t .	134
<i>Figure 6.3</i> 3D position dependent functions.....	135

<i>Figure 6.4</i>	Spatial variation of initial porosity: (a) random; (b) random with circular high porosity passage; (c) random with rectangular high porosity passage....	136
<i>Figure 6.5</i>	Averaged porosity along vertical traverses	137
<i>Figure 6.6</i>	Effects of variation in grate resistance on distribution of gas speed in a randomly packed bed with a circular passage after 250 s: (a) $\beta_{gt} = 10^4$; (b) $\beta_{gt} = 10^5$; (c) $\beta_{gt} = 10^6$	140
<i>Figure 6.7</i>	Effects of variation in grate resistance on distribution of solid temperature in a randomly packed bed with a circular passage after 250 s: (a) $\beta_{gt} = 10^4$; (b) $\beta_{gt} = 10^5$; (c) $\beta_{gt} = 10^6$	141
<i>Figure 6.8</i>	Effects of variation in grate resistance on distribution of pressure in a randomly packed bed with a circular passage after 250 s:.....	142
<i>Figure 6.9</i>	Streamtraces in a fuel bed containing a circular passage, with $\beta_{gt} = 10^6$, after 600 s.....	143
<i>Figure 6.10</i>	Effects of variation in grate resistance on distribution of gas speed in a randomly packed bed with a rectangular passage: (a) $\beta_{gt} = 10^4$; (b) $\beta_{gt} = 10^5$; (c) $\beta_{gt} = 10^6$	146
<i>Figure 6.11</i>	Effects of variation in grate resistance on distribution of solid phase temperature in a randomly packed bed with a rectangular passage: (a) $\beta_{gt} = 10^4$; (b) $\beta_{gt} = 10^5$; (c) $\beta_{gt} = 10^6$	147
<i>Figure 6.12</i>	Streamtraces in a fuel bed containing a rectangular passage, with $\beta_{gt} = 10^6$, after 600 s.....	148
<i>Figure 6.13</i>	Variation of standard deviation of outlet gas speed with different grate resistances	149
<i>Figure 7.1</i>	Schematic diagram showing a section of a grate with a porosity of 0.06 for three different passages.....	151
<i>Figure 7.2</i>	Simulated 3D computational domain with a solid grate section	154

Figure 7.3 Illustrating the variation in grate porosity for a passage with dimensions equal to D_h , where $D_h = 2, 4, \text{ or } 8 \text{ mm}$	155
Figure 7.4 Demonstrating how three differently sized passages lead to a grate with the same porosity, in this case $\varepsilon_{grate} = 0.06$	156
Figure 7.5 Particle shrinkage model.....	159
Figure 7.6 Heat transfer mechanisms to the grate surface.....	163
Figure 7.7 Comparison of measured and predicted species profiles through the bed at $t = 900 \text{ s}$	166
Figure 7.8 Bare grate – no ash layer: maximum temperatures as a function of peak gas speed entering the fuel bed for different passage sizes at an air flux of $0.2 \text{ kg/m}^2 \text{ s}$	169
Figure 7.9 Bare grate – no ash layer: maximum temperatures as a function of peak gas speed entering the fuel bed for different passage sizes at an air flux of $0.125 \text{ kg/m}^2 \text{ s}$	169
Figure 7.10 Bare grate – no ash layer: maximum temperatures as a function of peak gas speed entering the fuel bed for different passage sizes at an air flux of $0.05 \text{ kg/m}^2 \text{ s}$	170
Figure 7.11 Bare grate – no ash layer: mean conversion yield at the surface of the grates as a function of peak gas speed entering the fuel bed for different passage sizes at an inlet flux of $0.2 \text{ kg/m}^2 \text{ s}$	171
Figure 7.12 Bare grate – no ash layer: mean conversion yield at the surface of the grates as a function of peak gas speed entering the fuel bed for different passage sizes at an inlet flux of $0.125 \text{ kg/m}^2 \text{ s}$	171
Figure 7.13 Bare grate – no ash layer: mean conversion yield at the surface of the grates as a function of peak gas speed entering the fuel bed for different passage sizes at an inlet flux of $0.05 \text{ kg/m}^2 \text{ s}$	172
Figure 7.14 ‘Heating’ and ‘cooling’ surfaces of the grate section	173

<i>Figure 7.15</i> Ash covered grate: maximum temperatures as a function of peak gas speed entering the fuel bed for different passage sizes at an air flux of 0.2 $kg/m^2 s$.	175
<i>Figure 7.16</i> Ash covered grate: maximum temperatures as a function of peak gas speed entering the fuel bed for different passage sizes at an air flux of 0.125 $kg/m^2 s$.	176
<i>Figure 7.17</i> Ash covered grate: maximum temperatures as a function of peak gas speed entering the fuel bed for different passage sizes at an air flux of 0.05 $kg/m^2 s$.	176
<i>Figure 7.18</i> Ash covered grate: mean conversion yield at the surface of the grate as a function of peak gas speed entering the fuel bed for different passage sizes at an air flux of 0.2 $kg/m^2 s$.	177
<i>Figure 7.19</i> Ash covered grate: mean conversion yield at the surface of the grates as a function of peak gas speed entering the fuel bed for different passage sizes at an air flux of 0.125 $kg/m^2 s$.	178
<i>Figure 7.20</i> Ash covered grate: mean conversion yield at the surface of the grates as a function of peak gas speed entering the fuel bed for different passage sizes at an air flux of 0.05 $kg/m^2 s$.	178
<i>Figure 7.21</i> Bare grate – no ash layer: minimum oxygen concentration at the surface of the grate for different passage sizes at an inlet flux of 0.2 $kg/m^2 s$.	180
<i>Figure 7.22</i> Bare grate – no ash layer: minimum oxygen concentration at the surface of the grate for different passage sizes at an inlet flux of 0.125 $kg/m^2 s$.	180
<i>Figure 7.23</i> Bare grate – no ash layer: minimum oxygen concentration at the surface of the grate for different passage sizes at an inlet flux of 0.05 $kg/m^2 s$.	181
<i>Figure 7.24</i> Ash covered grate: minimum oxygen concentration at the surface of the grate for different passage sizes at an inlet flux of 0.2 $kg/m^2 s$.	182

<i>Figure 7.25</i> Ash covered grate: minimum oxygen concentration at the surface of the grate for different passage sizes at an inlet flux of $0.125 \text{ kg/m}^2 \text{ s}$	183
<i>Figure 7.26</i> Ash covered grate: minimum oxygen concentration at the surface of the grate for different passage sizes at an inlet flux of $0.05 \text{ kg/m}^2 \text{ s}$	183
<i>Figure 9.1</i> Schematic of a fixed-bed furnace showing how the primary air can be varied along the length of the grate.....	192
<i>Figure A.1</i> Mesh partitioned across three compute nodes	196
<i>Figure A.2</i> Partitioned mesh showing cells overlapping on two compute nodes..	197
<i>Figure A.3</i> Mesh partition showing extended external cells	198
<i>Figure A.4</i> Creating an array containing values from every cell in the domain	200
<i>Figure A.5</i> Cell/node links in a partitioned mesh	202
<i>Figure A.6</i> Mesh deformation without parallel considerations	204
<i>Figure A.7</i> Accumulated cell shrinkage	205
<i>Figure A.8</i> Common duplicated nodes	206
<i>Figure A.9</i> Node priority in 2D.....	207
<i>Figure A.10</i> Identifying outlying cells for nodes 1 – 4 in 2D	207
<i>Figure A.11</i> Node priority in 3D.....	208
<i>Figure A.12</i> Identifying outlying cells for nodes 5 – 8 in 3D	209
<i>Figure A.13</i> Default cell determines the displacement of any duplicated nodes ...	210
<i>Figure A.14</i> Procedure to ensure that duplicated cells are moved by the same amount.....	211
<i>Figure A.15</i> Mesh partition in parallel run at time t	212
<i>Figure A.16</i> Comparing an identical case run in serial and parallel	213
<i>Figure B.1</i> Comparing mole fraction of O_2 for different grid sizes	215
<i>Figure B.2</i> Comparing mole fraction of CO for different grid sizes	215

<i>Figure B.3</i>	Comparing gas speed for different grid sizes	216
<i>Figure B.4</i>	Comparing particle diameter for different grid sizes	216
<i>Figure B.5</i>	Comparing solid phase temperature for different grid sizes.....	217

LIST OF TABLES

<i>Table 1.1</i>	Breakdown of Irish TPES and imports by fuel type in 2009	5
<i>Table 1.2</i>	Typical properties of wood and coal.....	7
<i>Table 1.3</i>	Comparison of conversion technologies.....	15
<i>Table 3.1</i>	Conservation equations of the simulated domain	72
<i>Table 3.2</i>	Gas phase kinetic rates	75
<i>Table 3.3</i>	Solid phase kinetic rates	81
<i>Table 3.4</i>	Heats of solid phase reactions	82
<i>Table 5.1</i>	Parameter combinations investigated for channelling	114
<i>Table 5.2</i>	Initial conditions, boundary conditions, and material specifications.....	115
<i>Table 6.1</i>	Parameter combinations investigated for channelling	138
<i>Table 6.2</i>	Significant results from 3D simulated cases.....	139
<i>Table 7.1</i>	Parameter combinations investigated for channelling	157
<i>Table 7.2</i>	Initial conditions, boundary conditions, and material specifications.....	158
<i>Table C.1</i>	Conservation equations.....	219
<i>Table C.2</i>	Gas phase packed bed relations	220
<i>Table C.3</i>	Heat and mass transfer	222
<i>Table C.4</i>	Solid phase properties	223
<i>Table C.5</i>	Particle and bed shrinkage.....	225
<i>Table C.6</i>	Conversion equations – most common	226

NOMENCLATURE

Symbol	Name	Units
A	Pre exponential factor	<i>varies</i>
A_{spec}	Specific area: ratio of external surface area to volume	1/m
A_g	Active surface area per unit mass	m^2/kg
C	Molar concentration	$kmol/m^3$
C_m	Mass concentration	kg/m^3
c_p	Specific heat capacity	J/kg K
D	Diffusion coefficient	m^2/s
D_h	Hydraulic diameter	m
d_p	Particle (equivalent) diameter	m
E	Activation energy	J/kmol
f_b	Blowing factor	-
g	Gravity	m/s^2
ΔH	Reaction heat	J/kg
ΔH_f	Heat flux	W/m^2
h	Bed height	m
h_{ht}	Heat transfer coefficient	$W/m^2 K$
h_m	Mass transfer coefficient	m/s
k	Reaction rate	<i>varies</i>
k	Turbulence kinetic energy where specified	m^2/s^2
K_i	Intrinsic permeability	m^2
K_r	Relative permeability	m^2
L	Characteristic length	m
m	Mass	kg
M	Molecular weight	kg/kmol
n_{col}	Number of collapses per length scale	-
Nu	Nusselt number	-
Pr	Prandtl number	-
P	Pressure	Pa
R	Universal gas constant	J/kmol K
Re	Reynolds number	-
Sc	Schmidt number	-
Sh	Sherwood number	-
S_m	Mass source term	$kg/m^3 s$
S_p	Momentum source term	$kg/m^2 s^2$
S_Q	Energy source term	W/m^3

S_g	Gaseous reactions source term	$kg/m^3 s$
S_M	Drying source term	$kg/m^3 s$
S_V	Pyrolysis source term	$kg/m^3 s$
S_C	Heterogeneous reaction source term	$kg/m^3 s$
S_k	Turbulence production source term	$kg/m s^3$
S_ϵ	Eddy dissipation source term	$kg/m s^4$
t	Time	s
T	Temperature	K
u	Velocity	m/s
V	Volume	m^3
X	Completion factor	-
Y	Mass fraction	-
x, y	Cartesian coordinates [y upwards]	mm
Greek		
α	Permeability	m^2
β	Forcheimer constant	1/m
β_{gt}	Grate friction coefficient	1/m
γ	Characteristic particle size: $1/A_{spec}$	m
δ_{shr}	Shrinkage factor	-
δ_p	Particle shrinkage factor	-
ϵ	Bed void fraction/porosity	-
ϵ	Eddy dissipation rate	m^2/s^3
ζ	Weighting factor	-
η	Effectiveness factor	-
λ	Thermal conductivity	W/m K
μ	Viscosity	Pa s
ρ	Density	kg/m^3
ρ_{th}	Assumed density of wood fibres [1500]	kg/m^3
σ	Standard deviation	-
σ_b	Stefan-Boltzmann constant	$W/m^2 K^4$
τ_{ij}	Stress tensor	Pa
ν	Rate exponent	-
φ	Particle shrinkage parameter	-
ω	Emissivity	-
Φ	Thiele modulus	-
Ψ	Sphericity	-
Ω	Stoichiometric coefficient	-

Subscripts

0	Initial condition
acc	Accumulated (shrinkage)
b	Bound water
C	Char
char	characteristic
col	Collapse
eff	Effective
evap	evaporation
g	Gas phase
gr	Gas reaction
i, j, k	Species index /directional components
int	intrinsic
l	Free water
M	Moisture
p	Particle
prod	Products
rad	Radiation
react	Reactants
dat	Datum case
s	Solid phase
sd	Solid dry fuel
shr	Continuous shrinkage
sr1	Heat released during solid reaction
sr2	Net enthalpy of gases released/consumed
T	Tar
V	Volatiles
th	Thermal input to plant
e	Electrical output of plant

Abbreviations

AR	As received
CFD	Computational fluid dynamics
CRW	Combustible renewables and waste
d.b.a.f.	Dry basis ash free
EIA	Energy Information Administration
HHV	Higher heating value
IEA	International Energy Agency
LHV	Lower heating value

MSW	Municipal solid waste
SEAI	Sustainable Energy Authority of Ireland
TPES	Total primary energy supply
wb	Wet basis
WHO	World Health Organisation
wt	Weight

1. INTRODUCTION

1.1 Objective and Thesis Overview

The ever-growing environmental and availability concerns associated with fossil fuels have renewed interest in sustainable fuels, such as biomass. Due to transport costs, solid biomass is typically utilised in distributed, small-scale plants where fixed-bed, also termed packed bed, combustion in a grate furnace is one of the most common methods of thermochemical conversion, illustrated in *Figure 1.1*.

Grate furnaces are preferable at small scales, owing to their simplicity, versatility, and low investment cost. The ability to investigate the combustion processes within these furnaces by means of relatively low cost numerical models is desirable, and forms the basis of this study.

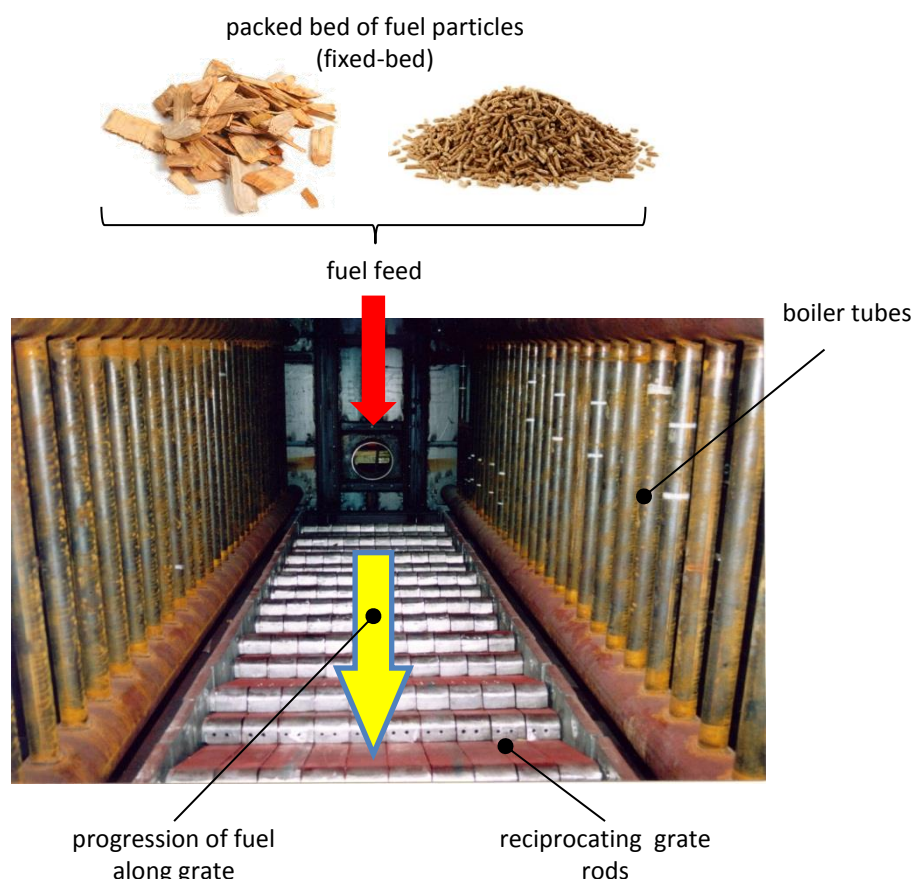


Figure 1.1 Image of industrial grate furnace. Image from [1].

One drawback of fixed-bed combustion is that the properties and structure within the bed can be highly non-uniform, in part due to the intrinsic nature of the fuel (*e.g.* variable composition), but mainly due to inadequate packing and/or mixing of the solid material on the grate [2]. Bed inhomogeneity leads to uneven combustion across the grate, which is believed to increase both emissions and material wear of the grate [3-5]. Addressing such irregularities requires an increased understanding of the combustion processes within the fuel bed.

The objective of this work is therefore to develop an unsteady, three-dimensional numerical model to describe solid fuel combustion in a packed bed, and then to utilise this model to investigate the optimising of grate design in industrial grate (fixed-bed) furnaces.

Chapter 1 outlines the motivation behind this study: the consumption of energy in today's society, and the role that renewables, biomass in particular, have to play. The biomass conversion process and conversion technologies are introduced, and the scope of the thesis is laid out. A review of previous research can be found in Chapter 2. Specifically, section 2.1 examines the submodels for the different thermochemical conversion processes of a solid fuel particle, while section 2.2 describes the state of the art in numerical modelling of fixed-bed biomass combustion.

Chapter 3 presents, in detail, the design and development of the new complete bed model and its integration with the commercial CFD package Fluent. Validation of the bed model is discussed in Chapter 4. A 2D analysis of factors affecting channelling, which is an undesirable phenomenon that may occur during packed bed combustion, is explained in Chapter 5. A 3D investigation of channelling is presented in Chapter 6. The 3D model is also employed to explore measures to reduce the wear of industrial grates, which is described in Chapter 7. Conclusions from the numerical investigations, recommendations for grate design, and future research directions are summarised in Chapter 8. Finally, parallelisation of the bed

model, mesh convergence plots, and a collation of the submodels required to simulate fixed-bed combustion are presented in the appendices.

1.2 Energy Consumption

1.2.1 Global energy consumption

The world currently (2012) consumes over 500 exajoules¹ (EJ), or the equivalent of 12730 million tonnes of oil (Mtoe), every year as shown in *Figure 1.2* [6]. This figure has been steadily increasing over the past four decades, and both the International Energy Agency (IEA) and Energy Information Administration (EIA) expect this trend to continue [7, 8]. This energy is supplied by a variety of sources, including coal, peat, oil, gas, nuclear, hydropower, combustible renewables and waste (CRW), and other renewable sources. In recent years, the rising concern over both peak oil and greenhouse gas emissions has led to an increased interest in renewable energy sources, which have the potential to address issues both of sustainability and of greenhouse gas emissions. According to the IEA, the term renewable energy sources includes CRW, hydropower, wind, solar, geothermal and ocean energy.

The majority of renewable energy is supplied by CRW, in turn defined as: biomass, biogas, liquid biofuels and the renewable portion of municipal waste². CRW accounted for 10% of the total energy supplied in 2010 (*Figure 1.3*) and this is predicted to increase by 11 – 19% by 2030, depending on policy assumptions (*Figure 1.4*). It is worth noting that the utilisation of CRW varies enormously between developing and developed countries, with the combustion of solid biomass for heating and cooking purposes in developing countries accounting for the majority of today's figure. In these countries, this typically occurs in unsophisticated furnaces operating in an unsustainable manner. For instance, the World Health

¹ 1×10^{18} Joules

² The non-biodegradable part of the waste is not technically considered renewable. However, a proper breakdown between renewables and non-renewables is not always available.

Organisation estimates that 1.6 million deaths a year are caused by indoor air pollution from cooking with solid biomass [9].

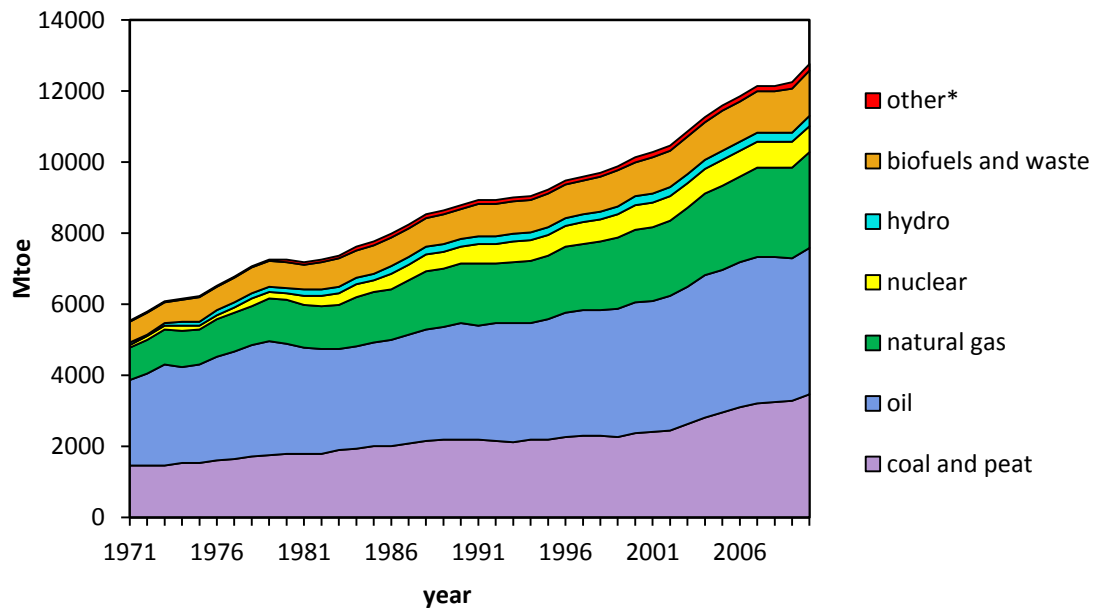


Figure 1.2 Evolution from 1971 to 2010 of world total primary energy supply (TPES) by fuel (Mtoe). *Other includes geothermal, wind, solar, heat etc. Data from [6].

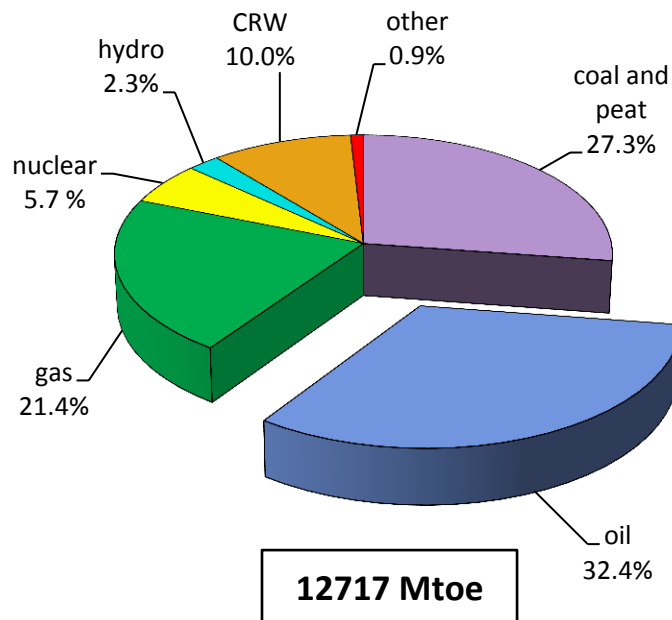


Figure 1.3 2010 fuel share of world TPES. Data from [6].

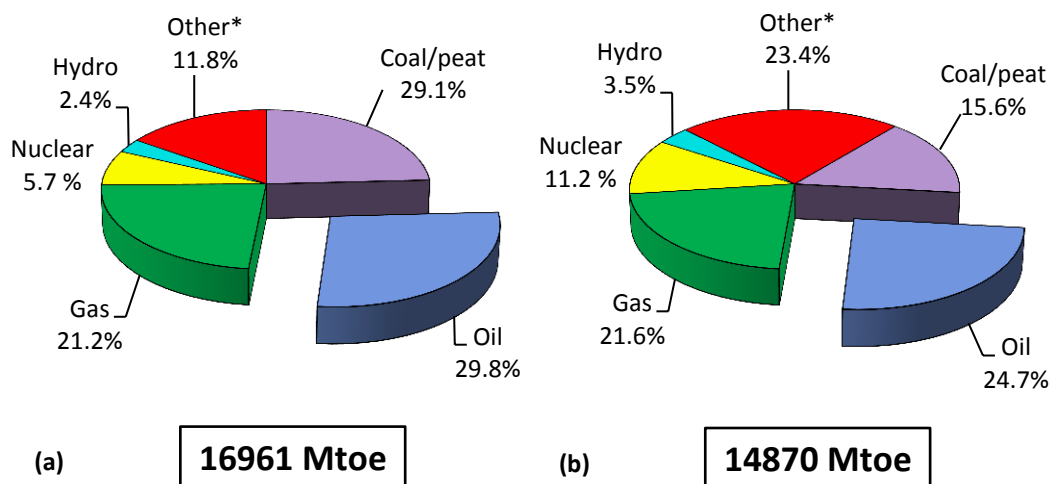


Figure 1.4 Predicted fuel shares of world TPES in 2030: (a) New policies scenario (b) Alternative 450 policy scenario. *Also includes CRW. Data from [6]

1.2.2 Irish energy consumption

Ireland is highly dependent on external fuel sources, and the most recent figures published (2009) [10] indicate that almost 90% of the Total Primary Energy Supply (TPES) is imported. These imports are comprised almost entirely of fossil-fuels (*Table 1.1*). Renewables offer a path to reducing this dependency and accounted for 3.6% of the TPES in 2009, a increase of 33% since 2006.

Table 1.1 Breakdown of Irish TPES and imports by fuel type in 2009

	TPES (ktoe)	TPES %	Import (ktoe)	% Fuel imported
Coal	1436	8.8	1596	100
Peat	845	5.2	-10	0
Oil	8964	54.5	9169	100
Gas	4491	27.5	4135	92
Elect. Imports	39	0.4	39	100
Renewables	581	3.6	42	7.9
Total	16356	100	14971	89.5

A breakdown of Irish renewable energy sources is shown in *Figure 1.5*, with solid biomass and wind constituting the majority.

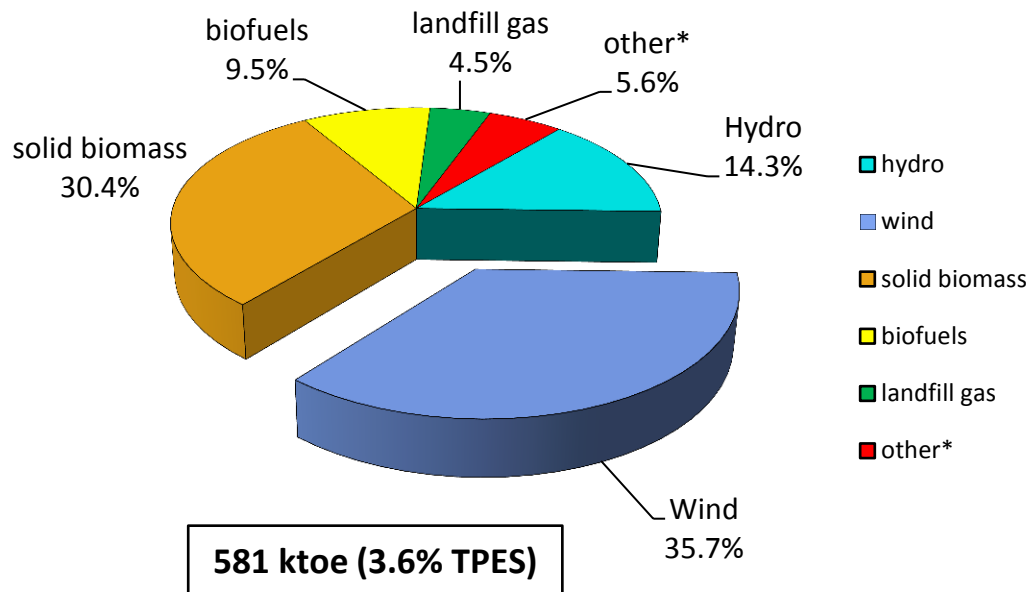


Figure 1.5 2009 share of Ireland's renewable sources. *Other includes geothermal, solar, and biogas. Adapted from [10].

1.3 Biomass as a Renewable Source of Energy

The IEA defines biomass as “any plant matter used directly as fuel or converted into fuels (e.g. charcoal) or electricity and/or heat. Included here are wood, vegetal waste (including wood waste and crops used for energy production), ethanol, animal materials/wastes and sulphite lyes”.

Biomass is a carbon neutral fuel. This means that the carbon released during consumption is balanced by the carbon consumed by photosynthesis during plant growth. Thus, the net contribution to atmospheric CO₂ is zero.

1.3.1 Describing biomass fuel: wood as basis

There are significant variations in the structure, composition, and properties of different biomass fuels, and of these, of municipal solid waste (MSW) in particular. The most commonly used biomass fuel is wood, or wood-derived fuels. Therefore, the structure of wood, which exhibits a basic structural similarity with most other land plants, has been chosen as the basis of this study.

Wood is typically comprised of three main components; cellulose, hemicellulose, and lignin. These generally constitute 95 – 98% *wt db* (weight of dry fuel) of the wood. The remainder consists of low-molecular-weight organic compounds and a small amount of inorganic compounds. The inorganic compounds, known as ash, generally constitute less than 1% *wt db* of the wood and consist of minerals such as potassium, sodium, sulphate, and chlorine [11]. The properties of wood will vary depending on the type, source, pretreatment factors, etc. Some typical properties of wood are compared with coal, its fossil-fuel counterpart in **Table 1.2**, where the higher heating value (HHV) is the gross calorific value of the fuel, or the heat released if all the combustion products are condensed; the ultimate analysis gives the chemical composition of the fuel; the proximate analysis characterises the major components, including moisture content, volatile content, fixed carbon, and ash; and the friability is a measure of how difficult it is to mill the fuel.

Table 1.2 Typical properties of wood and coal [12-16]

		Wood	Coal
Density (dry fuel) [$kg\ m^{-3}$]		400 - 600	1500
Higher heating value (HHV) [$MJ\ kg^{-1}$]		19.4 – 22.3	23 – 34
Friability		low	high
Ultimate analysis %wt db	C	49 – 52	65 – 85
	H	5.4 – 7.0	3.1 – 5.6
	O	40 – 44	3.4 – 13.8
	N	0.00 – 0.35	0.9 – 1.6
	S	0.00 – 0.07	0.4 – 4.3
Proximate analysis %wt db	moisture ^{3,4}	5 – 50	< 15
	volatiles	70 – 87	16 – 35
	char	12 – 30	35 – 80
	ash	0.2 – 3.4	6.0 – 23.3

³ Moisture content is specified as a percentage of the dry wood:

$$\text{Moisture content} = \frac{\text{Moist weight} - \text{dry weight}}{\text{dry weight}} \times 100$$

⁴ As used in combustion systems. Moisture content of green wood is approximately 60%.

1.3.2 Logistics

Energy density

Fuel transportation costs are typically proportional to the volume rather than the weight of fuel transported. The energy density [$MJ m^{-3}$] therefore gives an indication of transport cost; it is the product of the HHV and the density, and is inversely related to transportation costs. Based on *Table 1.2*, the energy density of coal is approximately 3 – 5 times that of wood, resulting in significantly lower transportation costs. To remain economically viable, plants burning wood must, therefore, be located close to the fuel source [17].

Furnace size

Biomass furnaces are significantly larger than coal furnaces of equivalent heat output for several reasons:

- The volatile content of wood is significantly higher than coal. Therefore, the combustion chamber must be larger to cope with the increased volume of combustible gases released.
- The energy density of wood is much lower than coal. To achieve the same heat output, a significantly larger volume of fuel must therefore be fired.
- Heat and mass transfer rates decrease as particle size increases. Because wood is difficult to mill into very small pieces, longer residence times are required to ensure complete combustion.

The increased furnace size and limited transport range places an economic restriction on the size of dedicated wood-fired plants. As a result, dedicated wood-firing plants are usually small to medium-scale plants, ranging from domestic stoves to $\sim 50 MW_e$ ($\sim 125 MW_{th}$) utility plants [17].

Firing wood in larger scale plants is typically done on a co-firing basis, where the wood is burned alongside another solid fuel, usually coal. The wood or biomass typically accounts for roughly 10 – 15% of the total output of a co-firing plant, such as the Drax power plant in the UK [18].

1.4 Overview of the Thermochemical Conversion of Biomass

The thermochemical conversion of thermally degradable fuels, such as biomass and coal, involves a number of distinct processes. By comparison with gaseous fuels, the overall process is complex, but it is generally accepted to occur through the following mechanisms [15, 19], as illustrated in *Figure 1.6*.

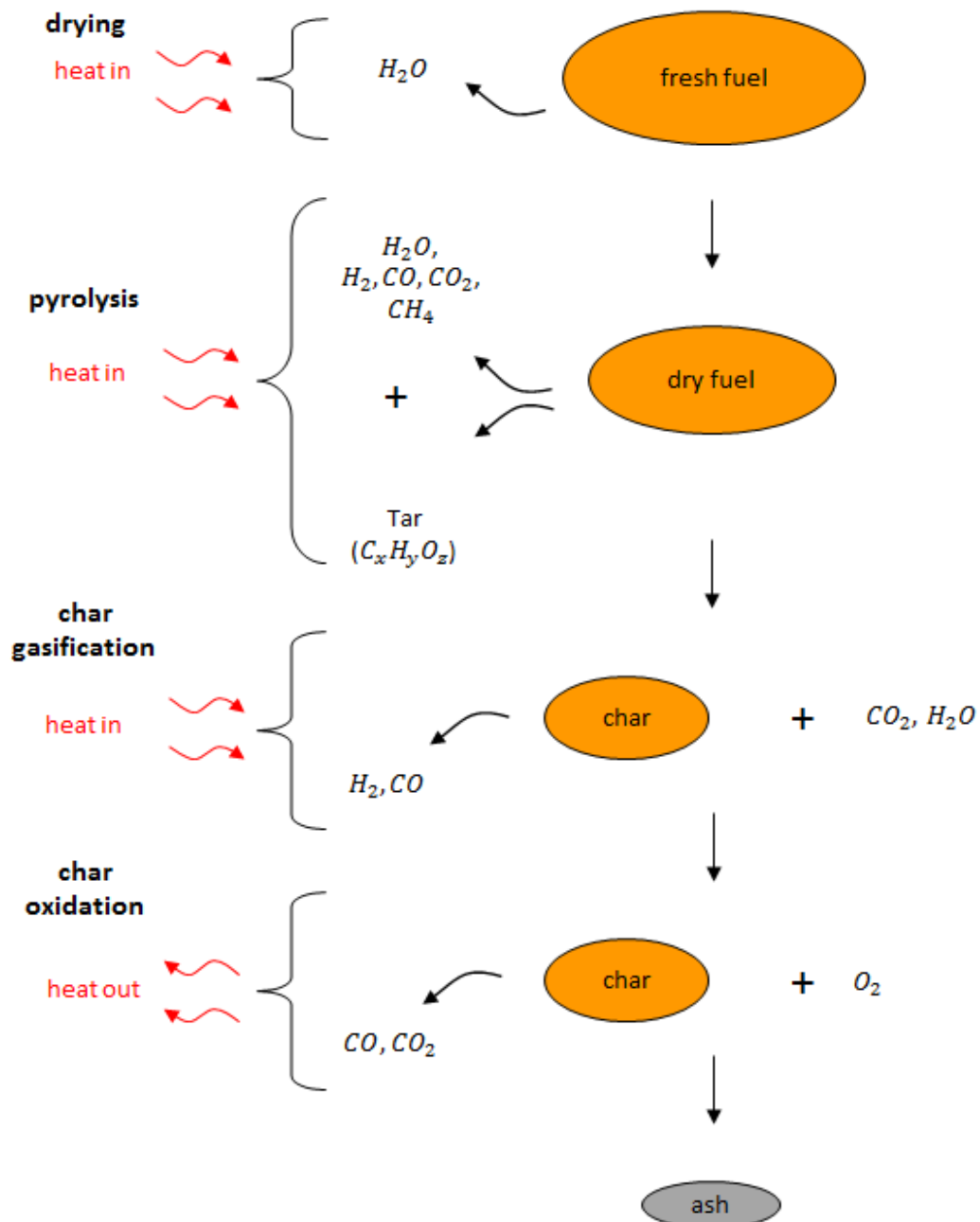


Figure 1.6 Separate stages of the thermal degradation of a wood particle. Each process is shown separately for clarity. In reality, the different stages may overlap.

Inert heating and drying

Upon entry to the combustor, heat is transferred to the fuel by conduction, convection, and radiation from the surroundings. Drying will occur below the boiling point due to diffusion of water vapour from the particle, but will increase rapidly once the boiling point is reached. This process is endothermic.

Pyrolysis

Pyrolysis, also referred to as devolatilisation, is the thermal degradation of the fuel in the *absence* of an oxidising agent. The pyrolysis rate is a function of temperature, pressure, heating rate, fuel type and composition. During this process, tars and a variety of low-molecular weight gases are released, leaving behind a highly carbonaceous fuel called char. The term devolatilisation will be synonymous with pyrolysis throughout this work. This process is also endothermic.

Gasification

This is the thermal degradation of the fuel in the *presence* of an oxidising agent. The term gasification refers to the heterogeneous reactions between the char created during pyrolysis and reactants *other* than oxygen, mainly CO_2 and H_2O . Gasification typically occurs when the char is reacted in sub-stoichiometric⁵ conditions at elevated temperatures ($> 700^\circ C$). During this process, additional low-molecular weight gases are produced. Throughout this work, the term gasification will refer to heterogeneous char reactions with reactants other than O_2 . These reactions are endothermic.

Combustion

This is defined as a complete oxidation of the fuel. The term can be applied to the heterogeneous reaction between O_2 and char, or the homogeneous reactions between O_2 and the combustible gases and tars produced during the pyrolysis and

⁵ In an idealised reaction, the stoichiometric ratio is the exact ratio of reagents to fuel required for a complete reaction. Above, it refers to the amount of oxygen required for complete combustion.

gasification processes. These reactions are exothermic and supply the heat required to sustain the preceding reactions. Upon completion of these reactions, only non-combustible inorganic matter, or ash, will remain.

Drying and pyrolysis are always the first stages of the combustion process (*Figure 1.6*). However, it is possible for all stages to occur simultaneously in a single particle, particularly in the case of larger particles where a thermal gradient may exist, as shown in *Figure 1.7*. Although complete combustion is the most widespread and proven method of biomass conversion, the production of gaseous and liquid biofuels via *sub-stoichiometric conversion* (i.e. pyrolysis and gasification) has seen renewed interest in recent years, since these fuels can be burned in internal combustion engines, primarily gas turbines for high efficiency power production. *Figure 1.8* illustrates the major chemical and physical phenomena occurring during solid conversion.

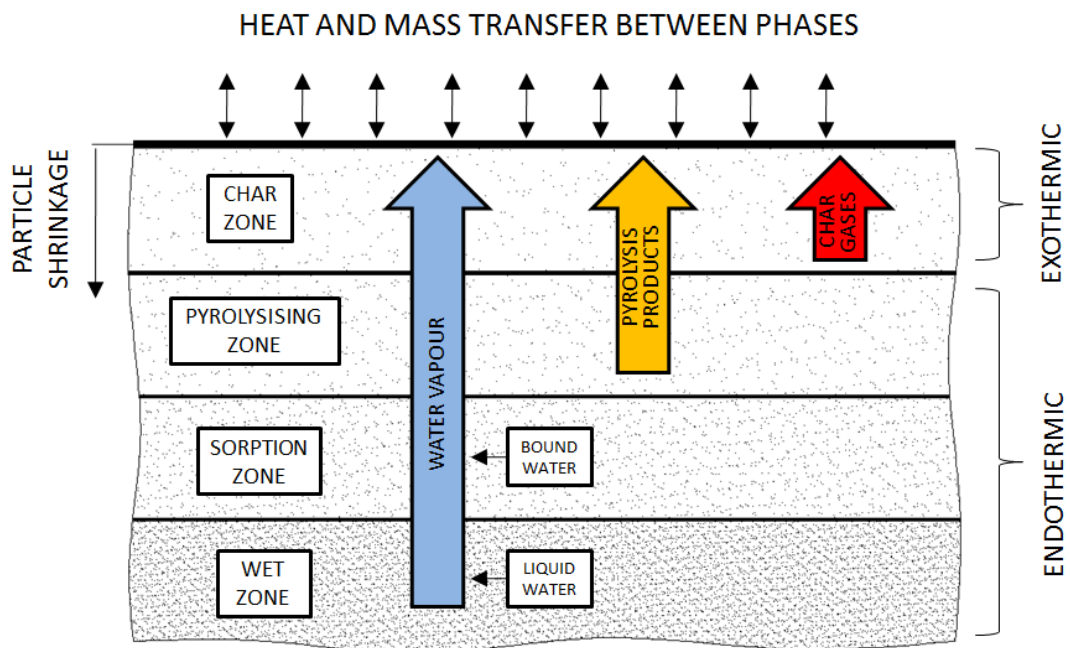


Figure 1.7 Schematic diagram of the thermal degradation process within a thermally thick particle. Adapted from [11].

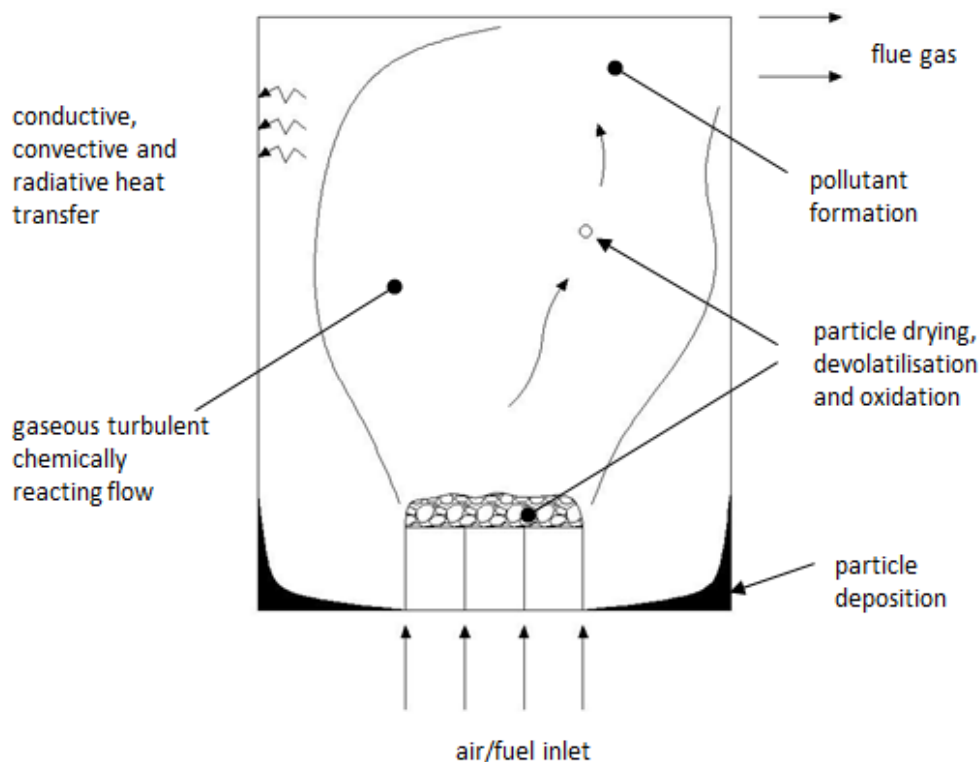


Figure 1.8 Major chemical and physical mechanisms during solid fuel combustion.

1.5 Thermochemical Conversion Technologies

1.5.1 Overview of conversion methods

There are three principal technologies used for the conversion of biomass: fixed-bed, or grate, furnaces; fluidised-bed reactors; and pulverised combustors (*Figure 1.9*). These furnaces will be described briefly below, with some key operating parameters outlined in *Table 1.3*. Fixed-bed conversion is the focus of this study, and is discussed in more detail in Section 1.5.2.

1.5.1.1 Fixed-bed (grate) conversion

Combustion in fixed-beds, also known as grate furnaces, is the simplest and most common method of converting the chemical energy stored in biomass to a more useful form of energy, *i.e.* heat, with open fires and domestic stoves being familiar examples. In these furnaces, drying, pyrolysis, char gasification, and char oxidation

takes place on a grate, with primary combustion air⁶ typically distributed through the grate.

Grate furnaces have the lowest investment cost of all conversion technologies, making them favourable to small-scale applications. Operational costs are also lower than other systems because grate furnaces are capable of burning untreated, moist fuel, ranging in size from pellets (6 – 10 mm) to wood logs [15]. Primary air velocity, typically 0.1 m/s in utility plants [20], is insufficient to lift the fuel particles, thus they lie in mutual contact and a well-defined fuel bed is formed.

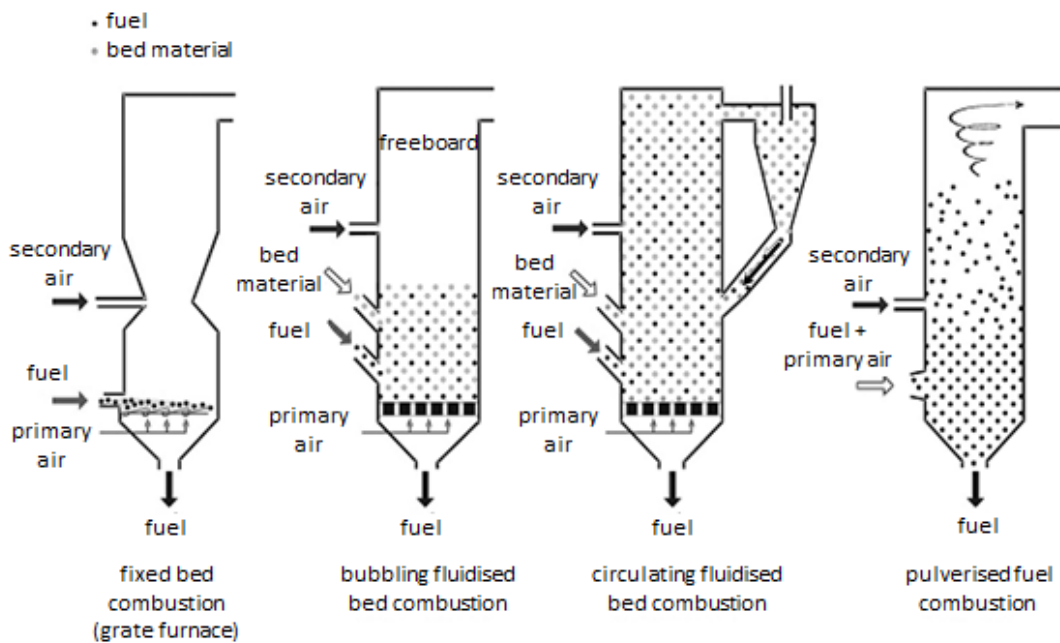


Figure 1.9 Principal combustion technologies for biomass. Adapted from [15].

⁶ Modern combustion systems typically use air *staging* to prevent incomplete combustion and to reduce NO_x emissions. Primary air is the air which first comes in contact with the fuel. Secondary (or even tertiary) air is typically supplied after partial oxidation of the solid has occurred. This serves to increase mixing and ensure complete combustion of released combustible gases and of any remaining solid.

1.5.1.2 Fluidised-bed conversion (FBC)

In a fluidised-bed convertor, the solid fuel is mixed with an inert material, typically sand. The vertical speed of the inlet air is sufficient to cause the bed material to become suspended, effectively making the entire mass of solids behave like a fluid; the different gas speeds encountered are shown in *Figure 1.10*. Unlike grate furnaces, the major component in the fuel-bed is an inert material such as sand (referred to as bed material), with the remainder consisting of fuel and fuel dependent additives. The bed material acts as a thermal store and significantly improves mixing and heat transfer when the fuel bed is fluidised. This promotes combustion at a lower and more uniform temperature than other systems, with significant benefits to emissions. Fluidised bed furnaces are also capable of burning low-quality, high-moisture fuels. There are two distinct types of FBC:

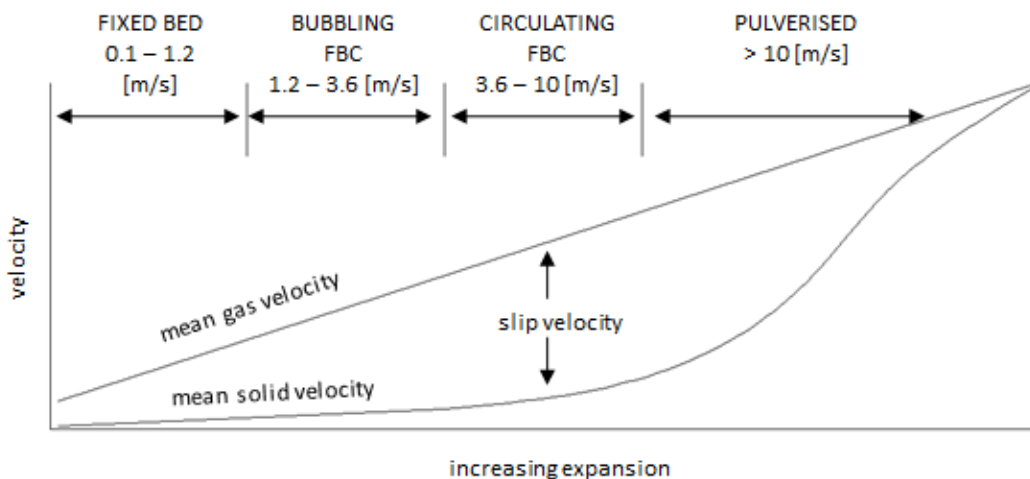


Figure 1.10 Fluidising velocity of air for various bed systems. Adapted from [12].

Bubbling fluidised-bed (BFB)

The vertical air speed is high enough to cause fluidisation of the fuel bed, but low enough to prevent solid particles from escaping the bed, termed elutriation.

Circulating fluidised-beds (CFB)

CFBs have a higher air speed than BFBs. This promotes elutriation of smaller, potentially unburned particles from the fuel bed. A cyclone is required downstream to separate these particles from the flue gas for their return to the fuel bed.

1.5.1.3 Pulverised fuel conversion

Pulverised fuel conversion is the dominant technology for coal-fired utility plants. The fuel is transported pneumatically to the furnace and remains entrained in the gas flow throughout the conversion process. To remain entrained, the gas flow must exceed the terminal velocity of the particle, which necessitates higher gas velocities and smaller particle sizes than either fixed-bed or fluidised-bed furnaces. Pulverised furnaces are also sensitive to moisture content in the fuel, owing to the limited residence time of the fuel particles. This technology is best suited to large-scale plants, such as coal-fired centralised utility plants. Due to the logistical issues discussed in Section 1.3.2, biomass is rarely the dedicated fuel source in these large-scale pulverised furnaces, but rather is co-fired with another fuel, typically coal.

Table 1.3 Comparison of conversion technologies [12, 15]

	Fixed	BFBC	CFBC	Pulverised
Fuel feed size ⁷ [mm]	<50	< 80	< 40	<2
Plant size [MW _{th}]	<20	>20	>30	>>30
Furnace temperature [K]	1350 – 1650	1050 – 1200	1050 – 1200	1450 – 1800
Air inlet velocity [m/s]	0.1 – 1.2	1.2 – 3.6	3.6 – 10	>10
Excess oxygen [%]	6 – 8	3 – 4	1 – 2	4 – 6
Moisture content (max) [%wt wb]	<65	<65	<65	<20
Operating costs	Low	High	High	High
Key issue	Non-homogeneous combustion	Very sensitive to agglomeration and fouling within the bed		Fuel sensitive

1.5.2 Fixed-bed conversion

As mentioned above, familiar examples of fixed-bed combustion include open fires and domestic stoves, where the fuel is fed in a batch-wise or intermittent manner. Batch-firing, while both simple and cheap, has an adverse impact on performance as

⁷ Qualitative comparison only: Fuel feed size is a function of the shape (*i.e.* specific area) and density of the fuel

it is very difficult to control the heat output, resulting in incomplete combustion and increased emissions [15].

As such, continuous firing is favoured for larger facilities and more sophisticated domestic burners. There are different configurations for supplying both fuel and air to the fixed bed, as illustrated in *Figure 1.11*.

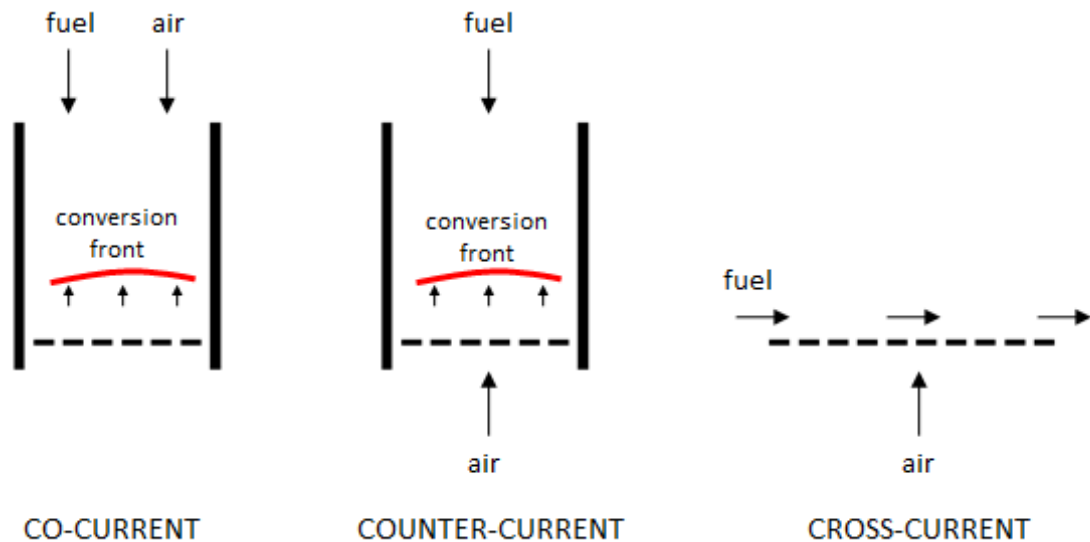


Figure 1.11 Fuel/air feed configurations in a fixed bed. Adapted from [3].

The *co-current* or *downdraft* arrangement is favoured for modern small-scale boilers and gasifiers because it provides a stable conversion (*i.e.* ignition) front, which travels in the opposite direction to the air supply. This setup also reduces the production of tars that can lead to issues such as fouling.

The *counter-current* or *updraft* arrangement is used in less sophisticated systems, such as open fires or old boilers, primarily due to its simplicity. The separation of fuel and air supply provides an inherent safety feature and since air flow is induced by natural convection, no fans are required. The downside is that this system is more difficult to control and tar production is higher than for other arrangements. Co-current and counter-current arrangements are normally used for fixed-grate furnaces and gasifiers, which are typically employed on a domestic or small-scale as they are the least expensive type of grate furnace.

Larger-scale industrial systems generally use more sophisticated moving grates. Moving grates are ideally suited to continuous firing because fuel can be injected at one end of the grate, and ash removed at the other, as illustrated in Figure 1.11. Fuel transport, and thus residence time, can be controlled by adjusting the movement of the grate. The distribution of primary air can also be controlled, enabling optimum fuel-air ratios at different stages of the conversion process. Gases released from the fuel-bed and any entrained particles will continue to burn above the fuel-bed in the freeboard, or overfire, region. This necessitates a secondary air supply to ensure the complete combustion of all the fuel (*Figure 1.12*). Advanced secondary air supplies play a significant role in mixing, burnout, and emissions in a grate-furnace, and are considered a breakthrough in the technology [21].

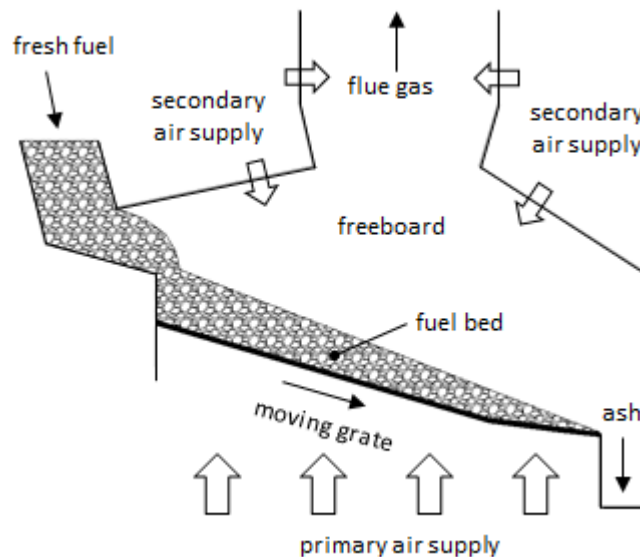


Figure 1.12 Schematic of a fixed-bed furnace with a moving grate

The most common types of moving grate are: travelling grates, where grate bars are arranged to form a conveyor which transports the fuel, *Figure 1.13* (a); sliding rod or reciprocating grates, where fuel transport is controlled by the reciprocating movement of the rods, *Figure 1.13* (b); and vibrating grates, where an inclined stationary grate vibrates and fuel transport is dictated primarily by gravity. Primary air is typically supplied beneath the grate, and is then distributed along and across the fuel bed via holes in the grate bars and/or the slots between them,

with measures generally taken to prevent air escaping between the grate and the furnace wall. The distribution of air along and across the grate has a significant effect on combustion in the fuel-bed, and is one of the most important parameters in the design of the grate [3].

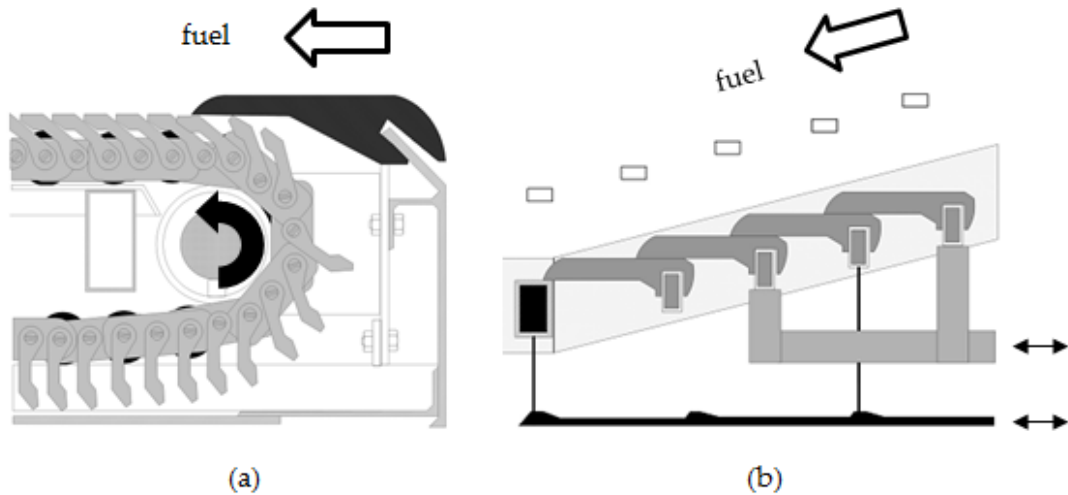


Figure 1.13 Types of moving grate: (a) travelling grate; (b) reciprocating grate. Adapted from [15].

1.5.3 Grate-firing – key issues

Yin *et al.* [21] provided a state-of-the-art review on biomass combustion in grate furnaces and grouped the main issues into pollutant emissions, fouling, and fuel-bed specific issues, as described below.

1.5.3.1 Pollutant emissions

Grate-fired boilers typically have a lower thermal efficiency than fluidised-bed or pulverised fuel boilers. This is the result of incomplete combustion, which can lead to increased emissions of CO , hydrocarbons (C_xH_y), tar, polycyclic aromatic hydrocarbons (PAH), and unburned char. The relatively high amount of elements such as chlorine (Cl) and heavy metal, which are present in some biomass fuels, can worsen the problem. As mentioned in 1.5.2, the secondary air supply plays a key role in addressing incomplete combustion. Nitrogen oxide (NO_x) emissions from biomass-fired grate furnaces are primarily due to the nitrogen contained in the fuel. As a

result, it is desirable to operate the fuel-bed under sub-stoichiometric conditions, which reduces the release of NO_x -forming precursors, including NH_3 , HCN and NO [21, 22]. This has important implications for the air distribution, and thus ignition rate, across the fuel bed.

1.5.3.2 Deposit formation and corrosion (fouling)

The high concentrations of Cl and metals, such as K and Na , which are present in biomass are known to cause deposition and corrosion [23-27]. Deposition and corrosion reduce, respectively, the functionality and the lifetime of the furnace, and are dependent on both fuel composition and on combustion conditions. In particular, biomass ash tends to contain large amounts of alkali salt; including KCl , $NaCl$, Na_2SO_4 and K_2SO_4 . These can lower the melting temperature of the ash causing it to adhere to boiler surfaces. It is worth noting that this problem is not confined to grate furnaces.

1.5.3.3 Fuel bed specific issues

One influential phenomenon in furnace performance, and a salient indicator of unbalanced combustion, is the 'channelling' which occurs when relatively porous passages develop due to non-uniformities within the fuel bed or alongside a bounding wall of the furnace. Whether caused by spatial variations in fuel properties or by fuel packing, these passages result in uneven air distribution, and thus combustion, which eventually causes a depression to form in the surface of the bed. The uneven combustion caused by channelling can also lead to an increase in emissions and grate wear. Mitigating the problem requires the optimisation of the grate design, the furnace controls, the fuel mixing, and the fuel feed processes [4, 5, 28].

Modifying the shape of the grate will also change combustion conditions near the grate surface, potentially affecting the rate of wear on the grate. Increased grate wear leads to an increase in maintenance costs and a reduction in availability, and should therefore be taken into account when optimising the design of the grate.

1.6 Modelling Combustion in a Grate Furnace

Biomass combustion in fixed-bed furnaces is complex and difficult to measure. The environment is hostile and difficult to observe, and the overall combustion process is highly complex, being influenced by a wide variety of parameters. As a result, conceptual modelling by means of computational fluid dynamics (CFD) has become a useful tool. Simulations based on validated models can give further insight into the combustion process and aid the optimisation of furnace design and operation. In particular, CFD is useful for investigating the influence of individual parameters, since these are easily altered to analyse their effect.

As illustrated in *Figure 1.12*, grate furnaces can effectively be divided into two regions: the fuel bed, comprised of both gaseous and particulate phases; and the freeboard, comprised of gas only. Depending on the objective, CFD can be used to predict combustion in the freeboard, in the fuel bed, or in both together.

1.6.1 Freeboard modelling

Submodels to simulate gas flow and gas phase combustion are a standard feature of commercial CFD packages. Modelling the gas-only freeboard is, therefore, relatively straightforward for tasks such as optimising the secondary air supply to increase mixing, improve burnout, and reduce emissions [21].

More specialised simulations, such as predicting the deposition of particulate matter on furnace surfaces or the formation of certain pollutants does, however, require the development and implementation of additional submodels by the user. A common challenge with freeboard-only models is assigning appropriate inlet conditions, *i.e.* composition, temperature, and flow characteristics of the gases leaving the fuel bed and entering the freeboard. These must be determined either by means of measurements or of a fuel bed model.

1.6.2 Fuel bed modelling

Owing to the complex conversion processes of the solid fuel particles, and the intense interactions between the particulate and gaseous phases, modelling the fuel bed in a grate furnace is inherently much more complicated – and thus more computationally demanding – than modelling the freeboard.

The submodels describing these conversion processes are not available as built-in features of current CFD packages; they must be developed and implemented by the user in order to investigate issues specific to the fuel bed.

1.7 Scope of this Thesis

The objective of this study is to design and develop a three-dimensional (3D) numerical model to predict solid fuel combustion in a packed bed, and to utilise this model to investigate the optimisation of the grate design in industrial fixed-bed furnaces.

To this end, an unsteady two-dimensional (2D) model is initially developed (Chapter 3), which includes drying, pyrolysis, and heterogeneous char reactions, and incorporates bed shrinkage processes comprised of both continuous shrinkage and abrupt collapses. This model is also capable of representing spatial non-uniformities which may occur throughout a bed, arising from irregular packing and non-homogeneous fuel composition. The model is validated (Chapter 4) – insofar as possible given the sparsity of measurements available – and then applied to investigate factors affecting channelling in a randomly-packed bed containing a high-porosity passage (Chapter 5). The factors investigated include resistance to flow through the grate, bed height, flue gas recirculation, and initial moisture content of the fuel. This section of the overall study has been published in a peer-reviewed journal [29].

The 2D model is then extended to three dimensions, while maintaining all features. This is the first 3D model capable of predicting the combustion and shrinkage of a

randomly packed bed of biomass. Owing to the computational demands of 3D fixed-bed predictions, the model is parallelised to improve practicality (Appendix A). The effect of grate resistance on channelling in a randomly-packed bed containing a high-porosity passage is examined for two differently shaped passages (Chapter 6). Results are compared with observations and with the previous 2D predictions.

Different grate designs are then investigated to determine measures to reduce grate wear (Chapter 7). High levels of wear are attributed to high grate temperatures and/or to a low concentration of oxygen at the surface of the grate, which potentially causes carburisation of the steel. These factors are affected by the shape of the grate, and the 3D model enables 3D features, such as the size and spacing of the holes in the grate, to be explored. Additional heat transfer mechanisms are included to account for heat transfer between the grate and the gas phase, and between the grate and the particulate phase. Suggestions for grate design are deduced from the predictions.

It should be noted that although this study focuses on the combustion of biomass, the model that is developed and the methodology applied are readily adaptable to other solid fuels, such as coal and municipal solid waste (MSW), given appropriate kinetic data.

2. REVIEW OF PREVIOUS WORK

This chapter presents two separate literature reviews. Section 2.1 collates the substantial number of different submodels available for each stage of the thermochemical conversion process of a solid fuel particle, including: drying; pyrolysis; and the heterogeneous char reactions, gasification and oxidation. Each submodel is explained, with common nomenclature used throughout.

Section 2.2 introduces the different approaches that have been used to model a fixed bed, and outlines the progress in fixed-bed modelling of biomass and waste over the past two decades. Existing work that is closely related to the objectives of this study is reviewed in more detail, and paths for improvement are highlighted.

2.1 Review of Thermochemical Conversion Models

2.1.1 Drying

The moisture content of wood-based biomass-fuels is highly variable and can account for over 100%wt db of the fuel. In wood, this water is present in three different forms⁸ [30]:

Free (liquid) water

The fibre saturation point, $X_{M,fspr}$, for wood is approximately 30%wt db. Above this point, $X_M > 30\%wt db$, free or liquid water occupies voids within the wood structure. Transport is due to capillary flow through the voids. The energy required to evaporate the water is the latent heat of evaporation (ΔH_{evap}).

Bound water

Bound water is water which is adsorbed and believed to be hydrogen-bonded to the cellulose and hemicellulose fibres. Below the fibre saturation point, $X_M \leq 30\% db$, all

⁸ Water contained within the chemical composition of the wood is not considered as part of the drying process.

moisture is believed to be bound to the wood fibres. Transport occurs due to diffusion of the water. Energy required to evaporate the water will have to overcome the latent heat of evaporation in addition to the heat of adsorption.

Water vapour

This is the result of the evaporation of bound and liquid water within the solid. Transport is due to convection and diffusion.

Solid fuels are typically injected into furnaces at relatively low temperatures to prevent premature fuel loss due to pyrolysis. Upon entry to the combustor, the fuel is then heated to the surrounding temperature. Drying will initially occur due to diffusion of water from the particle surface, but will increase rapidly once the evaporation temperature, approximately 100°C, is reached. Drying will initially occur at the outer boundary of the particle where the temperature is highest, but the drying front will move inwards due to heat and mass transport. Currently, there are four methods of modelling drying in CFD:

2.1.1.1 Constant temperature drying model

Drying begins when the fuel has reached a predefined temperature, T_{evap} , typically taken to be 100 °C. While at this temperature, all heat transferred to the fuel is used to vaporise any moisture present. No distinction is made between the forms of water present. The drying rate is limited solely by heat transfer to the particle [31]:

$$\frac{d\rho_M}{dt} = \begin{cases} -0.5 \frac{(T_s - T_{evap})\rho_s c_{p,s}}{\Delta H_M \Delta t}, & \text{if } T_s \geq T_{evap} \\ 0, & \text{if } T_s < T_{evap} \end{cases} \quad (2.1)$$

where $d\rho_M/dt$ is the mass loss of moisture from the solid phase, T_s is the temperature of the solid phase, T_{evap} is the predefined evaporation temperature, ρ_s is the density of the solid phase, $c_{p,s}$ is the specific heat capacity of the solid phase, ΔH_M the latent heat of evaporation, and Δt is the elapsed time. The major advantage of the constant temperature model is that experimentally observed trends, such as a temperature plateau around the evaporation temperature, are predicted without the need for data [31]. The disadvantage of the model is that it overlooks drying due to

transport and diffusion of bound water, which will occur below the set evaporation temperature. Furthermore, since drying is assumed to occur at a single predefined temperature, the drying zone is reduced to an infinitesimally thick front which propagates through the particle. This does not match experimental observations, and may cause discrepancies when the thickness of the drying zone is not negligible compared to the thickness of the particle [32]. Finally, because the moisture is released at a given temperature, for time dependent simulations this creates a step function in time, which can cause numerical instability. As a result, Eq. (2.1) is typically modified to improve stability. For example, both Yang *et al.* [33] and Collazo *et al.* [34] applied a relaxation factor to Eq. (2.1) which effectively means that only part of the heat transferred to the particle is consumed by drying, with the balance going to heating the particle above the evaporation temperature.

2.1.1.2 Kinetic method

An alternative is to represent the drying process as a chemical reaction [31, 35]:

$$\frac{d\rho_M}{dt} = -k_M\rho_M \quad (2.2)$$

where ρ_M is the density of moisture in the solid phase, and k_M is the reaction rate, defined by means of a first-order Arrhenius equation [36]:

$$k_M = A_M e^{-E_M/RT} \quad (2.3)$$

where A_M is the pre-exponential factor, and E_M is the activation energy. The kinetic model is numerically stable and accounts for a varying strength, or reduced drying rate, of bound water [31]. It also predicts the temperature profile of the fuel during the drying period better than the constant temperature model [32]. However, the kinetic constants, A_M and E_M in Eq. (2.3), are only valid for the conditions under which they are derived. This was illustrated by Peters and Bruch [31] who compared the kinetic and constant temperature models for drying of a large wood particle. When using the kinetic constants given by Chan *et al.* [35], they found that the kinetic model under-predicted the drying rate. Similarly, Bryden *et al.* [32]

adjusted the rate constants so that drying would occur within a desired temperature range, effectively tuning the model constants based on experience.

2.1.1.3 Algebraic drying model

In this model, drying is determined by a combination of heat transfer and vapour-liquid equilibrium. Similarly to the constant temperature model, when the solid reaches T_{evap} , all heat transferred to the fuel is used to vaporise any moisture present. However, T_{evap} is not assumed to be constant, but is instead expressed as a function of the moisture content of the fuel, Y_M . When Y_M is greater than 14.4% db, T_{evap} is typically set to 100°C, and the model behaves identically to the constant temperature model. When Y_M is less than 14.4%wt db, T_{evap} is determined by [37]:

$$T_{evap} = 1/(2.130 \times 10^{-3} + 2.778 \times 10^{-4} \ln(Y_M) + 9.997 \times 10^{-6} [\ln(Y_M)]^2 - 1.461 \times 10^{-5} [\ln(Y_M)]^3) \quad (2.4)$$

where Y_M is the mass fraction of moisture in the solid phase, expressed as a %wt db. The algebraic model of Alves and Figueiredo [37], is effectively an experimentally correlated improvement of the constant temperature model; while it improves performance, usage outside of the range of experimental conditions comes with a caveat.

2.1.1.4 Transport drying model

The transport model is the most sophisticated of the drying models, and attempts to capture the detailed transport mechanisms behind the drying process. These include the transport of bound water, of liquid water, and of water vapour within the fuel particle, followed by diffusion from the outer surface. For the conservation of *bound* water, transport is modelled as a diffusion process [11]:

$$\frac{\partial \rho_{M,b}}{\partial t} + \frac{\partial (\rho_{M,b} u_{M,b})}{\partial x} = S_{M,b} \quad (2.5)$$

$$\rho_{M,b} u_{M,b} = \rho_{SD} D_{eff,M} \frac{\partial}{\partial x} \left(\frac{\rho_{M,b}}{\rho_{SD}} \right) \quad (2.6)$$

where subscript b refers to bound water, $u_{M,b}$ is the velocity of the moisture, $D_{eff,M}$ is the molecular diffusion coefficient of water, and $S_{M,b}$ is the rate of desorption of bound water. For the conservation of liquid water, transport is due to capillarity:

$$\frac{\partial \rho_{M,l}}{\partial t} + \frac{\partial(\rho_{M,l}u_{M,l})}{\partial x} = S_{M,l} \quad (2.7)$$

where subscript l refers to liquid or free water, $S_{M,l}$ is the evaporation rate, and $u_{M,l}$ is given by Darcy's law:

$$u_{M,l} = -\frac{K_{i,l}K_{r,l}}{\mu_M} \frac{\partial P_l}{\partial x} \quad (2.8)$$

where $K_{i,l}$ is the intrinsic permeability for the water, $K_{r,l}$ is the relative permeability for the water, μ_M is the viscosity of liquid water, and P_l is the liquid pressure, which is related to the gaseous pressure by capillarity:

$$P_l = P_g - P_c \quad (2.9)$$

where P_g is the gas pressure, and P_c is the capillary pressure. To ensure the conservation of water vapour, transport is due to the combination of convection of the bulk gas together with diffusion within the bulk gas:

$$\frac{\partial Y_{M,g}\rho_g}{\partial t} + \frac{\partial(Y_{M,g}\rho_g u_g)}{\partial x} = \frac{\partial}{\partial x} \left(\rho_g D_{eff,M} \frac{\partial Y_{M,g}}{\partial x} \right) + S_{M,g} \quad (2.10)$$

where $Y_{M,g}$ is the mass fraction of water vapour in the gas phase, ρ_g is the density of the gas phase, u_g is the superficial velocity of the gas phase, and $S_{M,g}$ accounts for any sources of water vapour to the gas phase. The superficial gas velocity is described using Darcy's law:

$$u_g = -\frac{K_{i,g}K_{r,g}}{\mu_g} \frac{\partial P_g}{\partial x} \quad (2.11)$$

where $K_{i,g}$ is the intrinsic permeability for the water vapour, and $K_{r,g}$ is the relative permeability for the water vapour, and μ_g is the viscosity of the gas phase. Moisture loss occurs through the boundary of the particle, and is modelled by means of mass transfer correlations. Thus, the moisture loss through the particle boundary is:

$$\frac{d\rho_M}{dt} = S_{M,b} + S_{M,l} + S_{M,g} = h_m A (\rho_{M,sur} - \rho_{M,\infty}) \quad (2.12)$$

where $\rho_{M,sur}$ is the moisture density at the surface, $\rho_{M,\infty}$ is the ambient moisture density, A is the surface area at the boundary, and h_m is the mass transfer coefficient.

Free and bound water differ in their respective energy levels. Free water in the wood is treated as liquid water; therefore the energy required to change state is simply the heat of evaporation. The vaporisation of bound water, however, requires additional energy; this is accounted for by including the heat of desorption:

$$Y_M \geq Y_{M,fsp} \quad \Delta H_{tot} = \Delta H_M \quad (2.13)$$

$$Y_M < Y_{M,fsp} \quad \Delta H_{tot} = \Delta H_M + \Delta H_{sorp} \quad (2.14)$$

where $Y_{M,fsp}$ is the fibre saturation point (≈ 0.3 for wood), ΔH_{tot} is the total heat of reaction, and ΔH_{sorp} is the heat of desorption. Additional information on the transport model, including a detailed description of the model and the assumptions required for each variable, can be found in Grönli [11] and Ouelhazi [38].

2.1.1.5 Discussion of drying models

The transport model is the most detailed method of representing drying, but also the most computationally demanding because the particle shape and material properties must be finely resolved throughout the entire particle, and additional conservation equations must be solved for each form of water within the particle. Furthermore, the added complexity introduces a significant number of additional parameter variables, such as the intrinsic and relative permeability, capillary pressure, etc., many of which are difficult to determine experimentally. Discrepancies in the values of these parameters and variables may decrease the representativeness of the model, particularly in combustion situations where the structure of the wood is continuously changing.

The constant temperature model and the kinetic model are the most commonly utilised drying models in the literature, attributable to their simplicity. Alves and

Figueiredo [37] demonstrated, however, that neglecting moisture transport within the solid, free water in particular, limited the range of validity of drying models to moisture contents below 45%wt db. Within these limits, if suitable experimental data are available, the kinetic model is preferable; however, in the absence of suitable measurements, the constant temperature model should be used. Recommended changes to the constant temperature model include: accounting for the heat of desorption when the moisture content drops below the fibre saturation point; and accounting for drying that occurs below the boiling point, which is due to diffusion from the solid surface. However, without the inclusion of a detailed transport model, the surface concentration of moisture is generally unknown. This necessitates approximations for relating moisture concentration on the surface to mass fraction of moisture in the solid, such as the equilibrium mass/mole fraction method [39].

2.1.2 Pyrolysis (devolatilisation)

Pyrolysis is a chemical process, during which the solid fuel decomposes into light gases, condensable tars, and a highly carbonaceous solid, termed char. The process is complex owing to the large number of influencing factors, which include: heating rate, temperature history, particle size and shape, pressure, moisture content, and chemical composition [11, 40]. For simplification purposes, similar products are generally lumped together to form pseudo-species [41]:

- (1) *Char*: carbonaceous solid material which remains after pyrolysis.
- (2) *Tars*: high molecular weight products. These products are gaseous at elevated temperatures, but will condense as they approach room temperature.
- (3) *Gases*: lower molecular weight products, such as CO , CO_2 , H_2O , CH_4 , etc.
- (4) *Volatiles*: a further simplification where all tars and gases are represented as a lumped species.

2.1.2.1 Model classification

There are many different methods for describing biomass pyrolysis. However, the different reaction schemes can be classed either as empirical or as network models.

Empirical Models

The rate of loss of solid mass is correlated with temperature as the particle is heated to determine the reaction rate, typically expressed by means of an Arrhenius equation. The rates obtained are only valid for the experiments on which they are based [42], thus limiting the general applicability of these models.

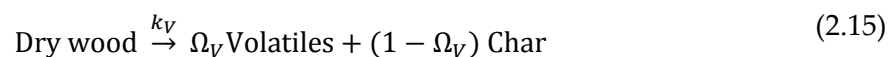
Network models

The more sophisticated network models are based on the physiochemical description of the fuel structure, represented using a network of linked aromatic and non-aromatic clusters [43]. As the temperature increases, the links between these clusters are randomly broken, causing fuel degradation. Statistical methods are applied to determine the result of broken links, *i.e.* whether char is formed, light gases are released, or a group of clusters break off the main structure to form tar. Methods of modelling the formation of gas, tar, and char vary between models. The network models are more generally applicable than the simpler kinetic models, but require substantial information input from the user.

The most commonly applied models are the empirical models, which are described in more detail below.

2.1.2.2 Single-step model

The single-step model is the simplest and most common method of describing biomass pyrolysis. A single reaction determines the decomposition of dry solid fuel into volatiles and char.



where k_V is a reaction rate, and Ω_V is a stoichiometric coefficient, or mass fraction, which represents the asymptotic volatile yield⁹, $\rho_{V,\infty} = \Omega_V \rho_{sd,0}$. This is the density of volatile matter contained in the initial dry fuel sample, $\rho_{sd,0}$, which must be assumed beforehand. The conversion rate is proportional to the density of volatile matter remaining in the fuel:

$$\frac{d\rho_{sd}}{dt} = -k_V \rho_V = -k_V \Omega_V \rho_{sd} \quad (2.16)$$

where $\rho_V = \Omega_V \rho_{sd}$ is the density of volatile matter remaining in the dry fuel. Note that the notation used here is not the same as that normally found in the literature, where the density of the volatile matter released, $\rho_{V,rel} = \rho_{V,\infty} - \rho_V$, is often used. The reaction rate, k_V , is typically described using a first-order Arrhenius reaction scheme [42, 44]:

$$k_V = A_V e^{-E_V/RT} \quad (2.17)$$

The lumped volatiles can be distributed across a number of product species by means of corresponding stoichiometric coefficients:

$$\Omega_V \text{Volatiles} = \sum_i \Omega_{V,i} \text{Volatile}_i \quad (2.18)$$

where the species coefficients, $\Omega_{V,i}$, are typically assumed beforehand and remain constant throughout. The major advantage with this model is its simplicity, and as a result the majority of published pyrolysis data correspond to this model, with reaction rate constants available for a wide range of biomass materials and experimental conditions. The assumed final volatile yield is, however, only valid for conditions corresponding to the experimental conditions, which limits applicability. The model cannot predict the generation rate of individual species; therefore, unless a lumped species approach is taken, species distribution must be determined beforehand.

⁹ This is the yield of volatiles obtained while determining k_V

2.1.2.3.2 Parallel step model – based on product distribution

In the model proposed by Shafizadeh and Chin [45], the primary degradation of dry wood is based on three parallel single-step reactions, which compete to form light gases, tar, and char:



$$\frac{d\rho_{sd}}{dt} = -\rho_{sd} \sum_{i=1}^3 k_{V,i} \quad (2.24)$$

where ρ_{sd} is the density of the dry fuel. The mass fraction of char produced, or the instantaneous char yield, can be determined using:

$$\Omega_{V,c} = \frac{k_{V,3}}{\sum_{i=1}^3 k_{V,i}} \quad (2.25)$$

The major advantage of this model is that the stoichiometric coefficients do not have to be assumed in advance; the yield of each product is determined by the temperature history of the fuel, since the formation of each product is described by means of a competing, temperature-dependent reaction.

2.1.2.3.3 Parallel step model – based on fuel composition

We recall that biomass is primarily comprised of cellulose, hemicellulose, and lignin (Section 1.3.1), the properties of which vary from one type of biomass to another. By assuming that the fuel constituents decompose independently, the total pyrolysis rate of the dry fuel can be determined by summing the pyrolysis rate of each individual component [41]. Each individual component may, in turn, be modelled using any of the pyrolysis submodels, *i.e.* Eq. (2.15), (2.19), or (2.23).



$$\frac{d\rho_{sd}}{dt} = \sum_i \frac{d\rho_i}{dt} \quad i = \text{cellulose, hemicellulose, lignin} \quad (2.27)$$

Once the decomposition rates of each component – *i.e.* cellulose, hemicellulose, and lignin in the case of biomass – are known, the pyrolysis rate of different fuels can be calculated simply by adjusting the mass fractions of each component.

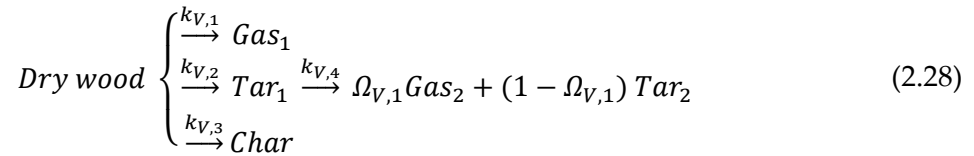
This method inherits the disadvantages of the particular model applied to each individual component. Moreover, possible reactions between the components are not considered [46].

2.1.2.4 Two-stage, semi-global models

The previous models have only addressed *primary* degradation of biomass; *secondary* reactions, such as tar cracking and repolymerisation, have not been considered. Tar cracking is the degradation of high-molecular-weight tars into lower-molecular-weight gases. This becomes important at high temperatures as the residence time increases, and can also occur in larger particles as the tar passes through the hot outer char layer [41]. Tars may also repolymerise to form char.

2.1.2.4.1 Tar cracking

Chan *et al.* [35] proposed a model based on the primary degradation scheme of Shafizadeh and Chin [45], where a consecutive single-step reaction is used to describe the cracking of primary tars into secondary gases and secondary tars:



$$\frac{d\rho_{sd}}{dt} = -(k_{V,1} + k_{V,2} + k_{V,3}) \rho_{sd} \quad (2.29)$$

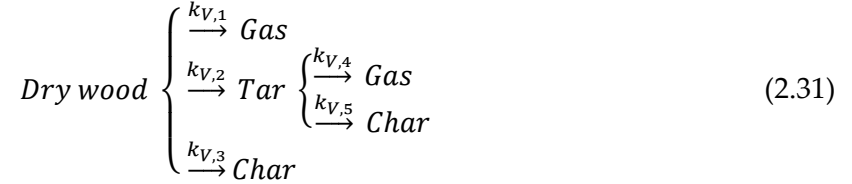
The net amount of tar formed is given as:

$$\frac{d\rho_T}{dt} = k_{V,2} \rho_{sd} - (k_{V,4} + k_{V,5}) \varepsilon \rho_T \quad (2.30)$$

where ε is the bed porosity, or void fraction. This disadvantage of this approach is that the stoichiometric coefficient for the secondary reaction, $\Omega_{V,1}$, must be assumed *a priori*. Furthermore, tar repolymerisation is neglected.

2.1.2.4.2 Tar cracking and repolymerisation

The model of Shafizadeh and Chin [45] can be further extended to include both tar cracking, to form lighter gases, and tar repolymerisation, to form char. These secondary reactions are generally implemented as competing single-step reactions [47, 48].



$$\frac{d\rho_{sd}}{dt} = -(k_{V,1} + k_{V,2} + k_{V,3}) \rho_{sd} \quad (2.32)$$

The total amount of char formed, including the secondary reaction is:

$$\frac{d\rho_C}{dt} = k_{V,3}\rho_{sd} + \varepsilon k_{V,5}\rho_T \quad (2.33)$$

Di Blasi [48] estimated the repolymerisation reaction, k_5 , as being forty times slower than the tar cracking reaction rate, k_4 , proposed by Liden *et al.* [49]. It is worth noting that such an assumption is effectively the same as assuming a constant mass stoichiometry for the secondary products, as done in Eq. (2.28).

2.1.2.5 Distributed activation energy models (DAEM)

The DAEM assumes that the evolution of pyrolysis products occurs through an infinite number of parallel single-step reactions, see Eq. (2.15). Each reaction may produce a distribution of products, a single species j can therefore be produced by one or more reactions i [50, 51]. Rewriting Eq. (2.16), which represents a single reaction, i , for species j :

$$\frac{d\rho_{j,i}}{dt} = -k_i\rho_{j,i} \quad (2.34)$$

where k_i is an Arrhenius type reaction of varying order. Rearranging the rate gives:

$$\frac{d\rho_{j,i}}{\rho_{j,i}} = -k_i dt \quad (2.35)$$

Integrating Eq. (2.35) gives the total density of species j remaining, recalling that ρ_j is the density of species j remaining in the fuel; therefore, $\rho_{j,i} = \rho_{j,i,\infty}$ when $t = 0$; and $\rho_{j,i} = 0$ when $t = \infty$:

$$\rho_{j,i} = \rho_{j,i,\infty} \exp\left(-\int_0^t k_i dt\right) \quad (2.36)$$

If $i = 1$, the model is identical to the single-step first order model, Eq. (2.16). For a finite number of reactions, the total amount of species j could be determined by summing the contribution of each reaction, similar to Eq. (2.20):

$$\rho_j = \sum_i \rho_{j,i,\infty} \exp\left(-\int_0^t k_i dt\right) \quad (2.37)$$

The DAEM, however, assumes an infinite number of equations. Individual reactions, i , are replaced by a continuous dependence on the activation energy, E , with a distribution curve of the activation energies, $f_j(E)$, to represent the differences in the activation energies of each reaction [52]. The density of species j available for release from reaction i , $\rho_{j,i,\infty}$, is instead represented as the density of species j with activation energies between E and $E + dE$ [53, 54]:

$$d\rho_j = \rho_{j,\infty} f_j(E) dE \quad (2.38)$$

The total amount of species j remaining at time t is then given by the integral [43, 50, 53, 55-61]:

$$\rho_j = \int_0^\infty \rho_{j,\infty} \exp\left(-\int_0^t k_i dt\right) f_j(E) dE \quad (2.39)$$

To simplify the analysis of data, a common assumption is that the pre-exponential factors, A_i , in all the kinetic rates, k_i , have the same value, A_0 [54]:

$$k_i = A_0 e^{-E_i/RT} \quad (2.40)$$

The distribution curve for the activation energies, $f_j(E)$, is often approximated using a normal distribution curve, although Weibull and Gamma distributions have also been used [62]. Methods of deriving the actual distribution curve of the activation energies by means of measurements have, therefore, been proposed, such as those by Miura [52, 60]. Some models also use a discrete number of activation energies at

set intervals, rather than a continuous distribution and are referred to as discrete activation energy models.

The major advantage of this approach is that the stoichiometric coefficients do not have to be assumed in advance. Typically, although it depends on the experiment, the evolution rate and cumulative yield of major products are determined for several (typically three) constant heating rates. The kinetic rates (A_0 and E_i), the standard deviation and mean activation energy for the distribution curve, and the precursor pool size (amount of mass which may lead to formation of species j) are determined from these experiments [50]. Since there are an infinite number of competing temperature-dependent reactions (via the distributed activation energy), the ultimate yield of each product is determined by the temperature history of the fuel.

Regarding implementation of the DAEM approach, assumptions regarding the constant pre-exponential factor, A_0 , and the shape of the distribution curve of activation energies are not always realistic, although the experimentally derived curve addresses the latter. Furthermore, extrapolating data from measurements is not straightforward, and the double integral in Eq. (2.39) is not trivial to implement numerically. Various methods are discussed in refs [50, 54, 58, 62, 63].

2.1.2.6 Network models for pyrolysis

The network models are the most sophisticated models currently available for pyrolysis. These fundamental models are based on assumptions of how the fuel structure changes as the fuel is heated. Like most solid fuel conversion submodels, their origins lie in coal combustion. However, because biomass pyrolysis is analogous to coal pyrolysis, they have been adapted to biomass fuels, although modifications are required to account for the different fuel structure and significantly higher proportions of hydrogen and oxygen (*Table 1.2*) in biomass.

The three coal based network models are:

- (1) the functional group model with depolymerisation, vaporisation and cross-linking (FG-DVC), proposed by Solomon *et al.* [64].
- (2) the chemical percolation devolatilisation (CPD) model proposed by Grant and Pugmire [65].
- (3) the FLASHCHAIN model proposed by Niksa [66].

They all include network modelling, structure characterisation, depolymerisation reactions, crosslinking reactions, and non-condensable gas, tar, and char formation [42]. The FG-DVC and FLASHCHAIN models have both been modified for use with biomass, resulting in bio-FGDVC [67, 68] and bio-FLASHCHAIN [69] respectively. Although network models are beyond the scope of this thesis, a brief description of the FLASHCHAIN model will be given below and information for the FG-DVC model is available at [70].

FLASHCHAIN

The FLASHCHAIN model proposed by Niksa and Kerstein takes elements from the DISCHAIN [71], DISARAY, and FLASHTWO models which the same authors had previously proposed [66]. In the FLASHCHAIN model, the fuel structure is represented by four components, see *Figure 2.1* (as originally designed for coal):

- (1) Aromatic groups attached pairwise (by either labile bridges or char links) to form linear chains.
- (2) Labile bridges, which link the aromatic groups.
- (3) Char links.
- (4) Peripheral groups, which are the remnants of broken bridges and branch out from the aromatic units. These essentially lead to gas formation.

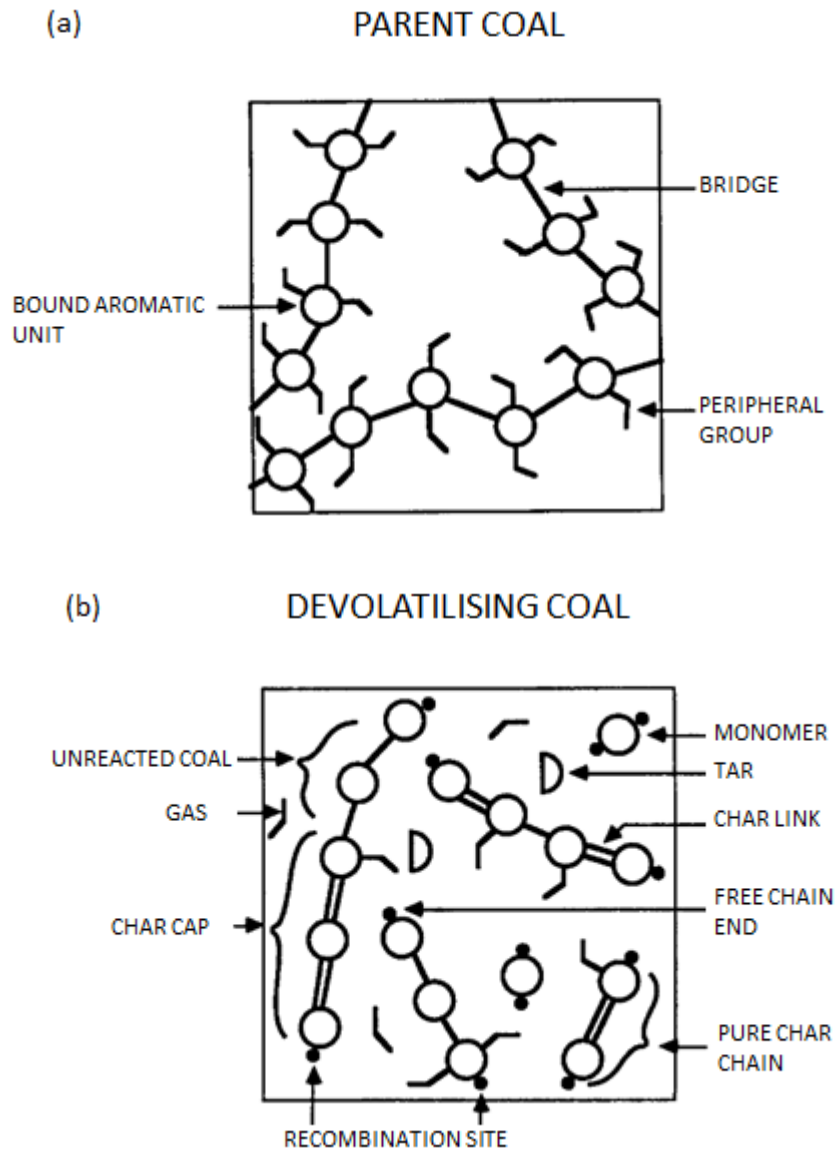


Figure 2.1 Illustrations of a devolatilising coal particle: (a) the initial reactant species and (b) all reactants, intermediate and product species is DISCHAIN.
Adapted from [71].

Thermal degradation is modelled using five chemical reactions for bridge dissociation, functional group elimination, tar formation, char formation, and gas formation:

- *Bridge dissociation* is modelled using a DAEM, see section 2.1.2.5. Owing to the large range of activation energies associated with various bridges, a normal distribution curve is assumed.

- *Chain statistics* are used to determine the likelihood that a broken bridge leads to the formation of a monomer, *i.e.* frees a single aromatic unit from a chain. Monomers may then either break up to form tar, or become reattached to a chain to form char.
- *Tar formation* is determined using an Arrhenius reaction.
- *Char formation* is determined using an Arrhenius reaction.
- *Gas formation* is modelled using two consecutive Arrhenius reactions. The first describes the formation of functional groups resulting from broken bridges. The second determines the rate at which these functional groups are converted into light gases.

The FLASHCHAIN model includes char links as a component of the fuel structure. The bridges between aromatic units are then described as either aliphatic labile bridges, or completely aromatic char links. This introduces a pathway, and thus reaction, whereby labile bridges can either be disassociated as in DISCHAIN, or condensed to form char links with an associated gas release, as in FLASHTWO. Yields are determined by probability expressions and competitive reactions, and are not assumed beforehand. As a result, the models capture the yield enhancement resulting from an increased heating rate.

However, the FLASHCHAIN model is only capable of predicting the distribution of gas, tar, and char. Individual species distribution is not possible. A complete description of the DISCHAIN and FLASHCHAIN models can be found in [66, 71-78].

2.1.2.7 Discussion of pyrolysis models

2.1.2.7.1 Heat of reaction

There are significant variations in the reported values for the heat of pyrolysis, ranging from endothermic to exothermic, for different particle sizes, heating rates, impurities, etc. Rath *et al.* [79] discovered a linear relationship between the heat of pyrolysis and the final char yield, and proposed that the variations in published

reaction heats are due to competition between the exothermic primary char formation and the endothermic volatile formation processes. Bellais [13] also noted that exothermic secondary reactions could explain the variations in the reported values. One can conclude that the heat of pyrolysis should therefore be correlated to the most appropriate experimental data.

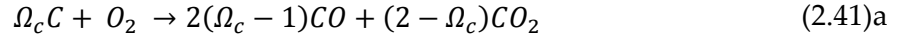
2.1.2.7.2 Conclusion

The single-step model provides an approximation; however, Grönli [11] concluded that a single reaction model is not sufficient to describe the decomposition of wood. According to Grönli [11], single-step models inadequately represent biomass pyrolysis, and should only be used as an approximation. Network models are the most detailed and generally applicable, but require more input from the user and add significant computational effort [42]. As a result, Williams *et al.* [80] employed a network model as a pre-processor, then implemented the predicted yields and kinetic rates using a single-step model. The parallel-step model, where reactions compete to form gas, tar, and char, or the two-stage semi-global models (when secondary reactions are important) are more realistic than a single-step model, but only require a moderate increase in computational effort. The disadvantage is that kinetic data for these models are not as widely available as for the single-step model, limiting their application to certain fuels.

2.1.3 Heterogeneous reaction models

Char is a porous, carbon-rich solid which is formed during pyrolysis. In addition to carbon, which typically constitutes over 90% of the char [81], small amounts of hydrogen, oxygen, nitrogen, sulphur, and inorganic matter or ash, are also present. Oxidation of the char occurs through heterogeneous reactions between the solid char and gaseous reactants; the main reactants are oxygen, carbon dioxide, and water vapour. The reaction with oxygen is simply termed char combustion, while char gasification refers to the reaction between char and any gaseous reactant other

than oxygen. If the char is assumed to be pure carbon, the reactions can be described as follows¹⁰:



Heterogeneous reaction rates are influenced by many factors, including: the total active surface area, the local gas reactant concentration, local temperature, pressure, char structure, and char composition. The overall reaction scheme can be described by three basic processes [82]:

1. Diffusion of mass and heat through the boundary layer surrounding the solid fuel.
2. Diffusion of mass and heat within the porous structure of the fuel.
3. Reaction of gases with solid surfaces.

Since char is a porous material, the total surface area is a combination of the internal and external surface areas of the particle, see *Figure 2.2*. The pore structure determines the internal surface area, and is identified by the specific internal volume, V_{pore} , the specific internal surface area, A_{pore} , and the distribution of pore size. Adsorption isotherms, such as the BET isotherm [82], are commonly employed to characterise the pore structure. Because the heterogeneous reactions are dependent both on the diffusion rate of the reactant to the particle surface, and on the chemical reaction rate at the surface, the overall reaction rate is limited by the

¹⁰ There are three possible reactions between char (carbon) and oxygen, see discussion Section 2.1.3.3.

- Zone I: The chemical reaction is slow with respect to the diffusion of the reactant, effectively limiting the overall reaction rate. Therefore, reactants have time to penetrate the porous structure and the concentration is uniform throughout. The reaction order in this regime is said to be the true, rather than the apparent, reaction order.
- Zone II: The chemical reaction and the diffusion of the reactant occur on a similar timescale. The chemical reaction is fast enough that the reactant cannot diffuse through the porous structure fast enough to maintain a uniform concentration throughout the fuel.
- Zone III: The chemical reaction rate is so fast that the concentration of the reactant approaches zero. The overall reaction rate is limited by the diffusion rate of the reactants.

Models describing these heterogeneous reactions can be classified as *global models*, which determine the overall rate per unit mass of the fuel using an “apparent” chemical reaction order, or as more fundamental *intrinsic models*, which determine the overall rate per unit internal surface area of the particle using the “true” chemical reaction order.

2.1.3.1 Global reaction models

The most commonly used global rate model is that of Baum and Street [86], or some variant, as quoted in [80, 87, 88]. This model is based on a spherical particle of carbon, which reacts with O_2 to form CO only, with an assumed reaction order of unity:

$$\frac{d\rho_C}{dt} = -\frac{6}{d_p} \frac{k_D k_C}{k_D + k_C} P_{O_2} \quad (2.44)$$

$$k_C = A\Psi e^{-E/RT} \quad (2.45)$$

$$k_D = \frac{h_m M_{carbon}}{RT_{avg}} \quad (2.46)$$

$$h_m = \frac{NuD_{eff,AB,O_2}}{d_p} \quad (2.47)$$

$$D_{eff,AB,O_2} = D_{AB,O_2} \frac{P_{ref}}{P} \left(\frac{T_g}{T_{ref}} \right)^{1.75} \quad (2.48)$$

$$T_{avg} = \frac{T_p + T_g}{2} \quad (2.49)$$

where: d_p is the diameter of the particle, k_c is the apparent or observed chemical reaction rate based on the partial pressure of the reactant [$s\ m^{-1}$], k_D is the diffusion rate, D_{eff,AB,O_2} is the effective diffusion coefficient, D_{AB,O_2} is the binary diffusion coefficient of oxygen in nitrogen, Ψ is the ratio of the area of the reacting surface to that of the external surface of a sphere of equivalent volume, h_m is mass transfer coefficient, Nu is the Nusselt number, assumed to be 2 for a spherical particle, T_{avg} is the average temperature of the particle and the gas, P is the gas pressure, with subscript ref denoting the reference conditions under which D_{AB,O_2} is derived.

There are many modified versions of the global model published in the literature. It is worth noting, however, that the units for the chemical reaction rate, and thus for the diffusion rate, are dependent on the experimental procedure. Furthermore, the relationship between the diffusion rate and the chemical reaction rate depends on the apparent reaction order. This relationship can be derived from [89]:

$$Reactivity = h_m(C_{m,g} - C_{m,s}) = k_c (C_{m,s})^n \quad (2.50)$$

where the reactivity is the reaction rate per unit area [$kg\ m^{-2}\ s^{-1}$], C_m is the mass concentration of the reactant, n is the apparent reaction order, and k_c has units [$kg\ m^{-2}\ s^{-1}\ (kg\ m^{-3})^{-n}$].

Assuming a reaction order of unity ($n = 1$) and eliminating the unknown surface concentration, $C_{m,s}$, the familiar result is:

$$Reactivity = C_{m,g} \frac{h_m k_c}{h_m + k_c} \quad (2.51)$$

The reactivity may also be determined in terms of the partial pressure, rather than of the concentration, of the reactant; this leads to Eq. (2.44) when the reaction order is assumed to be unity:

$$Reactivity = k_D(P_g - P_s) = k_C (P_s)^n \quad (2.52)$$

$$Reactivity = P_g \frac{k_D k_C}{k_D + k_C} \quad (2.53)$$

where k_C has units [$kg\ m^{-2}\ s^{-1}\ (Pa)^{-n}$]. Multiplying Eqs. (2.51) and (2.53) by the specific area of the particle, which is the external surface area per unit volume, gives the overall reaction rate in terms of mass per unit volume [$kg\ m^{-3}\ s^{-1}$]. As described, the reaction order determines the relationship between the chemical rate and the diffusion rate, and also the units for the chemical reaction rate itself. Equations (2.51) and (2.53) must therefore be modified if the reaction order is not unity, in order to ensure dimensional homogeneity.

The global model can be modified to account for non-spherical particles, reactions with different stoichiometric coefficients, and influences of the packed bed, which will affect the Nusselt number correlation and the diffusion rate. For example, the global model for mass loss of non-spherical char particles in a packed-bed, as used by Johansson [90] and Hermansson [91], is as follows:

$$\frac{d\rho_{c,k}}{dt} = -\frac{A_p}{V_p} M_{carbon} \Omega_{c,k} k_{eff,k} C_{O_2} \quad (2.54)$$

$$k_{eff,k} = \frac{k_{C,k} h_{m,k}}{k_{C,k} + h_{m,k}} \quad (2.55)$$

$$h_m = \frac{D_{eff,k} Nu}{d_p} \quad (2.56)$$

$$Nu = (2 + 1.1 Sc^{1/3} Re^{0.6}) \quad (2.57)$$

$$D_{eff,k} = 0.8 D_{eff,AB,k} + 0.5 |u_g| d_p \quad (2.58)$$

where A_p is surface area of the particle, V_p is volume of the particle, C is the molar concentration of the reactant [$kmol\ m^{-3}$], Ω_c is the relevant stoichiometric coefficient from Eqs. (2.41) – (2.43), Nu is the Nusselt number correlation of Wakao and Kaguei for a packed bed [92], $D_{eff,k}$ is the effective diffusion coefficient in a packed bed, also from [92], and the subscript k refers to oxygen, carbon dioxide, or water vapour.

The global model is the most commonly published model for char reactions. As a result, there is an abundant source of kinetic data available. The model is, however, restricted to the experimental conditions, and is therefore only valid over limited temperature and pressure ranges [82]. Furthermore, since the reaction rate is determined per unit mass of the particle, *i.e.* it accounts for the influence of many factors, such as the internal surface area, char reactivity, etc., the model is not capable of distinguishing between chars of different porous structure that are otherwise similar.

2.1.3.2 Intrinsic reactivity models

The global model described in section 2.1.3.1 is based on a *global* (per unit mass) chemical reaction rate, k_c . This is an observed reaction rate, where it is assumed that the chemical reaction occurs on the external surface of the particle only, and therefore does not take account of the internal porous structure of the char. *Intrinsic* (per unit area) models are based on the active surface area available within the char. Depending on their complexity, some may also include a more fundamental description of the mechanisms governing surface reactions. Such mechanisms are based on active site theory which describes the adsorption of reactants to the surface, and desorption of products from the surface of the fuel, typically derived using Langmuir-Hinshelwood kinetics, more information is available in [82]. Since intrinsic models are based on the active surface area available, the internal pore structure of the fuel must be characterised in some way.

2.1.3.2.1 Intrinsic reactivity model – Smith

Smith [89] proposed that in the absence of mass transfer or pore diffusion limitations (*i.e.* Zone I regime, $h_m \gg k_c$), the burnout rate is determined by the intrinsic reactivity, k_{int} , and the partial pressure (or mass concentration) of oxygen at the surface:

$$\frac{d\rho_c}{dt} = -\frac{A_p}{V_p} k_{int} P_{O_2}^m \quad (2.59)$$

Under practical conditions, however, combustion may occur in any regime (*i.e.* Zones I – IV), and mass transfer must therefore be taken into account. This is done using an effective chemical reaction rate, which is calculated from the intrinsic reactivity:

$$k_C = \eta\gamma\rho_{sd}A_gk_{int} \quad (2.60)$$

where η is the effectiveness factor; this is the ratio of the actual combustion rate to the rate attainable if no pore-diffusion existed. It is a function of the Thiele modulus, see [82, 89]. γ is the characteristic size of the particle, which is the ratio of volume to external surface area (V_p/A_p), m is the true chemical reaction order, and A_g is the specific surface area per unit mass of the particle [$m^2 \text{ kg}^{-1}$].

Similarly to the global model, the relationship between the diffusion rate and the effective chemical reaction rate is derived from Eq. (2.50), although the apparent reaction order, n , is replaced by the true reaction order, m . The effective chemical reaction rate, k_C , is then substituted into the resulting equation, *i.e.* Eqs. (2.53) or (2.51) if $m = 1$.

The Thiele modulus for a cylindrical or spherical fuel particle, assuming a first order reaction, can be calculated using [82]:

$$\Phi = \frac{d_p}{2} \left(\frac{k'_{int}}{\Omega D_{e,pore}} \right)^{1/2} \quad (2.61)$$

where k'_{int} is the volume intrinsic reaction rate, based on the mass concentration rather than the partial pressure of the oxidant, given by:

$$k'_{int} = \rho_{sd}A_gk_{int} \quad (2.62)$$

where k_{int} has units [$\text{kg m}^{-2} \text{ s}^{-1} (\text{kg m}^{-3})^{-m}$]. If Knudsen diffusion is neglected, the effective diffusivity in the pores, $D_{e,pore}$, is given by:

$$D_{e,pore} = \frac{D_{eff}\epsilon_{char}}{\tau} \quad (2.63)$$

where D_{eff} is the effective molecular diffusivity of the reactant, ϵ_{char} is the porosity of the char, and τ is the tortuosity of the pores, commonly assumed to be 2. If the

intrinsic reaction rate, k_{int} , is given in terms of the partial pressure, Eq. (2.62) must be adjusted to ensure dimensional homogeneity:

$$k'_{int} = \rho_{sd} A_g k_{int} \frac{P_{ox}}{\rho_{ox}} = \rho_{sd} A_g k_{int} \frac{RT}{M_{ox}} \quad (2.64)$$

where k_{int} has units $[kg\ m^{-2}\ s^{-1}(Pa)^{-m}]$. For irregularly shaped particles and an m^{th} order reaction, the Thiele modulus can be approximated using:

$$\Phi = \gamma \left(\frac{(m+1)k'_{int} C_{m,s}^{m-1}}{2\Omega D_{e,pore}} \right)^{1/2} \quad (2.65)$$

where $C_{m,s}$ is the surface mass concentration. The effectiveness factor, η , is then calculated using the Thiele modulus as follows:

$$\eta = \frac{3}{\Phi} \left(\frac{1}{\tanh \Phi} - \frac{1}{\Phi} \right) \quad (2.66)$$

Equation (2.60) illustrates how the apparent chemical reaction rate applied in the global model (section 2.1.3.1) basically combines the effects of the intrinsic reactivity of the char, k_{int} , and the accessibility of the internal surface area, governed by the effectiveness factor, η . The effectiveness factor is a function of the reactivity and decreases as the reactivity increases. It represents the reduced utilisation of the internal surface area as the chemical reaction rate increases (*i.e.* transition from zone I – III, see **Figure 2.3**), since reactants are consumed before they can fully penetrate the particle [82]. The major advantage of this more fundamental approach is that once the reactivity and the structure of the char are determined, the intrinsic model is not limited by the experimental conditions. Furthermore, the reactivity of one char can be extrapolated to other chars of similar composition by modifying the structural parameters, ε_{char} , τ , γ , and A_g , further increasing the general applicability of the model. A major drawback, however, is that assumptions are required regarding how these structural parameters will change during combustion. A common, although unrealistic assumption, is that they remain constant during burnout, see unreacted core model in section 2.1.3.3.1.

2.1.3.2.2 *Extended reaction model*

There is concern that the chemical reaction rate appearing in Eqs. (2.50) and (2.52) is not suitable for char reactions. Essenhigh and Mescher [93] claim that a Langmuir type equation, which describes, separately, the adsorption of reactants to the surface, and the desorption of products from the surface, is more appropriate, particularly at elevated temperatures. Essenhigh *et al.* [93, 94] therefore proposed an extended reaction model, where the chemical reaction is described by means of a Langmuir adsorption-desorption model. The overall reaction rate, including diffusion, is given by:

$$\frac{1}{k_{eff}} = \frac{1}{k_D X_{Ox}} + \frac{1}{\epsilon k_a X_{Ox}} + \frac{1}{\epsilon k_d} \quad (2.67)$$

where ϵ is the reaction penetration factor based on the Thiele modulus, analogous to the effectiveness factor described for the intrinsic model. k_a and k_d are, respectively, adsorption and desorption rates, both expressed by means of an Arrhenius equation.

The major disadvantage of this model is that published kinetic data are very sparse. Until these become available, the model is simply not applicable to biomass.

2.1.3.3 **Discussion of heterogeneous reactions**

2.1.3.3.1 *Products from char combustion*

There is some disparity in the literature regarding the products of char combustion. While it is occasionally assumed that there is only a single product, either CO or CO_2 (Eq. (2.41)b and (2.41)c, respectively), it is generally accepted that *both* CO and CO_2 are primary products of char combustion, as shown in Eq. (2.41)a. The ratio of CO to CO_2 is reported to vary with temperature, and is typically expressed using an Arrhenius expression [83, 90, 95-97]:

$$\frac{CO}{CO_2} = A e^{-E/RT} \quad (2.68)$$

The stoichiometric coefficient at any temperature can then be found by rearranging Eq. (2.41)a to yield:

$$\Omega = \frac{2(1 + CO/CO_2)}{2 + CO/CO_2} \quad (2.69)$$

2.1.3.3.2 *Char structure*

The size, density, and internal structure of a particle may change as the particle burns. Since heterogeneous reactions depend on the available surface area, submodels are required to account for these changes. Owing to its simplicity, the most commonly published submodel is the unreacted core model [51, 82], where the internal pore structure is assumed to remain constant during conversion. The size and density of the particle are then inversely related, with changes described as a function of mass loss [89]. A common assumption is that the density also remains constant during char oxidation, with particle shrinkage directly proportional to mass loss. This submodel is ideally suited to a global reaction model, where the internal pore structure is not considered; however, this submodel is also frequently employed for the intrinsic reaction models, as mentioned in section 2.1.3.2.1. More sophisticated submodels attempt to characterise the change in the internal porous structure during the combustion process; these include the random pore model [98-100], and the pore tree model [101].

2.1.3.3.3 *Char composition*

To simplify the reactions, the char is commonly assumed to be pure carbon, resulting in Eqs. (2.41) – (2.43). However, in reality the char will contain 5-10%wt db of other elements, mainly hydrogen and oxygen [81, 97]. This can be taken into account by modifying the heterogeneous reactions, as done in [97], as well as the calorific value of the char, which can be estimated from [102].

2.1.3.3.4 *Heat of reaction*

Char primarily reacts with oxygen, carbon dioxide, and water vapour. There is some scatter in the literature regarding exact heats of reaction; however, the char combustion (Eq.(2.41)a/b/c) and char gasification reactions (Eqs. (2.42) and (2.43))

are accepted as exothermic and endothermic respectively, with gasification values available in [97, 103]. The heat released during char combustion is a function of the calorific value of the fuel and the of combustion product(s). This necessitates assumptions about the char composition, and the combustion reaction, *i.e.* whether combustion is represented by Eq. (2.41)a, (2.41)b, or (2.41)c, as described in section 2.1.3.3.1.

2.1.3.3.5 Conclusion of heterogeneous submodels

The intrinsic reactivity models provides a better representation of the heterogeneous reactions than a global model; however, there are difficulties in determining the exact form of the intrinsic reactivity, k_{int} , the internal surface area, A_g , and the effectiveness factor, η , as the reaction proceeds [87, 89]. Williams *et al.* [87] reported that at a single temperature, there are wide variations in the reactivity of different chars, owing to impurities and differences in the char structure. Furthermore, the same authors also suggest that due to particle irregularities, variations in biomass reactivity are more pronounced than coal chars, and consequently the intrinsic reactivity model is difficult to apply without using crude estimates for internal surface area and reaction constants. On the other hand, if suitable data are available, the global model is simple to implement and requires no additional assumptions.

2.1.4 Discussion on thermochemical conversion models

Owing to their simplicity, the constant temperature model and the kinetic model are the most commonly utilised drying models in the literature. In the absence of suitable data for the kinetic model, the constant temperature model should be used, since it gives a reasonable approximation without any experimentally derived inputs. The transport model is more representative of the actual drying process; however, it is worth noting that this model requires extensive input/assumptions from the user which may diminish the potential benefits.

Investigations into the pyrolysis of biomass fuels indicated that a single step pyrolysis model cannot closely represent the decomposition process and should

only be used as an approximation [11]. If an approximation is sufficient, then the single step model is ideal since it is the simplest to implement, the least computationally expensive, and there is a dearth of kinetic data available. However, given the relevant kinetic data, a more sophisticated model such as a parallel step model, DAEM, or network model should be used. One of the main benefits is that these models account for the dependency of the char yield on the heating rate of the fuel. Of these, the parallel step model offers a significant improvement on the single step model for only a moderate increase in effort and computational expense. It is worth noting, however, that the distributed activation energy model (DAEM) and the network models require a substantial increase in effort to implement and significantly more information from the user.

The heterogeneous char reactions can be divided into two categories: the combustion reaction with oxygen, and the slower gasification reactions. At the temperatures typically present in a furnace, the char combustion rate is generally limited by the diffusion of oxygen to the particles, with the chemical reaction rate primarily acting to control the ignition temperature of the fuel. Since the reaction is, therefore, primarily limited to the outer surface of the particle (zone III/IV combustion, see *Figure 2.3*), the difference between the simple global model and the more complicated intrinsic model is negligible [104]. The global model is therefore sufficient provided appropriate kinetic data is available.

For the slower gasification models, however, the overall reaction rate is likely to be limited both by the chemical reaction rate *and* by the diffusion rate of the reactant to the particle. As a result, the reactions may occur on both the internal and external surfaces of the char particle (zone I/II combustion, see *Figure 2.3*) and are better described by means of an intrinsic model. It is worth noting that the main drawback of the intrinsic model is that it necessitates assumptions regarding the initial internal structure of the char and how this structure changes during burnout. These assumptions vary widely across the literature, for biomass in particular, which may occlude the benefits associated with this model.

2.2 Review of Fixed-Bed Modelling

2.2.1 Fixed-bed simulation methods

In fixed-bed or grate furnaces, aerodynamic forces are insufficient to lift the majority of the particles. As a result, particles lie in contact, with voids between them, forming a well-defined fuel bed, as shown in *Figure 2.4*.

In our case, the objective is to simulate a section of a packed or fixed fuel bed in a biomass furnace. Consider the “as modelled” two-dimensional section highlighted in *Figure 2.4*. There are four approaches for achieving this [105]:

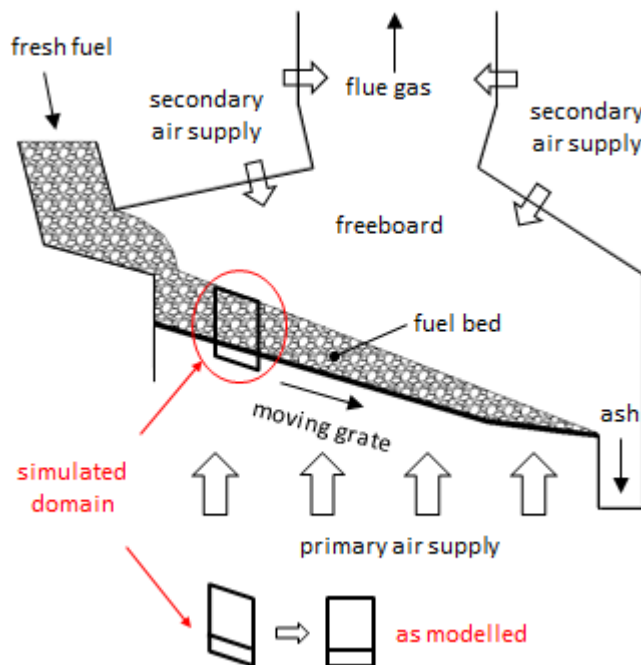


Figure 2.4 Schematic of fixed-bed furnace

- (1) An Eulerian-Eulerian approach [83, 90, 91, 104, 106-110]: The solid phase is represented as a continuum, and individual particles are not tracked (*Figure 2.5*). This can be subcategorised depending on how the solid phase is represented; whether as a porous medium, or using the theory of granular flow.

- (2) An Eulerian-Lagrangian/Discrete Particle Model (DPM) approach [111-113]: Each particle, and its properties, is tracked throughout the computational domain (*Figure 2.6*).
- (3) A neighbouring layer approach [114-116]: The bed is split into four layers representing fresh fuel, dry fuel, char, and ash (*Figure 2.7*).
- (4) A well-stirred reactor model (WSR) [117]: the bed is represented by a cascade of well-stirred, also termed perfectly stirred reactors; in a WSR, transport rates are assumed to be much higher than chemical rates (*Figure 2.8*). The properties with the reactor are therefore uniform throughout, and only the chemical rates need be determined.

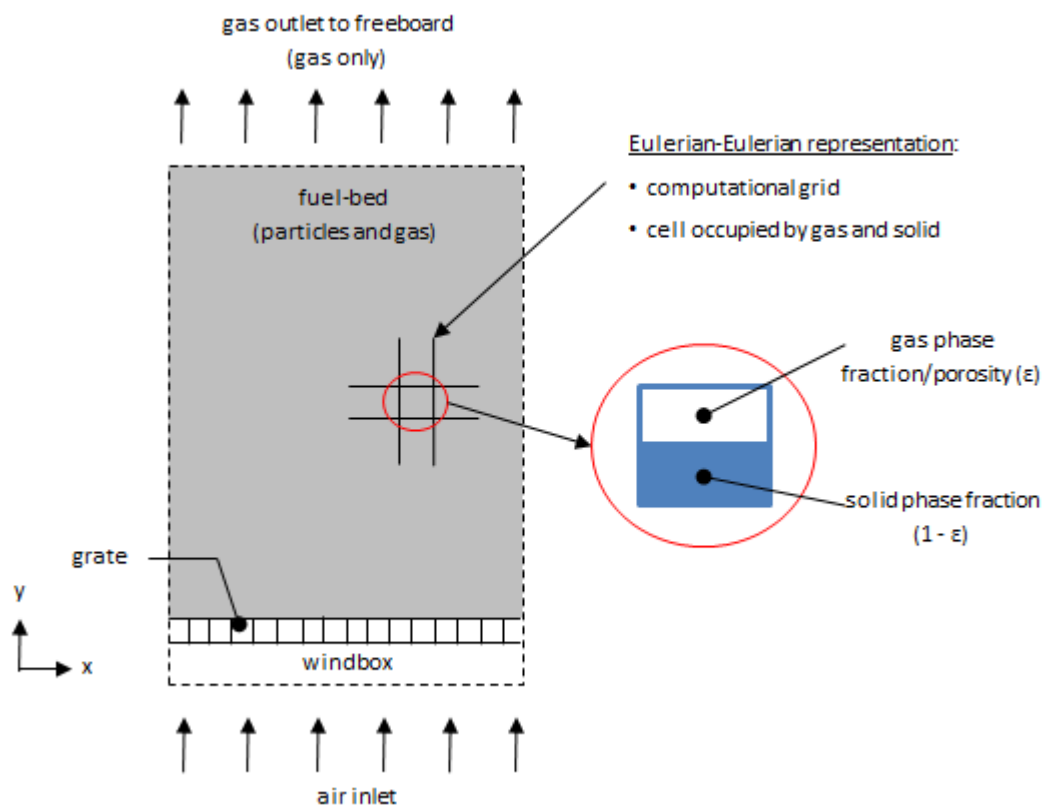


Figure 2.5 Eulerian – Eulerian approach

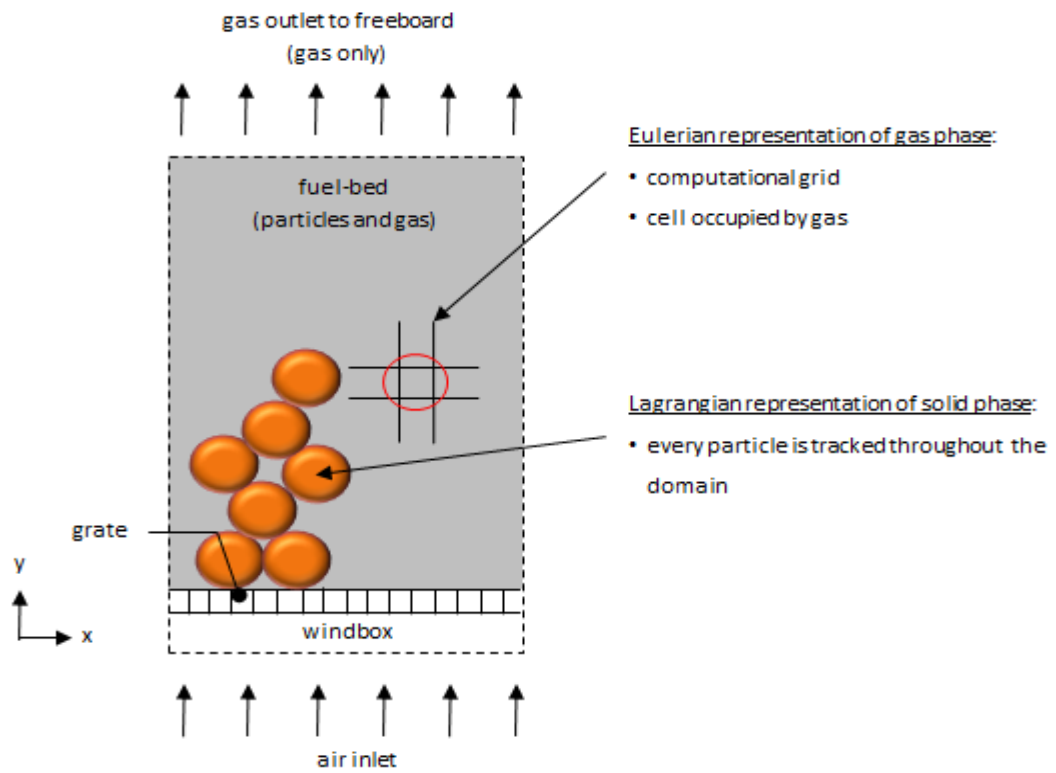


Figure 2.6 Eulerian-Lagrangian approach

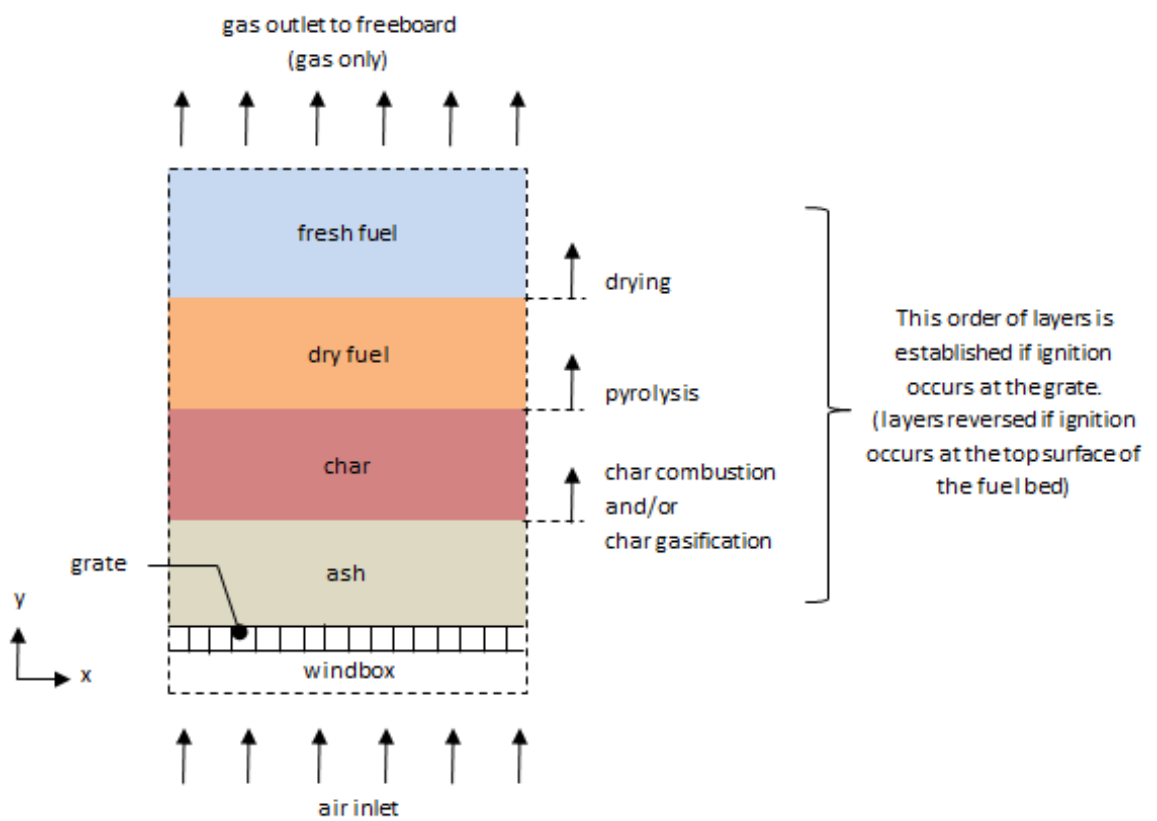


Figure 2.7 Neighbouring layer approach

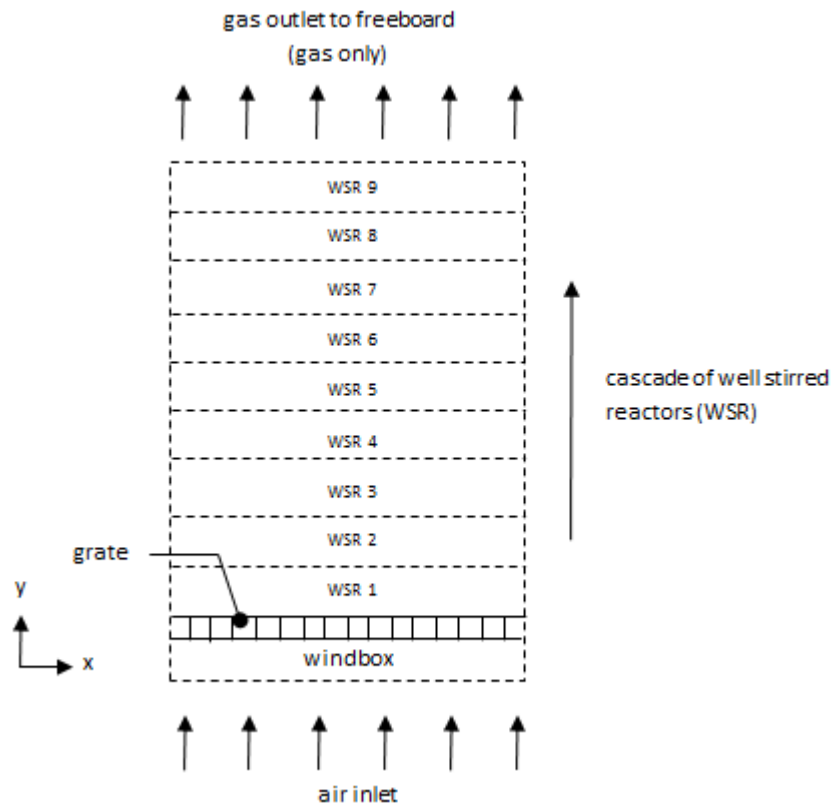


Figure 2.8 Cascading reactor model

2.2.2 Implementation approach

As already noted in Section 1.7, the objective of this work is to develop an unsteady, 3D numerical model to describe solid fuel combustion in a packed bed. While there are many examples of in-house code throughout the literature, implementing the model into an existing CFD platform has two major benefits: it reduces development effort and increases availability for industrial applications. There are several CFD packages available that might be explored to accomplish this: the commercial packages, Fluent and CFX; and the open source packages, MFIX [118] and OpenFOAM [119]. CFX was initially tested, and although simulations of pulverised furnaces were carried out using the built-in particle submodels with minor user modifications, it lacked the flexibility required to develop and integrate a complete fixed-bed model. Fluent, however, enables the user to implement their own functions into the solution process with relative ease, and is therefore chosen as the basis for the work carried out here. This software uses a finite-volume method

to discretise the domain, with conservation equations applied to each cell in the resulting grid, or mesh.

The Eulerian-Eulerian and Eulerian-DPM approaches are applicable to Fluent, and are therefore discussed further.

2.2.2.1 Eulerian-Eulerian (porous medium) approach

Both the gas phase and the solid phase are modelled as continua, where the conditions of each phase are volume-averaged over each computational cell, as shown in *Figure 2.5*. To accurately capture the flow field within the domain, the grid resolution, or cell size, should be set according to the smallest length-scales present, which is typically the length-scale of the fluid flow. The continuum approach enables conservation equations to be applied to each phase; however, since a cell may contain more than one phase, the conservation equations must be adjusted by the respective volume fraction of each phase present.

With this approach, individual particles are not physically represented. Instead, characteristic values for particle size, properties, and composition are solved for each cell. These values are used as an input for well-established fluid mechanics correlations and combustion kinetics.

This approach has several advantages over the Eulerian-Eulerian (granular) or Eulerian-Lagrangian approaches: it is the most computationally inexpensive, the volume fractions of each phase are easily applied and adjusted, and bed shrinkage can be controlled. The disadvantage is that, in reality, particles may be larger than the computational cells. In this case, they would span across several cells, with variable conditions at the particle's surface. This is not taken into account in an Eulerian representation of the solid phase, reducing the representativeness of any Eulerian-Eulerian approach.

Simulation of fixed-bed combustion using a porous medium approach is not currently available as a standard feature in any commercial CFD package. The user

must therefore create functions to describe every aspect of a burning fuel-bed. This includes the conservation equations for the solid phase, and source terms to account for: species generation/consumption, flow resistance through the bed, production of turbulence, heat released/consumed, and any changes to the bed structure. All of these additional conservation equations and source terms can be incorporated into the Fluent solver by means of, respectively, user-defined scalars (UDS) and user-defined functions (UDF).

2.2.2.2 Eulerian-Eulerian (granular) approach

Similarly to the porous medium approach, both phases are modelled as continua, with the governing equations adjusted by the phasic volume fraction. However, the solid phase is now instead modelled as a granular phase, using the kinetic theory of granular flow. The granular phase is effectively a fluid, with pseudo-properties and additional constitutive equations introduced to account for interphase and intraphase interactions, such as particle collisions.

This approach is available as a built-in multiphase model in Fluent; however, particle conversion submodels are not included, and must be defined using UDFs. A major limitation of this approach is that only a single characteristic size can be specified for each granular phase, which is unsuited to combustion simulations, since the particle size will be continuously changing. Moreover, the phasic volume fraction of each individual cell cannot be controlled by the user; hence submodels to represent bed shrinkage cannot be implemented.

2.2.2.3 Eulerian-Lagrangian approach

A Lagrangian representation of the solid phase involves tracking individual particles, which can exchange mass, momentum, and energy with the fluid phase. The Lagrangian approach, termed a discrete phase model (DPM)¹¹, enables particle conversion submodels to be readily applied to each particle. The DPM and the

¹¹ Also termed a discrete particle model (DPM), or the discrete element method (DEM)

associated particle conversion submodels are built-in features of Fluent. The DPM is the most realistic method of representing the particulate phase; however, it is also the most computationally expensive. Furthermore, the localised bed void fraction cannot be directly controlled by the user, and the submodels needed to represent the contact forces between rough, non-spherical particles are not part of the standard features.

2.2.3 One-dimensional (1D) bed models

Significant work has been done on fixed-bed modelling, which has been comprehensively reviewed by Yin *et al.* [21]. The majority of fixed-bed models in the literature are *one-dimensional* transient models based on the porous media approximation, whose purpose is to predict bed temperature, species profiles, and ignition rates. While the same principles apply when modelling the fixed-bed combustion of different solid fuels, the focus in the present study is confined to biomass and waste fuels.

Fatehi and Kaviany [107] developed a one-dimensional model to predict ignition velocities in a packed bed. Both pyrolysis and char oxidation were considered, although thermal equilibrium was assumed between solid and gas phases. Bryden and Ragland [109] developed a steady-state model for thermally thick biomass particles in a deep fixed-bed combustor. Momentum transport was neglected for both the gaseous and solid phases, with velocity profiles instead determined as a function of bed height and consumption rate. The model was capable of predicting the influence of operational parameters on the combustor, and the rate of heat release. Saastamoinen *et al.* [120] performed a sensitivity analysis of ignition rates in a fixed-bed wood combustor by means of a simplified model based on energy balances. Shin and Choi [106] presented a one-dimensional two-phase model for waste combustion, which included global models for pyrolysis, char combustion, and gas combustion. The model was used to predict ignition rates and investigate the different combustion regimes (oxygen-limited, reaction-limited, and extinction by convection) encountered as the air supply rate was increased.

Goh *et al.* [116] outlined the development of a comprehensive incinerator bed model (FLIC), which has since been used extensively by the SUWIC group at Sheffield University. The model includes transport equations for each phase, detailed chemical kinetics, and bed shrinkage. One-dimensional usage of the model includes investigating NO_x emissions from an incinerator [121], the effect of fuel properties on biomass combustion [122-125], transient effects in a MSW incinerator [126], and the slow pyrolysis of different wastes [127].

Zhou *et al.* [83] presented a model to predict the ignition rates, species profiles, and temperature profiles in a fixed-bed burning straw. The model included drying, pyrolysis, heterogeneous char reactions, and the homogeneous combustion of volatiles and tar; it was later extended to address the formation of nitric oxides during combustion [128]. More recently, Johansson *et al.* [90] performed an in-depth sensitivity analysis on the influence of parameter values on the predictions; the gas mixing rates, solid conductivity, heat and mass transfer coefficients, etc., were varied to ascertain their effects.

Cooper and Hallett [104] produced a model for the combustion of char particles in a fixed-bed with constant height, such as a pot furnace. Solid fuel was fed at the top of the bed, moved downward in the bed as the solid was consumed, and eventually left the domain as ash. The mass and energy of the solid phase were conserved by including inlet and outlet boundary conditions to account for, respectively, the addition of fresh fuel at the top of the bed, and ash falling through the grate. The boundary conditions were adjusted to keep the overall bed height constant. An additional transport equation was included to determine the variation of particle mass, and thus size, with height in the bed, with the solution used as an input for the conversion rates and fluid mechanics correlations. Ryan and Hallett [129] later included an ash model, based on the assumption that ash released during combustion occupied the void fractions between particles. The presence of ash resulted in reduced heat and mass transfer rates to the particle. Finally, Girgis and Hallett [130] extended the model from char combustion to dry wood combustion, by

including a pyrolysis reaction. A similar model was developed by Di Blasi [97] to simulate the gasification of wood in a constant-height fixed-bed reactor. Drying was simulated by means of a diffusion model, but the effect of ash was neglected.

2.2.4 Two-dimensional (2D) bed models

Van der Lans *et al.* [20] developed a simplified one-phase, 2D model to predict species and temperature profiles in a fixed-bed straw furnace. The model was effectively a one-dimensional transient model with a predetermined horizontal velocity for the solid phase, which represented grate movement. Ryu *et al.* [131] extended the one-dimensional transient bed model of Shin and Choi [106] to *two-dimensions*. The one-dimensional model was used to solve a vertical slice, or column, of the fuel bed. The progression of fuel along the grate was then represented by transferring the time-dependent solution from one vertical section to the adjacent section at discrete time intervals; horizontal gradients are neglected with this approach. The bed model was also coupled to a separate freeboard simulation, which was solved using a commercial CFD package. Kaer [132] also expanded a one-dimensional transient model to two dimensions using the same approach, termed “walking column”. The model included drying, pyrolysis, char reactions, and bed shrinkage for a straw bed. Similarly to Ryu *et al.*, the stand-alone bed model was also employed in a full-scale furnace simulation, which included a straw fuel bed and freeboard, with the latter simulated using commercial software [110]. This simulation was later extended to incorporate an ash deposition model to investigate the formation of deposits on the surfaces of the furnace [133]. Miljkovic *et al.* [134] also utilised the “walking column” approach to develop a 2D model of straw combustion in a moving-grate furnace; the influence of primary air on the combustion process was examined.

The FLIC bed model introduced in Section 2.2.3 has also been extended for 2D applications. Yang *et al.* [135] predicted the conversion of MSW along the length of a travelling grate. Similarly to Van der Lans *et al.* [20], the solid phase had a constant horizontal velocity; this was predefined as the speed of the grate. This

model was also used to carry out a parameter study [136, 137], to investigate the effect of a substoichiometric air supply on the conversion of MSW in a travelling grate [138], and to examine the conversion of an incinerator from a complete combustor to a gasifier [139]. To represent the gradients that occur in larger particles, Yang *et al.* [140-142] developed a novel double mesh method, where cells were identified as void cells, inner cells, or boundary cells. Gas phase equations were solved in the void cells, solid phase equations were solved in the inner cells, and the phases were coupled through the boundary cells. A 2D axi-symmetric version of the model was later developed and applied to predict the combustion of a single biomass particle [33]. The particle was highly resolved, enabling secondary reactions, such as tar cracking within the particle, to be modelled.

Hermansson and Thunman [143] developed a detailed model to simulate the fixed-bed combustion of char particles. To evaluate measures of reducing grate wear, the simulation included a detailed description of the grate, with heat transfer mechanisms to the neighbouring gaseous and particulate phases. Several configurations of grate shape were simulated to provide recommendations for the design of the grate.

2.2.5 Three-dimensional (3D) bed models

Due to the growth in available computational power, *three-dimensional* models have also become possible in recent years. Collazo *et al.* [34] developed a 3D model, which included a fully-coupled fixed-bed and freeboard. The model was implemented into the CFD package Fluent, and included drying, pyrolysis, and char reactions. Transport of the solid phase was neglected, and bed shrinkage was not incorporated; hence, solid phase consumption resulted purely in an increase in the porosity of the bed. Model predictions were compared with measurements from a pot furnace, where ignition occurred at the top surface of the bed. Collazo *et al.* [144] later used their approach to model a small-scale biomass boiler, although the bed model was significantly simplified, owing to the associated computational expense.

Mehrabian *et al.* [145, 146] devised a novel 3D model to predict bed evolution of an underfed burner by coupling two separate multiphase approaches, an Eulerian-Eulerian (granular) and Eulerian-discrete phase model (DPM), which simulated the fluid mechanics and thermal conversion of the solid particles respectively.

Buczynski *et al.* [147] established a solid fuel combustion model, which employed coal kinetics, but was otherwise applicable to biomass. Drying, pyrolysis, heterogeneous char reactions, and solid phase transport were included; bed shrinkage was not modelled. Similarly to Collazo *et al.* [34], model predictions were compared with measurements from a pot furnace. The most comprehensive 3D model published to date appears to be that of Kurz *et al.* [148], which included both a moving fuel bed and a freeboard. The model included drying, pyrolysis, and char reactions, with a predefined horizontal solid phase velocity; governing equations were solved using the University of Stuttgart's AIOLOS code. An entire reciprocating grate test facility firing wood chips was simulated, and the model was validated using measurements from their test facility. It is worth noting that these measurements did not include detailed bed data.

2.2.6 Particle models

To account for the temperature and conversion gradients seen in larger particles, Wurzenberger *et al.* [149] incorporated a one-dimensional particle model into the transient bed model, known as a "1D+1D" model. The particle was treated as a porous medium with thermal equilibrium assumed between phases. Conversion and species evolution within the particle were solved using spherical coordinates before being handed back to the bed system.

Thunman *et al.* [150] also proposed a one-dimensional particle model, based on moving fronts, or control volumes, within the particle. The momentum equation was not solved within the particle; the product gases were instead assumed to flow outward from the centre of the particle, with the speed calculated as a function of conversion. The particle model was applicable to spheres, cylinders, or

parallelepipeds, and was incorporated into a one-dimensional bed model to investigate co-current and counter-current combustion in a grate furnace [151, 152].

The particle model of Porteiro *et al.* [153, 154] was based on the particle discretisation scheme proposed by Thunman *et al.* [150], and included drying, a parallel-step pyrolysis model, and char oxidation, although char gasification was neglected. The hydrogen released during pyrolysis was assumed to react with oxygen upon reaching the particle exterior, retarding the diffusion of oxygen to the char surface. This particle model was later used to develop a well-stirred reactor (zero-dimensional) bed model, where the bed consisted of a finite number of particles with different granulometry [155]. The integral effects of all particles were coupled, as boundary conditions, to a separate freeboard simulation, giving a prediction of the overall furnace performance.

Peters *et al.* [111] developed a similar one-dimensional particle model, but this was implemented as a discrete particle model (DPM) using a Eulerian-Lagrangian approach to the fixed-bed [112, 113]. As noted in section 2.2.2.3, the main difference between a DPM approach and a simpler Eulerian-Eulerian approach is that the location of the particle's surface is known, because individual particles are tracked. The boundary conditions at the particle surface, and thus coupling between the DPM and the gas phase, are therefore influenced by the occupied gas phase cell. The gas phase was modelled as one-dimensional flow through a porous medium.

In a practical packed bed, the conditions at the surface of an individual particle are unlikely to be uniform, meaning that temperature, mass transfer, etc., cannot be completely described by a one-dimensional particle model [141]. Johansson *et al.* [156] developed a 2D particle model, which was coupled to a one-dimensional transient bed model. They compared results from a standard one-dimensional porous media bed model, a 1D particle + 1D bed model, and a 2D particle + 1D bed model, to determine the influence of particle gradients on the results. They concluded that for larger particles (> 2 cm), the inclusion of a 2D particle model has

a significant effect (~15%) on the prediction of the conversion front, volatile release rate, and temperature profiles, with the effect less influential for smaller particles (< 0.5 cm). However, they also noted that this difference is within the uncertainty of model parameters and experimental scatter. Therefore, the porous media approximation is reasonable to use, except where stoichiometry in the conversion front is not of concern, *e.g.* for NO_x predictions. In addition, they concluded that a one-dimensional particle model overpredicted the influence of particle gradients.

2.2.7 Particle mixing models

In fixed grates, the fuel particles are assumed to move in the gravitational (*i.e.* downward) direction only, owing to the consumption of the fuel lying beneath. As a result, published bed models typically include, as a function of fuel conversion, either bed shrinkage or a negative vertical velocity for the fuel phase. In moving grates, the fuel also has a horizontal velocity component, since it advances along the grate over time. A common assumption is that the fuel progresses at the same velocity as the grate; hence, moving grate models are often realised by extending a fixed grate model by means of either a walking column approach or a predefined horizontal velocity for the solid phase. Although this assumption is plausible for travelling grates (see Section 1.5.2), it is not realistic for all types of moving grate, in particular, not for reciprocating grates where the oscillating rods lead to particle mixing.

Yang *et al.* [157] developed a diffusion model, analogous to Fick's law for the diffusion of gases, to account for particle mixing in the fuel bed. The diffusion coefficient was derived experimentally, and implemented as transport diffusion in the conservation equations for the solid phase components: moisture, dry fuel, char, and ash. The diffusion model did not, however, affect the overall velocity of the solid phase, *i.e.* the horizontal velocity, or advection, remained constant.

Peters *et al.* [158] developed an approach to quantify particle mixing in a moving grate. The motion of spherical particles of different size on a forward acting grate

were predicted by means of a discrete element method (DEM), which enabled the path and velocity of each particle to be tracked. A set of forces, and resulting moments, were included to account for fluid drag forces, buoyancy, and particle-particle contact. The predictions were then used to qualify the mixing intensity for that grate. A similar approach was taken by Kruggel-Emden *et al.* [159] where a DEM was employed to investigate particle mixing in different grate designs. Moreover, 3D predictions were compared to the equivalent 2D approximation, with both producing similar results. The DEM was solved using the parallelised code developed at LEAT in the University of Bochum. Simsek *et al.* [160] later extended this code to include combustion of the particles, and coupled a 2D DEM bed model to a 3D freeboard model, which was solved using commercial software. Additional information related to the work at LEAT is available at [161-163].

2.2.8 Randomly-packed bed models

The limitation of the aforementioned predictions is that they were initialised under the assumption of *uniform* properties throughout the fuel bed. This precludes the investigation of uneven combustion within the bed, which is prevalent in grate furnaces firing solid fuels such as biomass, and is believed to develop as a result of non-uniform bed properties. A common instigator of non-uniform bed properties is the fuel feeding mechanism, and despite the variety of feeders available for fixed-beds, poor fuel distribution in the bed remains an issue [164].

One influential phenomenon in furnace performance, and a salient indicator of unbalanced combustion, is the ‘channelling’ which occurs when relatively porous passages develop due to non-uniformities within the fuel bed or alongside a bounding wall of the furnace. Whether caused by spatial variations in fuel properties or by fuel packing, *i.e.* distribution, these passages result in uneven air distribution, and thus combustion, which eventually causes a depression to form in the surface of the bed.

To study this phenomenon, Yang *et al.* [28] simulated a randomly-packed bed of *spherical* particles. The resistance to flow through the grate was varied to assess its effect on channelling; this effect was quantified by means of the velocity deviation at the top surface on the fuel bed. Yang *et al.* [165] also simulated valley growth in burning bed by creating a relatively porous passage in the centre of an otherwise *uniformly* packed bed.

In their model, Hermansson and Thunman [91] also investigated the influence of grate resistance on central and wall-bounded channelling in a burning char bed, with channels induced at both the centre and the wall of a randomly packed bed respectively. Based on observations from operational furnaces, they proposed that bed shrinkage was a combination of continual shrinkage and instantaneous collapses. Their shrinkage model was the first to reproduce this behaviour.

2.2.9 Discussion

Investigations into measures to reduce channelling in randomly-packed beds have been limited to the effect of grate resistance [28]; alternative operational parameters have been overlooked. A systematic analysis of parameters that influence channelling could provide valuable insight into possible causes, and more importantly, into measures to mitigate the issue. Furthermore, investigations published to date appear to have been carried out using only 2D models, even though channelling is 3D in nature. A 3D model would enable the investigation of features that cannot be represented in a 2D model, such as channelling caused by differently shaped passages in a randomly-packed bed. Finally, the only published computational analysis to include a detailed description of the grate, for the purpose of shape optimisation, was limited to 2D, which precludes the investigation of 3D features, such as an array of openings in the grate. A 3D model could be used to investigate the different effects of the shape, size, and spacing of passages in a grate, and comprises part of the present work.

3. MODEL DESCRIPTION

A central part of this of study is to design, develop, and implement a two-dimensional, and then three-dimensional model that describes the mechanics, thermofluidics, and thermochemical processes which occur in the fixed-bed combustion of solid fuels. For reasons outlined in Section 2.2.2, the approach adopted is to build the model as an extension of the Fluent code, which effectively acts as the compute engine (*i.e.* solver). This extension is made up of a large number of additional modules that implement the submodels describing each chemical and physical process. The overall bed model is complex owing to the number of interdependent modules, each of which is integrated into the Fluent code by means of user-defined functions (UDFs). Each UDF must be designed, coded in its entirety, and then verified to work as expected; programming is carried out using the C programming language. A brief outline of all UDFs used is given in Appendix D. In addition to the core conversion modules, ancillary aspects, such as the parallelisation of the overall model, formed a significant proportion of the work.

This chapter describes our complete bed model, including all submodels and their integration into the CFD package, Fluent.

3.1 Overview

Fluent employs the finite volume method to discretise the computational domain into a large number of cells, each of which is bounded by a number of nodes, as shown in *Figure 3.1*. To determine the overall flow field, conservation equations are solved for each cell, which then stores the generated variables, such as temperature, density, and velocity, among many others. In our model, the domain is initially discretised into uniform quadrilateral (2D) or cubic (3D) cells. This is a requirement of the model, and the computational domain must therefore be compatible with quadrilateral or cubic cells.

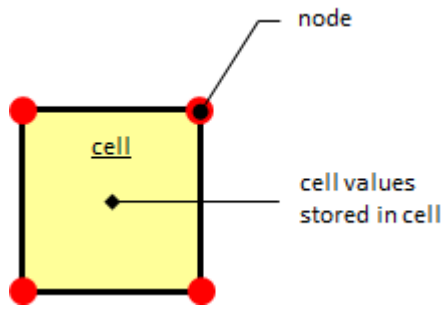


Figure 3.1 Computational cell and surrounding nodes

Numerous interdependent chemical and physical phenomena arise during fixed-bed combustion. The presence of the particulate (solid) phase causes a resistance to the gaseous flow, creates turbulence, and has a significant effect on the thermal dispersion, mass dispersion, and mixing-rate of gas phase species. Heat and mass transfer between the solid and gas phases have a major influence on the chemical reactions, which include the drying, pyrolysis, gasification, and combustion of the solid phase, along with the oxidation of any combustible gases released from the solid. The subsequent conversion of the solid causes its composition to change and the particles, and thus fuel bed, to shrink.

The solid phase is treated as a continuum and is modelled using the porous medium model in Fluent. This Eulerian approach is less computationally expensive than a Lagrangian approach, where individual particles are tracked, and is also well suited to the investigation of void evolution within the bed. In an Eulerian approach, individual particles are not tracked, but instead are represented by assigning an initial notational particle ‘geometry’ to each cell. This ‘geometry’ includes information such as the particle diameter (d_p), volume (V_p), and shape, which are used as inputs for the conversion rates and for the fluid mechanics correlations; they are updated based on fuel consumption within each individual cell.

All solid fuel conversion takes place in the fuel bed, which shrinks over time as the fuel is consumed. Aside from the particle geometry, the local state of the solid phase is described using five scalars: bed void fraction (or porosity), solid phase

temperature, moisture density, dry fuel density, and char density. All remaining fuel properties are determined based on the instantaneous local composition.

The following assumptions provide the basis for the bed model:

- The fuel bed is treated as a continuum and modelled as a porous medium.
- A continuous shrinkage process, and also instantaneous collapses, occur within the fuel bed.
- The solid phase momentum equation is neglected.
- There is an absence of thermal equilibrium between phases.
- Particles are thermally thin – see section 3.3.2.
- Drying described using constant temperature model.
- Pyrolysis represented using one-stage parallel reaction model.
- The heterogeneous char reactions, gasification and combustion, are included.
- Eddy dissipation model (EDM) is used for homogeneous combustion rates.
- Gas phase combustion is included.
- The transport of gases within solid phase is neglected; product gases are released immediately upon formation.
- The heat of the heterogeneous reactions is taken up by the solid phase; product gases are released at the same temperature as the solid phase.
- There is no elutriation of particles from the bed, *i.e.* small particles are not carried away from the bed by the gas flow.

3.2 Gas Phase

The gas phase and solid phase energy are solved using the Navier-Stokes equations, with the inclusion of additional source terms to account for the burning fuel bed. The seven conservation equations describing the fuel bed are listed in *Table 3.1*.

Table 3.1 Conservation equations of the simulated domain – gas phase unless stated

Mass (continuity)	$\frac{\partial}{\partial t}(\varepsilon\rho_g) + \frac{\partial}{\partial x_i}(\varepsilon\rho_g u_i) = S_m$	(3.1)
--------------------------	---	-------

Momentum	$\frac{\partial}{\partial t}(\varepsilon\rho_g u_i) + \frac{\partial}{\partial x_j}(\varepsilon\rho_g u_i u_j) = -\varepsilon \frac{\partial P}{\partial x_i} + \frac{\partial}{\partial x_j}(\varepsilon \tau_{ij}) + \varepsilon \rho_g g + S_{p,i}$	(3.2)
-----------------	--	-------

Species	$\frac{\partial}{\partial t}(\varepsilon Y_k \rho_g) + \frac{\partial}{\partial x_i}(\varepsilon Y_k \rho_g u_i) = \frac{\partial}{\partial x_i}(\varepsilon \rho_g D_{eff,k} \frac{\partial Y_k}{\partial x_i}) + S_{M,k} + S_{V,k} + S_{C,k} + S_{g,k}$	(3.3)
----------------	---	-------

Energy	$\frac{\partial}{\partial t}(\varepsilon \rho_g c_{p,g} T_g) + \frac{\partial}{\partial x_i}(\varepsilon \rho_g u_i c_{p,g} T_g) = \frac{\partial}{\partial x_i}(\varepsilon \lambda_{g,eff} \frac{\partial T_g}{\partial x_i}) + S_{Q,ht} + S_{Q,gr} + S_{Q,sr2}$	(3.4)
---------------	--	-------

Energy (solid)	$\frac{\partial}{\partial t}((1 - \varepsilon) \rho_s c_{p,s} T_s) = \frac{\partial}{\partial x_i}((1 - \varepsilon) \lambda_{s,eff} \frac{\partial T_s}{\partial x_i}) - S_{Q,ht} + S_{Q,sr1} - S_{Q,sr2}$	(3.5)
-----------------------	---	-------

Turbulent energy	$\frac{\partial}{\partial t}(\varepsilon \rho_g k) + \frac{\partial}{\partial x_i}(\varepsilon \rho_g u_i k) = \frac{\partial}{\partial x_i}(\varepsilon (\mu + \frac{\mu_t}{\sigma_k}) \frac{\partial k}{\partial x_i}) + G_k + G_b - \rho_g \varepsilon_d + S_k$	(3.6)
-------------------------	--	-------

Turbulent dissipation	$\frac{\partial}{\partial t}(\varepsilon \rho_g \epsilon) + \frac{\partial}{\partial x_i}(\varepsilon \rho_g u_i \epsilon) = \frac{\partial}{\partial x_i}(\varepsilon (\mu + \frac{\mu_t}{\sigma_\epsilon}) \frac{\partial \epsilon}{\partial x_i}) + C_1 \frac{\epsilon}{K} (G_k + C_3 G_b) - C_2 \rho_g \frac{\epsilon^2}{K} + S_\epsilon$	(3.7)
------------------------------	---	-------

where $C_1 = 1.44$, $C_2 = 1.92$, $C_3 = 0.09$, $\sigma_k = 1.0$, $\sigma_\epsilon = 1.3$

3.2.1 Thermal and mass dispersion

Dispersion of the gaseous species is strongly influenced by the presence of the packed bed, and effective dispersion coefficients are calculated using the correlation of Wakao and Kaguei [92], with binary diffusion coefficients, $D_{eff,AB,ref,k}$ taken from Massman [166]:

$$D_{eff,k} = 0.8 D_{eff,AB,k} + 0.5 |u_g| d_p \quad (3.8)$$

$$D_{eff,AB,k} = D_{AB,ref,k} \left(\frac{T_g}{T_{ref}} \right)^{1.75} \quad (3.9)$$

where u_g is the speed of the gas, T_g is the gas temperature, and T_{ref} is a reference temperature. Similarly, the effective thermal dispersion of the gas phase is given by [92]:

$$\lambda_{g,eff} = 0.8 \lambda_g + 0.5 c_{p,g} \rho_g |u_g| d_p \quad (3.10)$$

where λ_g is the gas conductivity, and $c_{p,g}$ is the specific heat capacity of the gas.

3.2.2 Resistance to gas flow

Resistance to gas flow is accounted for by means of a sink to the gas phase momentum equation, Eq. (3.2), which results in a pressure drop through the fuel bed. The resistance is calculated using the Ergun equation [88]:

$$S_{p,i} = - \left(\frac{\mu}{\alpha} u_i + \beta \rho_g |u| u_i \right) \quad (3.11)$$

where u is the gas velocity, ρ_g is the gas density, u_i is the velocity of the gas, and μ is the viscosity. The standard correlations for permeability, α , and Forchheimer constant, β , in Eq. (3.11) are modified for use with rough particles [167]:

$$\alpha = \frac{\varepsilon^3 d_p^2}{180(1-\varepsilon)^2} \quad (3.12)$$

$$\beta = \frac{4(1-\varepsilon)}{\varepsilon^3 d_p} \quad (3.13)$$

where ε is the local void fraction or porosity, and d_p is the particle diameter. The resistance to gas flow through the grate is calculated using [28]:

$$S_{p,i} = -\beta_{gt} \rho_g |u| u_i \quad (3.14)$$

where β_{grate} is the inertial resistance coefficient of the grate, which is analogous to the Forchheimer constant for the fuel bed.

3.2.3 Turbulence

Turbulence is modelled by means of the standard $k - \epsilon$ (SKE) turbulence model, with the effects of the packed bed accounted for using source terms for energy production, k , and dissipation, ϵ . Nakayama and Kuwahara [168] proposed turbulent source terms based on the Ergun equation, Eq. (3.11), using the standard correlations for α and β . They noted that the source terms could be adapted to more specific situations by modifying the correlations for α and β , Eqs. (3.12) and (3.13) respectively, in our case. In the absence of better correlations, however, the original source terms are used here, thus we take:

$$S_k = \frac{1.75(1-\epsilon)}{\epsilon d_p} |u_g|^3 \quad (3.15)$$

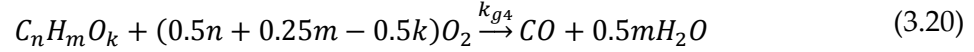
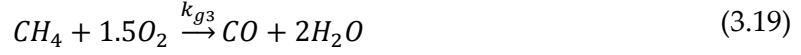
$$S_\epsilon = \frac{4.55c_2(1-\epsilon)^2}{\epsilon^2 d_p^2} |u_g|^4 \quad (3.16)$$

3.2.4 Homogeneous reactions

Any of the several gas phase reactions may be limited either by chemical kinetics or by mixing rates. The finite-rate/eddy dissipation model (EDM) computes both rates for every reaction, and then uses the slower of the two. The EDM calculates the gas mixing rate using k and ϵ in a similar manner to alternative formulations for gas mixing rates in packed beds [135, 169]. Therefore, the EDM may under-predict the gas mixing rate unless the appropriate source terms for k , Eq. (3.15), and ϵ , Eq. (3.16), are included. The default values for the mixing constants in the standard EDM are used in this work. However, Yin *et al.* [21] noted how these may need to be modified to obtain the best match between predictions and measurements, as in [4, 137].

The combustion mechanism of Westbrook and Dryer [170] is used to describe the partial oxidation of tar and light hydrocarbons as well as the complete oxidation of

carbon monoxide and hydrogen. Thus the full set of chemical reactions employed are as follows:



These reactions are implemented using the EDM model available in Fluent [88], which calculates the resulting species source terms, $S_{g,k}$ (Eq. (3.3)), and the gas phase energy source term, $S_{Q,gr}$ (Eq. (3.4)). The kinetic rates used for these reactions, and their corresponding sources, are listed in *Table 3.2*.

Table 3.2 Gas phase kinetic rates [$kmol/m^3 \cdot s$]

k_{g1}	$1.3 \times 10^{11} \exp(-1.2554 \times 10^8 / RT_g) C_{CO} C_{O_2}^{0.5} C_{H_2O}^{0.5}$	[171]
k_{g2}	$1 \times 10^{11} \exp(-8.3145 \times 10^7 / RT_g) C_{H_2} C_{O_2}^{0.5}$	[97]
k_{g3}	$5.012 \times 10^{11} \exp(-2 \times 10^8 / RT_g) C_{CH_4}^{0.5} C_{O_2}$	[34]
k_{g4}	$9.2 \times 10^6 \exp(-8.023 \times 10^7 / RT_g) C_{TAR}^{0.5} C_{O_2}$	[109]
k_{g5a}	$2.78 \exp(-1.2554 \times 10^7 / RT_g) C_{CO} C_{H_2O}$	[91]
k_{g5b}	$93.69 \exp(-4.659 \times 10^7 / RT_g) C_{CO_2} C_{H_2}$	[91]

3.3 Fuel Phase

Biomass is the focus of this study, compressed wood pellets in particular, which have a significantly higher bulk density than typical wood-derived fuels. However, it is noted that the submodels described below are applicable to other solid fuels. The connection between some of these particle-scale submodels, from the heat and

mass transfer between each phase, to the thermochemical conversion and subsequent physical changes of the particle phase, is illustrated in *Figure 3.2*.

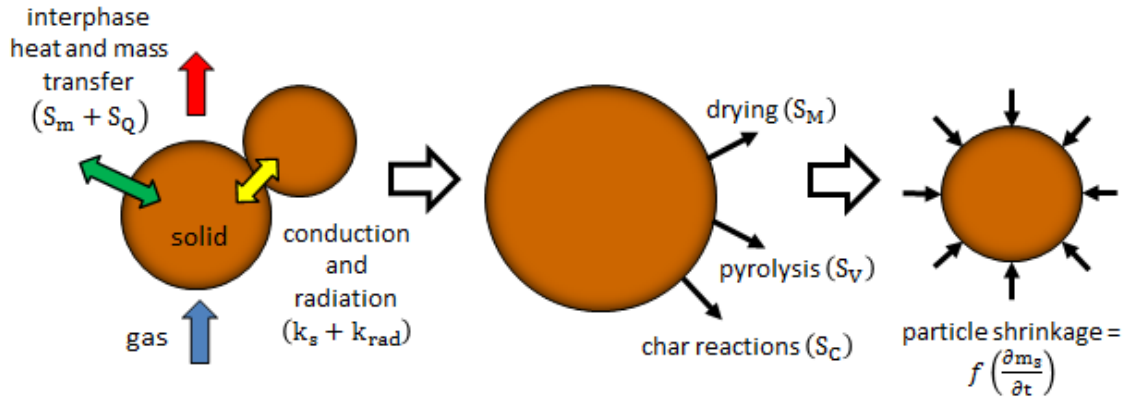


Figure 3.2 Sequence of particle-scale processes.

3.3.1 Heat and mass transfer

The interphase heat transfer coefficient, h_{ht} , is determined using the well-known Nusselt number, Nu , correlation of Wakao and Kaguei [92]:

$$Nu = 2 + 1.1Pr^{1/3} Re^{0.6} \quad (3.23)$$

$$h_{ht} = \frac{\lambda_{g,eff} Nu}{d_{p,s}} \quad (3.24)$$

$$Re = \frac{\rho_g u_g d_p}{\mu_g} \quad (3.25)$$

$$Pr = \frac{c_{p,g} \mu_g}{\lambda_{g,eff}} \quad (3.26)$$

where Re is the Reynolds number, and Pr is the Prandtl number. The source term to the gas phase, and corresponding sink to the solid phase is [90]:

$$S_{Q,ht} = A_{spec} h_{ht} (T_s - T_g) \quad (3.27)$$

$$A_{spec} = \frac{(1 - \varepsilon) A_p}{V_p} = \frac{6(1 - \varepsilon)}{\Psi d_p} \quad (3.28)$$

where Ψ is the sphericity of the particle. The sphericity is the ratio of the surface area of an equivalent volume sphere to the surface area of the particle. In an Eulerian-Eulerian representation of the fuel bed, a source term is averaged over an entire cell. Since a cell contains both a solid and a gas phase, the surface area to

volume ratio of the particle (A_p/V_p) must be adjusted by the volume fraction of the solid phase in that cell ($1 - \varepsilon$); this also affects the heterogeneous reaction rates, section 3.3.5. The interphase mass transfer coefficient is calculated in a similar manner using the analogous Sherwood number, Sh , also from Wakao and Kaguei [92]:

$$Sh = 2 + 1.1Sc^{1/3} Re^{0.6} \quad (3.29)$$

$$h_{m,k} = \frac{D_{eff,k} Sh}{d_{p,s}} \quad (3.30)$$

$$Sc = \frac{\mu_g}{\rho_g D_{eff,k}} \quad (3.31)$$

3.3.2 Thermally-thin assumption

The temperature distribution in a particle determines the different rates of conversion. If the temperature is uniform, drying, pyrolysis, and char reactions occur sequentially; if temperature gradients are present, these processes may occur simultaneously. The temperature distribution is characterised by means of the Biot number, Bi [172]:

$$Bi = \frac{h_{ht} L_c}{\lambda_s} \quad (3.32)$$

where L_c can be approximated as V_p/A_p (*i.e.* $\Psi d_p/6$) for irregularly-shaped particles, or more conservatively, as d_p . To account for the influence of the packed bed, Yang *et al.* [124] proposed a modified Biot number:

$$Bi' = \varepsilon Bi \quad (3.33)$$

If $Bi' \gg 1$, then a significant temperature gradient exists inside the particle; otherwise the particle can be considered thermally-thin. Depending on the selection of L_c , a typical modified Biot number in the cases investigated is $0.5 < Bi' < 3$.

This implies that temperature gradients may exist within the particle, and that a thermally-thin assumption is not strictly representative. However, Yang *et al.* [124]

proposed that particles smaller than 30 mm in diameter, with similar Biot numbers to this study, could be approximated as thermally-thin without causing a significant error. This assumption is supported by the work of Johansson *et al.* [156], who investigated the influence of intraparticle gradients in the modelling of fixed-bed combustion. They concluded that the thermally-thin assumption does not have an appreciable effect on the predicted results, with the exception of NO_x predictions, until particles become larger than 20 mm.

Since the particles investigated here are significantly smaller than 20 mm, and NO_x are not considered, the thermally-thin assumption is therefore deemed adequate, as has been done in earlier studies [91, 97, 104, 106].

Furthermore, it will be appreciated that to capture the detailed effects of temperature gradients within the particle would require a separate particle model, see section 2.2.6, which would be outside the scope of this study.

3.3.3 Drying

Drying is assumed to occur at a predefined temperature using the constant temperature evaporation model of Peters *et al.* [111]. To ensure numerical stability, the drying rate is modified so that only a fraction of the available heat is used for evaporation, with the remainder heating the solid above the evaporation temperature, T_{evap} . A similar approach has been taken elsewhere [33, 34], and the resulting drying rate is:

$$\frac{d\rho_M}{dt} = \begin{cases} -0.5 \frac{(T_s - T_{evap})\rho_s c_{p,s}}{\Delta H_M \Delta t}, & \text{if } T_s \geq T_{evap} \\ 0, & \text{if } T_s < T_{evap} \end{cases} \quad (3.34)$$

where ΔH_M is the latent heat of evaporation, Δt is the timestep, and the source term to the gas phase is:

$$S_{M,H_2O} = -\frac{d\rho_M}{dt} \quad (3.35)$$

3.3.4 Pyrolysis

Pyrolysis is described using three parallel, first-order reactions for conversion into gas, tar, and char, Eq. (3.36). Each reaction is described by means of an Arrhenius rate coefficient, Eq. (3.37), with reaction constants given in *Table 3.3*.



$$k_{V,i} = A_{V,i} e^{-E_{V,i}/RT} \quad (3.37)$$

where k_V has units 1/s, A_V is a pre-exponential constant, and E_V is the activation energy. The total mass loss of dry fuel is the sum of these reactions, Eq. (3.38). Of this mass loss, the fraction which is converted to char is determined using Eq. (3.39), with the mass of char formed given by Eq. (3.40); all char formed remains in the solid phase and is assumed to be pure carbon. The composition of the volatiles released from the solid phase during pyrolysis are calculated using the approach of Thunman *et al.* [102], see section 3.3.10. This approach determines the mass fraction of each individual species by means of an element and energy balance, which is based on the ultimate analysis and lower heating value (LHV) of the dry feedstock. The mass fraction of char formed, Eq. (3.39), is used as an input for this approach to ensure the conservation of mass, elementary composition, and energy throughout the pyrolysis process. Once the mass fraction of each species is known, the corresponding source term to the gas phase is given by Eq. (3.41). The specific heat of tar is approximated as that of benzene, while its composition and LHV are taken as $C_6H_8O_1$ and 26 MJ/kg respectively [102]. Pyrolysis is assumed to be endothermic with the heat of reaction taken as 300 kJ/kg [79].

$$\frac{d\rho_{sd}}{dt} = -\rho_{sd} \sum_{i=1}^3 k_{V,i} \quad (3.38)$$

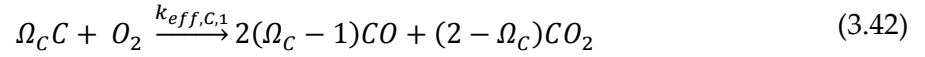
$$Y_{V,C} = \frac{k_{V,3}}{\sum_{i=1}^3 k_{V,i}} \quad (3.39)$$

$$\frac{d\rho_c}{dt} = -Y_{V,c} \frac{d\rho_{sd}}{dt} \quad (3.40)$$

$$S_{V,k} = -Y_{V,k} \frac{d\rho_{sd}}{dt} \quad (3.41)$$

3.3.5 Char oxidation and char gasification

The heterogeneous reactions considered are char oxidation with O_2 , and char gasification with CO_2 and H_2O :



A global reaction scheme is used in this study, where the effective conversion rate depends on the apparent chemical reaction rate and on the rate of diffusion of reactants to the surface of the particle. If a temperature gradient exists within the particle, the conversion processes will overlap, and the efflux of volatiles from the particle during pyrolysis will reduce the diffusion of reactants to the particle surface [112]. To account for the presence of small gradients, as noted in section 3.3.2, a pseudo “blowing factor”, f_b , is introduced to limit the heterogeneous reactions while pyrolysis is ongoing, as in [34]. An alternative formulation for f_b is used here instead of a Dirac type function, but general applicability comes with a caveat. The non-spherical particle shape is accounted for by means of sphericity [173], which relates the particle surface area to that of a sphere of equivalent volume. The resulting reaction rates for Eqs. (3.42) – (3.44) are described by:

$$\frac{d\rho_{c,j}}{dt} = -f_b A_{spec} M_C \Omega_C k_{eff,c,j} \quad (3.45)$$

$$k_{eff,c,j} = \frac{k_{C,j} h_{m,k}}{k_{C,j} + h_{m,k}} C_k \quad (3.46)$$

$$k_{C,j} = A_{C,j} e^{-E_{C,j}/RT} \quad (3.47)$$

$$f_b = 1 - \frac{\rho_{sd}}{\rho_{sd,0}} \quad (3.48)$$

where the value for $j = 1, 2, \text{ or } 3$, and i refers to $O_2, CO_2, \text{ or } H_2O$. $k_{c,j}$ and $h_{m,i}$ both have units m/s, and C_i is the molar concentration of the reactant. The corresponding source terms for the gas phase can be determined from the char consumption rate:

$$S_{c,k,j} = \Omega_{k,j} \frac{M_k}{M_C} \frac{d\rho_{c,j}}{dt} \quad (3.49)$$

where Ω is the stoichiometric coefficient, M_k is the molecular weight of the species, and M_C is the molecular weight of carbon. The kinetic rates, and their sources, for all solid phase reactions are listed in **Table 3.3**.

Table 3.3 Solid phase kinetic rates (1/s)

$k_{V,1}$	$1.435 \times 10^4 \exp(-8.86 \times 10^7 / RT_s)$	[47]
$k_{V,2}$	$4.125 \times 10^6 \exp(-1.127 \times 10^8 / RT_s)$	[47]
$k_{V,3}$	$7.377 \times 10^5 \exp(-1.065 \times 10^8 / RT_s)$	[47]
$k_{C,1}$	$4 \times 10^3 \exp(-8 \times 10^4 / RT_s)$	[174]
$k_{C,2}$	$3.6 \times 10^4 \exp(-1.76 \times 10^8 / RT_s)$	[91]
$k_{C,3}$	$3.42 \exp(-1.297 \times 10^8 / RT_s)$	[156]
Ω_C	$\frac{2(1 + 4.3 \exp(-3390/T_s))}{2 + 4.3 \exp(-3390/T_s)}$	[174]

The heat associated with each solid phase reaction is assumed to be taken up by the solid phase. The total heat source to the solid phase energy equation, Eq. (3.5), is the sum of all these reactions:

$$S_{Q,sr1} = \sum_{\rho_s} \Delta H_{r,i} \frac{\partial \rho_{s,i}}{\partial t} \quad i = \text{drying, pyrolysis, char reactions} \quad (3.50)$$

where ΔH_r is the heat of reaction, specified per mass char for the char reactions; these are summarised in

Table 3.4 for the solid phase reactions considered. To ensure mass conservation, the total mass source to the gas phase is equal to the mass of solid fuel consumed:

$$S_m = \sum_{\rho_s} \frac{\partial \rho_{s,i}}{\partial t} \quad i = \text{drying, pyrolysis, char reactions} \quad (3.51)$$

Table 3.4 Heats of solid phase reactions (J/kg)

drying		$H_{r,M} = -2.2465 \times 10^6$	
pyrolysis		$H_{r,V} = -3 \times 10^5$	[79]
char gasification	$C + CO_2$	$H_{r,C1} = -14.3833 \times 10^6$	[97]
	$C + H_2O$	$H_{r,C2} = -10.95 \times 10^6$	[97]
char combustion	$C + O_2 \rightarrow CO$	$H_{r,C3a} = 9.8 \times 10^6$	[86]
(function of both)	$C + O_2 \rightarrow CO_2$	$H_{r,C3b} = 33.1 \times 10^6$	[86]
		$H_{r,C3} = (2(\Omega_C - 1)H_{r,C3a} + (2 - \Omega_C)H_{r,C3b})/\Omega_C$	

3.3.6 Thermal conductivity

The thermal conductivity of wood varies with temperature, density, composition (which includes moisture content), structure, and the direction of heat transfer with respect to the grain. Furthermore, in porous media such as wood particles and fixed beds, interstitial radiation can contribute towards the overall heat transfer. A simplified model is used here, where radiation between particles is modelled as diffusion by employing an effective thermal conductivity for the solid phase [11, 175]:

$$\lambda_{s,eff} = \lambda_s + \lambda_{rad} \quad (3.52)$$

Since a typical fuel particle is porous, it will contain gas, which is assumed to be in thermal equilibrium with the solid phase at the particle scale. The thermal conductivity of the solid particle, λ_s , is therefore calculated using a combination of any gas contained within and a mass-weighted average of the solid phase components:

$$\lambda_s = \varepsilon_p \lambda_g + \sum_k Y_k \lambda_k \quad (3.53)$$

The porosity of the particle can be estimated by assuming a theoretical density for the compacted, void free solid, and comparing this with the apparent density of the solid phase:

$$\varepsilon_p = 1 - \frac{\rho_s}{\rho_{th}} \quad (3.54)$$

The theoretical density of the virgin solid is here assumed to be 1500 [kg/m³] [11, 30, 176]. The radiative contribution of the effective thermal conductivity is taken as [175]:

$$\lambda_{rad} = 4\varepsilon\sigma_b\omega d_p T_s^3 \quad (3.55)$$

The effective thermal conductivity has a significant influence on the ignition rate within the fuel bed. Several submodels were therefore tested to achieve the best match with the measured ignition rates of Porteiro [173, 177, 178]¹²; this was obtained using the submodel outlined in this section. Alternative submodels are listed in Appendix C.

3.3.7 Specific heat capacity

The specific heat capacity is calculated in a similar manner to the thermal conductivity; using a mass-weighted average of the solid phase components:

$$c_{p,s} = \sum_k Y_k c_{p,k} \quad (3.56)$$

where Y_k is the mass fraction of a solid component.

3.3.8 Particle shrinkage

A common assumption made in modelling is that the particles do not shrink during the pyrolysis stage, with the mass loss reflected in a decreasing density; the density then remains constant during the char reactions stage, causing a decrease in particle size [34, 97, 130]. This is quite unrealistic; measurements by Thunman *et al.* [150] show particle shrinkage to vary by between 20 to 50% during pyrolysis.

Because particle shrinkage is a driving factor in channel formation, it is necessary to represent this behaviour in the present work. Two particle shrinkage submodels are therefore displayed:

¹² Other factors such as drying rate, devolatilisation rate, and air flow rate will also affect the ignition rate, therefore a parametric study was done to determine the appropriate conductivity model and values

If a *single-step pyrolysis model* with an assumed final char yield, $\rho_{C,\infty}$, is used, the shrinkage can be related to the initial amount of each component in the solid phase, modified from [90]:

$$V_p = V_{p,0} \left(1 - \delta_{p,M} \left(1 - \frac{\rho_M}{\rho_{M,0}} \right) - \delta_{p,sd} \left(1 - \frac{\rho_{sd}}{\rho_{sd,0}} \right) - \delta_{p,C} \left(\frac{\rho_{C,burned}}{\rho_{C,\infty}} \right) \right) \quad (3.57)$$

$$\delta_{p,M} = \varphi_M X_{m,0} \quad (3.58)$$

$$\delta_{p,sd} = \varphi_{sd} (1 - \delta_{p,M}) \quad (3.59)$$

$$\delta_{p,A} = \frac{X_{m,0} \rho_{s,0}}{(1 - \varepsilon_A) \rho_A} \quad (3.60)$$

$$\delta_{p,C} = 1 - \delta_{p,M} - \delta_{p,sd} - \delta_{p,A} \quad (3.61)$$

The shrinkage constants for drying, φ_M , and devolatilisation of the dry solid, φ_{sd} , were chosen as 0.2 and 0.4 respectively to reproduce the observations of Thunman *et al.* [150].

For a *parallel reaction pyrolysis model*, the final char yield is not assumed beforehand, but is determined by the temperature history of the particle, rendering Eq. (3.57) inapplicable. Therefore, shrinkage is approximated by assuming the particle volume to decrease linearly with the dry fuel mass and increase with char mass [48]:

$$V_p = V_{p,0} \left(\frac{\rho_{sd}}{\rho_{sd,0}} + \varphi_C \frac{\rho_C}{\rho_{sd,0}} \right) \quad (3.62)$$

The shrinkage constant, φ_C , is selected based on the expected char yield from pyrolysis. However, since the actual char yield, Eq. (3.46), depends on the temperature history of the particle, so too will the shrinkage. The shrinkage constant, φ , is here chosen to be 2.5 to reproduce the measurements of Thunman *et al.* [150] for the expected char yield.

It is worth noting that both submodels have been developed and tested; however, following the validation of the overall bed model, only the latter (Eq. (3.62)) was utilised. In the event that a single-step pyrolysis model is required, which can be

activated by changing a single switch in our source code, the appropriate particle shrinkage submodel is automatically selected.

3.3.9 Density of the solid phase within the cell

The density of the solid phase is determined by relating the fictitious particle volume to the mass of the solid phase in the cell, according to:

$$\rho_s = \rho_{s,0} \left(\frac{m_s}{m_{s,0}} \right) \left(\frac{V_{p,0}}{V_p} \right) \quad (3.63)$$

3.3.10 Volatile gas composition

To ensure the conservation of energy and chemical elements, the combined composition and specific enthalpies of all gases generated during the pyrolysis of the solid phase, must be balanced against the solid fuel consumed. This is done using the approach of Thunman *et al.* [102], which will now be outlined as applied in the present model.

The elemental species were balanced using the following set of equations. Only the major elements, C, H, and O were balanced. Minor species were neglected.

$$X_{j,wood} = \sum_{i=1}^n Y_i X_{j,i} \quad (3.64)$$

where j is the element being balanced (C, H, O), and i is the species released from the solid (char, tar, CO , CO_2 , CH_4 , H_2O , H_2). Thunman subdivided the wood into volatiles and char:

$$X_{j,wood} = Y_V X_{j,V} + Y_{Char} X_{j,Char} \quad (3.65)$$

Including the particular gaseous species selected for this work – tar, CO , CO_2 , CH_4 , H_2O , and H_2 – this becomes:

$$X_{C,wood} = Y_V \left(\frac{Y_{CO}}{M_{CO}} + \frac{Y_{CO_2}}{M_{CO_2}} + \frac{Y_{CH_4}}{M_{CH_4}} + n \frac{Y_{C_n H_m O_k}}{M_{C_n H_m O_k}} \right) M_C + Y_{Char} X_{C,Char} \quad (3.66)$$

$$X_{H_2,wood} = Y_V \left(2 \frac{Y_{CH_4}}{M_{CH_4}} + \frac{m}{2} \frac{Y_{C_n H_m O_k}}{M_{C_n H_m O_k}} + \frac{Y_{H_2}}{M_{H_2}} + \frac{Y_{H_2O}}{M_{H_2O}} \right) M_{H_2} + Y_{Char} X_{H_2,Char} \quad (3.67)$$

$$X_{O_2,wood} = Y_V \left(\frac{1}{2} \frac{\gamma_{CO}}{M_{CO}} + \frac{\gamma_{CO_2}}{M_{CO_2}} + \frac{k}{2} \frac{\gamma_{C_nH_mO_k}}{M_{C_nH_mO_k}} + \frac{1}{2} \frac{\gamma_{H_2O}}{M_{H_2O}} \right) M_{O_2} + Y_{Char} X_{O_2,Char} \quad (3.68)$$

where γ_i is the mass fraction of species i in the volatile gases released, and Y_{Char} is the mass fraction of char released given by Eq. (3.46)¹³.

$$\begin{bmatrix} \gamma_{H_2O} \\ \gamma_{H_2} \\ \gamma_{CO} \\ \gamma_{CO_2} \\ \gamma_{CH_4} \\ \gamma_{C_nH_mO_k} \end{bmatrix} = \begin{bmatrix} 0 & 0 & 1/M_{CO} & 1/M_{CO_2} & 1/M_{CH_4} & n/M_{C_nH_mO_k} \\ 1/M_{H_2O} & 1/M_{H_2} & 0 & 0 & 2/M_{CH_4} & m/2M_{C_nH_mO_k} \\ 1/2M_{H_2O} & 0 & 1/2M_{CO} & 1/2M_{CO_2} & 0 & k/2M_{C_nH_mO_k} \\ \xi_{H_2O} & \xi_{H_2} & \xi_{CO} & \xi_{CO_2} & \xi_{CH_4} & \xi_{C_nH_mO_k} \\ 0 & 0 & 1 & -\Omega_1 & 0 & 0 \\ 0 & 0 & 0 & -\Omega_2 & 1 & 0 \end{bmatrix}^{-1} \begin{bmatrix} X_{C,V}/M_C \\ X_{H_2,V}/M_{H_2} \\ X_{O_2,V}/M_{O_2} \\ \kappa \\ 0 \\ 0 \end{bmatrix} \quad (3.69)$$

The equivalent heating values of the individual, ξ , and combined, κ , species and the empirically derived ratio of CH_4 to CO_2 , Ω_2 , are calculated as described by Thunman *et al.* The resulting set of equations is stiff and can produce unrealistic results if care is not taken. Therefore, the empirical ratio Ω_2 is bound to the temperatures of the experiment from which it was derived, and the ratio of CO to CO_2 , Ω_1 , is set to a constant value of 3.0, in order to reproduce the measurements of Girgis and Hallett [130]. Furthermore, the composition and heating value of the tar are assumed to be C_6H_8O and 26 (MJ/kg) respectively, as these produce reasonable results in all scenarios tested.

3.3.11 Energy released

All interphase mass transfer will have a corresponding energy transfer. This is calculated by assuming that all gas species are transferred at the same temperature as the phase from which they are released. The resulting energy source to the gas phase, and corresponding sink to the solid phase, is given by [91]:

¹³ This would correspond to the asymptotic (or final) char yield in the single-step pyrolysis model.

$$S_{Q,sr2} = \sum_k \left(S_{s,k,prod} \int_{T_{ref}}^{T_s} c_{p,k} dT - S_{s,k,react} \int_{T_{ref}}^{T_g} c_{p,k} dT \right) \quad (3.70)$$

where $S_{s,k}$ is the mass of each species consumed/released during drying, pyrolysis, and the char reactions, and T_{ref} is the reference temperature for all gas sources/sinks in Fluent [88].

3.4 Ignition Mechanisms

Combustion behaviour in a grate furnace using a cross-current arrangement (Section 1.5.2) will differ significantly depending on where the fuel bed is ignited. If ignited from the *top surface* of the bed, the ignition front progresses in the direction opposite to the air flow, known as *counter-current combustion*. A narrow reaction front is established, since the heat flows in the opposite direction to the supply air [20, 21, 83, 120, 179]. If ignited from *just above the grate*, heat flows in the same direction as the air flow, resulting in a thicker reaction front, termed *co-current combustion*. In this case, the ignition is most likely caused by the residual heat in the grate and/or fragments of burning char which become lodged in the grate bars. These ignition mechanisms, and the resulting combustion behaviour, are illustrated in *Figure 3.3*.

Investigations into ignition behaviour in operational moving-grate furnaces indicate that ignition occurs just above the grate surface [152, 179-181].

Because the aim of this study is to investigate combustion in fixed-bed (moving-grate) furnaces, ignition in the computations to be described is usually set to occur just above the grate. The only exceptions are where the model is being validated using the pot furnace experiments of Porteiro *et al.* [177], Girgis and Hallett [130], and Ryan and Hallett [129], where the fuel bed is ignited from the top surface.

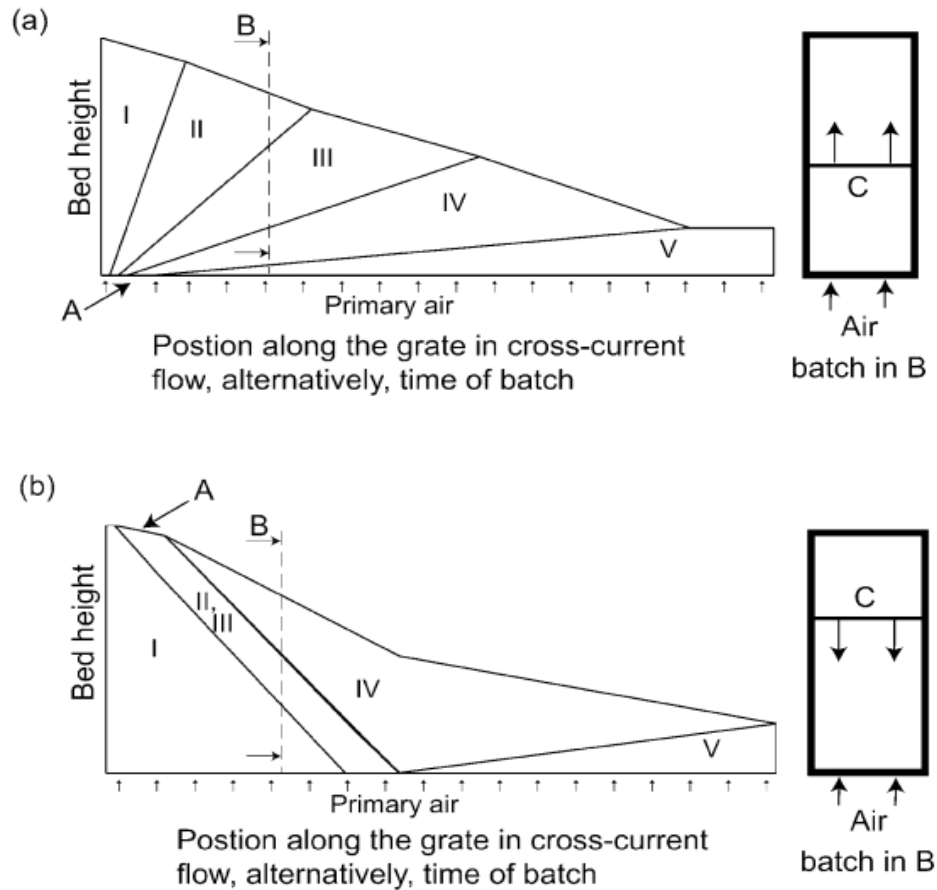


Figure 3.3 Combustion behaviour in a cross-current flow unit: (a) Ignition at grate surface (b) Ignition from surface. A: Point of ignition, B: Vertical section, C: Reaction/Ignition front. I: Unreacted fuel, II: Drying, III: Devolatilisation, IV: Char oxidation/gasification, V: Ash. (adapted from [152])

3.5 Bed Shrinkage

Regression of the fuel bed surface is modelled by shrinking the computational domain. This is done using a new mesh deformation UDF¹⁴ that has been designed and coded as part of this work, which alters the position of each node in the fuel bed zone during the solution procedure within Fluent. The deformation routine is simplified by assuming that the transport of mass and momentum of the solid phase is negligible, and that deformation only occurs in the gravitational, which here

¹⁴ DEFINE_GRID_MOTION

corresponds to the negative y-direction. Therefore, it is only necessary to update the y-position of each node, see *Figure 3.1*.

As one cell shrinks, all the cells directly above it will also “slide” down. To facilitate this, the domain is initially discretised into uniform quadrilateral cells, forming clearly distinguishable columns of cells, as shown in *Figure 3.4*. Furthermore, a user-defined coordinate system is established to identify the relative location of each cell (*Figure 3.5*); the user-defined x, y, and z (if 3D) coordinates are therefore stored in user-defined memory (UDM); these are simply memory locations that are linked to each individual cell, which the user can control.

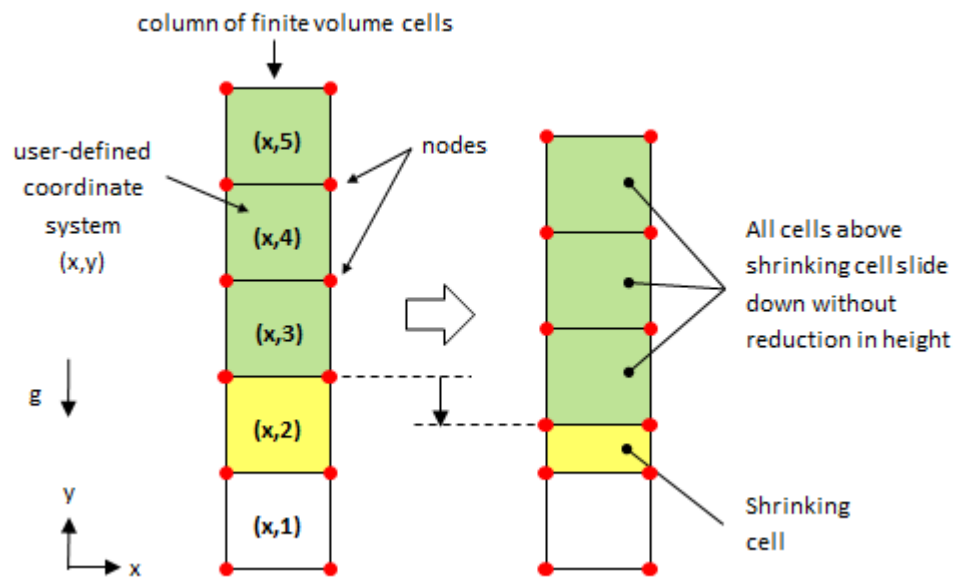


Figure 3.4 Overview of bed shrinkage

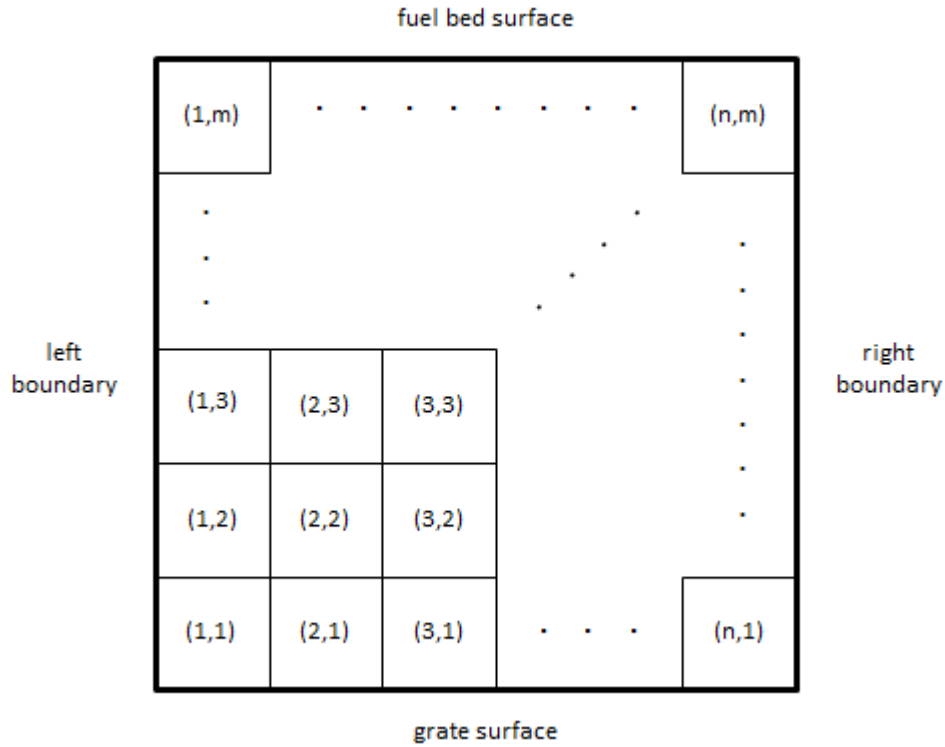


Figure 3.5 User-defined coordinate system applied to every cell

3.5.1 Description of shrinkage submodel

The conversion and resulting shrinkage of the fuel particles will cause the fuel bed to contract in the gravitational direction. In our Eulerian representation of the fuel bed, the particle shrinkage is converted into a total volume change for the computational cell:

$$\frac{\partial V}{\partial t} = \frac{1}{(1 - \varepsilon_0)} \frac{\partial V_s}{\partial t} \quad (3.71)$$

where V is the volume of the computational cell, V_s is the volume of the solid phase in the cell, and ε_0 is the initial porosity of the computational cell. This is then converted into a total linear shrinkage in the gravitational direction, according to:

$$\frac{\partial y}{\partial t} = \frac{1}{\Delta x \Delta z} \frac{\partial V}{\partial t} \quad (3.72)$$

Based on observations from operating furnaces, Hermansson *et al.* [5] concluded that the bed shrinkage is erratic, consisting of both continual shrinkage and sporadic collapses. To reproduce their observations, the shrinkage model of Hermansson

and Thunman [91] is employed here, whereby a proportion of the total shrinkage, allocated using a shrinkage factor, δ_{shr} , is immediately implemented as continual cell shrinkage, Eq. (3.73); the remainder causes an increase in the local porosity of the corresponding cell, which eventually leads to a collapse. This shrinkage model is illustrated in *Figure 3.6*. A shrinkage factor of 1 implies that the computational cell continuously shrinks in proportion to the solid phase, thus maintaining the bed porosity. A shrinkage factor of 0 will cause the porosity to increase towards unity (*i.e.* completely occupied by gas), while the volume of the computational cell remains constant.

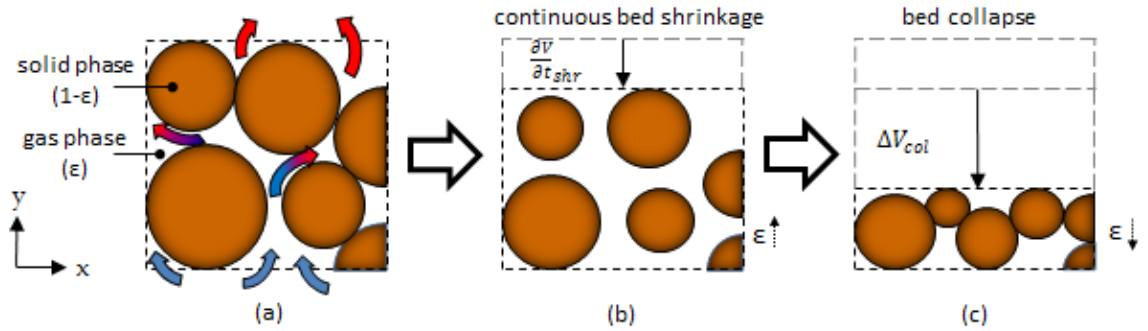


Figure 3.6 Fuel bed shrinkage processes: (a) initial region; (b) same space following continuous shrinkage; (c) same space upon application of bed collapse

$$\frac{\partial V}{\partial t_{shr}} = \delta_{shr} \frac{\partial V}{\partial t} \quad (3.73)$$

$$\epsilon = 1 - V_s/V \quad (3.74)$$

In this model, when the bed porosity reaches a critical value, ϵ_{col} , a collapse will occur, causing the bed to shrink abruptly and the local (in this context, cell by cell) porosity to decrease. By assuming the local cell porosity after the collapse to return to its initial, randomly generated porosity, ϵ_0 , the collapse shrinkage, ΔV_{col} , can be described in terms of the total accumulated shrinkage:

$$\Delta V_{col} = (1 - \delta_{shr}) \Delta V_{shr,acc} \quad (3.75)$$

$$\epsilon = \epsilon_0 \quad (3.76)$$

Other parameters required are the length scale of (*i.e.* region affected by) the collapses, L_{col} , and the number of collapses which occur within a region during the combustion process, n_{col} , the latter being used to define the collapse porosity from the completion factor of the conversion process, X .

$$\varepsilon_{col} = \varepsilon \{when X = 1/n_{col}\} \quad (3.77)$$

$$X = 1 - M_s/M_{s,0} \quad (3.78)$$

Hermansson and Thunman [91] observed a single collapse to occur within a length scale ($n_{col} = 1$), typically when combustion approached completion. To replicate this behaviour, the collapse porosity, which is determined individually for each cell, is here set equal to the local porosity when conversion is 95% complete, *i.e.* $X = 0.95$. The length scale of the collapses must be at least one particle diameter. Particles may be larger than cells (see section 4.1); to allow for this possibility, the collapse criterion ($\varepsilon > \varepsilon_{col}$) must be evaluated across multiple neighbouring cells. The values for shrinkage factor, δ_{shr} , collapse length scale, L_{col} , and the number of collapses per length scale, n_{col} , are taken from the work of Hermansson and Thunman [91].

3.5.2 Node identification

The majority of nodes in a mesh are common to multiple cells, with corner nodes being the only exception. If a node were permitted to be moved by every cell in contact, duplicated displacements would occur. To prevent conflicts of this type, each cell is given control only of a single node; this node must be in the same relative position for each cell to ensure that the mesh deforms in unison. Assuming that the deformation of a cell can be described by only a single node introduces an inherent numerical error; however, this numerical error becomes very small as the number of cells is increased.

3.5.2.1 Shrinkage implementation in the 2D modelling case

In the 2D implementation of bed shrinkage, each cell controls its upper right node; effectively the node with the maximum x and y position within that cell, see *Figure*

3.7. Thus, the upper left node will be moved by the adjacent cell to the left, the bottom right node by the cell below, and the bottom left node by the cell below and to the left. The exception is at the left-most boundary of the domain, where both of the upper nodes must be moved, since there is no cell to the left.

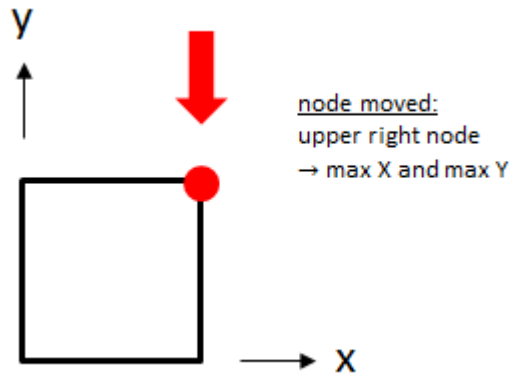


Figure 3.7 Node moved in 2D

To ensure that each cell moves the correct node every time, a node sorting algorithm is employed to identify the relative position of all nodes that define that particular cell. The algorithm first identifies the two x-most (right) nodes, and then determines which of these is the upper right node. All four nodes are identified in the same manner. The algorithm is computationally expensive, and it is therefore advantageous to run it only once. To facilitate this, the algorithm is run when the solution is initialised, and the relative position of each node is stored using node user-defined memory (NUDM); this is memory which is linked to each individual node. It is worth bearing in mind that a node is common to all surrounding cells, and will have a different position relative to each one (*Figure 3.8*). The global number that identifies each adjacent cell is stored in a particular NUDM location; the location is determined by the position of the node relative to that cell. An interior node in a 2D quadrilateral mesh is common to four surrounding cells, of which it may be the upper right, upper left, lower right, or lower left node relative to each cell. There are, therefore, four memory locations corresponding to the relative position of the node with respect to each cell, as shown in *Figure 3.8*.

In the deformation routine, which is called on a cell by cell basis, the relative position of each node in a particular cell can then be identified by searching for the global number of that cell in the NUDM of each of its nodes. When the cell number is found, the particular NUDM location in which it is found identifies the position of the node relative to that cell. For example, if the cell number matches the cell number stored in NUDM (1), then the node is the upper right node of that cell, if it matches the number in NUDM (2), then the node is the lower right node of that cell, and so on.

The NUDM method requires only four conditional checks to identify the position of each node, compared to up to fourteen needed for the initial sorting algorithm. Because the appropriate nodes must be identified before every cell/node manipulation, using the NUDM method during the simulation, instead of the complete sorting algorithm, significantly increases the efficiency of the deformation routine.

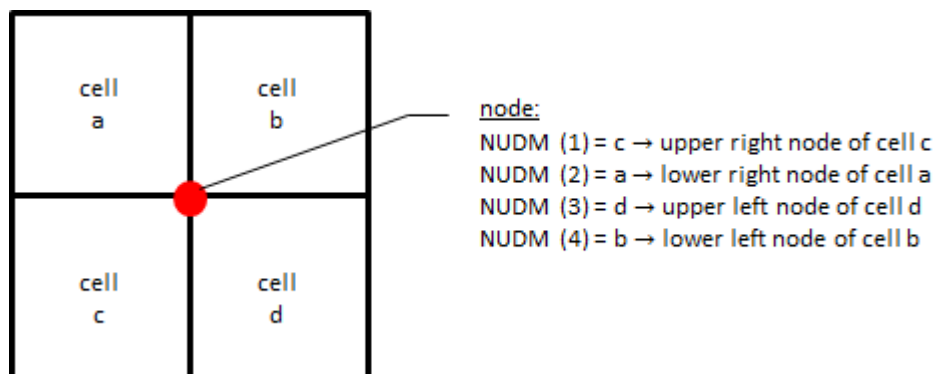


Figure 3.8 NUDM storage of node position relative to the surrounding cells

3.5.2.2 Shrinkage implementation in the 3D modelling case

In 3D, the front upper right node is moved; effectively the node with the maximum x , y , and z coordinates, *Figure 3.9*. Therefore, the front upper left node will be moved by the cell to the left, the back upper right node by the cell behind, the back upper left node by the cell behind and to the left, and the bottom nodes by the corresponding cells beneath. At the left (minimum- x) boundary, the front upper left

nodes must be moved, since there is no cell to the left. Similarly, at the back (minimum-z) boundary, the back upper right node must be moved since there is no cell behind. At the back left corner, all four of the upper nodes must be moved.

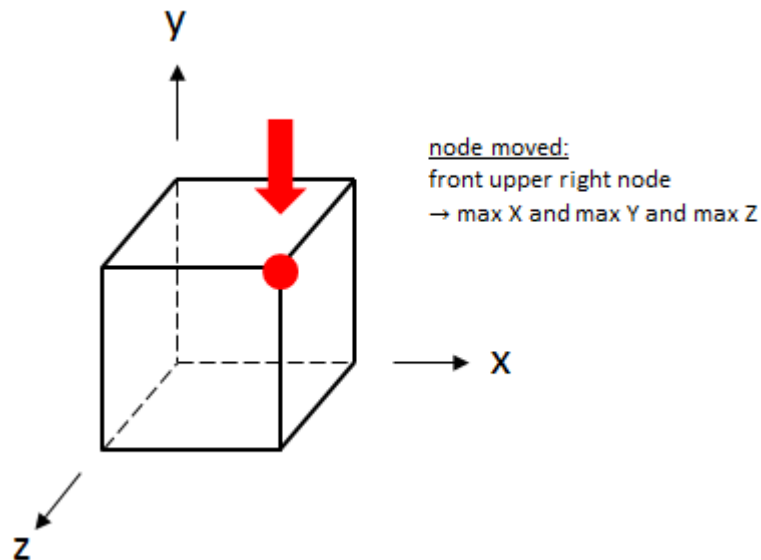


Figure 3.9 Node moved in 3D

The 3D node sorting algorithm works on the same basis as the 2D algorithm. It first identifies the four x-most (right) nodes, from these it then determines the two z-most (front) nodes, and finally, which is the upper front right node. All eight nodes are identified in this manner.

As in 2D, the relative position of each node is then stored in NUDM; now, however, eight memory locations are required, since an interior node will be common to eight cells in 3D, as opposed to four cells in 2D. The initial 3D node sorting algorithm is considerably more operations than the 2D algorithm, requiring up to fifty conditional checks to sort all the nodes in a cell. The NUDM method only requires eight conditional checks to identify the position of each node in 3D. The increase in efficiency gained by using the NUDM method during the calculation is, therefore, much more significant for 3D computations.

3.5.3 Implementation

The implementation of the deformation routine is the same for 2D and 3D, unless otherwise stated.

3.5.3.1 Collapse filter

As described in section 3.5.1, the length scale of a collapse may be larger than the length scale of a computational cell. In this case, the collapse must be evaluated and then implemented across a group of neighbouring cells, which collapse simultaneously. To this end, a filtering process is used. The deformation routine loops over every cell in the domain in turn, a secondary cell loop¹⁵ then determines any cells that lie within the collapse radius of the primary cell, *i.e.* it forms a discrete *collapse volume* consisting of multiple cells. If the majority of this collapse volume has a greater porosity than the collapse porosity, and the previous number of collapses does not exceed the experimentally derived number of collapses per length scale, n_{col} , then all of the cells within the collapse volume are marked for collapse. Furthermore, all cells lying directly beneath the cells within the collapse volume are also marked for collapse. This filtering process is expensive, and is therefore only implemented if at least one cell is ready for collapse.

3.5.3.2 Node manipulation

The deformation routine loops over every cell in the domain. If the cell has been marked for collapse, the total linear shrinkage is the sum of the continuous shrinkage, Eq. (3.73), and the accumulated collapse shrinkage, Eq. (3.75). Otherwise, the total linear shrinkage is determined by the continuous shrinkage only. Each cell then identifies the node, or nodes¹⁶, which it controls by means of the NUDM method described in Section 3.5.2. Once identified, the appropriate node(s) is

¹⁵ A secondary cell loop is a loop that is called within a primary cell loop.

¹⁶ Recall that cells at the left (x-min) boundary or, in 3D, back (z-min) boundary control more than one node.

moved in the gravitational or negative y-direction by the calculated total linear shrinkage. At this point, the local porosity is updated according to Eq. (3.74).

The “sliding” effect is implemented by performing a secondary cell loop, which identifies any cell lying directly above the primary cell. Each secondary cell then identifies the node it controls, and moves it by the total linear shrinkage of the primary cell, thus “sliding” downwards while retaining its height.

The implementation of the shrinkage model in the deformation routine is outlined as a flow diagram in *Figure 3.10*.

3.6 Solution Procedure

The solution process follows the cascading scale approach proposed by Hermansson and Thunman [91], where variables are updated on three different time scales: a *fluid-flow scale*, a *particle scale*, and a *multi-particle scale*. The gas flow has the shortest time and smallest length scales, and is influenced by the physical presence and conversion processes of the solid phase.

The time scales associated with changes to the particle phase are much longer than those of the gas phase. We therefore assume, for computational efficiency in particular, that the particle phase and gas phase are effectively decoupled while the governing equations are solved iteratively. The local porosity, solid phase properties, and particle size, are then updated using the converged solution of the governing equations before the next timestep begins, an approach also taken in [91, 165].

The largest length and time scale deals with global movement of the fuel bed. This is movement that might take longer than a single timestep to come about; it is realised by checking for the collapse criteria at the end of every timestep, and then implementing the global movement model if required.

Throughout this work, the multi-particle scale refers only to fuel bed collapses, which occur as a result of local increases in porosity that accrue over multiple timesteps. However, it could also be used with the “walking column” approach, to describe the progression of fuel along the grate.

The interaction of conservation equations, source terms, and the overall solution procedure is shown in *Figure 3.11*, illustrating the cascading scale approach. The SIMPLE algorithm is used to solve the conservation equations, with under-relaxation factors of 0.7 for momentum, 0.8 for all species, and 0.9 for the energy equations [88]. The absolute criteria for convergence are set to 10^{-6} for the energy equations, Eq. (3.4) and Eq. (3.5), and 10^{-3} for all other conservation equations in *Table 3.1*.

3.7 Summary

A complete, transient, fixed-bed combustion model has been described. The submodels necessary to describe the chemical and physical phenomena that occur in a burning bed of solid fuel, and the implementation of these submodels into a commercial CFD package, Fluent, has been explained. The mesh deformation routine required to represent bed shrinkage has been explicated for a 2D or 3D numerical model.

It is worth noting that the fixed-bed combustion model is computationally expensive. The mesh deformation routine is particularly demanding, and increases run times by approximately 15 – 20% in a 2D run; in the 3D case, this can be expected to be an even greater overhead. A 2D simulation can be carried out in a serial run on a standalone workstation in a reasonable amount of time, *i.e.* hours to days depending on the run time and the size of the domain. On such a computer, the run times for 3D simulations, however, are prohibitive. Ideally, 3D cases should be run in parallel on high performance computers or clusters. This requires parallelisation of the model, which is outlined in detail in Appendix A.

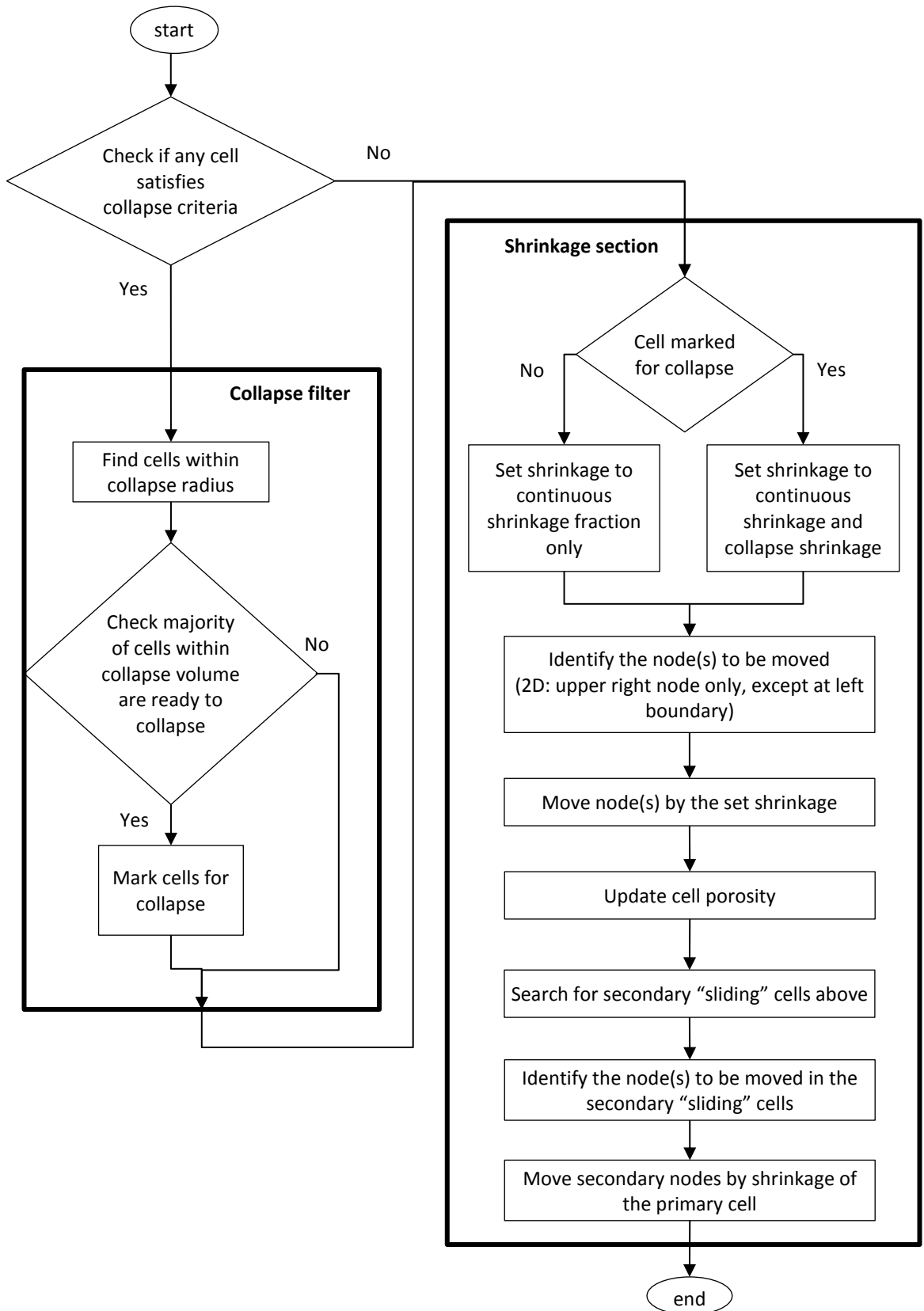


Figure 3.10 Implementation of deformation routine

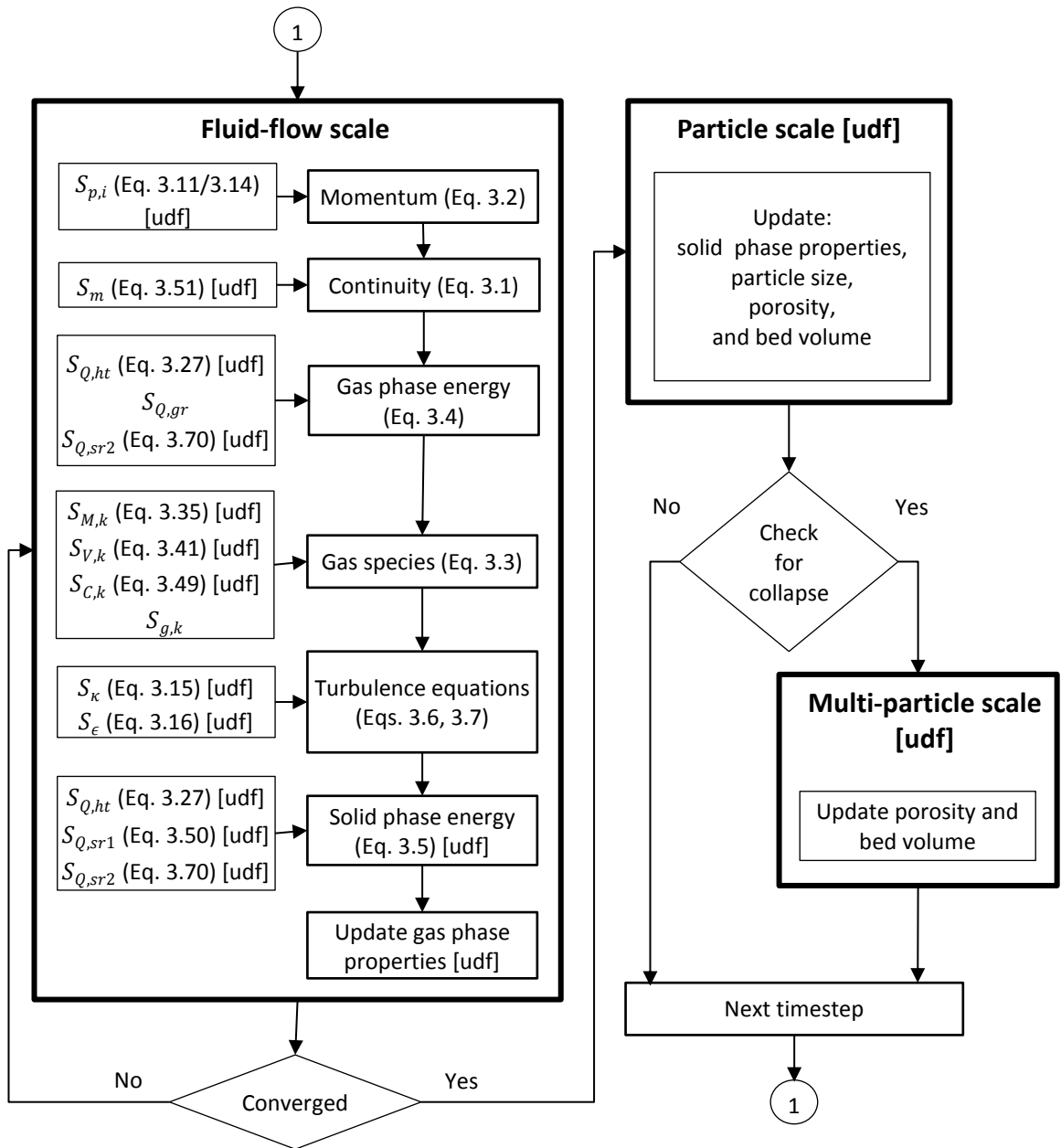


Figure 3.11 Equation interaction and solution procedure

4. VALIDATION

Detailed measurements within a biomass fuel bed are very desirable for the purpose of validating modelling methods, but, as noted earlier (in section 1.6), are difficult to obtain. From the very limited range of combustion data published, we have selected the ignition rate (the speed at which the ignition front progresses in counter-current combustion) and the concentration of selected species through the fuel bed as the key measures of overall model performance. To allow comparison with the one-dimensional, time-dependent data available, the 2D model was initialised with uniform conditions across the fuel bed, and thus behaved as a one-dimensional model. Predictions along a vertical traverse through the bed could then be compared with the experimental results.

4.1 Mesh Resolution

Several meshes of varying initial resolution were tested to ensure that results were independent of the mesh spacing. The cell sizes investigated were 10×10 , 5×5 , 2.5×2.5 , 2×2 , 1.667×1.667 , and 1.25×1.25 , all given in mm. Each mesh was tested using the complete bed model with uniform initial conditions across the bed. Predicted values of pertinent variables were then extracted along a vertical traverse through the bed, and plotted for comparison with each other; these included: cell porosity, O_2 mole fraction, CO mole fraction, CO_2 mole fraction, gas phase temperature, solid phase temperature, gas speed, and particle diameter.

Plots of the CO_2 mole fraction (*i.e.* % of total gas volume) and the gas phase temperature are shown, respectively, in *Figure 4.1* and *Figure 4.2*. Plots of both variables are comparable for all the meshes investigated, although they became almost indistinguishable, *i.e.* mesh independent, once the grid size is reduced to 2.5 mm or less. The same trend is apparent for all variables compared, with additional plots shown in Appendix B. We elected to use a slightly narrower grid than necessary to be conservative; therefore, the initial grid size is set as 2 mm.

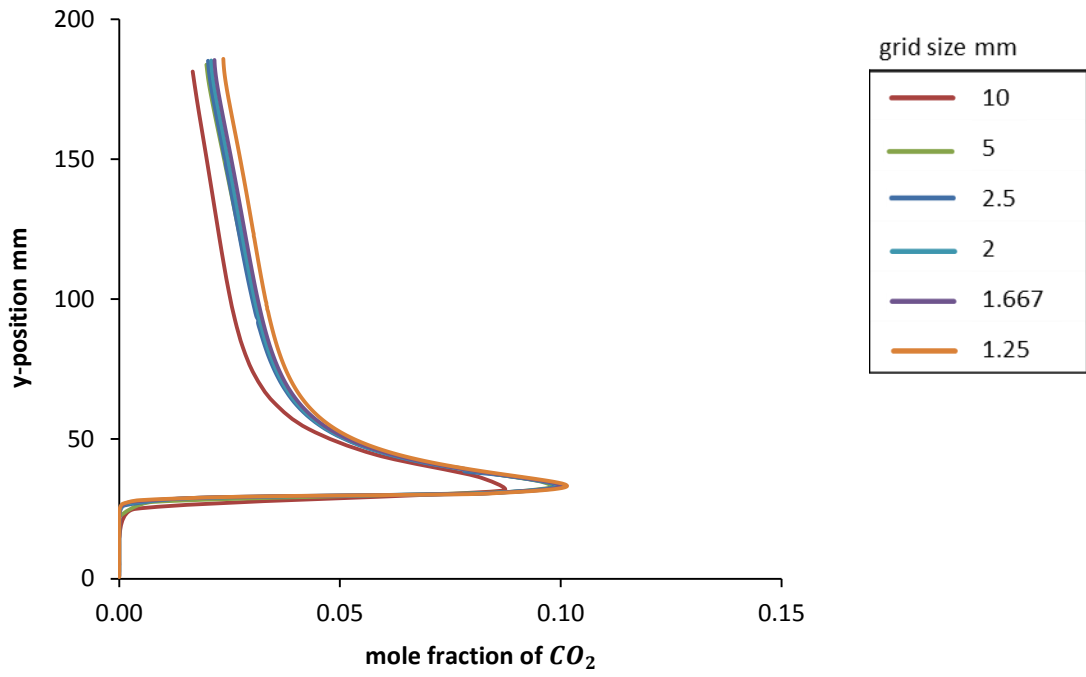


Figure 4.1 Comparing mole fraction of CO_2 for different grid sizes

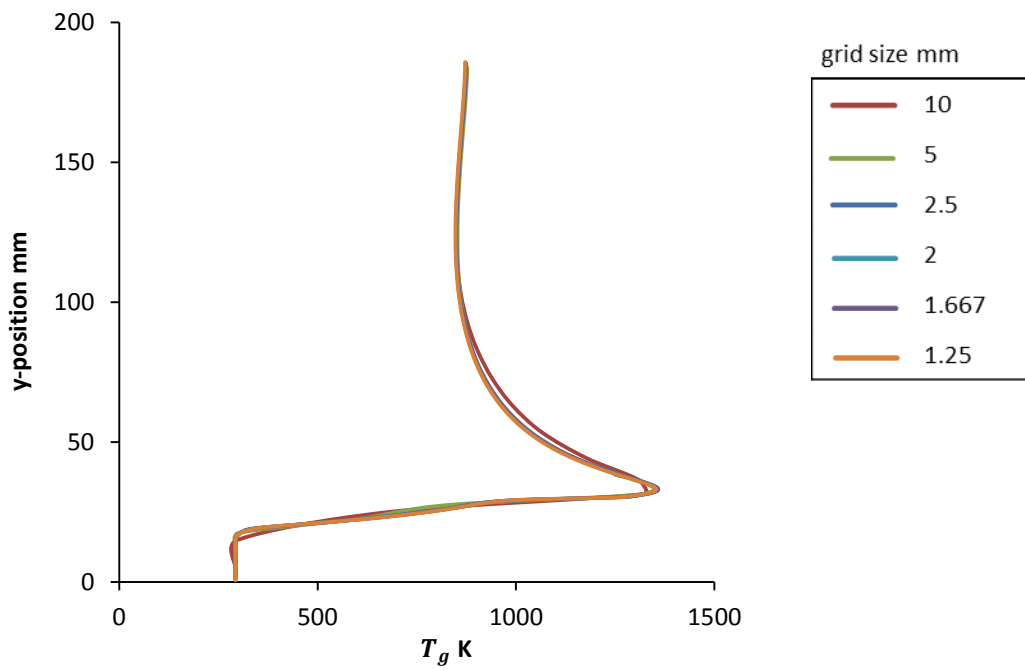


Figure 4.2 Comparing gas phase temperature for different grid sizes

4.2 Ignition Rates

The predicted ignition rates were compared with the measurements of Porteiro *et al.* [177] by igniting the top of the fuel bed and tracking the speed of the reaction front as it progressed downwards towards the grate. The front velocity was calculated by dividing the vertical distance between two points by the difference in time taken for each point to reach a predefined ignition temperature, taken as 973 K. The ignition rate is obtained by multiplying the velocity by the bulk density of the solid phase, given by:

$$\dot{m}_{ign} = \frac{z_2 - z_1}{\Delta t} \rho_{s,0}(1 - \bar{\varepsilon}_0) \quad (4.1)$$

Results from measurements and model predictions for several inlet air flow rates are shown in *Figure 4.3*. The ignition rate was initially unsteady while combustion was being established. This transient, start-up behaviour typically lasted less than 100 s, after which the ignition rate reached a steady-state. Combustion was simulated for 900 s, allowing the bed to reach a sufficiently advanced state. The predicted ignition rates were then averaged over the duration of the simulation, excluding the transient start-up period. It is worth noting that the total simulated time had no effect on the predicted ignition rates, since the ignition rate advanced at a steady speed after the start-up stage.

4.2.1 Model calibration

In order to obtain a close match between measured and predicted ignition rates, a significant amount of model calibration was necessary. The first step involved identifying a number of parameters that influenced the ignition rate, including the solid phase thermal conductivity, the pyrolysis model and the corresponding reaction constants, the blowing factor, the particle-particle radiation model, and the model for the effective thermal diffusivity of the solid phase. Various relevant models/values for each of the parameters listed above were taken from the literature and varied, in turn, to ascertain their effect on the predicted ignition rate.

Owing to the complexity of the overall model, the exact effect of different combinations of these parameters proved difficult to infer in advance. As a result, different arrangements were compared on a trial and error basis until the combination which provided the best match between measurements and predictions was determined. The culmination of the model calibration process is presented in section 4.2.2.

4.2.2 Final results

Predicted ignition rates closely match the data in the sub-stoichiometric zone. For low air flow rates predictions slightly exceed measurements; nonetheless, the peak ignition rate is closely captured, as is the subsequent fall off in the ignition rate due to convective cooling. In line with the observations of Porteiro *et al.* [177, 178], the model also predicts a decreasing reaction zone thickness as the air flow rate increases. Deviations between measurements and predictions occur at higher fluxes where the model prematurely predicts extinction. In practice, any combustible gases leaving the bed will be completely burned in the freeboard. Some of the heat produced will be radiated back to the bed helping to sustain combustion, but will only penetrate a finite depth below the surface [120]. This is expected to have an increased effect at higher air flow rates due to the narrowing reaction zone, which brings the ignition front closer to the surface of the bed. Since the freeboard region and the associated radiation effects are excluded in the present simulations, this is the most likely cause of the differences in predicted and measured ignition rates at the higher fluxes. Collazo *et al.* [34] also validated their model using the same data. Both models achieve similar agreement between predictions and measurements in the sub-stoichiometric region. Their model, which included the freeboard, performed better in the fuel lean regime; however, it also prematurely predicted extinction. Recalling that the goal of the present study is to investigate channelling in modern industrial grate furnaces, where combustion in the fuel bed typically takes place under sub-stoichiometric conditions, and ignition occurs from just above the grate, the model performance is acceptable.

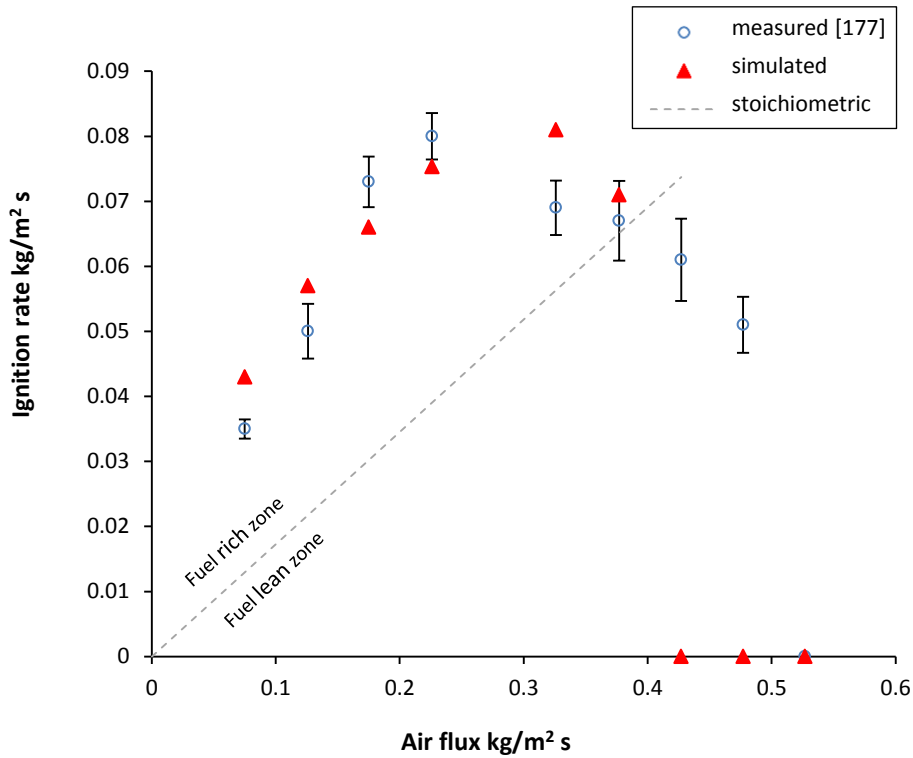


Figure 4.3 Steady-state ignition rate for different air flow rates after 900 s

4.3 Species Profiles

Girgis and Hallett [130], as already mentioned, measured species concentrations throughout the depth of a burning bed of woodchips. The experiment was carried out in a pot furnace where the bed height and porosity were maintained by periodically packing additional fuel; as a result, the species profiles effectively reach a steady-state. For comparison, in our computational model the fuel size and composition and all boundary conditions were set to match the experiment. All other model parameters were identical to those used to predict the ignition rates in section 4.2.2; although the fuel bed was ignited just above the grate. Since our model applies to a transient, shrinking bed, species profiles gradually change as combustion proceeds. Species profiles were therefore taken when the char reactions had extended to approximately 100 mm above the grate, since this matched experimental observations; this occurred approximately 1200 s after ignition. The

predicted species profiles through the bed were then compared with the measurements, illustrated in *Figure 4.4*.

The predicted mass fractions of CO , tar (C_6H_8O), and CH_4 at the top of the bed (*i.e.* $y = 200$ mm) all match the sparse data well. Discrepancies between the measured and the predicted CO and CO_2 profiles are due predominantly to the CO_2 gasification reaction, but may also be accounted for by differences in the rates of pyrolysis, and in the ratios of species produced during pyrolysis. Since char particles are typically quite porous, the gasification reactions are likely to extend to the particle interior, and an intrinsic reaction rate might be more suitable than the simpler global reaction rate employed here. Girgis and Hallett [130] also compared predictions from their model with the same measurements. An excellent match was achieved; however, it is worth noting that the pyrolysis reaction, gasification reactions, and the ratio of pyrolysis products were tuned to improve agreement. A similar approach could be taken here; however, this would affect the ignition rates. Moreover, although the mismatch in CO and CO_2 owing to the exothermic gasification and pyrolysis reactions will have a small effect on the bed temperature, it is not expected to significantly influence the channelling behaviour across cases. Published models are typically validated by means of either ignition rates or species profiles. Here, the overall model performance was compared with both measures, and a satisfactory agreement was achieved.

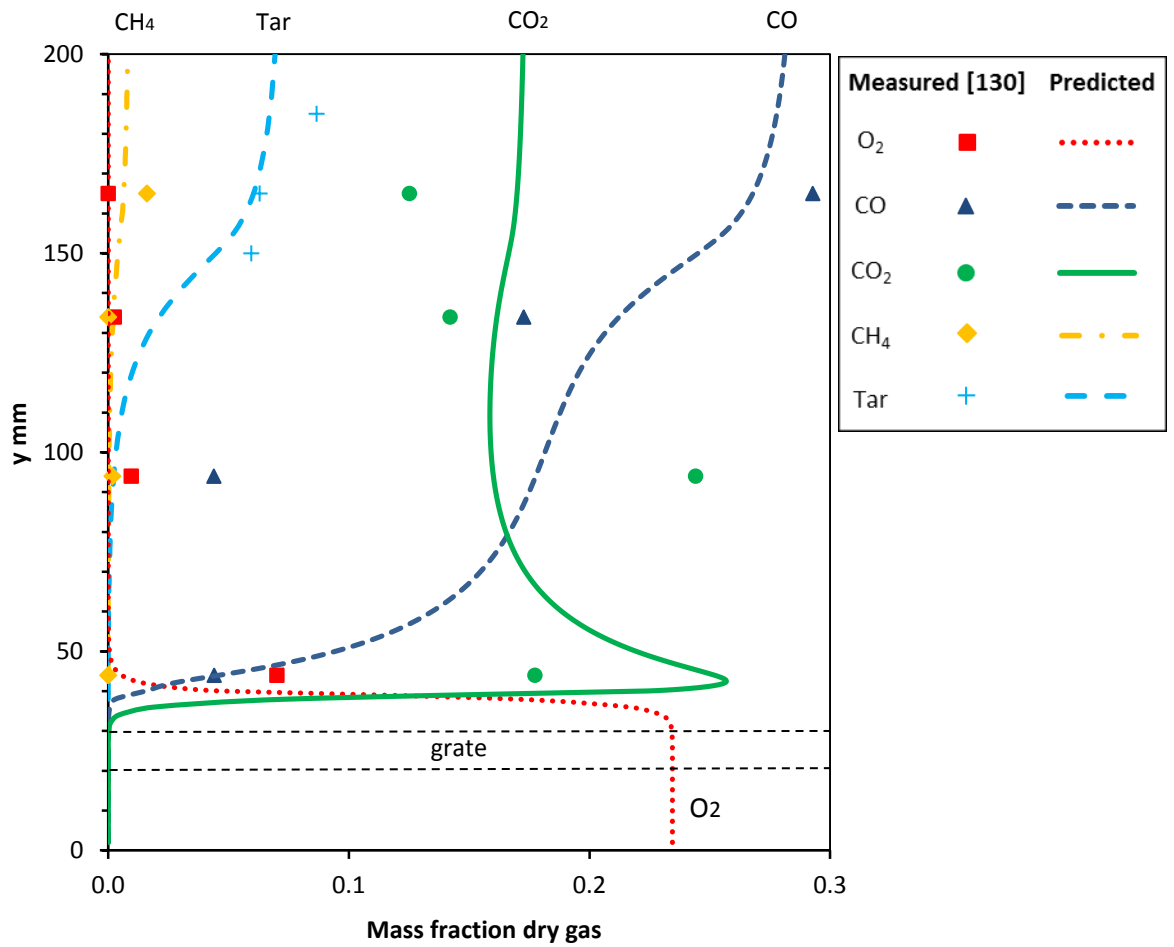


Figure 4.4 Comparison of measured and predicted species profiles through the bed at $t = 1200$ s

4.4 Summary and Discussion

To ensure mesh independence, the fixed-bed combustion model developed in Chapter 3 was tested for six meshes of increasingly fine resolution. Results exhibited mesh independence when the initial grid size was 2.5 mm or less. To ensure sufficient resolution, a more conservative initial grid size of 2 mm was selected for all simulations to follow.

The model was then validated using measurements for ignition rates at different inlet air fluxes, and also by means of measured species profiles through a biomass fuel bed. The predicted ignition rates compared well with the measurements of

Porteiro *et al.* [177], and with the predictions of Collazo *et al.* [34]. The predicted profiles for CO and CO_2 deviated from the measurements and predictions of Girgis and Hallett [130]; however, the composition of the gas leaving the bed, the trends within the bed, and all other species profiles were comparable. Furthermore, published models are typically validated using either ignition rates or species profiles. Our overall model performance was compared with both measures, without employing case-specific tuning of pyrolysis and gasification reaction sub-models or of parameters such as ratios of pyrolysis species, and an acceptable agreement was achieved.

5. 2D INVESTIGATION OF CHANNELLING IN FIXED-BED COMBUSTION

5.1 Objective and Overview

The objective of this section is to perform a systematic analysis of the parameters influencing channelling in fixed-bed biomass combustion. To investigate factors affecting channelling, a 2D numerical analysis is performed on a section of a randomly packed fuel bed in a biomass furnace, see *Figure 2.4*. The spatial variation in porosity caused by the random packing of fuel particles is described in section 5.2, and the parameters investigated are covered in section section 5.3. The results are presented in section 5.4 and discussed in section 5.5.

Highlighted in *Figure 2.4* is the simulated section of the fuel bed, which is treated as a packed bed that is moving along with the grate. The slope of the grate and disturbances due to grate motion, such as particle mixing, are ignored. The computational domain is divided into three zones: a packed fuel bed, a grate, and an air plenum or windbox, as shown in *Figure 5.1*. The zones are linked by means of standard fluid-fluid interfaces between the fuel bed and the grate, and the windbox and the grate. Because the focus here is on the evolution of the fuel bed, the combustion of product gases in the freeboard above the fuel bed is not modelled, but can be readily incorporated if required, given the computational resources. The grate is modelled as an isotropic, perfectly-porous medium. All zones are discretised using uniform 2×2 mm quadrilateral cells (see section 4.1).

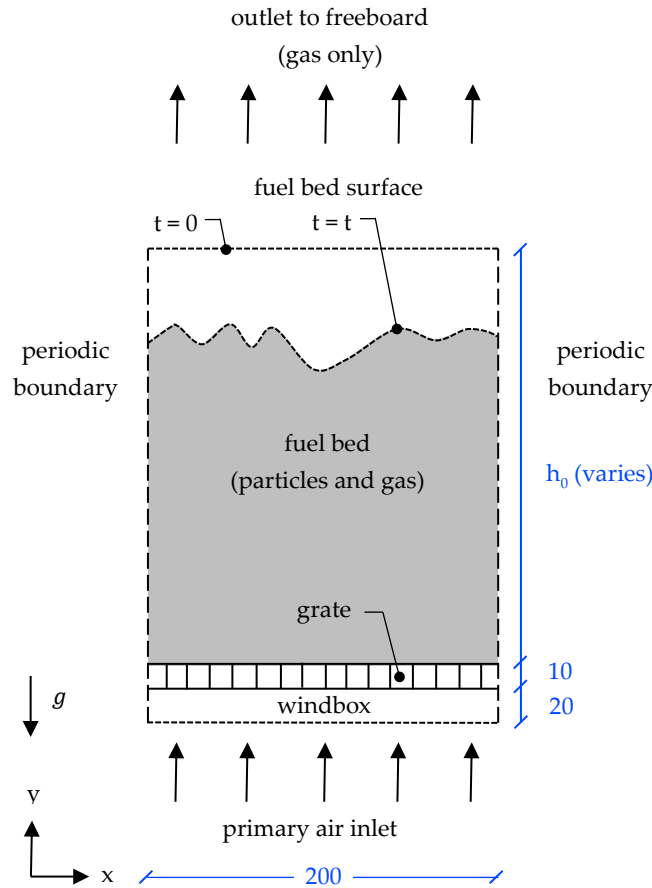


Figure 5.1 Simulated domain showing shape of fuel bed surface after time t (dimensions in mm)

5.2 Initial Bed Porosity

A packed bed is essentially a pile of solid particles, of various shapes and different sizes, supported on a grate and bounded by the furnace walls. These particles lie in contact with surrounding particles, with voids forming between them. If this bed of particles is superimposed by a computational mesh, or grid, each cell within that grid may be entirely occupied by either the gas phase or the solid phase, or partially occupied by both. The volume fraction of a cell occupied by the gas phase is described by the bed porosity or void fraction. In a typical, randomly packed fuel bed, this void fraction will vary spatially. While Yang *et al.* [28] developed a model to describe this variation for a bed of multi-sized spherical particles, measurements

with irregularly shaped particles [182] show that the spatial distribution of the porosity may be represented by a normal distribution:

$$E(\varepsilon) = \frac{1}{(2\pi\sigma_\varepsilon)^{1/2}} \exp^{-(\varepsilon-\bar{\varepsilon})^2/2\sigma_\varepsilon} \quad (5.1)$$

where E denotes the expected local porosity in this case. This enables us to define a randomly packed fuel bed, and to vary its mean porosity, $\bar{\varepsilon}$, and standard deviation from the mean, σ_ε . The spatial variation of porosity is implemented numerically using the Polar Method [183] to generate a random porosity for each individual cell in accordance with Eq. (5.1). In reality, the local (*i.e.* cell) porosity can vary between 0 and 1 (*i.e.* entirely solid or entirely gas); however, a lower limit of 0.1 is enforced here for numerical stability.

Hermansson and Thunman [91] approximated σ_ε as 0.1 to reproduce the measurements of Montillet and Le Coq [182]; this value is also used in this work.

Figure 5.2 (a) shows the initial spatial distribution of porosity in a randomly packed fuel bed, as described by Eq. (5.1), where $\bar{\varepsilon} = 0.42$ and $\sigma_\varepsilon = 0.1$. Also shown is the depth-averaged variation of porosity across the fuel bed.

As already noted, our focus is on factors that influence channelling; to this end, a single, relatively porous passage is induced in the centre of the fixed-bed by adjusting the randomly generated cell porosity (*Figure 5.2* (a)) by means of a position-dependent function. To provide a smooth transition to the high porosity passage, this function is based on the shape of a standard normal distribution bell curve, also derived from Eq. (5.1), and shown in *Figure 5.3* (a) with $\bar{\varepsilon} = 0$ and $\sigma_\varepsilon = 1$. However, the parameters for Eq. (5.1) are adjusted to produce a shape function, which spans 50 mm, in the centre of the domain ($\bar{x} = 100$ mm), as shown in *Figure 5.3* (b). In line with previous studies [91, 165], the average porosity in the relatively porous passage is desired to be approximately 30% higher than the mean porosity of the fuel bed. Since the maximum value of the shape function is 0.4 (when $x = \bar{x}$),

the existing, randomly generated porosity is therefore modified for every cell throughout the entire domain as follows:

$$\varepsilon = \varepsilon(1 + (3/4)\zeta) \quad (5.2)$$

where ζ is the value of the shape function shown in *Figure 5.3* (b), determined by means of the x position of the relevant cell.. The resulting initial distribution is shown in *Figure 5.2* (b).

5.3 Parameters Investigated

The key factors in channelling appear to be the grate resistance, and, to a lesser extent, the bed height [28, 91]. The numerical work of Hermansson and Thunman [91] with a burning bed of randomly packed char, indicated that channelling can be reduced by increasing the grate resistance, and thus pressure drop induced across the grate.

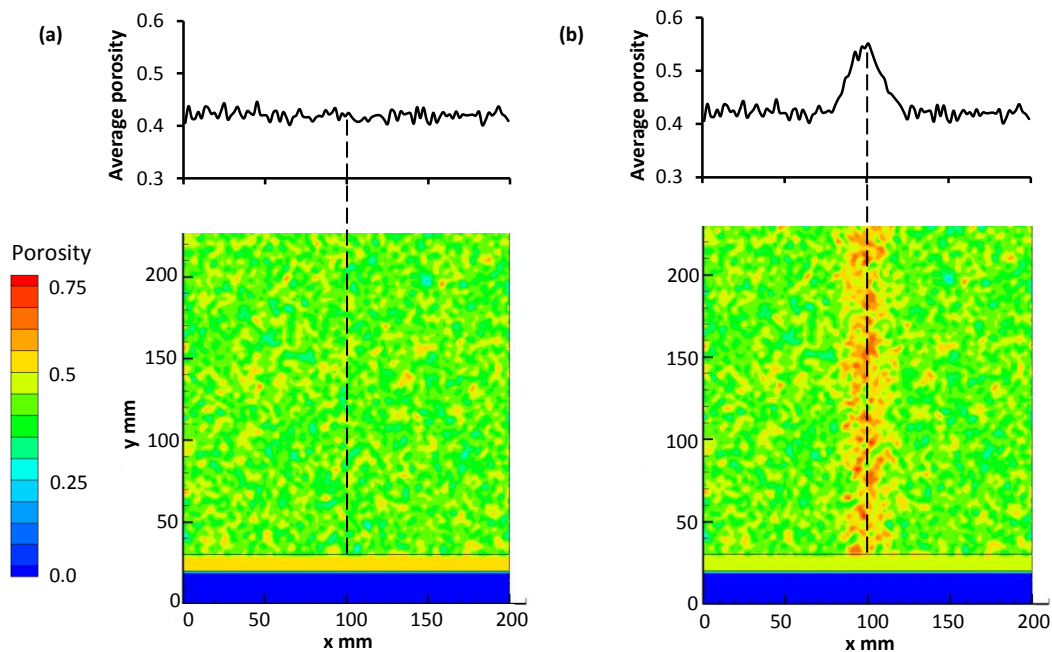


Figure 5.2 Fuel bed porosity – initial distribution and corresponding variations of average over vertical traverses: (a) randomly packed bed; (b) randomly packed fuel bed with relatively high porosity passage

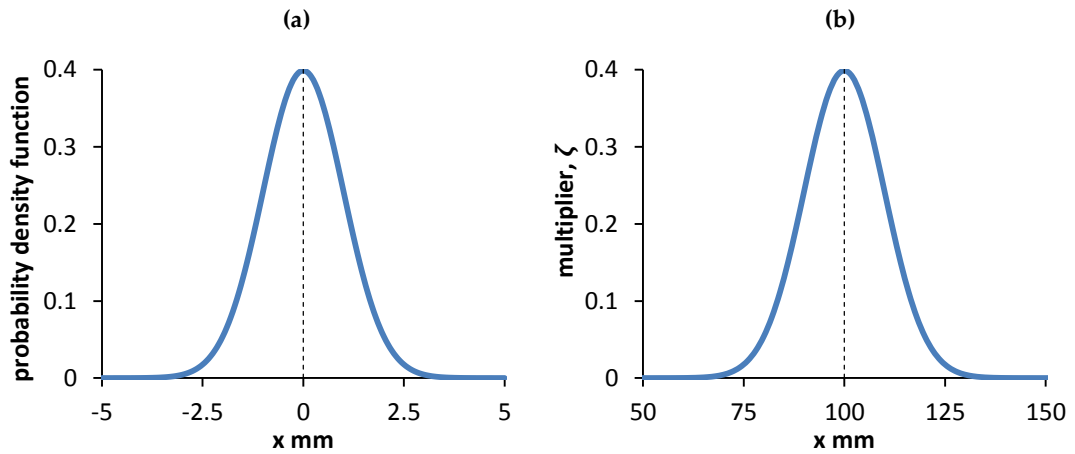


Figure 5.3 Position-dependent shape function: (a) initial shape; (b) multiplier used to modify the existing random porosity and create a relatively porous passage

Yang *et al.* [28] drew a similar conclusion for the uneven distribution of air through a bed of randomly-packed spheres, but remarked how the effect waned for deeper fuel beds, becoming inconsequential for a bed height above 200 mm. Here, therefore, three different grate resistances will each be tested for three different initial bed heights. Based on the predictions of Yang *et al.* [28], the initial bed heights will be taken as 100, 200, and 300 mm. This corresponds to a cold-flow pressure drop of 30, 60, and 90 Pa (respectively, 10, 20, and 30 Pa along the centreline of the relatively porous passage), through the fuel bed. The grate is represented as a uniformly porous medium. The resistance to flow through the grate is determined by means of the grate friction coefficient, β_{gt} , in Eq. (3.14), which is calculated based on cold-flow pressure drops of 1, 10, and 100 Pa, through the grate.

In addition to the grate's shape (which determines its resistance to flow), the effects that operational parameters have on channelling are also of interest. The parameters selected for investigation here are: the initial moisture content of the fuel, $X_{m,0}$, and the level of flue gas recirculation (FGR), which is widely employed to reduce NO_x emissions. FGR involves recycling a portion of the flue gas (up to 60% [184]) by mixing it with the air supply. In this case the flue gas is mixed with the

primary air supply below the grate, comprising up to 30% of the total gas mixture. The composition and temperature of the flue gas is taken as 3% O_2 , 13% CO_2 , and 25% H_2O , by mass, at 423 K [143].

All cases considered are outlined in *Table 5.1*.

Table 5.1 Parameter combinations investigated for channelling

Case	$\beta_{gt} (\times 10^4)$	FGR (%)	$X_{m,0}$ (% w. b.)	$h_{bed,0}$ (mm)
1 a/b/c	1/10/100	0	0	100
2 a/b/c	1/10/100	0	0	200
3 a/b/c	1/10/100	0	0	300
4 a/b/c	100	15/30/45	0	200
5 a/b/c	100	0	15/30/45	200

The initial conditions, boundary conditions, and material specifications, unless shown in , are the same for all cases, as described in *Table 5.2*.

Table 5.2 Initial conditions, boundary conditions, and material specifications

Fuel bed	<i>Formula</i> (d.b.a.f.)	$C_1H_{1.48}O_{0.71}$	[177]	
	Moisture (% <i>w.b.</i>)	6.2	[177]	
	Volatiles (% <i>w.b.</i>)	68.9	[177]	
	Char (% <i>w.b.</i>)	24.2	[177]	
	Ash (% <i>w.b.</i>)	0.7	[177]	
	LHV (MJ/kg dry fuel)	16.3	[177]	
	$\rho_{s,0}$ (kg/m^3)	1180	[177]	
	Mean porosity, $\bar{\varepsilon}_0$ (-)	0.42	[177]	
	$d_{p,0}$ (mm)	3.8	[177]	
	Sphericity, Ψ (-)	0.87	[177]	
	λ_M ($W/m \cdot K$)	0.58	[153]	
	λ_W ($W/m \cdot K$)	0.35	[185]	
	λ_C ($W/m \cdot K$)	0.1	[153]	
	$c_{p,M}$ ($J/kg \cdot K$)	4180	[153]	
	$c_{p,W}$ ($J/kg \cdot K$)	$1500 + T_s$	[11]	
	$c_{p,C}$ ($J/kg \cdot K$)	2110	[186]	
	$c_{p,A}$ ($J/kg \cdot K$)	$754 - 0.586(T_s - 273)$	[186]	
	ω_C, ω_{grate} (-)	0.85	[153]	
	ρ_{th} (kg/m^3)	1500	[11]	
	Porous passage	$\bar{\varepsilon}_{centreline}$ (-)	$1.3 \bar{\varepsilon}_0$	
Width (mm)		50		
Grate	Depth, h_{grate} (mm)	10		
	ρ_{grate} (kg/m^3)	7300		
	λ_{grate} ($W/m \cdot K$)	30		
	$c_{p,grate}$ ($J/kg \cdot K$)	500		
	ε_{grate} (-)	0.5		
Boundary conditions	Inlet mass flux	$0.15 (kg/m^2 \cdot s)$		
	Inlet temperature	293 (K)		
	Inlet gas composition	21% vol O_2		
		1% vol H_2O		
		10% turbulent intensity		
	Outlet pressure	atmospheric pressure		
	Backflow conditions	normal to boundary face values set to adjacent boundary cell		
Ignition	1000 K to bottom 1 cm			

5.4 Results

All cases were run successfully for a minimum simulated time of 600 s using a timestep of 1 s. The largest cases took 30 – 36 CPU hours to run on an Intel Q6600 with 4 GB RAM. The predicted results for variations of grate resistance, bed height, FGR, and initial moisture content are presented in *Figure 5.4 - Figure 5.15*.

To quantify the effect of channelling, the standard deviation of the gas speed across the outlet (the top surface of the bed, the shape of which is evolving with time), is calculated at each timestep:

$$\sigma_{u,t} = \left(\sum_{i=1}^N (u_g - \overline{u_g})^2 / (N - 1) \right)^{1/2} \quad (5.3)$$

where N is the total number of cells across the top surface of the bed, u_g is the gas speed of a cell, and $\overline{u_g}$ is the average speed over the top surface. The standard deviation, $\sigma_{u,t}$, is then further time-averaged over the entire prediction period as follows:

$$\widetilde{\sigma}_u = \frac{1}{\Delta t} \sum_{t=t_0}^{t_0+\Delta t} \sigma_{u,t} \quad (5.4)$$

The time-averaged deviations are then normalised with respect to a datum case:

$$\widehat{\sigma}_u = (\widetilde{\sigma}_u - \widetilde{\sigma}_{u,dat}) / \widetilde{\sigma}_{u,dat} \quad (5.5)$$

A positive value of $\widehat{\sigma}_u$ indicates that the exit flow is less uniformly distributed than in the datum case. The datum case does not contain the high porosity passage (see *Figure 5.2 (a)*) and has a grate friction coefficient of 10^6 , but is otherwise identical to the cases investigated.

5.4.1 Grate resistance

The effects of increasing grate resistance are shown in *Figure 5.4* for the shallow (100 mm) bed. For the lowest grate resistance (*Figure 5.4 (a)*), virtually all of the fuel in the passage has been consumed, leaving a valley that extends through the entire depth of the bed. Once this happens, the overall conversion rate, and thus

temperature and velocity, will begin to decline. This occurs because the gas takes the low resistance path (*i.e.* flows through the opening), where the fuel has already been consumed. Increasing the grate resistance (*Figure 5.4* (b) and (c)) reduces the rate of formation of the valley and the peak temperature in the bed; this is a result of the air being less unevenly distributed, which reduces the conversion rate in the relatively porous passage.

The influences of grate resistance for a 200 mm bed are shown in *Figure 5.5*. As with the shallower bed, increasing the grate resistance has a beneficial effect, reducing both the rate of formation of the valley and the peak temperature in the bed. The differences between the three cases are comparatively smaller than for the 100 mm bed, showing that the effect of grate resistance is reduced for deeper beds. A similar trend follows for the 300 mm fuel bed, *Figure 5.6*. The valley size is reduced as the grate resistance increases; however, the differences are less evident than for the shallower beds. Furthermore, a clear trend in the peak temperatures is no longer discernible, implying similar combustion conditions across cases (a), (b), and (c).

velocity m/s

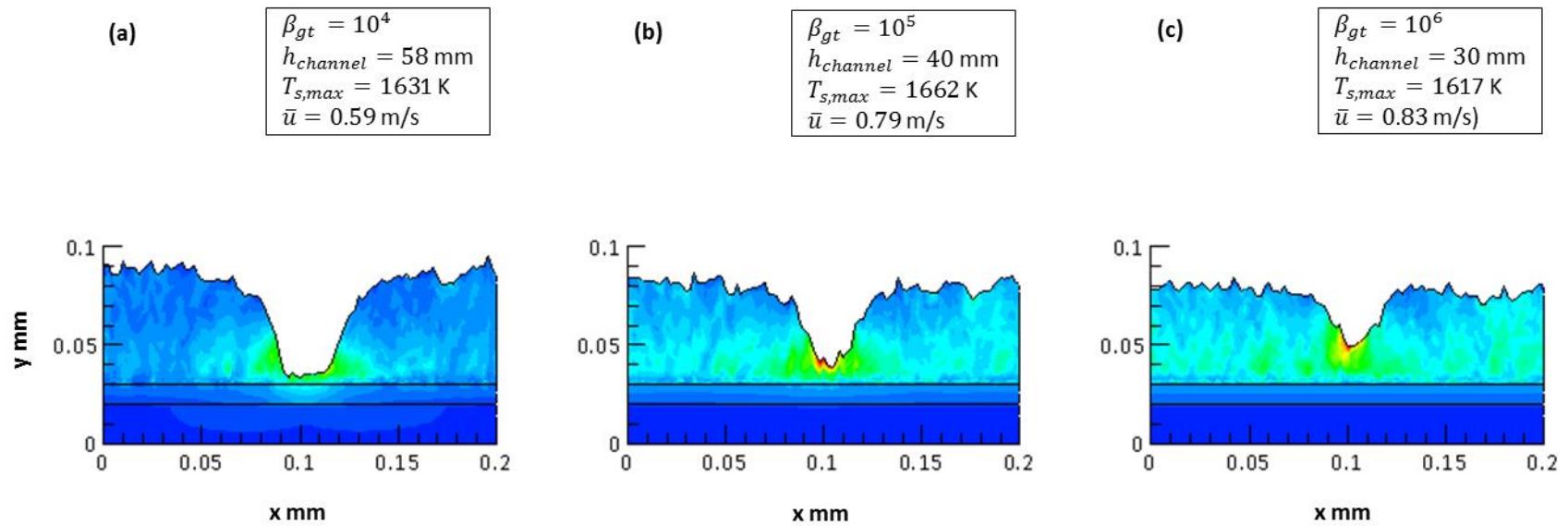
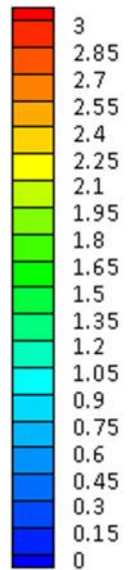


Figure 5.4 Effects of grate resistance on distribution of flow speed: $t = 600$ s, $h_0 = 100$ mm. $h_{channel}$ is the depth of the valley formed, taken as the distance between the lowest point of the depression formed and the average height of the surface of the bed, excluding the depressed region.

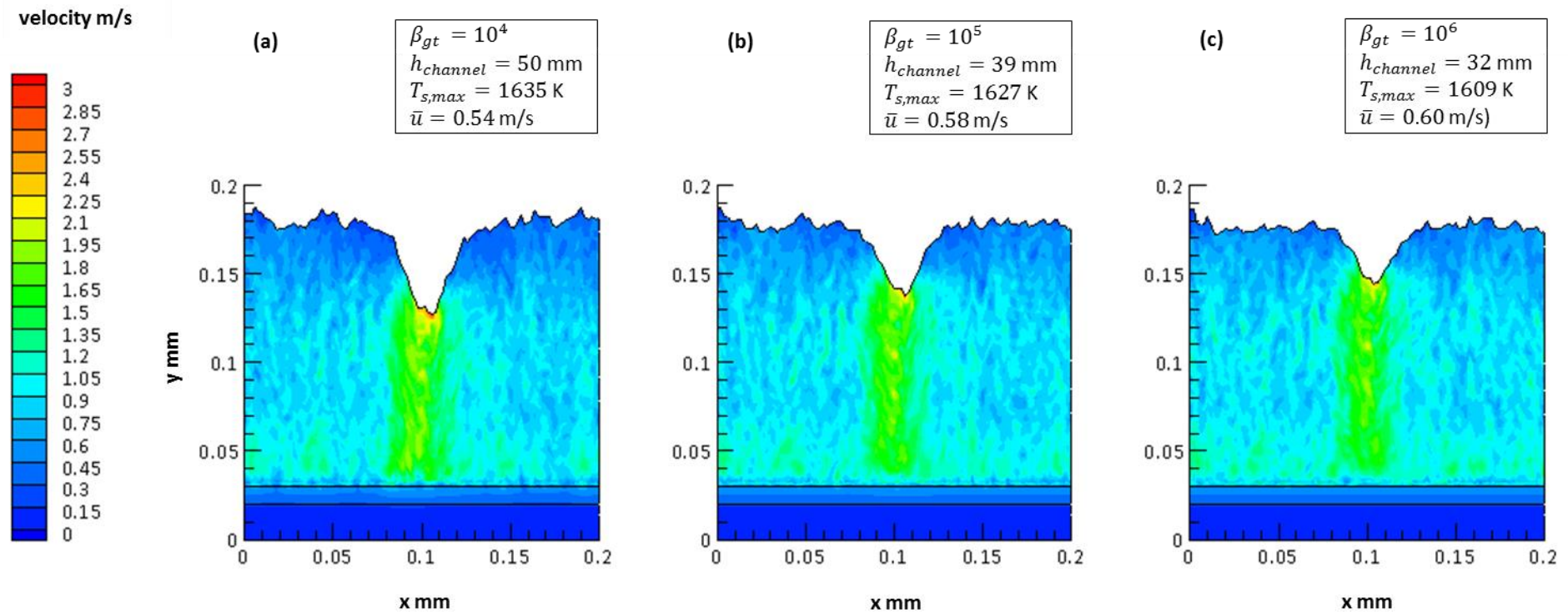


Figure 5.5 Effects of grate resistance on distribution of flow speed: $t = 600$ s, $h_0 = 200$ mm

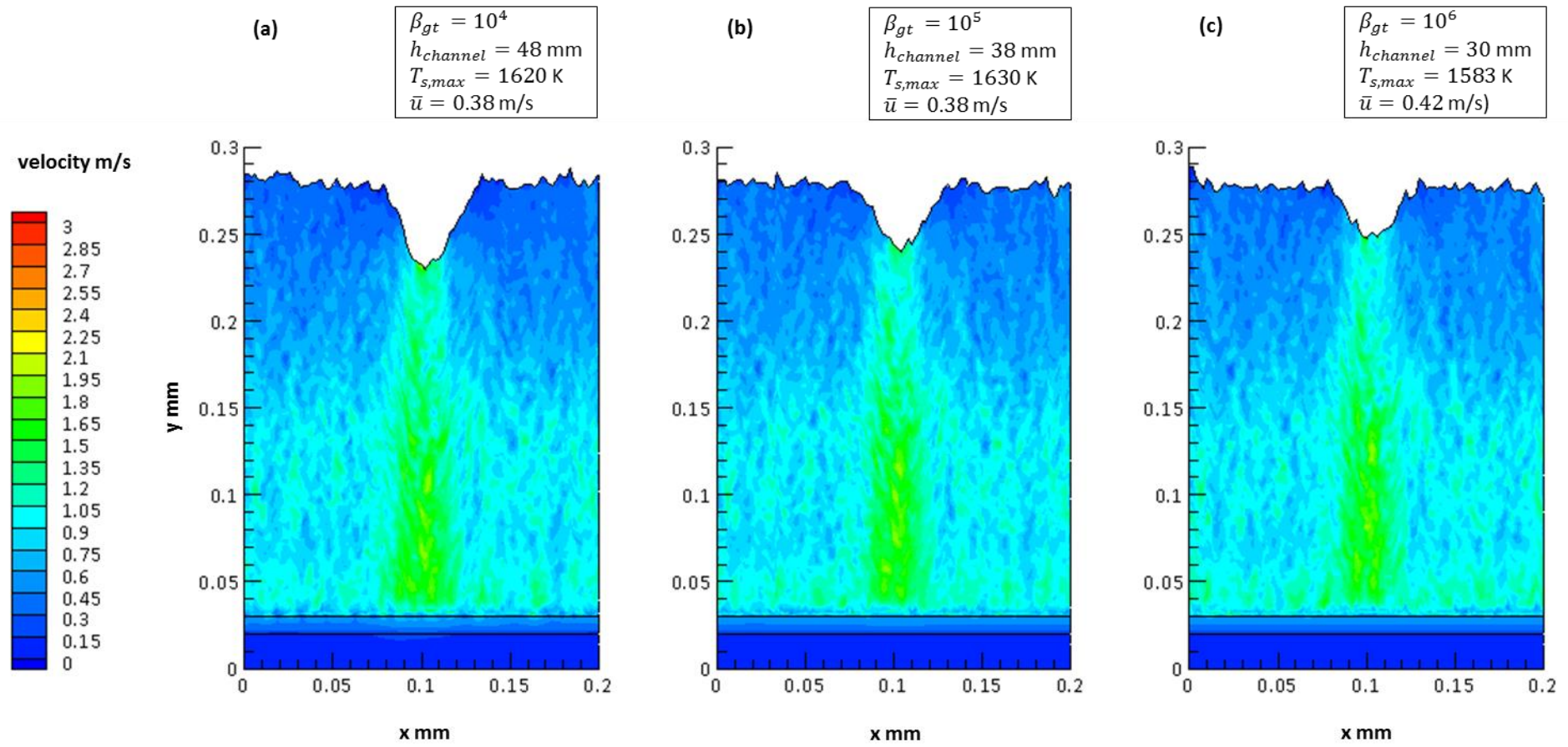


Figure 5.6 Effects of grate resistance on distribution of flow speed: $t = 600$ s, $h_0 = 300$ mm

Increasing the flow resistance through the grate reduces channelling in all cases, because the gas will flow towards the path of least resistance, which is determined by the combined resistance of the grate and the fuel bed in this case. Consider *Figure 5.7*, which shows the deviation of the gas flow speed across the top surface of the bed as a function of the relative resistance of the grate, given by:

$$\frac{\Delta P_{grate}}{\Delta P_{bed} + \Delta P_{grate}} \quad (5.6)$$

$$\Delta P_{bed} = \left(\frac{\mu}{\alpha} u_i + \beta \rho_g |u| u_i \right) h_0 \quad (5.7)$$

$$\Delta P_{grate} = (\beta_{gt} \rho_g |u| u_i) h_{grate} \quad (5.8)$$

where ΔP_{grate} and ΔP_{bed} are the pressure drops through the depth of the grate and the bed, respectively. Both ΔP_{grate} and ΔP_{bed} are calculated using the initial cold-flow conditions, with the α and β terms (Eq. (3.12) and Eq. (3.13) respectively) in ΔP_{bed} determined using the mean porosity of the bed. If the grate resistance is relatively low compared with the bed (*i.e.* the relative resistance approaches 0), the overall resistance is dominated by the vertical resistance through the bed, and the deviation of gas flow becomes sensitive to (horizontal) variations across the bed. The difference between the high-porosity (*i.e.* low resistance) passage and the rest of the bed will, therefore, have a significant effect. As the relative resistance of the grate is increased, the overall resistance is less affected by that of the bed; thus, any spatial variations in resistance across the bed also become less influential.

This is supported by observations from operational furnaces, where it is seen that the likelihood of channelling occurring is reduced with the use of high resistance grates [5]. This relationship between the deviation of the gas flow and the relative resistance of the grate is highly non-linear, highlighting the importance of avoiding grates with a low relative resistance. A general rule of thumb is that the resistance through the grate should be at least equal to the resistance through the bed [143]. This is supported by *Figure 5.7*, which shows that, in all cases, the deviation of gas flow is beginning to level out by this point (relative resistance = 0.5).

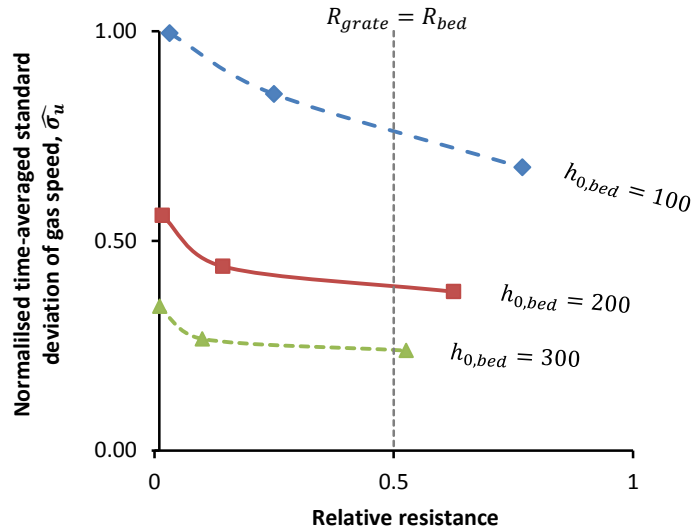


Figure 5.7 Variation of standard deviation of outlet gas speed with different grate resistances as a function of the relative resistance of the grate

Figure 5.8 reveals a linear relationship between the deviation of gas flow and the log of the relative resistance; the slope of each line indicates the effectiveness of increasing the grate resistance. These results are also plotted as a function of the initial bed height in **Figure 5.9**. In line with previous investigations [28], the efficacy of high resistance grates diminishes for deeper beds, because the gas flow eventually becomes redirected towards the passage, regardless of grate resistance. This can be visualised in **Figure 5.10**, which shows that the predicted capture area of a 50 mm wide passage is approximately 100 mm after 600 s for the middle case ($h_0 = 200$ mm, $\beta_{gt} = 10^5$); the majority of the gas only deviates towards the high porosity passage after it has already passed the grate. Deeper beds simply provide additional time for this to occur.

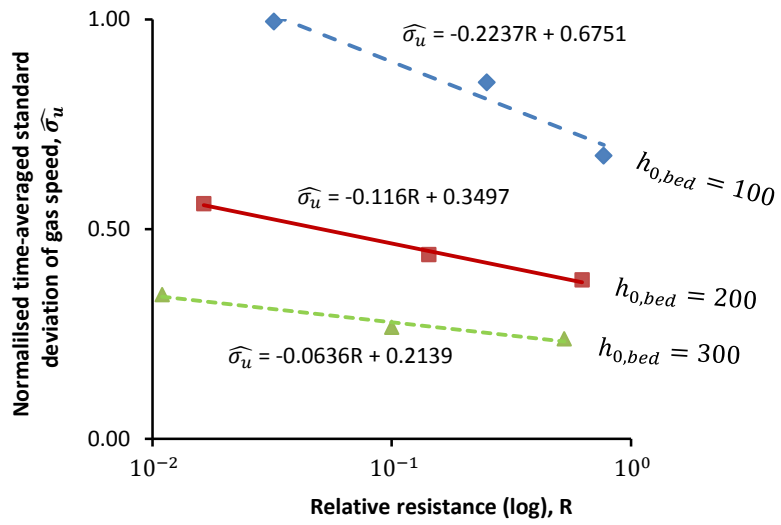


Figure 5.8 Variation of standard deviation of outlet gas speed with different grate resistances as a function of the log of the relative the fuel bed

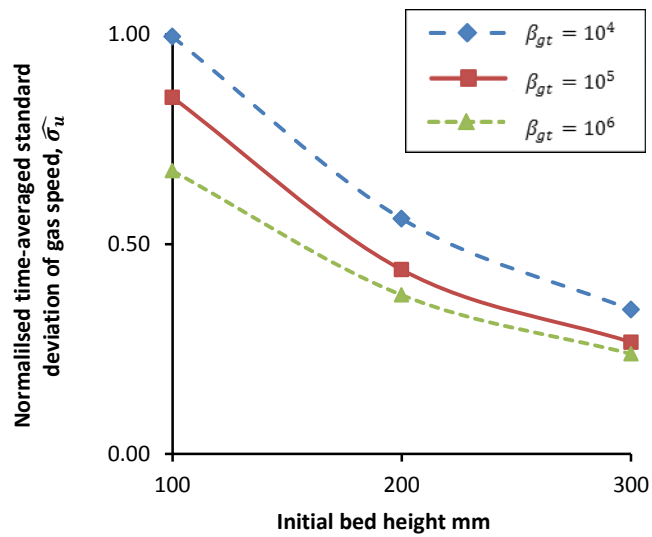


Figure 5.9 Variation of standard deviation of outlet gas speed with different grate resistances as a function of the initial height of the fuel bed

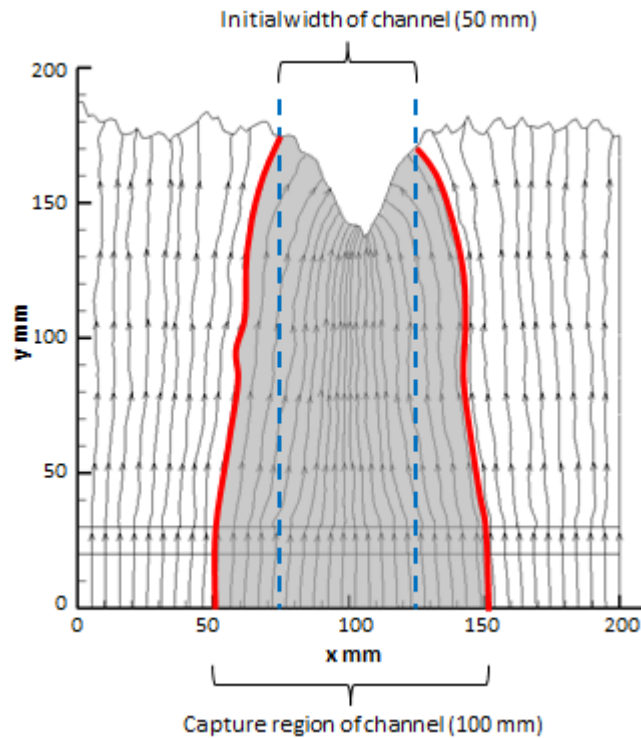


Figure 5.10 Gas pathlines demonstrating the capture area of a 50 mm passage after 600 s for the 200 mm bed with $\beta_{gt} = 10^5$

Figure 5.10 also implies that deviations in gas flow due to a porous passage cannot be completely eradicated by grate design. This is supported by **Figure 5.8**, which shows that even if the grate resistance approaches infinity (*i.e.* the log of the relative resistance approaches 1), the normalised time-averaged deviation of gas flow, in all cases, will still be greater than 0. Nevertheless, increasing the grate resistance constitutes an effective measure for reducing channelling at all bed heights investigated.

The results may be summarised as follows:

- As the grate resistance is increased, in all cases, the air flow becomes more evenly distributed.
- The effectiveness of high resistance grates diminishes for deeper beds.
- Increasing the grate resistance can reduce, but not eradicate, the uneven distribution of air flow caused by a relatively porous passage in the fuel bed.

- The resistance of the grate should be equal to or greater than the resistance of the bed.

5.4.2 Flue gas recirculation (FGR)

Inclusion of FGR increases the temperature and velocity of gas entering through the inlet below the grate, without reducing the oxygen supply (see section 5.4.2). As a result, the overall conversion rate within the bed, and thus the shrinkage rate, increases with FGR. Since FGR causes the bed to burn faster, for comparison between the different cases, we compare conditions when the bed has reduced to the same height in each case. The influence of FGR in a 200 mm bed is illustrated in *Figure 5.11* with corresponding elapsed times and the pyrolysis front, here determined to be when the mass fraction of char, Y_c , reaches 10 %. *Figure 5.12* shows the influence of FGR of the temperatures of the gas and solid phases, with temperatures plotted along a vertical traverse in the centre of the bed, since peak temperatures occur in the passage.

As FGR is increased, the gas becomes less evenly distributed (*Figure 5.13*), but the results may be obscured by the higher mean gas flow rate, which must be taken into consideration. Therefore, we can only compare the cases using the depth of the depression formed, which grows as FGR is increased. However, the overall influence of FGR appears small, showing only a 5% enlargement in valley depth for a 15% boost in FGR. On the other hand, one of the key benefits associated with FGR, lower peak temperatures, is evident in *Figure 5.11* and *Figure 5.12*. This is a well-known feature of FGR and further reinforces model performance.

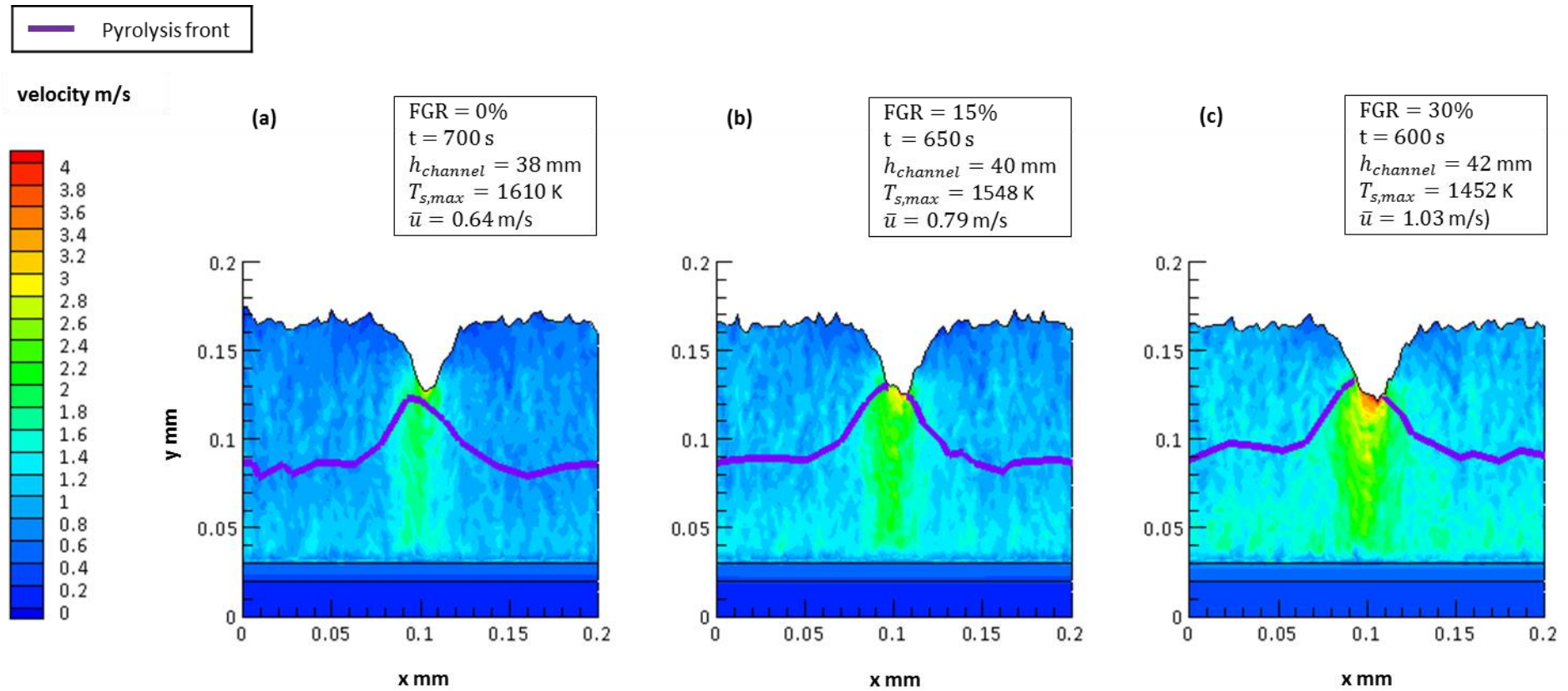


Figure 5.11 Effects of flue gas recirculation on distribution of flow speed: $h_0 = 200$ mm, $\beta_{gt} = 10^6$

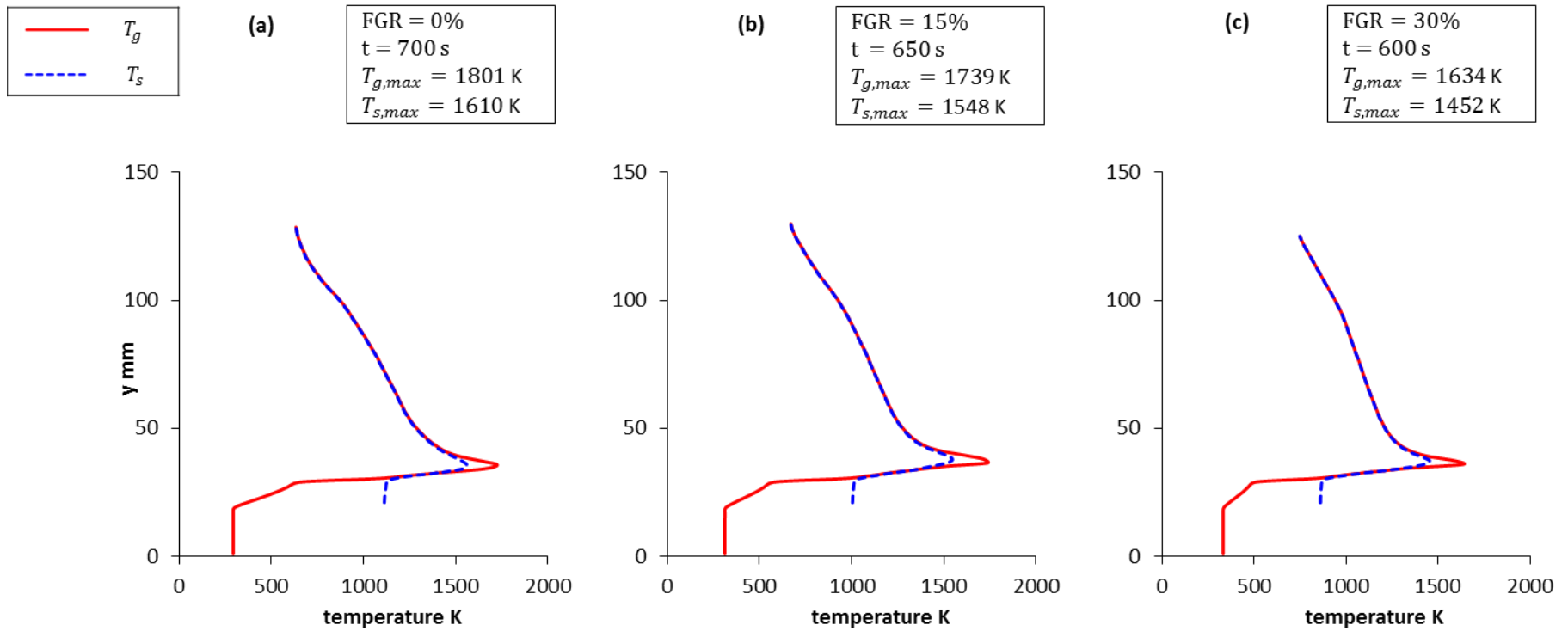


Figure 5.12 Effects of flue gas recirculation on the centreline temperatures ($x = 100$ mm) for the gas and solid phases

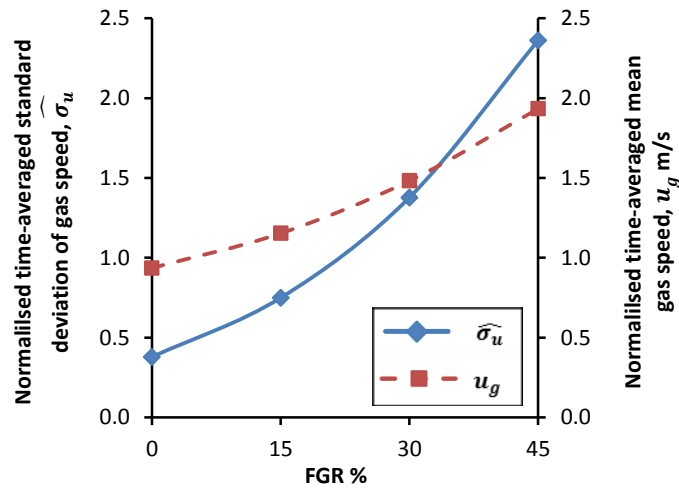
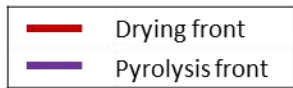


Figure 5.13 Variation of mean and standard deviation of outlet gas speed with flue gas recirculation

5.4.3 Moisture content

The impact of the initial moisture content of the fuel in a 200 mm fuel bed is described in *Figure 5.14* and *Figure 5.15*. The initial mass of fuel is the same for each case; it should therefore be noted that increasing the initial moisture content causes a reduction in the mass of combustible fuel present. Under combustion conditions, the fuel is rapidly dried by the heat emanating from the combustion reactions taking place lower down in the bed, resulting in a thin drying front moving upwards through the fuel bed, ahead of the pyrolysis front.

The gas becomes less evenly distributed for the wetter fuels (*Figure 5.15*), but the faster mean flow rate may belie these results, and should be taken into account. As with FGR, we can therefore only compare the cases using the valley depth. Because the relatively fast drying process causes the bed to shrink faster, conditions are compared when the bed height, excluding the sunken region, in each case has fallen to roughly the same level. Based on this, wetter fuels result in marginally deeper indentations; however, the influence appears inappreciable as modelled here. It is worth bearing in mind that the depth of the valley formed is influenced by the



velocity m/s

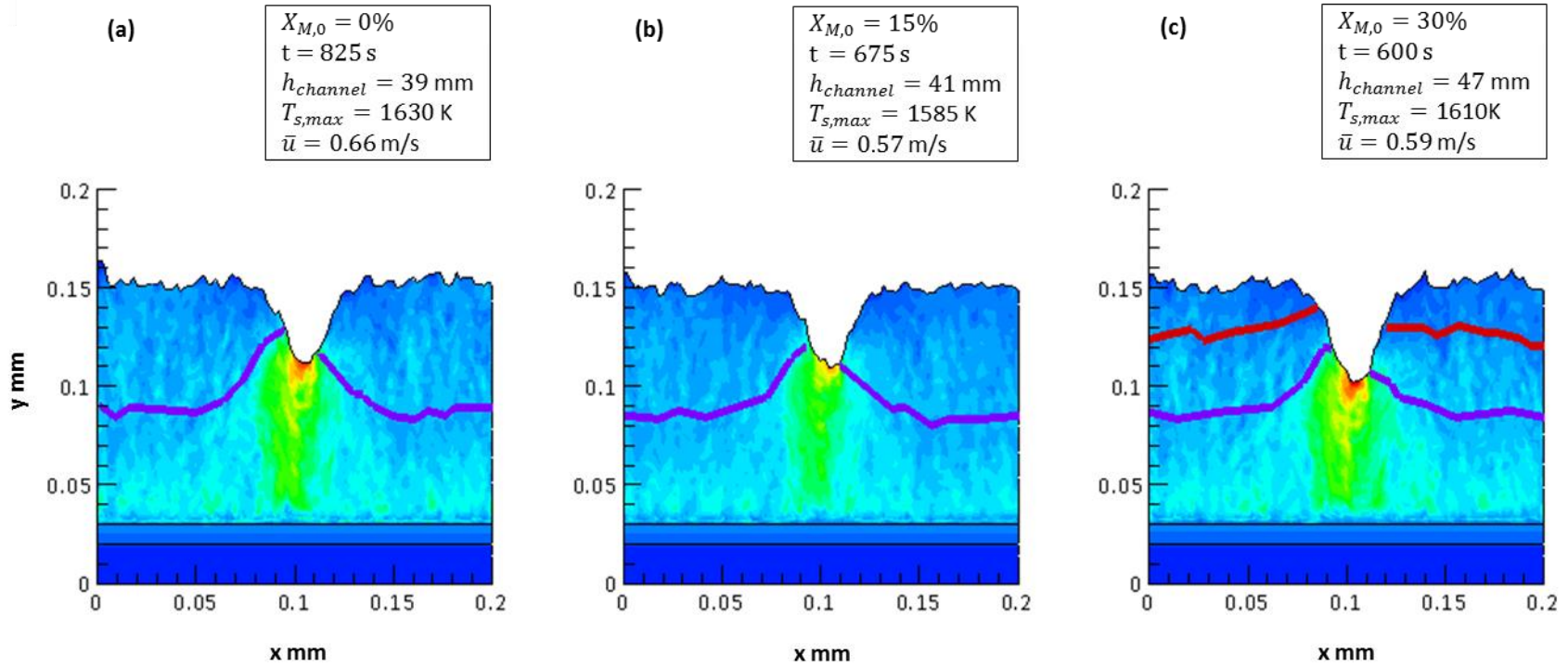
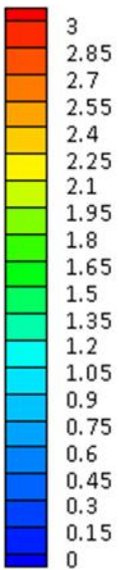


Figure 5.14 Effects of initial fuel moisture content on distribution of flow speed: $h_0 = 200 \text{ mm}$, $\beta_{gt} = 10^6$

shrinkage parameters for each of the particle and bed models; correlations for the latter, in the absence of more appropriate data, are here sourced from an experiment employing char particles. More generally applicable shrinkage parameters require additional measurements for fuels of different composition and shape.

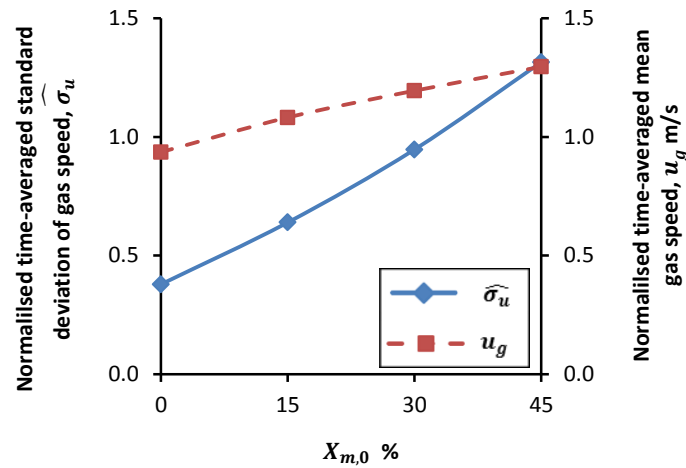


Figure 5.15 Variation of mean and standard deviation of outlet gas speed with initial moisture content

5.5 Discussion

The 2D fixed-bed combustion model that was developed and validated in Chapters 3 and 4, respectively, was applied to investigate factors that influence channelling in a randomly packed bed containing a high porosity passage. The influence of flow resistance through the grate and bed height were compared with previous observations. Additional factors investigated include flue gas recirculation and initial moisture content of the fuel.

As expected, increasing the grate resistance reduces, but does not eradicate, channelling. A higher grate resistance improves the distribution of inlet gas (*i.e.* primary air) to the fuel bed because it obscures the effect of any porous passages in the bed, thus indirectly retards flow from deviating towards the passage. For deeper beds, however, the effectiveness of grate resistance diminishes because the gas has more residence time within the bed to track towards the high porosity

passage. These predictions tally with observations from several operational furnaces [5] and previous numerical studies [28, 91].

Novel factors investigated include the initial moisture content and level of flue gas recirculation. Increasing the initial moisture content from 0 to 30 % has a weak influence; nonetheless, valley growth increases with moisture content, showing a propensity for wetter fuels to amplify channelling. The impact of flue gas recirculation on channel formation appears to be insignificant, although its benefits, such as reduced peak temperature, were apparent.

Previous researchers [91] have suggested that a 2D representation can be expected to capture the major characteristics of channelling. The current approach can be employed to investigate non-uniformities across the bed other than random packing, including; non-uniform grate resistance, non-uniform air supply, and non-uniform fuel composition (fuel type, moisture content, etc.). In practice, however, any relatively porous passages formed due to random packing or other irregularities are likely to be 3D. For this reason it is desirable to extend the present method to a fully 3D model.

6. 3D MODEL OF CHANNELLING IN FIXED-BED COMBUSTION

6.1 Objective and Overview

The objective of this section is to perform a 3D investigation of channelling in fixed-bed biomass combustion. In Chapter 5, the grate resistance, bed height, initial fuel moisture content, and level of flue gas recirculation were examined to ascertain their influence on the channelling phenomena. Channelling was instigated by inducing a relatively porous passage in a randomly packed bed. The 2D analysis indicated that the resistance to flow through the grate, or the relative resistance of the grate compared with the bed, had a significant effect on channelling.

In practice, however, any spatial variations in fuel packing, or other irregularities, which may lead to channelling, are likely to be 3D in nature. The effect of the resistance to flow through the grate is, therefore, re-examined by means of a 3D model. As in Chapter 5, the 3D numerical analysis is performed on a section of a randomly-packed fuel bed in a biomass furnace, as illustrated in *Figure 6.1*. The spatial variation in porosity caused by the random packing of fuel particles is described in section 6.2, with the investigated parameters outlined in section 6.3. The results are presented in section 6.4, and discussed in section 6.5.

Highlighted in *Figure 6.1* is the simulated section of the fuel bed. Similarly to the 2D analysis in Chapter 5, the freeboard is not modelled, the grate is treated as an isotropic, perfectly porous medium, and both the slope of the grate and disturbances caused by grate motion are neglected. The 3D computational domain is divided into three zones: a packed fuel bed, a grate, and a windbox, as shown in *Figure 6.2*. The zones are linked by means of standard fluid-fluid interfaces and the sides of the domain are coupled by means of translational periodicity between opposing faces. All zones are discretised using uniform $2 \times 2 \times 2$ mm cubic cells.

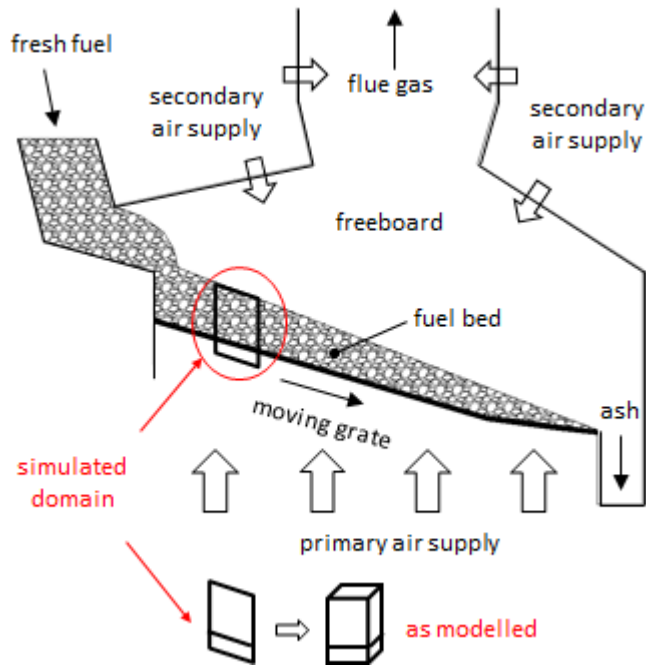


Figure 6.1 Schematic diagram of a grate furnace showing the simulated domain

6.2 Initial Bed Porosity

Following on from the 2D analysis in Chapter 5, the porosity of the randomly-packed bed is defined by means of a normal distribution (Eq. (5.1)), with mean porosity, $\bar{\epsilon} = 0.42$, and standard deviation from the mean, $\sigma_{\epsilon} = 0.1$. In a similar manner to the 2D investigation, a single, relatively porous passage is induced in the centre of the fixed-bed by adjusting the random cell porosity by means of a position-dependent function. The major difference here is that the 3D model enables passages of different shape to be represented.

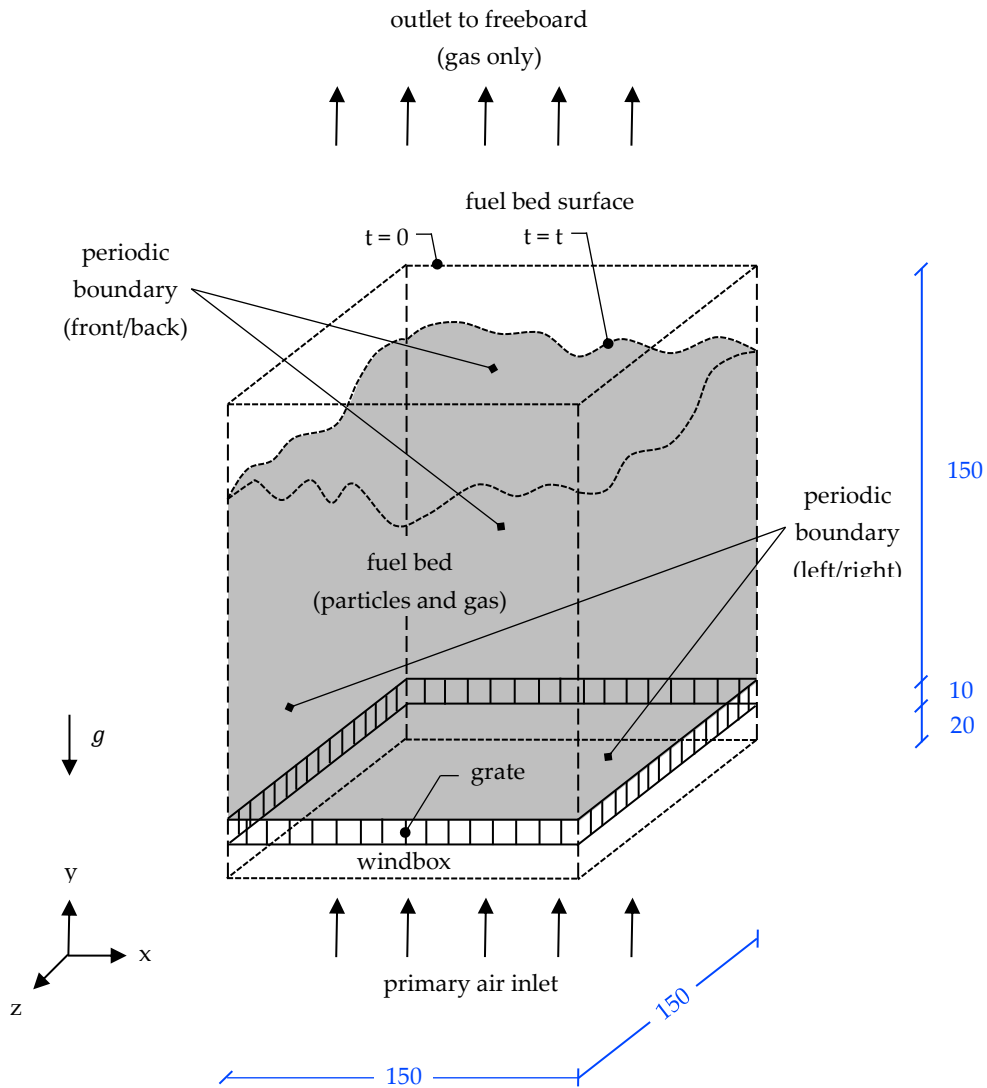


Figure 6.2 Simulated 3D domain showing shape of fuel bed surface after time t (dimensions in mm)

Since the passages formed during channelling are typically expected to be fairly circular, the first high-porosity passage is circular in shape, and runs through the depth of the bed. To provide a smooth transition to the high porosity passage, the corresponding position-dependent function is based on the shape of an axisymmetric normal distribution bell curve, derived from Eq. (5.1), with $\bar{\varepsilon} = 0$ and $\sigma_{\varepsilon} = 1$. Similarly to Chapter 5, the parameters for Eq. (5.1) are adjusted to produce a shape function, in this case with a base diameter of 50 mm, in the centre of the domain ($\bar{x} = 75$ mm, $\bar{z} = 75$ mm), as shown in **Figure 6.3** (a). The resulting multiplier is greatest when $x = \bar{x}$, and $z = \bar{z}$, but quickly drops off as cells move away from

the centre of the domain. The high-porosity passage is then created by modifying the randomly-generated porosity, shown in *Figure 6.4* (a) for a randomly packed 3D fuel bed without a passage, according to Eq. (5.2). The resulting distribution of porosity in a randomly packed bed with a circular passage is portrayed in *Figure 6.4* (b). The depth-averaged porosities in a randomly packed bed, and a randomly packed bed with a circular channel, are illustrated, respectively, in *Figure 6.5* (a) and *Figure 6.5* (b). The second high-porosity passage is rectangular in shape, and is effectively a 3D representation of the 2D approximation, see

Figure 5.2. The corresponding position function is therefore based on an extruded normal distribution bell curve. The parameters are adjusted to produce a 3D wedge, with a base of 50 mm, as shown in *Figure 6.3* (b). The porosity of each individual cell is modified as before, with the resulting distribution of porosity presented in *Figure 6.4* (c); the depth-averaged porosity across the bed is displayed in *Figure 6.5* (c).

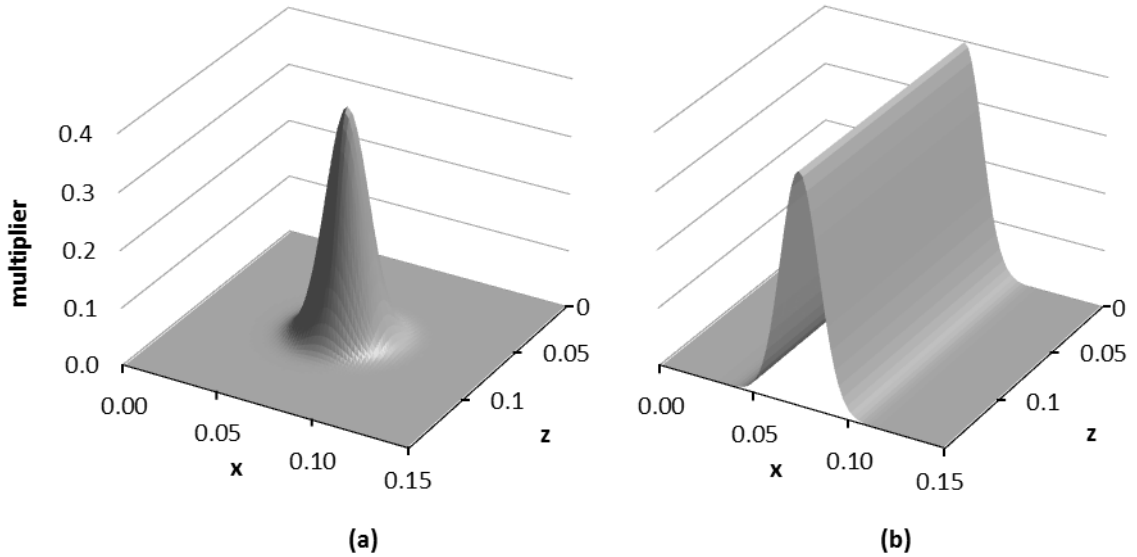


Figure 6.3 3D position dependent functions

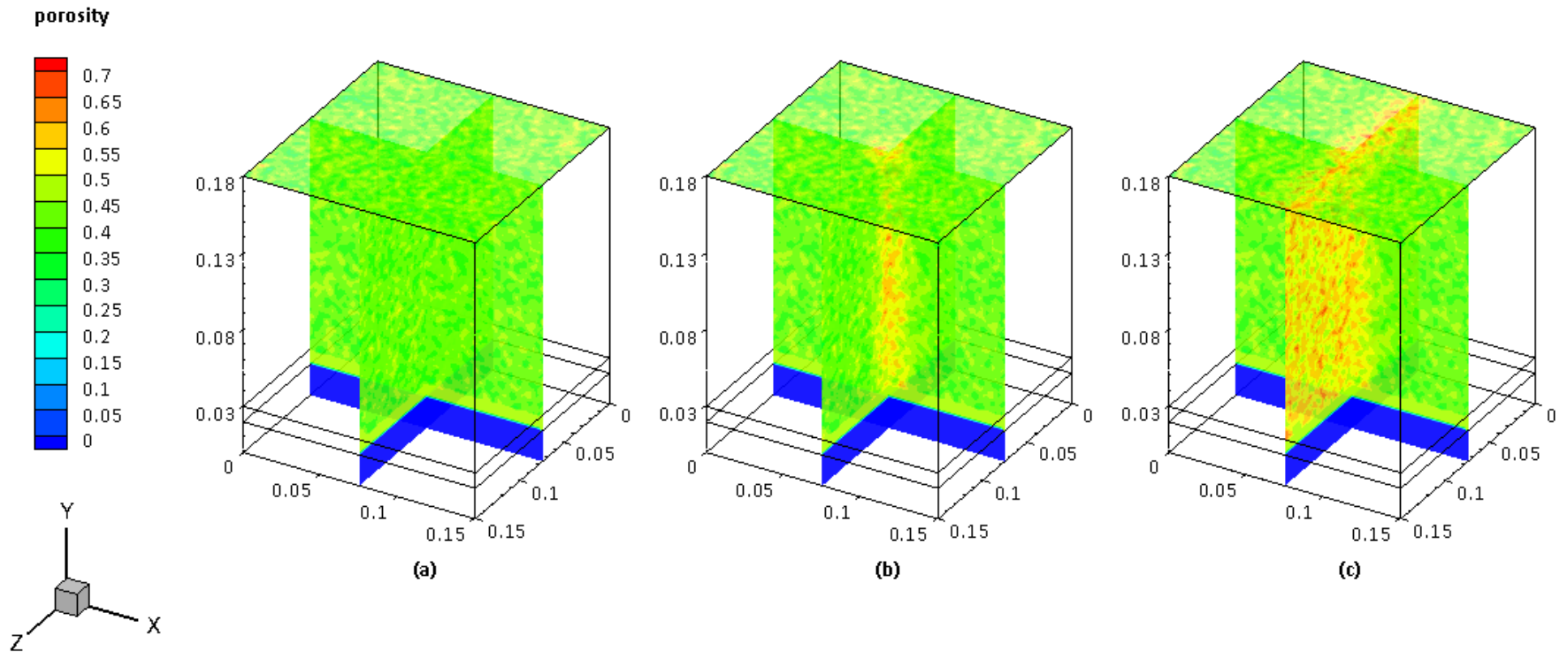


Figure 6.4 Spatial variation of initial porosity: (a) random; (b) random with circular high porosity passage; (c) random with rectangular high porosity passage

porosity

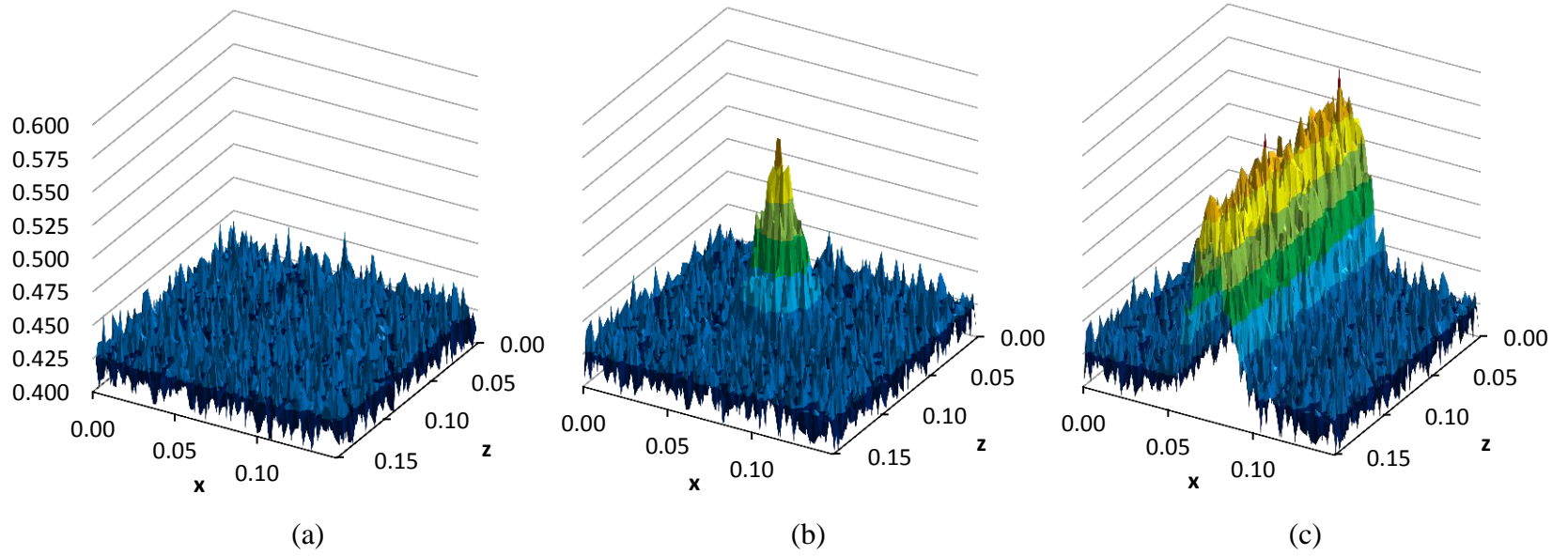
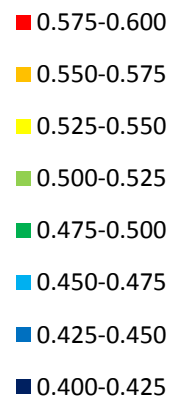


Figure 6.5 Averaged porosity along vertical traverses

6.3 Parameters Investigated

Based on 2D investigations, the most influential factor in channelling appears to be the resistance to flow through the grate, see chapter 5 and refs [28, 91]. Here, therefore, the effect of grate resistance will be re-examined in three-dimensions. To this end, three different grate resistances will each be tested for two differently shaped passages through the fuel bed. The grate is represented as a uniformly porous medium, with the grate friction coefficient, β_{gt} , calculated based on cold-flow pressure drops of 1, 10, and 100 Pa through the grate. In all cases, the initial bed height is 150 mm, which corresponds to an initial cold-flow pressure drop of 45 Pa (15 Pa along the centreline of the relatively porous passage).

The seven cases considered are outlined in *Table 6.1*.

Table 6.1 Parameter combinations investigated for channelling

Case	Passage shape	β_{gt} ($\times 10^4$)
reference	none	
1 a/b/c	circular	1/10/100
2 a/b/c	rectangular	1/10/100

The initial conditions, boundary conditions, and material specifications are identical to those used in Chapter 5, as described in *Table 5.2*.

6.4 Results

The HPC system available [187] is an SGI Altix ICE 8200EX cluster with 320 compute nodes. Each compute node contains 2 Intel Xeon X5650 hex-core processors and 24 GB RAM. All cases were run successfully for a simulated time of 250 s using a timestep of 1 s. Each case took between 50 and 60 walltime hours when run in parallel across 2 compute nodes (24 CPU cores). The predicted results for variations of grate resistance for the two different types of passage are presented in *Figure 6.6 - Figure 6.13*.

As described in section 5.4, the channelling effect is again quantified by means of the normalised, time-averaged standard deviation of gas flow at the top surface of the bed, Eqs. (5.3) - (5.5). The datum case does not contain a high porosity passage, see *Figure 6.4* (a), and has a grate friction coefficient, β_{gt} , of 10^6 , but is otherwise identical to the cases investigated.

To aid visual comparison, critical values resulting from all cases are tabulated in *Table 6.2*.

Table 6.2 Significant results from 3D simulated cases

Case	1a	1 b	1 c	2 a	2 b	2 c
$\beta_{gt} (\times 10^4)$	1	10	100	1	10	100
passage type	circular	circular	circular	rect. ¹⁷	rect.	rect.
$h_{channel}$ (mm)	10	9	8	13	11	10
$T_{s,max}$ (K)	1600	1580	1557	1594	1570	1561
\bar{u} (m/s)	0.53	0.53	0.53	0.52	0.52	0.52

6.4.1 Circular passage

Figure 6.6 illustrates the influence of the grate resistance on the spatial variation of gas speed in a bed containing a circular high porosity passage. As the grate resistance is increased, the peak gas speed in the passage drops off, indicating that less air deviates towards the passage. A similar trend is observed for the peak temperature of the particulate phase, as shown in *Figure 6.7*. For the lowest grate resistance, *Figure 6.7* (a), the crater that has formed as a result of the circular passage is approximately 10 mm deep, and the peak temperature of the particulate phase is 1600 K. Increasing the grate resistance reduces the peak temperature and the depth of the crater, as portrayed in *Figure 6.7* (b) and (c). This is a result of the air being less unevenly distributed, which reduces the conversion rate in the relatively porous passage.

¹⁷ rectangular

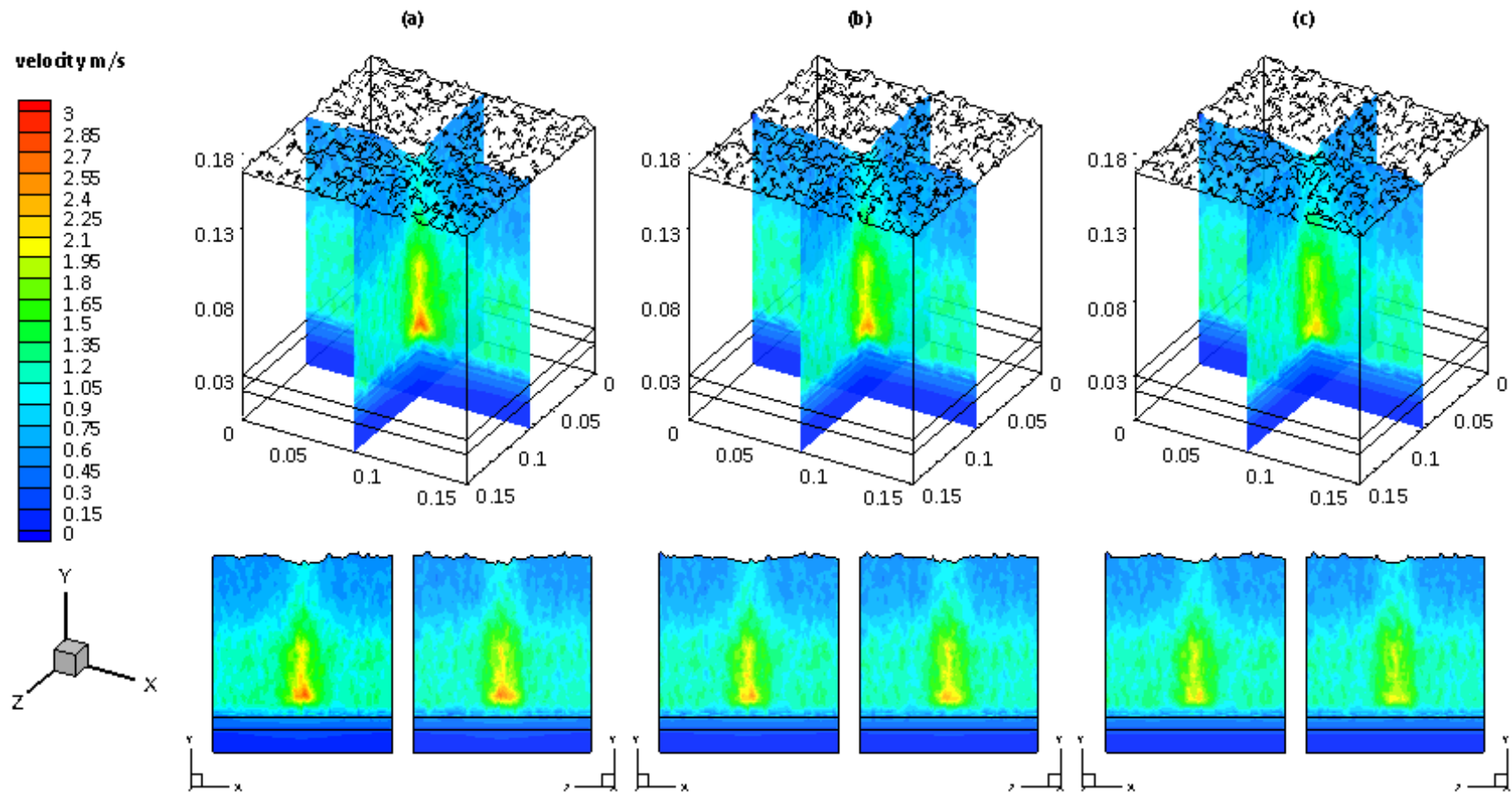


Figure 6.6 Effects of variation in grate resistance on distribution of gas speed in a randomly packed bed with a circular passage after 250 s: (a) $\beta_{gt} = 10^4$; (b) $\beta_{gt} = 10^5$; (c) $\beta_{gt} = 10^6$.

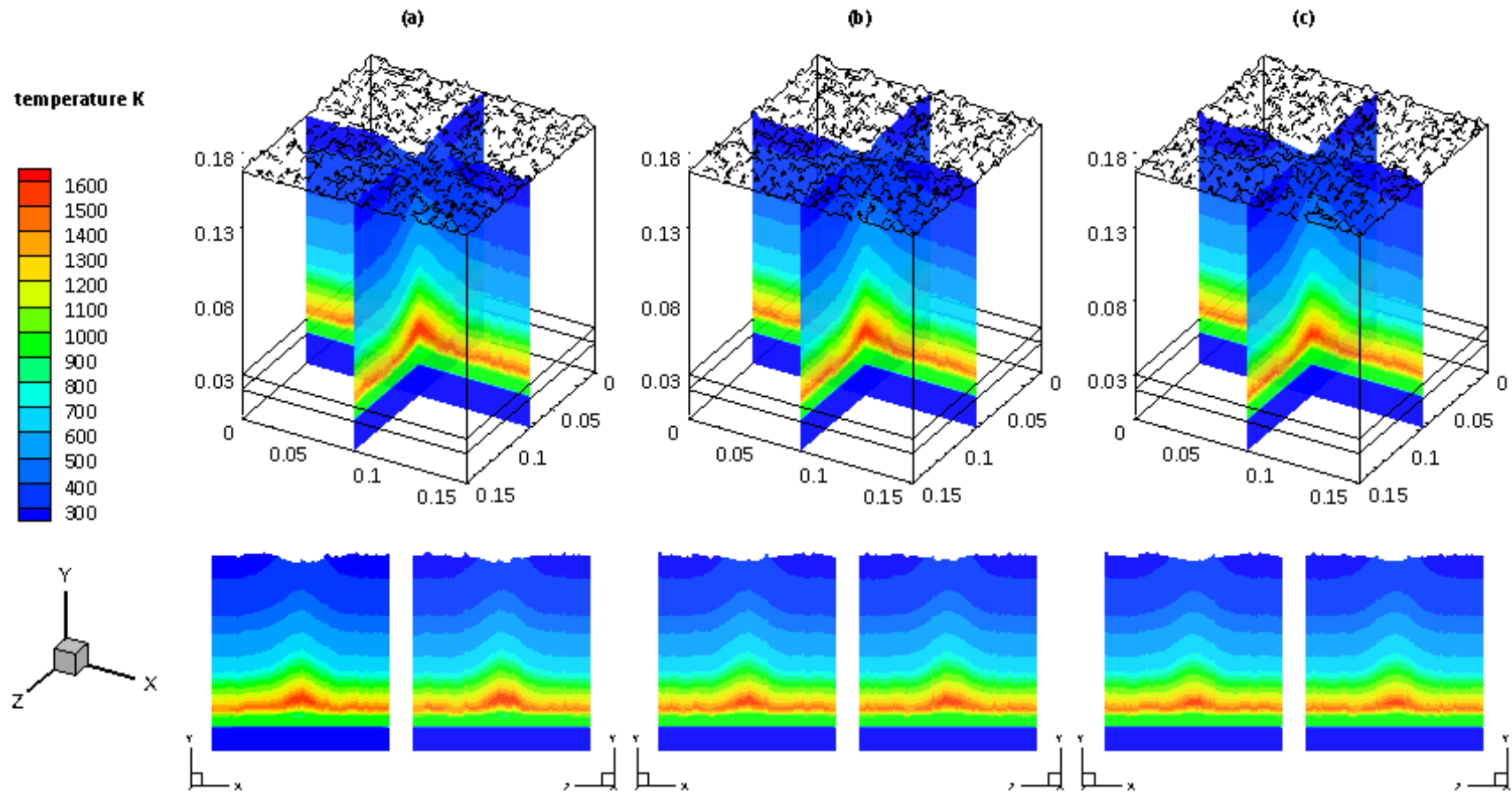


Figure 6.7 Effects of variation in grate resistance on distribution of solid temperature in a randomly packed bed with a circular passage after 250 s:
 (a) $\beta_{gt} = 10^4$; (b) $\beta_{gt} = 10^5$; (c) $\beta_{gt} = 10^6$.

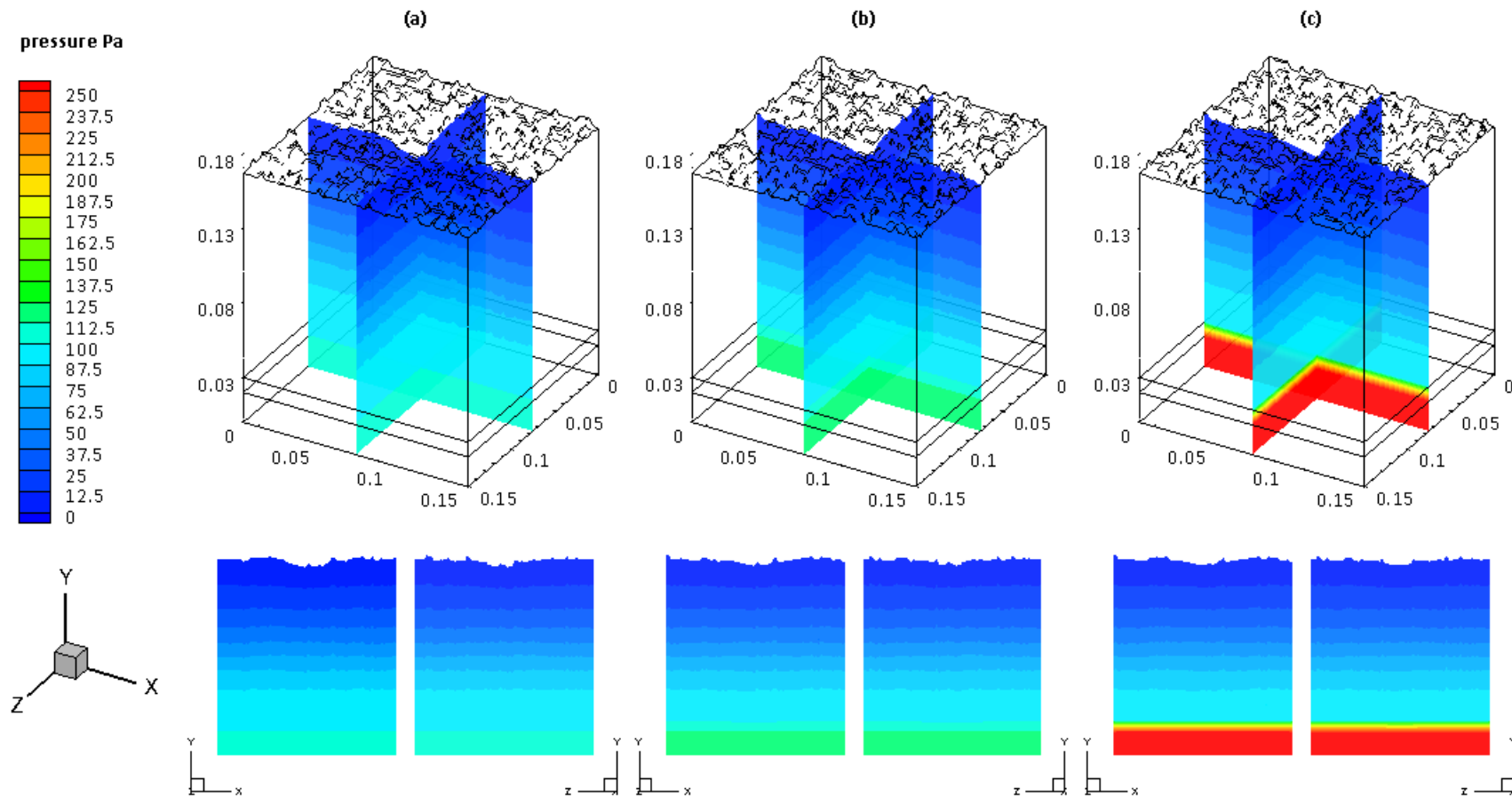


Figure 6.8 Effects of variation in grate resistance on distribution of pressure in a randomly packed bed with a circular passage after 250 s:
 (a) $\beta_{gt} = 10^4$; (b) $\beta_{gt} = 10^5$; (c) $\beta_{gt} = 10^6$.

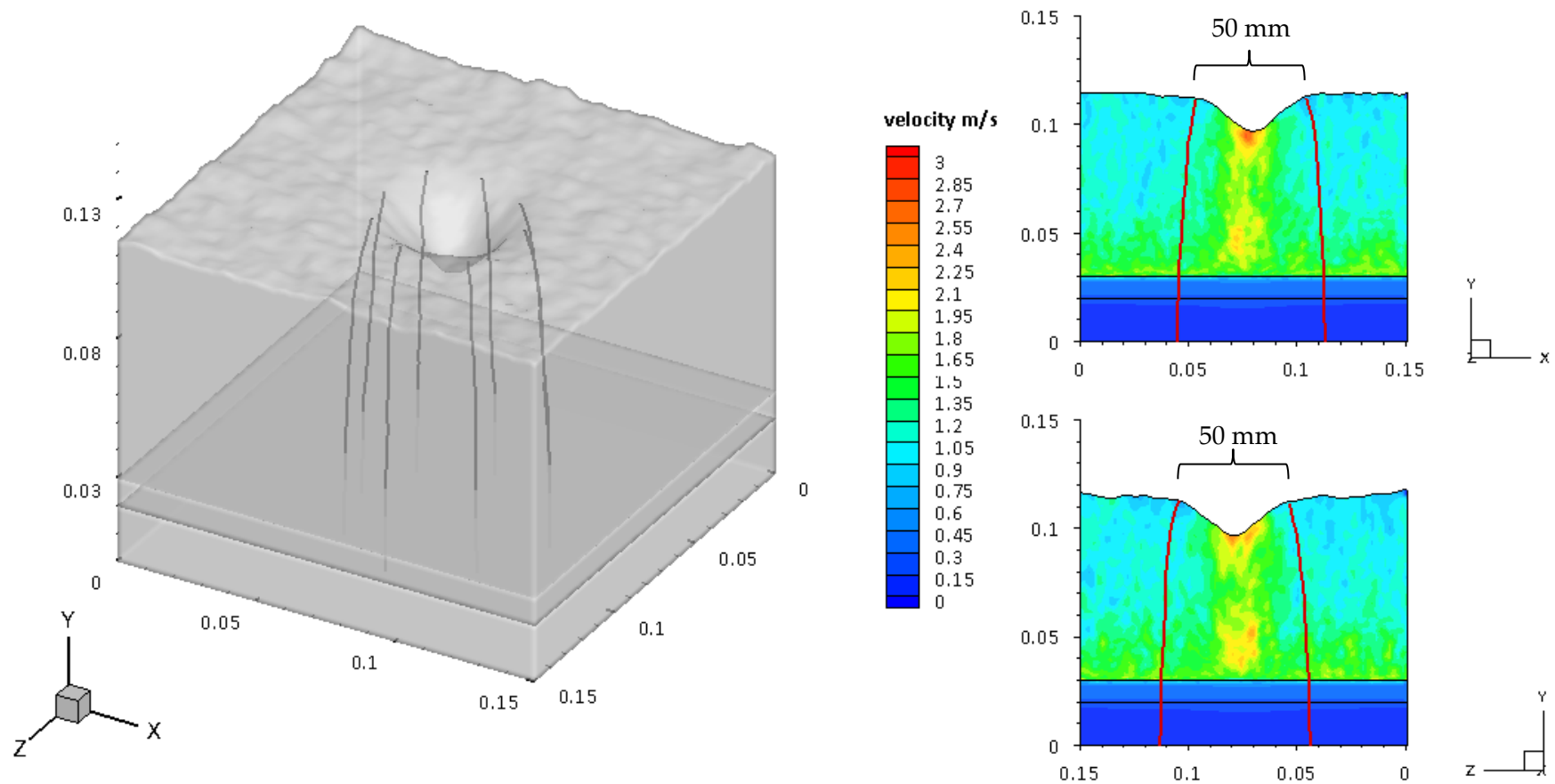


Figure 6.9 Streamtraces in a fuel bed containing a circular passage, with $\beta_{gt} = 10^6$, after 600 s.

As described in section 5.4.1, the overall resistance (*i.e.* bed plus grate) becomes dominated by the grate as the relative resistance of the grate is increased. This effectively desensitises the gas flow to any spatial variations in resistance across the bed caused by, for instance, a porous passage. To demonstrate the effect this has on the overall gas pressure, the spatial distribution of gas pressure is shown in *Figure 6.8*. *Figure 6.9* demonstrates that after 600 s¹⁸ with $\beta_{gt} = 10^6$, the predicted capture area for a circular passage with a diameter of 50 mm is a circular area with a diameter of approximately 67 mm, or 1.8 times the area of the passage itself. The majority of the gas only deviates towards the high porosity passage after it has already passed the grate.

6.4.2 Rectangular passage

Figure 6.10 illustrates the influence of the grate resistance on the spatial variation of the gas speed in a bed containing a rectangular passage. Similarly to the circular passage cases (*Figure 6.6*), the peak gas speed in the passage drops off as the grate resistance is increased. *Figure 6.11* shows the temperature variation of the particulate phase for the rectangular cases, and highlights the same trends as the circular passage (*Figure 6.7*); both the depth of the valley, which has formed as a result of the rectangular passage, and the peak temperature of the particulate phase, decrease as the grate resistance is increased.

However, comparing the two types of passage for the same simulated time and grate resistance, the valleys formed as a result of the linear passages are deeper than the corresponding craters caused by the circular passages. This can be explained by considering *Figure 6.12*, which demonstrates that, after 600 s¹⁸ with $\beta_{gt} = 10^6$, the predicted capture area for a rectangular passage with a width of 50 mm is a

¹⁸ To visualise the capture area, two cases were run for 600 s, one for a circular passage, and another for a rectangular passage. It should be noted that for these cases the bed shrinkage was implemented as continuous shrinkage only (*i.e.* no abrupt collapses, which skips the multi-particle scale section of the code) in order to reduce the run time.

rectangular area with a width of approximately 82 mm, or 1.6 times the area of the passage itself. Similarly to the circular passage (*Figure 6.9*), the majority of the gas only deviates towards the high porosity passage after it has already passed the grate.

The trends observed for both the circular passage and the rectangular passage are supported by the standard deviation of the gas flow at the top surface of the bed, shown in *Figure 6.13*, which also indicates that the air becomes less unevenly distributed as the grate resistance is increased, regardless of the type of passage in the bed. Although the standard deviation of gas flow does not appear to decline significantly for the circular passage, it is worth noting that the statistical analysis is carried out across the surface of the entire bed. Since the circular passage accounts for a significantly smaller percentage of the total bed surface area than the rectangular passage, deviations for the circular passage are somewhat occluded in the statistical analysis.

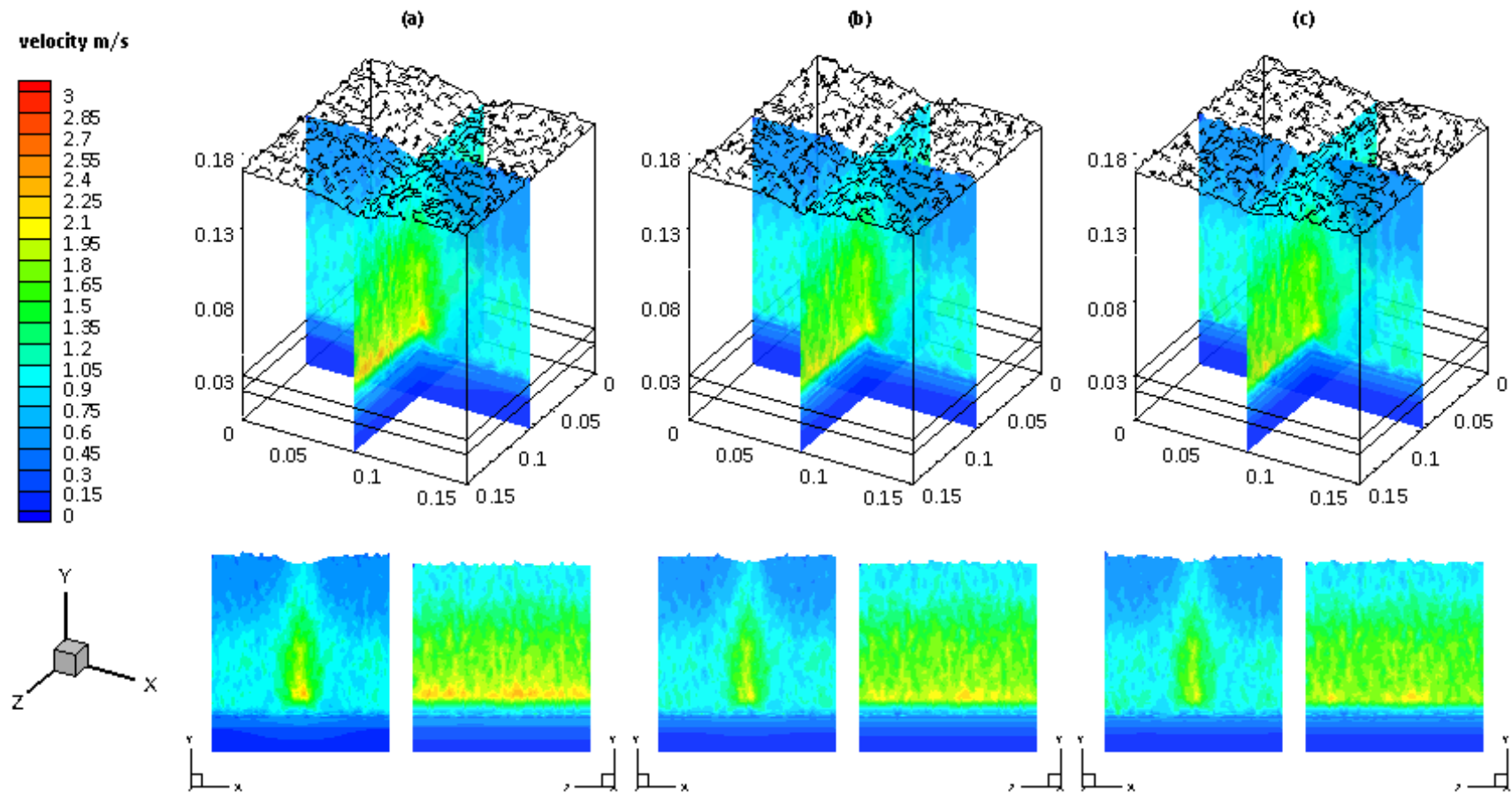


Figure 6.10 Effects of variation in grate resistance on distribution of gas speed in a randomly packed bed with a rectangular passage: (a) $\beta_{gt} = 10^4$; (b) $\beta_{gt} = 10^5$; (c) $\beta_{gt} = 10^6$.

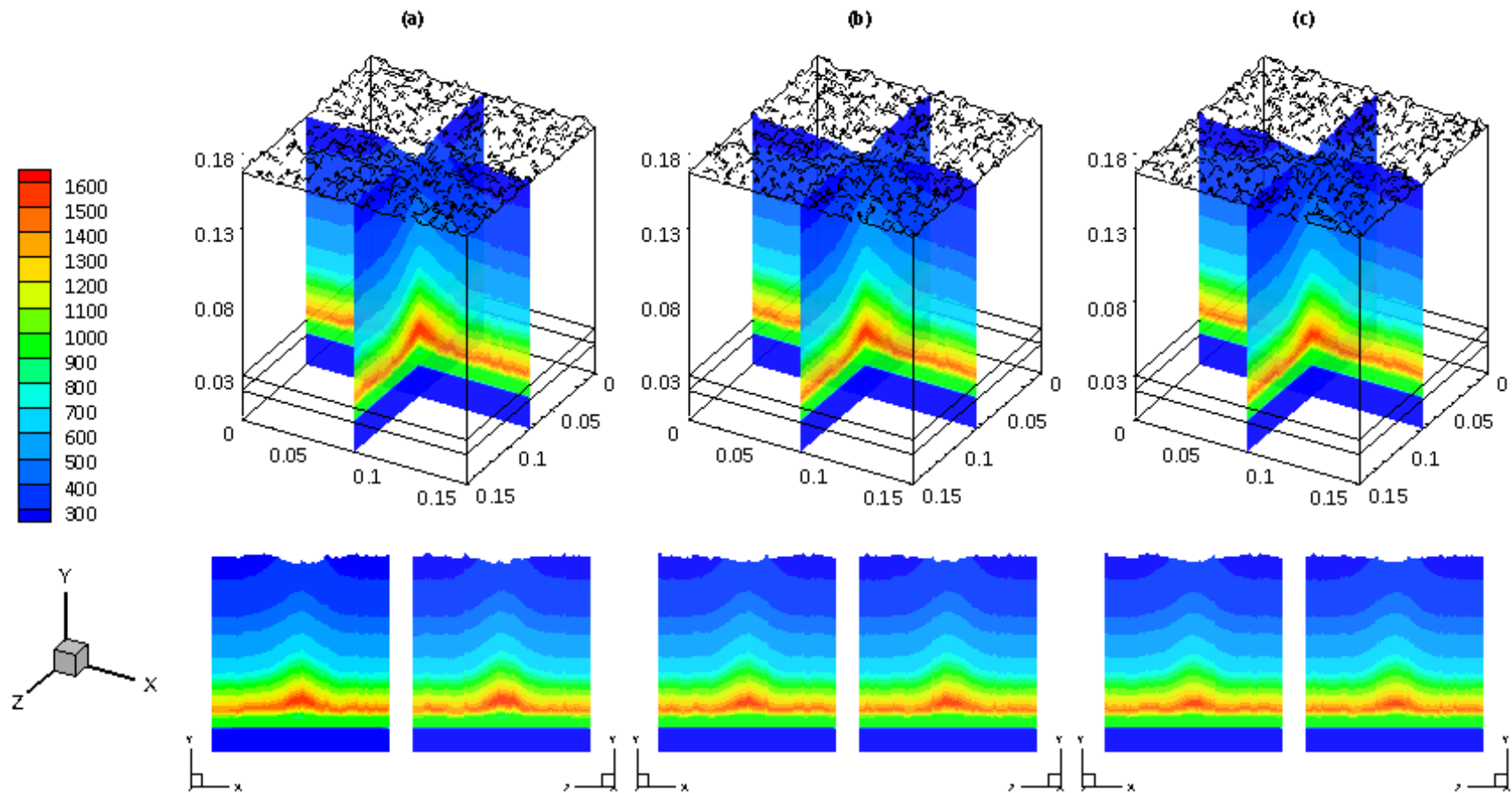


Figure 6.11 Effects of variation in grate resistance on distribution of solid phase temperature in a randomly packed bed with a rectangular passage:
 (a) $\beta_{gt} = 10^4$; (b) $\beta_{gt} = 10^5$; (c) $\beta_{gt} = 10^6$.

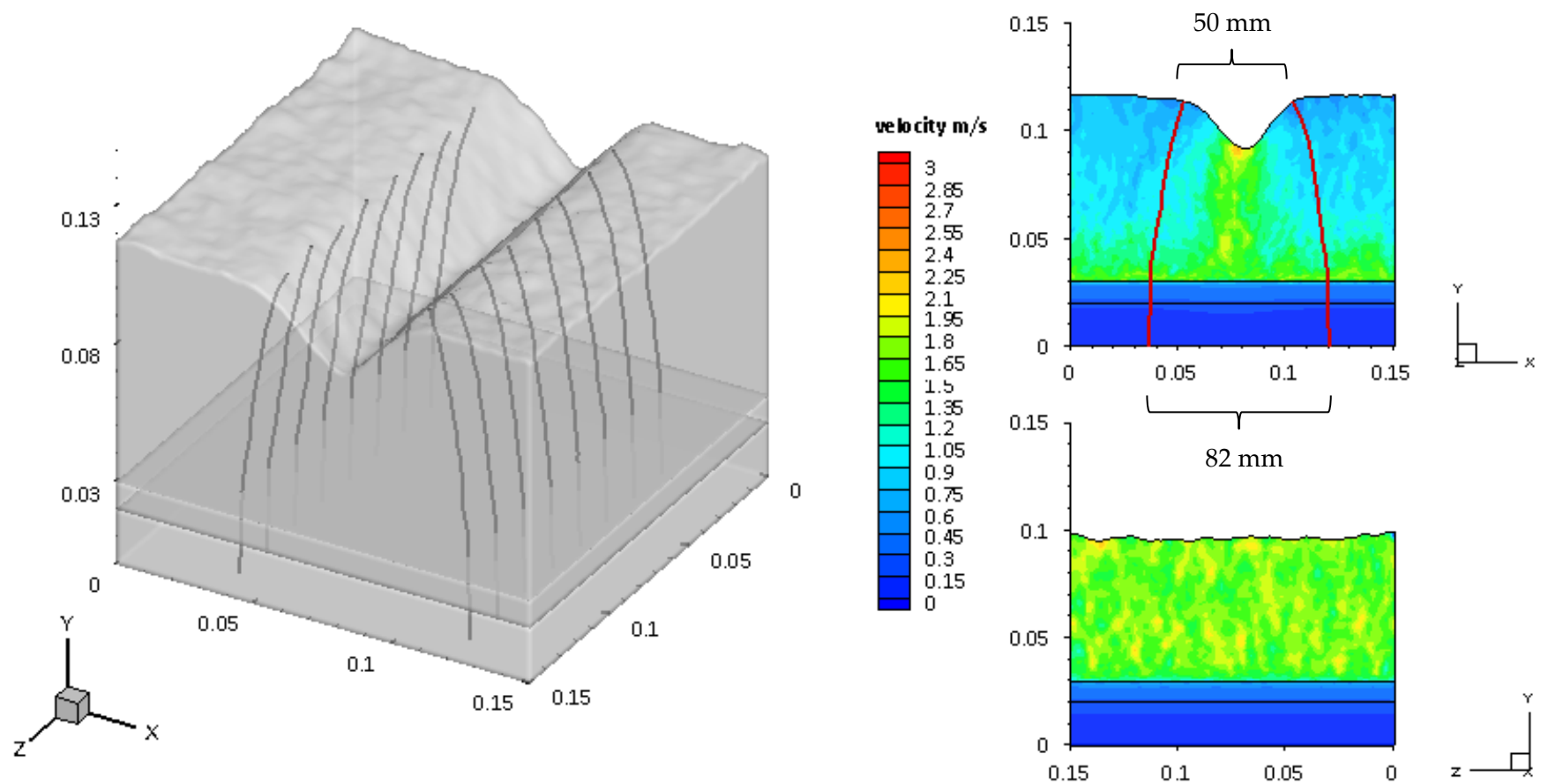


Figure 6.12 Streamtraces in a fuel bed containing a rectangular passage, with $\beta_{gt} = 10^6$, after 600 s.

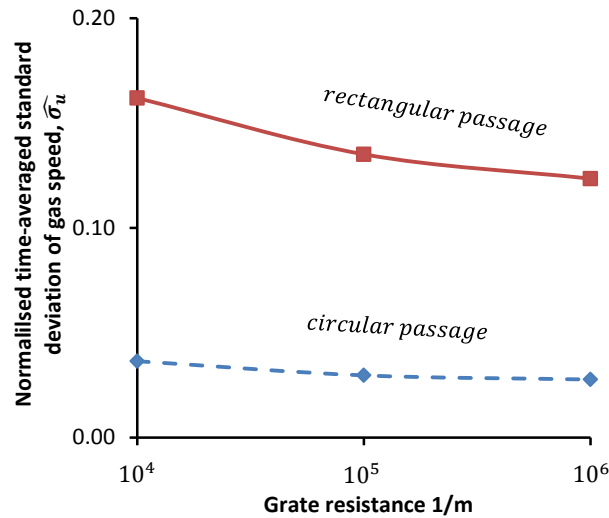


Figure 6.13 Variation of standard deviation of outlet gas speed with different grate resistances

It is also worth bearing in mind that the simulated time of 250 s¹⁹ in the 3D cases is shorter than in the 2D investigations, each of which ran for 600 s. As a result, the fuel bed is in a less advanced state of combustion, as seen in *Figure 6.6* and *Figure 6.10*, where the dips forming in the surface of the bed are comparatively less defined than in the 2D cases, see section 5.4.1. Consequently, the standard deviation of gas speed is also lower, which precludes a direct comparison; nonetheless, the predicted trends are unaffected.

6.5 Discussion

The 2D method employed to investigate the factors affecting channelling (Chapter 5) was extended to three dimensions. To examine possible discrepancies between a 3D representation of a fuel bed and a 2D approximation, the 3D model was applied to reinvestigate the effect of the grate resistance on channelling, since this was identified as an influential factor in the channelling phenomenon in the 2D analysis.

¹⁹ The two cases which were run for 600 s (*Figure 6.9* and *Figure 6.12*) are excluded here because abrupt bed collapses were not simulated in these cases, see footnote 18.

Regarding the grate resistance, the 3D investigation produced the same trends as the 2D investigation; this indicates that a 2D analysis provides a reasonable approximation of an actual randomly-packed bed. However, comparing a 3D circular passage with a 3D rectangular passage, differences are seen: the dips formed are more pronounced for the rectangular passages, whereas the relative capture area is larger for the circular passage. These differences, which cannot be differentiated in a 2D approximation, indicate that a 2D representation of the fuel bed is of limited use when modelling a 3D process, such as channelling. In any event, to investigate 3D features, such as the shape of a grate, a 3D model is necessary.

7. 3D INVESTIGATION OF MEASURES TO REDUCE GRATE WEAR

7.1 Objective

The objective of this section is to investigate measures to reduce grate wear in fixed-bed combustion. To examine the factors that affect grate wear, a 3D analysis is performed on a section of a grate, the shape of which is varied, as illustrated in *Figure 7.1*. Potential causes of grate wear are introduced in section 7.2. An overview of the simulated domain is presented in section 7.3, with the parameters investigated outlined in section 7.4. The numerical model described in Chapter 3 is extended to enable the grate analysis; these alterations, and the validation of the modified model are described, respectively, in sections 7.5 and 7.6. The results are shown in section 7.7, and discussed in section 7.8.

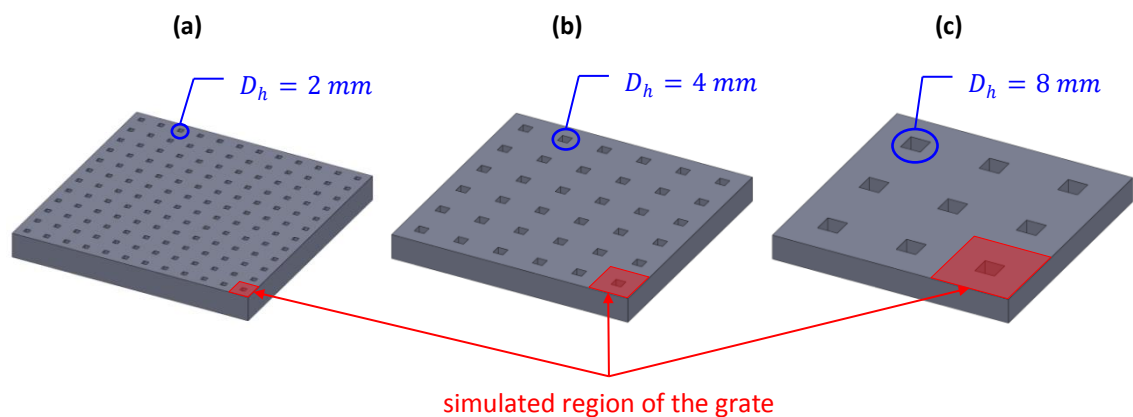


Figure 7.1 Schematic diagram showing a section of a grate with a porosity of 0.06 for three different passages

7.2 Background

Hermansson and Thunman [143] summarised the possible paths to grate degradation, which includes excessive grate temperatures and chemical deterioration. Grate bars are typically comprised of nickel chromium steels that can operate in temperatures of 1175 – 1425 K, a temperature that can be exceeded if the

grate is directly exposed to radiation from the furnace chamber, *i.e.* unless it is covered by a layer of fuel and/or ash. However, significant deterioration of the grate has been reported in operational furnaces despite sufficient coverage of the grate. The reported deterioration is, therefore, most likely caused either by excessive heat transfer from the burning fuel bed or by chemical attack of the grate material.

Sorell [188] outlined the different forms of chemical attack in a high temperature environment. Gaseous corrosion is the most prevalent form of attack, primarily due to oxidation, sulfidation, and chlorination. Of these, chlorination tends to be the most aggressive form of metal corrosion, particularly since biomass fuels typically contain a relatively high concentration of chlorine [189, 190]. Asteman [191] summarised how chlorine corrosion can be retarded by the formation of certain oxides on the surface of the metal, such as chromium oxide.

Non-corrosive chemical attack includes carburisation and nitrification, where carbon and nitrogen, respectively, diffuse into the steel, debasing the metallurgical properties of the material. Similarly to gaseous corrosion, several authors [192-195] have suggested that oxides (chromium oxide in particular), are the main form of protection against carburisation. Owing to the carbon-rich/oxygen-lean, high-temperature environment at the surface of the grate, Hermansson and Thunman [143] hypothesised that carburisation, which begins to occur at temperatures of circa 975 K, could be a primary cause of grate deterioration in furnaces.

Since the formation of oxides on the metal's surface appears to act as a barrier to material degradation [192-195], the oxygen concentration at the grate's surface, which is required to maintain a protective oxide layer, is investigated here with a view to avoiding purely reducing conditions; this is a similar approach to that of Hermansson and Thunman [143].

7.3 Overview

Similarly to the numerical investigations described in Chapters 5 and 6, the computational domain is divided into three zones: a packed fuel bed, a grate, and an air plenum or windbox, as illustrated in *Figure 6.2*. In Chapters 5 and 6, however, the grate is treated as an isotropic, perfectly porous medium; this precludes investigating the effects of the shape of the grate, which can influence grate wear [143]. Since the focus here is on grate wear, the shape of the grate must be incorporated to ascertain its effects. The grate is therefore represented as a solid body in the computational domain. To capture the effects of the grate's shape, it is only necessary to simulate a small section under the assumption of spatial periodicity. The simulated region, in this case a single passage and the surrounding area²⁰, is highlighted in *Figure 7.1* for three different grate shapes. *Figure 7.2* demonstrates how each grate section is integrated into the overall computational domain, which is discretised into 1×1 mm cells²¹.

As described in section 3.4, ignition in moving grate furnaces is believed to occur just above the grate. As a result, a layer of char quickly forms on top of the grate, effectively separating the grate from the fresh fuel. The combustion of the char provides the heat required for the pyrolysis and drying reactions above, and results in a gradually increasing layer of ash next to the grate, as illustrated in *Figure 3.3(a)*. Since the focus here is on grate wear, and therefore on the combustion conditions in the vicinity of the grate surface, it is only necessary to capture the combustion of the char layer just above the grate. Hence, the simulated fuel bed, shown in *Figure 7.2*, is assumed to be comprised purely of char. Furthermore, to isolate the influence of

²⁰ The simulated region can be further divided into quadrants by assuming planes of symmetry (xy and zy) through the centre of the passage. However, owing to the slightly asymmetric nature of the mesh deformation, *i.e.* each cell moves its front upper right node in 3D, this assumption is not exercised to avoid potential discrepancies.

²¹ To improve the resolution near the grate, the grid size is reduced from the 2 mm used throughout the rest of this study, see section 4.1.

the grate's shape, the initial porosity of the fuel bed is assumed to be uniform throughout.

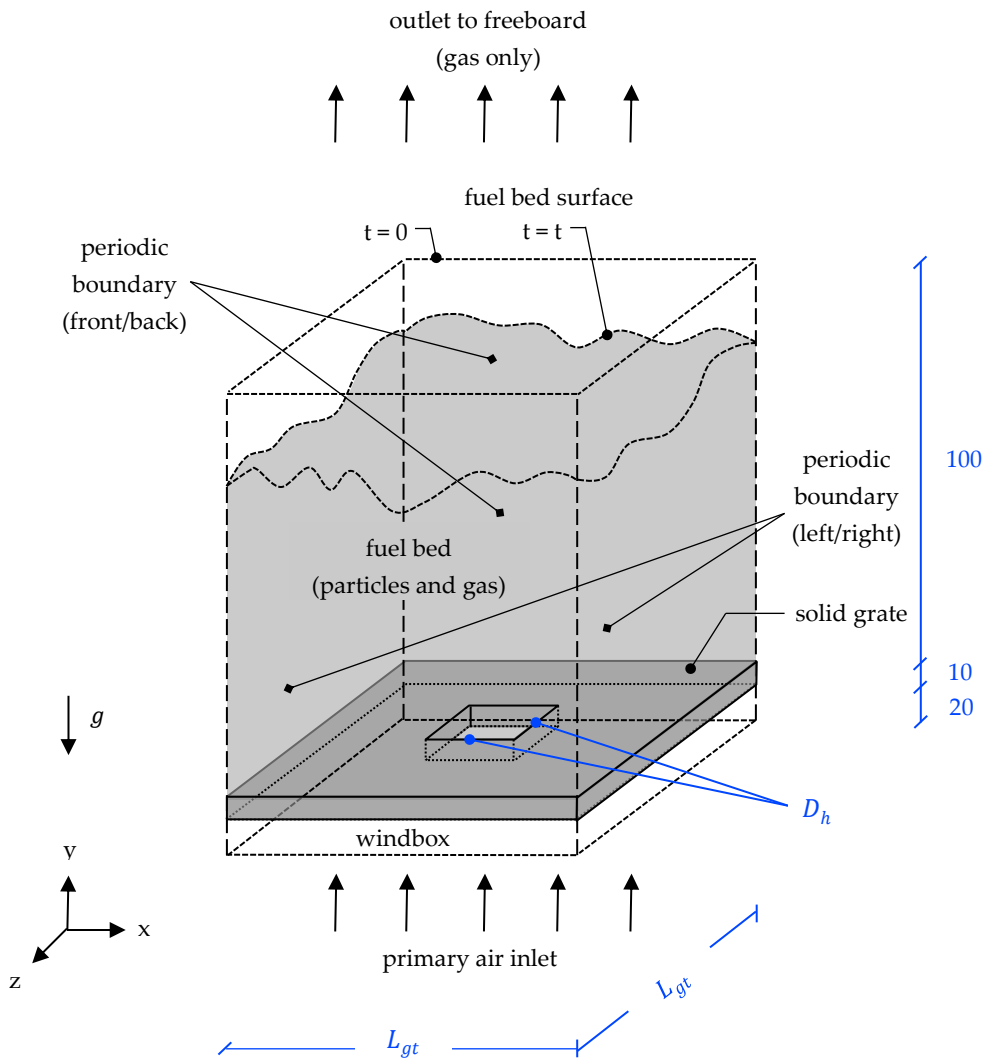


Figure 7.2 Simulated 3D computational domain with a solid grate section

7.4 Parameters Investigated

The key factors in grate deterioration appear to be excessive temperatures and corrosion, with the latter linked to a low oxygen concentration at the surface of the grate, as described in section 7.2. The 2D numerical work of Hermansson and Thunman [143] indicated the importance of the inlet flux and the shape of the grate (the size and spacing of the passages) on the grate temperature and local oxygen concentration. However, a 2D model cannot represent 3D features, such as grate

holes²², which are typically found in operational furnaces. To this end, three different passage sizes, D_h , will each be tested for three different grate porosities, ε_{grate} . The passages are approximated as square, with hydraulic diameter D_h . The porosity of the grate, and overall size of the simulated region, is determined by the distance between each passage, L_{gt} , as demonstrated in *Figure 7.3*.

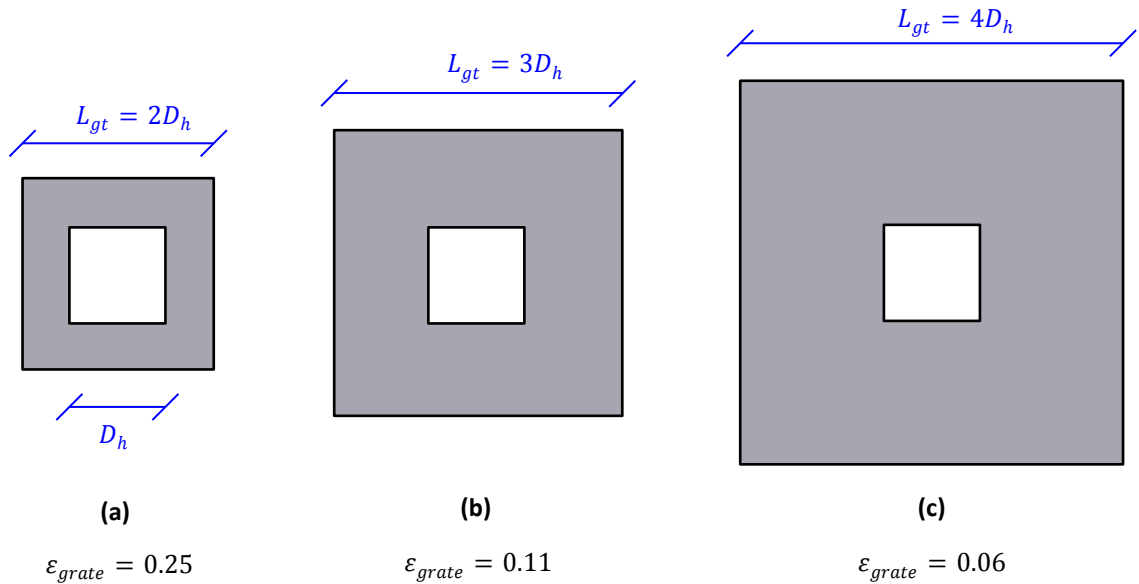


Figure 7.3 Illustrating the variation in grate porosity for a passage with dimensions equal to D_h , where $D_h = 2, 4, \text{ or } 8 \text{ mm}$.

Similarly to the work of Hermansson and Thunman [143], the passages are taken to have hydraulic diameters, D_h , of 2, 4, and 8 mm. To aid visualisation, Figure 7.4 portrays the three differently sized passages investigated, which are overlaid for the same overall grate porosity; this depicts the relationship between the size of the passage, the distance between each passage, and the grate porosity.

²² Although a 2D axi-symmetric model could represent the grate hole itself, it could not capture the corners of the surrounding area.

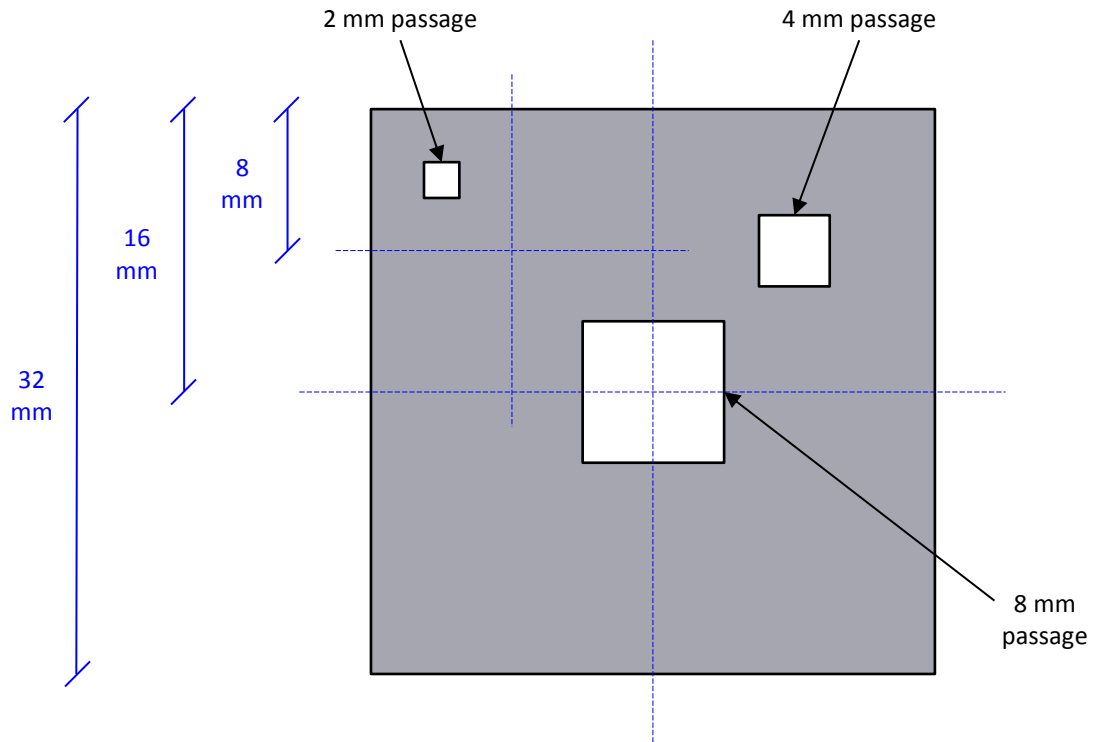


Figure 7.4 Demonstrating how three differently sized passages lead to a grate with the same porosity, in this case $\varepsilon_{grate} = 0.06$.

Each grate design is also examined for three different inlet fluxes. Finally, the thickness of the ash layer on the surface of the grate is expected to have a significant impact on the dispersion of oxygen across the surface of the grate. While the model accounts for the increase in the ash layer as combustion proceeds, it is quite probable that in a continuously operating furnace, a thin layer of ash is always present on the grate. All of the aforementioned cases are therefore tested for two scenarios: no initial ash layer, $h_{A,0} = 0 \text{ mm}$, and an initial ash layer with thickness, $h_{A,0} = 2 \text{ mm}$. This results in a total of 54 cases, which are outlined in **Table 7.1**.

Table 7.1 Parameter combinations investigated for channelling

Case	D_h (mm)	ε (-)	l_0 (mm)	inlet flux (kg/m^2s)	$h_{A,0}$ (mm)
1 a/b/c i/ii	2	0.25	4	0.05/0.125/0.2	0/2
2 a/b/c i/ii	2	0.11	6	0.05/0.125/0.2	0/2
3 a/b/c i/ii	2	0.06	8	0.05/0.125/0.2	0/2
4 a/b/c i/ii	4	0.25	8	0.05/0.125/0.2	0/2
5 a/b/c i/ii	4	0.11	12	0.05/0.125/0.2	0/2
6 a/b/c i/ii	4	0.25	16	0.05/0.125/0.2	0/2
7 a/b/c i/ii	8	0.11	16	0.05/0.125/0.2	0/2
8 a/b/c i/ii	8	0.06	24	0.05/0.125/0.2	0/2
9 a/b/c i/ii	8	0.25	32	0.05/0.125/0.2	0/2

The initial conditions, boundary conditions, and material specifications are described in *Table 7.2*.

7.5 Model Description

The model used here is largely unchanged from the model described in detail in Chapter 3. However, some minor changes have been made to improve the match between measurements and predictions of species profiles in a char-only fuel bed. Since the ash content of the fuel is significant, the effect of ash released during conversion is considered. Furthermore, additional heat transfer submodels are required for the grate surfaces. All modifications and extensions to the existing 3D model are described in detail below.

7.5.1 CO_2 gasification

The CO_2 gasification reaction (Eq. (3.43)) is described by means of an intrinsic reaction scheme based on the partial pressure of CO_2 . The overall reaction rate is given by Eq. (3.45) as before; however, $k_{eff,j}$ is replaced by the partial pressure equivalent, Eq. (2.53), with the first order global chemical reaction rate employed in Eq. (2.53), instead described by means of a first order intrinsic reaction rate, Eq.(2.60).

Table 7.2 Initial conditions, boundary conditions, and material specifications

Fuel bed	Char (% w.b.)	92.4	[129]
	Ash (% w.b.)	7.6	[129]
	$\rho_{C,0}$ (kg/m^3)	700	[129]
	$\rho_{A,0}$ (kg/m^3)	1810	[129]
	Ash porosity ε_A (-)	0.65	[129]
	Char porosity ε_C (-)	0.55	[129]
	Char tortuosity τ_C (-)	2	[129]
	Char internal area A_g (m^3/kg)	3.409×10^4	[129]
	Bed porosity, ε_0 (-)	0.42	[129]
	$d_{p,0}$ (mm)	7.6	[129]
	$l_{p,0}$ (mm)	10	[129]
	λ_C ($W/m \cdot K$)	0.1	[185]
	λ_A ($W/m \cdot K$)	1.09	[186]
	$c_{p,C}$ ($J/kg \cdot K$)	2110	[186]
	$c_{p,A}$ ($J/kg \cdot K$)	$754 - 0.586(T_s - 273)$	[186]
	ω_C, ω_{grate} (-)	0.85	[153]
	ρ_{th} (kg/m^3)	1500	[11]
Grate	h_{grate} (mm)	10	
	ρ_{grate} (kg/m^3)	7300	
	λ_{grate} ($W/m \cdot K$)	30	
	$c_{p,grate}$ ($J/kg \cdot K$)	500	
Boundary conditions	Gas inlet	293 (K)	
		21% vol O_2	
		1% vol H_2O	
		10% turbulent intensity	
	Gas outlet	atmospheric pressure	
	backflow: normal to boundary, variables equal to boundary cell		
	Ignition	1000 K to entire bed	
	Grate surface	no slip	
		variable h_{ht}	

7.5.2 Particle properties

7.5.2.1 Geometry

The one-dimensional cylindrical particle model of Thunman *et al.* [150] is employed to describe the geometry of the particle as it shrinks. Particle shrinkage occurs through equidistant regression from all surfaces, as shown in *Figure 7.5*:

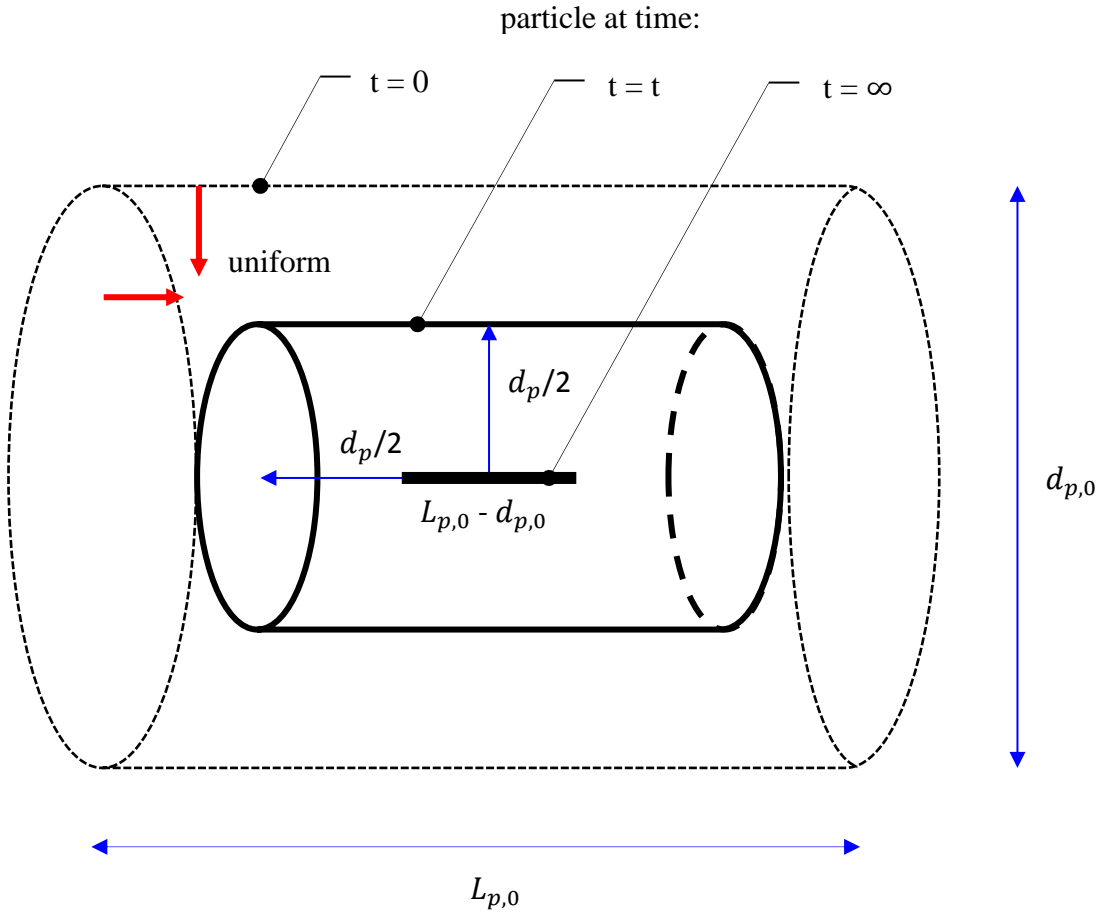


Figure 7.5 Particle shrinkage model

The volume of the particle at any time can then be defined in terms of a single variable, d_p :

$$V_p = \pi \frac{d_p^2}{4} (d_p + L_{p,0} - d_{p,0}) \quad (7.1)$$

If the volume of the particle is known (see section 7.5.2.2), the diameter, and thus length, can be calculated by inverting Eq. (7.1) to obtain:

$$d_p = \frac{2}{3} \left[\left\{ \frac{1}{2}(-2a^3 + 27V^* + W) \right\}^{1/3} + \left\{ \frac{1}{2}(-2a^3 + 27V^* - W) \right\}^{1/3} - a \right] \quad (7.2)$$

$$W = (V^*(729V^* - 108a^3))^{1/2} \quad (7.3)$$

$$a = (L_{p,0} - d_{p,0})/2 \quad (7.4)$$

$$V^* = V_p/2\pi \quad (7.5)$$

$$l_p = d_p + L_{p,0} - d_{p,0} \quad (7.6)$$

The characteristic diameter of the particle, which replaces d_p in all correlations, is given by:

$$d_{p,char} = \left(\frac{3}{2} d_p^2 l_p \right)^{1/3} \quad (7.7)$$

The specific area of the particle, A_{spec} , also follows:

$$A_{spec} = \frac{\pi d_p (d_p/2 + l_p)}{V_p} \quad (7.8)$$

7.5.2.2 Density and shrinkage

Owing to the significant amount of ash in the fuel, its effect on the interphase heat and mass transfer rates must be considered. To this end, the ash released during char conversion is assumed to form a thin layer on the exterior of the particle. Particle shrinkage is therefore based on a reacting core model, where the char core shrinks during conversion, but the ash layer becomes thicker. To determine the thickness of the ash layer, the overall density of the particle is first calculated in terms of its components²³:

$$\rho_{sd} = \left(\frac{Y_C}{\rho_C} + \frac{Y_A}{(1 - \varepsilon_A)\rho_A} \right)^{-1} \quad (7.9)$$

²³ This is contrary to the earlier simulations (Section 3.3.8) that include drying, pyrolysis, and char reactions, where the density of each component is unknown. The particle volume is therefore calculated first by means of Eq. (3.56) or (3.61), and the overall density is then determined based on this value (Eq. (3.62)).

The overall volume of the particle, *i.e.* char core and ash layer, can then be determined by:

$$V_p = V_{p,0} \left(\frac{m_{sd}}{m_{sd,0}} \right) \left(\frac{\rho_{sd,0}}{\rho_{sd}} \right) \quad (7.10)$$

The density of the char core is assumed to remain constant during conversion, a common assumption [91, 97, 104]. The volume of the char core is therefore given by:

$$V_C = V_{p,0} \left(\frac{Y_C m_{sd}}{m_{s,0}} \right) \quad (7.11)$$

Finally, the thickness of the ash layer is calculated in terms of the characteristic diameters of the char core and the overall particle:

$$\delta_A = (d_{p,char} - d_{c,char})/2 \quad (7.12)$$

7.5.3 Heat and mass transfer with ash build-up

The presence of ash affects the diffusion of reactants to the surface of the char and the conduction of heat through the particle. Since the ash is assumed to form a layer around the char core, effective diffusive terms are calculated by considering the char core and ash as layers in series.

By analogy to conductivity in an electrical circuit, the thermal conductivity of the solid, λ_s , in Eq. (3.52) is therefore modified to account for the ash layer as follows:

$$\lambda_s = \frac{d_{p,char}}{2} \left(\frac{d_{c,char}/2}{\varepsilon_C \lambda_g + \sum_k Y_{k,0} \lambda_k} + \frac{\delta_A}{\varepsilon_A \lambda_g + (1 - \varepsilon_A) \lambda_A} \right)^{-1} \quad (7.13)$$

where subscript k refers to both the char and the ash in the initial fuel sample. An effective interphase mass transfer coefficient is determined in a similar manner. The diffusivity of the reactants in the ash layer is given by [146]:

$$D_{A,k} = \varepsilon_A^2 D_{eff,AB,k} \quad (7.14)$$

The mass transfer through the ash layer can then be calculated using [91, 196]:

$$h_{m,A,k} = \frac{D_{eff,A,k}}{\delta_A} \quad (7.15)$$

Finally, the effective mass transfer coefficient is a function of the mass transfer to the particle, $h_{m,k}$ (Eq. (3.30)), and the mass transfer through the ash layer:

$$h_{m,k,eff} = \left(\frac{1}{h_{m,k}} + \frac{1}{h_{m,A,k}} \right)^{-1} \quad (7.16)$$

The effective mass transfer coefficient, $h_{m,k,eff}$, is then applied when calculating the heterogeneous reaction rates, replacing $h_{m,k}$ in Eq. (3.47).

7.5.4 Heat transfer to the grate

The heat transfer between the solid grate and the gas/particle phases is implemented in Fluent by specifying the appropriate heat flux for each grate surface. A coupled wall interface is required to access solver variables, *i.e.* temperature, from both sides of the grate surface (grate and gas/particle phase). An equal, but opposite heat flux must be applied to both interfaces comprising the coupled wall, *i.e.* heat transferred from gas/particle phase is equal to the heat transferred to the grate. The total heat flux may comprise radiation and convection; conduction between the grate and the particle phase is assumed to be negligible²⁴, and radiation from the furnace walls is not considered because it is assumed that the grate is always covered with a layer of fuel and/or ash [12]. The heat transfer mechanisms applied to each surface are illustrated in *Figure 7.6*; although the local heat flux at each face is automatically calculated, the expected direction of heat flow, *i.e.* heating or cooling with respect to the grate, is also indicated.

²⁴ Assuming point contact between the particles and the grate

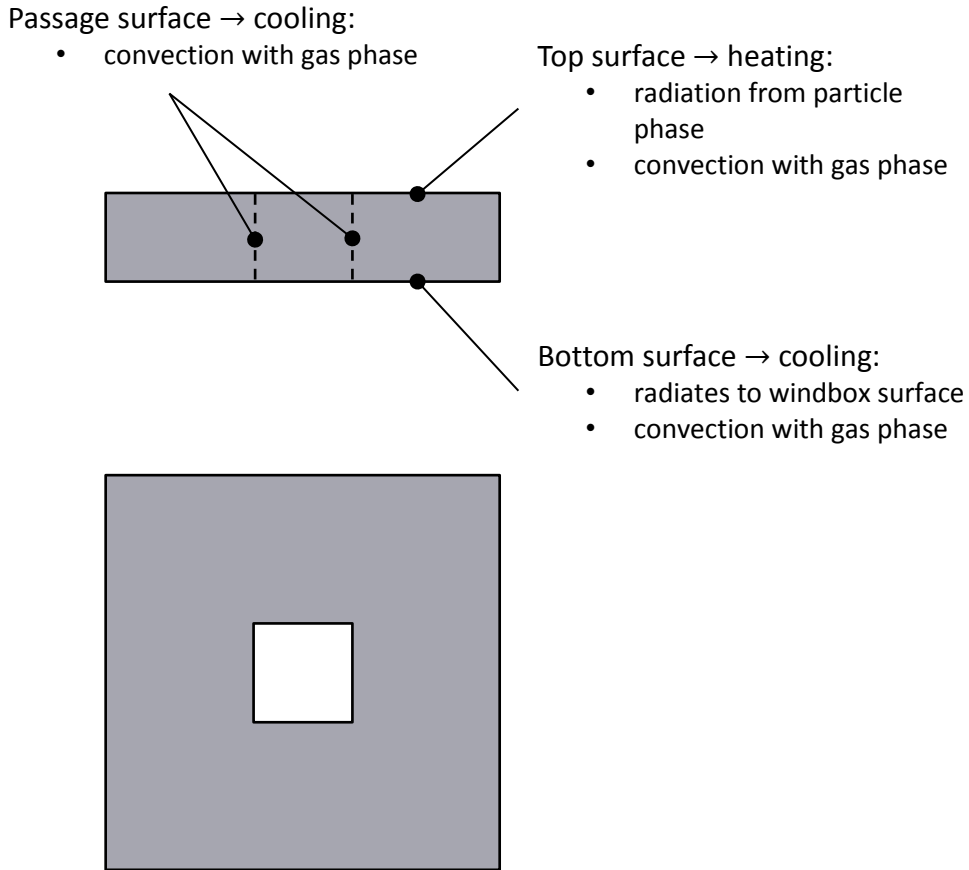


Figure 7.6 Heat transfer mechanisms to the grate surface

Top/bottom surfaces

- Radiation

$$\Delta H_{f,rad} = \sigma_b \omega (T_s^4 - T_{gt}^4) \quad (7.17)$$

where $\Delta H_{f,rad}$ is the radiative flux, σ_b is the Stefan-Boltzmann constant, ω is the emissivity, T_{gt} is the temperature of the grate surface, and T_s refers to either the temperature of the particulate phase at the top surface of the grate, or the temperature of the windbox at the bottom surface of the grate, which is assumed to be equal to the temperature of the inlet air.

- Convection

In the same manner as the convective heat transfer between the gas phase and particulate phase (Eq. (3.24)), the convective flux, $\Delta H_{f,con}$, is described

by means of a Nusselt number correlation for flat plates, taken from Incropera *et al.* [172].

$$\Delta H_{f,con} = h_{ht} (T_g - T_{gt}) \quad (7.18)$$

$$h_{ht} = \frac{\lambda_{g,eff} Nu}{L_{char}} \quad (7.19)$$

$$Nu = 0.332 Pr^{1/3} Re^{0.5} \quad (7.20)$$

where the characteristic length, L_{char} , is approximated as 10 mm for all cases; this is used to calculate both the heat transfer coefficient, h_{ht} , and the Reynolds number, Re . In reality this length varies slightly with the gas flow and the distance between passages without having a significant impact on the results, as a similar approximation was used in [143]. It is worth noting that only the laminar Nu is included here, since the Re here is several orders of magnitude below typical transitional Re for flat plates.

Passages

Radiation from the passage surfaces is neglected for two reasons: firstly, owing to symmetrical conditions, opposite passage surfaces should be at the same temperature; and secondly, the view factor between passage surfaces and external surfaces is considered negligible. Convection is, therefore, the only heat transfer mechanism considered in the grate passages. The corresponding Nusselt number correlations are also taken from Incropera *et al.* [172]:

$$h_{ht} = \frac{\lambda_{g,eff} Nu}{D_h} \quad (7.21)$$

$$Nu = 1.86 \left(\frac{Pr Re D_h}{h_{grate}} \right)^{1/3} \quad Re < 10^4 \quad (7.22)$$

$$Nu = 0.23 Pr^{0.4} Re^{0.8} \quad Re \geq 10^4 \quad (7.23)$$

7.6 Validation

Ryan and Hallett [129] measured species concentrations throughout the depth of a burning bed of char. For comparison, in our computational model the fuel size and composition and all boundary conditions, were set to match their experimental values. For the validation case, the grate was modelled as a perfectly porous medium with a porosity of 0.5, which approximates the experimental setup (3 mm bars spaced 3.3 mm apart). To reduce the necessary simulated time, the entire fuel bed was initially set to 1000 K. It is worth noting that this cannot be done if drying and/or pyrolysis are being modelled since these are driven by heat alone; in the char only case, where conversion is limited by the oxygen concentration, the effect on the final species and temperature profiles is negligible. Furthermore, owing to the significant amount of ash present at the time the measurements were taken, an initial 16 mm ash layer at the bottom of the fuel bed was also included to reduce the simulated time required; this layer grows thicker as the simulation proceeds. Similarly to section 4.3, a snapshot of species profiles is required to compare our transient, shrinking bed model, to the constant height, effectively steady-state measurements of Ryan and Hallett [129]. The simulation was therefore allowed to develop until the thickness layer of ash at the bottom of the fuel bed matched the experiment, indicated by the drop-off in O_2 in *Figure 7.7*; this occurred after 900 s at which point the predicted species profiles along a vertical traverse were plotted. The comparison of predictions with measurements is illustrated in *Figure 7.7*.

The predicted mass fractions of all species match the data well. Slight discrepancies between the measured and the predicted CO and CO_2 profiles are due to the CO_2 gasification reaction; however, peak concentrations, and the overall trend are a close match. The predicted and measured temperatures do not match as closely as the species profiles. The model predicts maximum temperatures of $T_s = 1300 K$, and $T_g = 1500 K$, which occur in the oxidation zone. This is where maximum temperatures are expected, owing to the highly exothermic homogeneous and heterogeneous oxidation reactions. The measured temperature increased in the

reduction zone, which is identified by the decline in CO_2 due to its consumption in the gasification reaction; this indicates some experimental error since the temperature should not increase because the endothermic CO_2 and H_2O gasification reactions become dominant. Although the model slightly underpredicted the peak temperatures, similar pot furnace experiments [120] have reported maximum temperatures of circa 1550 K. Bearing this in mind, a satisfactory agreement between predictions and measurements is achieved.

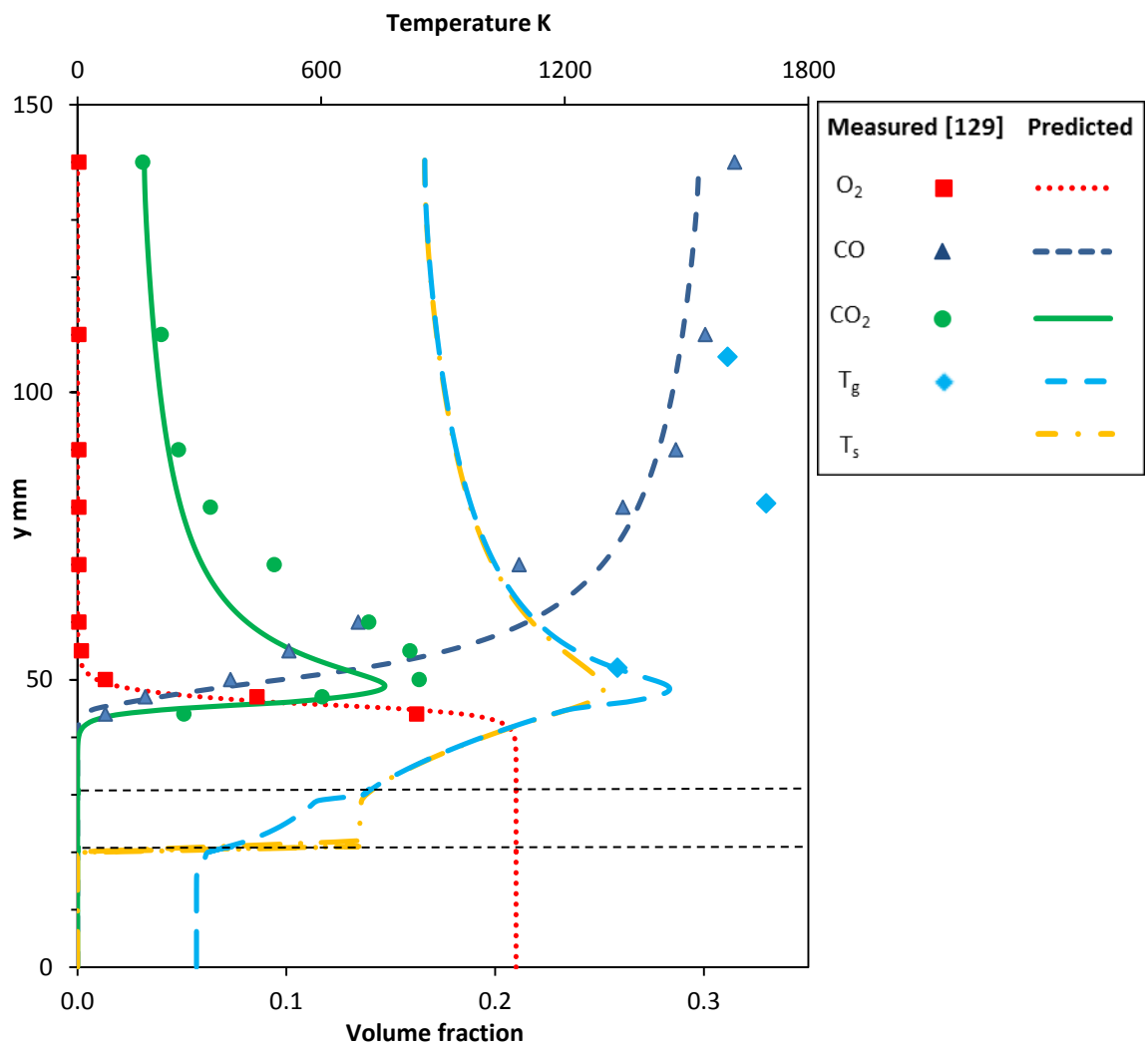


Figure 7.7 Comparison of measured and predicted species profiles through the bed at $t = 900$ s

7.7 Results

All cases were run successfully for a minimum simulated time of 600 s using a timestep of 1 s. The run time varied proportionately with the size of the computational domain. All cases were run on the same HPC system described in Section 6.4, with the largest cases taking between 8 – 10 walltime hours to run. The predicted results for variations of passage size, grate porosity (passage spacing), inlet flux, and initial ash layer are presented in *Figure 7.8 – Figure 7.26*. It is worth noting that each individual result presented here is taken when the grate temperature has peaked in that particular case.

7.7.1 Temperature

The results for the peak grate temperatures are presented separately for the cases containing, respectively, no ash layer and a 2 mm ash layer. The gas speed plotted in all figures hereinafter refers to the maximum gas speed entering the bottom of the fuel bed. It is primarily a function of the porosity of the grate, and increases as the grate porosity decreases ($\epsilon_{grate} = 0.25, 0.11, \text{ and } 0.06$), in accordance with mass conservation; however, other factors, such as heat transfer to the gas in the passage, also have an effect.

7.7.1.1 Bare grate – no ash layer

The effects of changing the hydraulic diameter of the passage, and the overall porosity of the grate, on the maximum temperatures in both the bed and the grate, are shown in *Figure 7.8* for an inlet flux of $0.2 \text{ kg/m}^2\text{s}$; quadratic fits are applied between relevant points for clarity. Peak temperatures of almost 1100 K, which are below the metallurgical limits quoted for most grate steels, are predicted for the larger passages. For the three grate porosities investigated, the peak temperature of the grate decreased with the size of the passage, with a difference of almost 200 K between the 2 mm and the 8 mm passages for the most porous grate (gas speed $\approx 2.5 \text{ m/s}$).

Since the bed temperatures were comparable, or even slightly higher for the smaller passages, this indicates that smaller passages have an increased cooling effect on the grate. This can be explained by considering the relatively cold inlet air ($T_g < T_{gt}$) that flows through the passages, effectively cooling the grate, as illustrated in *Figure 7.6*. The rate of heat transfer from the grate to the gas in the passages is a function of the heat transfer coefficient, h_{ht} , which is, in turn, a function of the hydraulic diameter of the passage. Combining Eq. (3.27) for h_{ht} , and the relevant Nusselt number correlation for laminar flow, Eq. (7.22), reveals that $h_{ht} \propto D_h^{-1/3}$; similarly, $h_{ht} \propto D_h^{-0.2}$ for turbulent flow. In other words, the heat transfer coefficient, thus cooling effect, increases as the passage size decreases, regardless of the flow regime.

The same trend is predicted for inlet fluxes of 0.05 and 0.125 kg/m^2s , shown in *Figure 7.9* and *Figure 7.10* respectively, although the difference between the three differently sized passages becomes less appreciable as the inlet flux, thus overall velocity, is decreased. It is also worth noting that the maximum temperatures both in the fuel bed and in the grate drop off as the air flow rate is reduced, following from *Figure 7.8* to *Figure 7.10*.

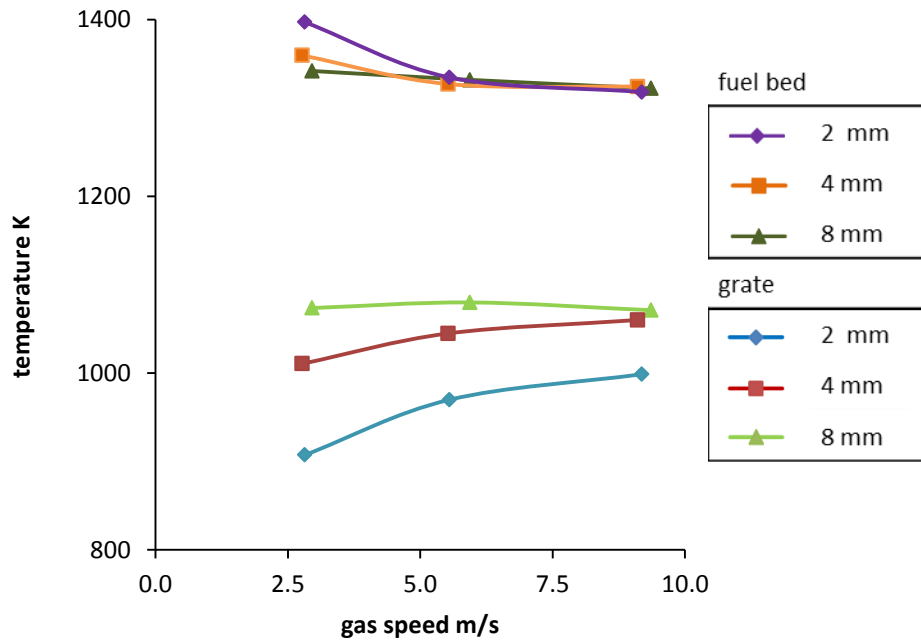


Figure 7.8 Bare grate – no ash layer: maximum temperatures as a function of peak gas speed entering the fuel bed for different passage sizes at an air flux of $0.2 \text{ kg/m}^2 \text{ s}$.

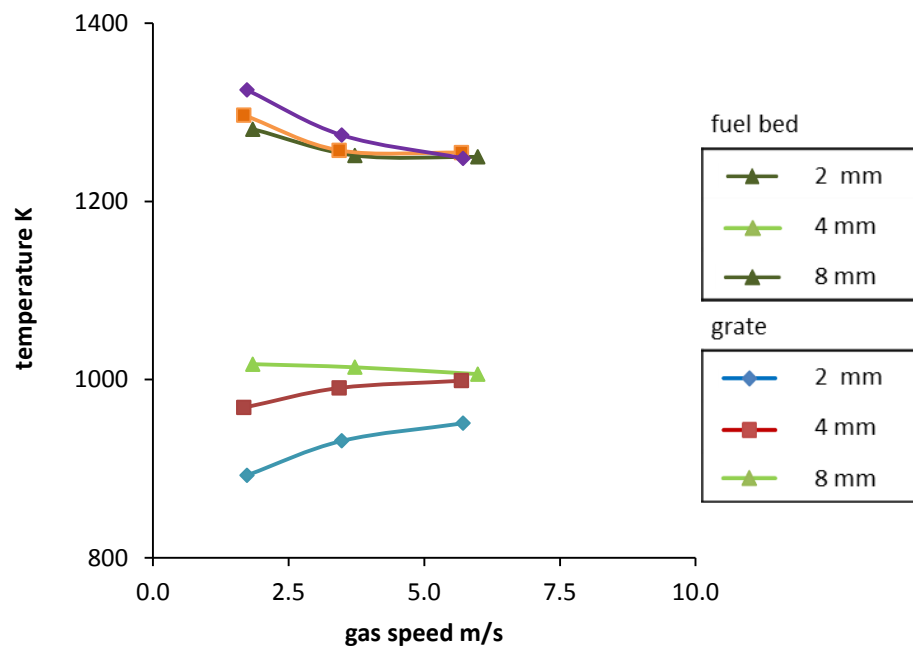


Figure 7.9 Bare grate – no ash layer: maximum temperatures as a function of peak gas speed entering the fuel bed for different passage sizes at an air flux of $0.125 \text{ kg/m}^2 \text{ s}$.

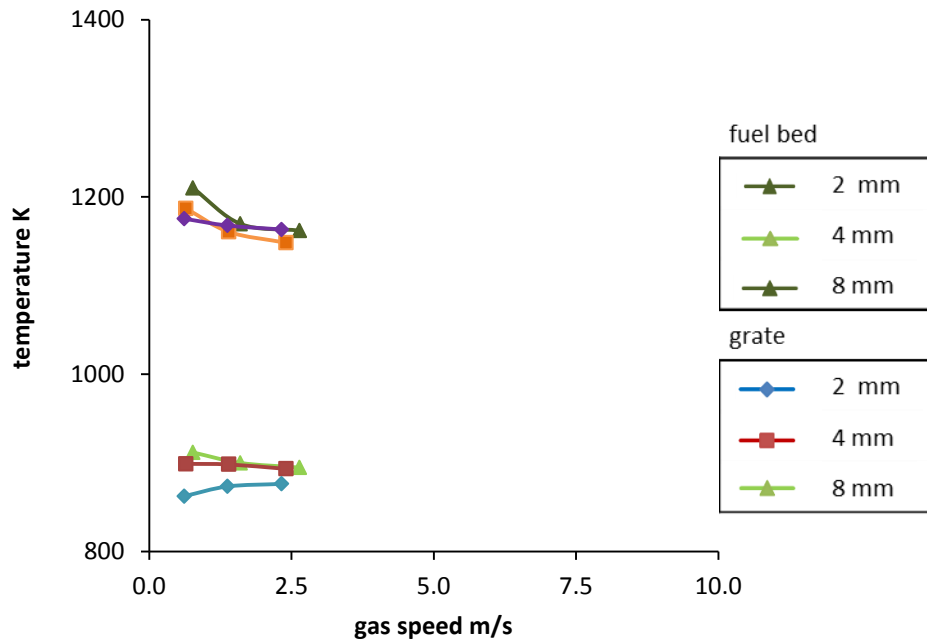


Figure 7.10 Bare grate – no ash layer: maximum temperatures as a function of peak gas speed entering the fuel bed for different passage sizes at an air flux of $0.05 \text{ kg/m}^2 \text{ s}$.

Figure 7.8 also indicates that, for the 2 mm and 4 mm passages, the peak temperature of the grate increases as the gas speed increases, *i.e.* as the porosity of the grate decreases. A previous 2D numerical study [143] implied the opposite, that at a constant air flow rate, higher gas speeds reduced the maximum temperature experienced by the grate. That study also indicated that both higher gas speeds and larger passages reduced the average conversion yield next to the grate. It was proposed that this was the cause of the reduced grate temperatures; that the combustion front effectively became disjointed. However, our model also predicts that the conversion yield next to the grate declines if either the gas speed or the passage size is increased, as illustrated in *Figure 7.11*, *Figure 7.12*, and *Figure 7.13* for inlet fluxes of 0.2, 0.125, and $0.05 \text{ kg/m}^2 \text{ s}$ respectively; note the different y-axis range in *Figure 7.13*. The drop-off in the conversion yield can be explained by considering the distance between passages, which increases as the passage diameter increases (*Figure 7.4*), or as the porosity of the grate decreases (*Figure 7.3*).

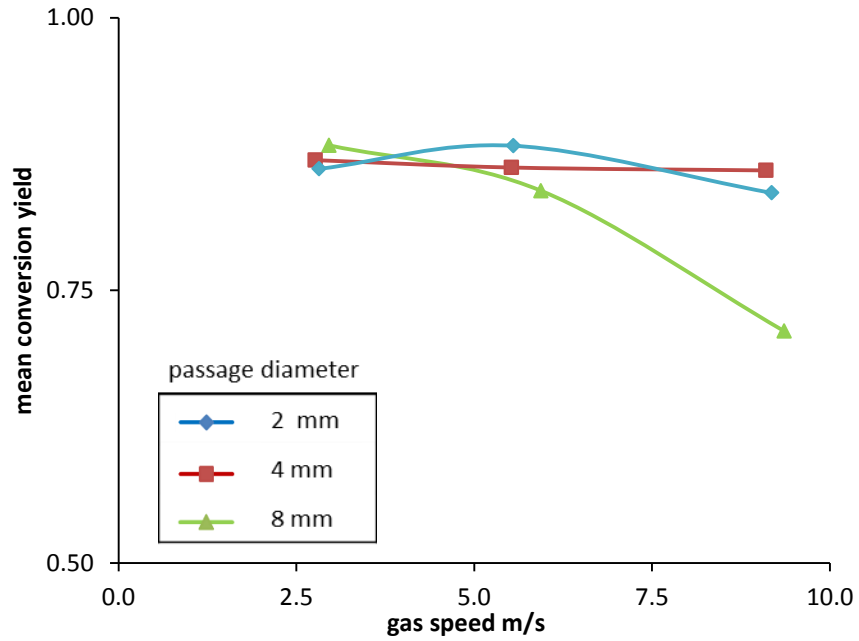


Figure 7.11 Bare grate – no ash layer: mean conversion yield at the surface of the grates as a function of peak gas speed entering the fuel bed for different passage sizes at an inlet flux of $0.2 \text{ kg/m}^2 \text{ s}$.

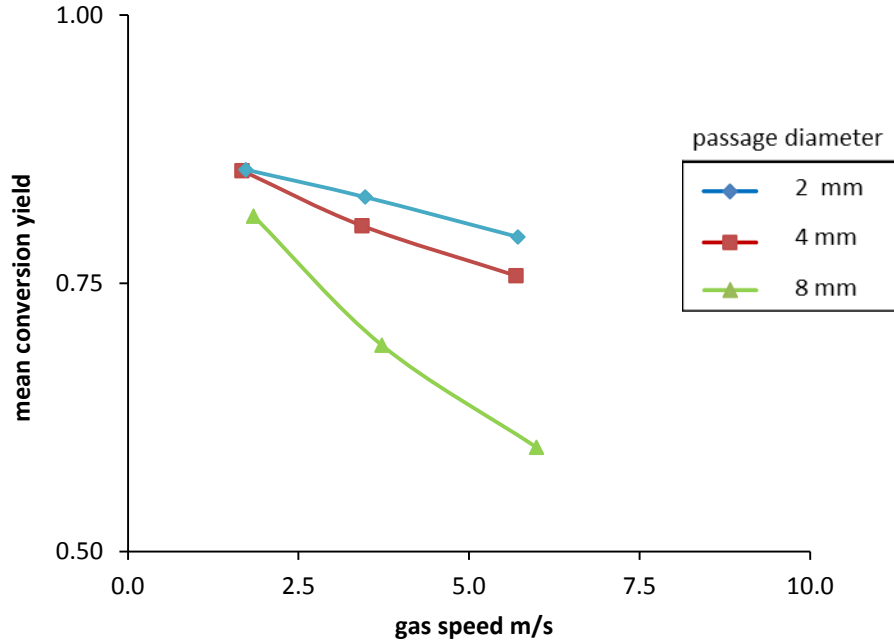


Figure 7.12 Bare grate – no ash layer: mean conversion yield at the surface of the grates as a function of peak gas speed entering the fuel bed for different passage sizes at an inlet flux of $0.125 \text{ kg/m}^2 \text{ s}$.

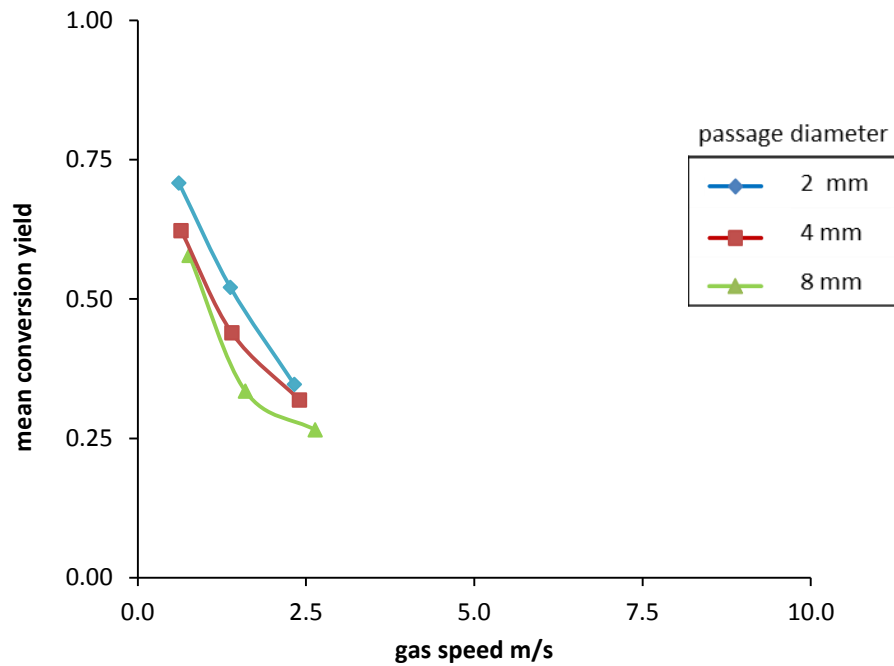


Figure 7.13 Bare grate – no ash layer: mean conversion yield at the surface of the grates as a function of peak gas speed entering the fuel bed for different passage sizes at an inlet flux of $0.05 \text{ kg/m}^2 \text{ s}$.

Since both models predicted similar trends for the conversion yield, yet opposite trends for the grate temperature, the conversion yield is unlikely to be the most influential factor on the grate temperature. The link between greater gas speeds, *i.e.* reduced porosity, and higher grate temperatures is therefore considered here on two fronts: the gas speed, and the grate porosity.

Gas speed

A faster gas flow through the passages results in a higher heat transfer coefficient, since both $\lambda_{g,eff}$ and Nu in Eq. (3.24) are a function of gas speed, thereby increasing grate cooling. However, faster gas flow also increases the mass transfer coefficient, Eq. (3.30), and the gas mixing rate ($EDM: \propto \epsilon/k$) [88], which are typically the limiting rates for, respectively, char combustion and homogeneous combustion, *i.e.* it may increase the combustion rate in the vicinity of the passage exit. Finally, although the local combustion rate increases with gas speed, so too, does the cooling effect on the fuel, and the dispersion of heat.

To summarise, the overall effect of the gas speed on the grate temperature is difficult to quantify due to many conflicting phenomena. Since it is not clear whether the higher gas speed caused the increase in the grate temperature, an alternative rationale is required.

Grate shape

During combustion, heat is transferred to the grate via its upper surface, while heat is transferred from the grate through the bottom surface and the four interior surfaces of the passage. The area of each surface is a function of the grate's shape, as illustrated in *Figure 7.14*. The ratio of the area of the 'heating' surfaces to the area of the 'cooling' surfaces is here considered, since it impacts the net heat flux to the grate, thus the peak grate temperature.

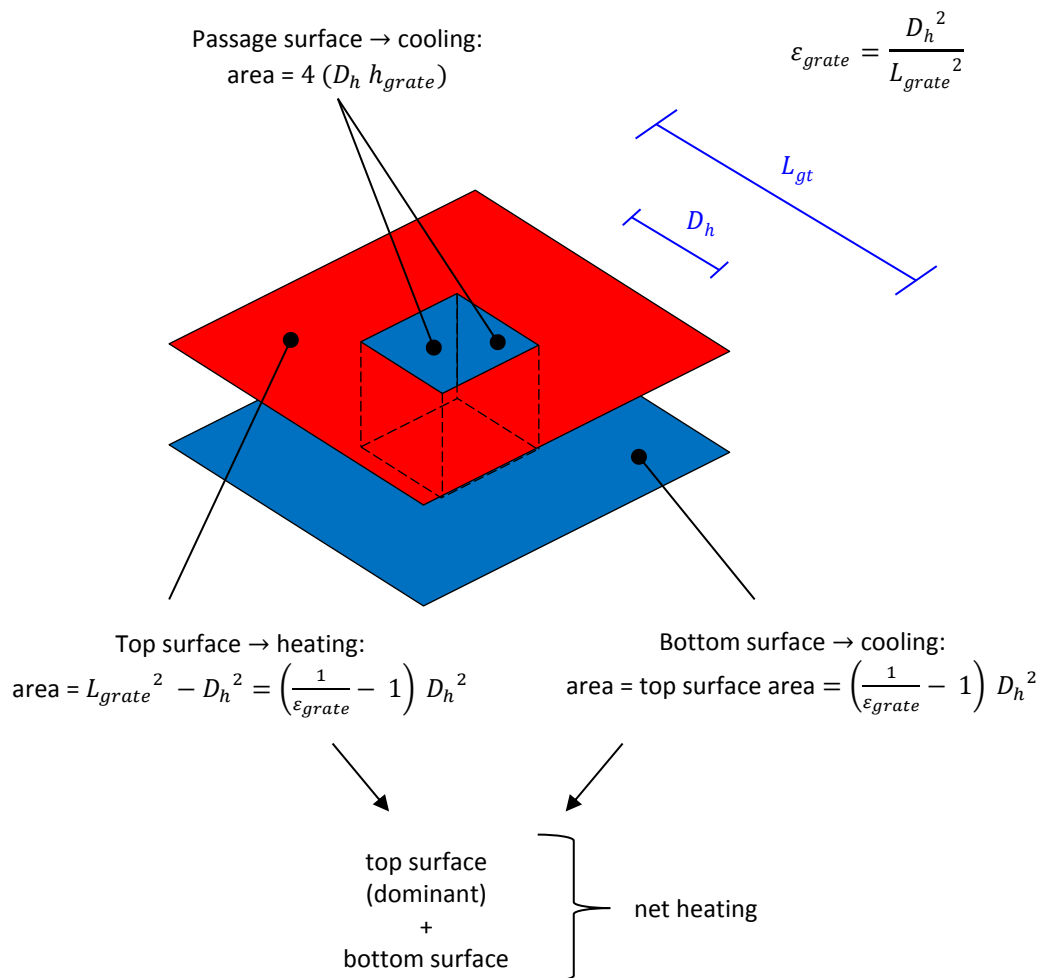


Figure 7.14 'Heating' and 'cooling' surfaces of the grate section

A simple relationship between the heating surfaces and the cooling surfaces can be determined by noting that the top and bottom surfaces have the same area regardless of the grate's shape. Since the top surface is dominant during combustion, *i.e.* the grate gains more heat through the top surface than it loses through the bottom surface, only the net heating effect through the top surface need be considered. A basic relationship between the heating surfaces and the cooling surfaces is therefore given by:

$$\frac{\text{top surface area (heating)}}{\text{passage surface area (cooling)}} = \frac{(\varepsilon_{grate}^{-1} - 1) D_h}{4 h_{grate}} \quad (7.24)$$

Considering the depth of the grate, h_{grate} , as constant, this relationship divulges two things: firstly, for a constant grate porosity, the ratio of the heating surface area to the cooling surface area increases with passage diameter, D_h ; secondly, for a given passage diameter, the ratio of the heating surface area to the cooling surface area will also increase as the grate porosity is reduced. Since the net heat transfer to the grate is affected by this ratio, the maximum temperature of the grate can be expected to increase with this ratio, *i.e.* as D_h becomes larger, or the grate porosity is reduced. This gives an insight into the expected trends, and supports our predictions.

The major trends predicted may be summarised as follows:

- (1) The peak temperature of the grate increases as the passages become larger.
- (2) For the 2 mm and 4 mm passages, the peak temperature of the grate increases as the gas speed increases, *i.e.* the porosity of the grate decreases.
- (3) The effect of the gas speed declines as the passages get larger, becoming inconsequential for the 8 mm passage.

7.7.1.2 Grate covered by 2 mm initial ash layer

The simulations described in section 7.7.1.1 were also carried out with an initial ash layer of 2 mm on the upper surface of the grate. The maximum predicted temperatures in both the bed and the grate are shown in *Figure 7.15*, *Figure 7.16*, and *Figure 7.17* for inlet fluxes of 0.2, 0.125, and 0.05 kg/m^2s , respectively. Similar trends were predicted in all cases, with a negligible difference between the maximum temperatures.

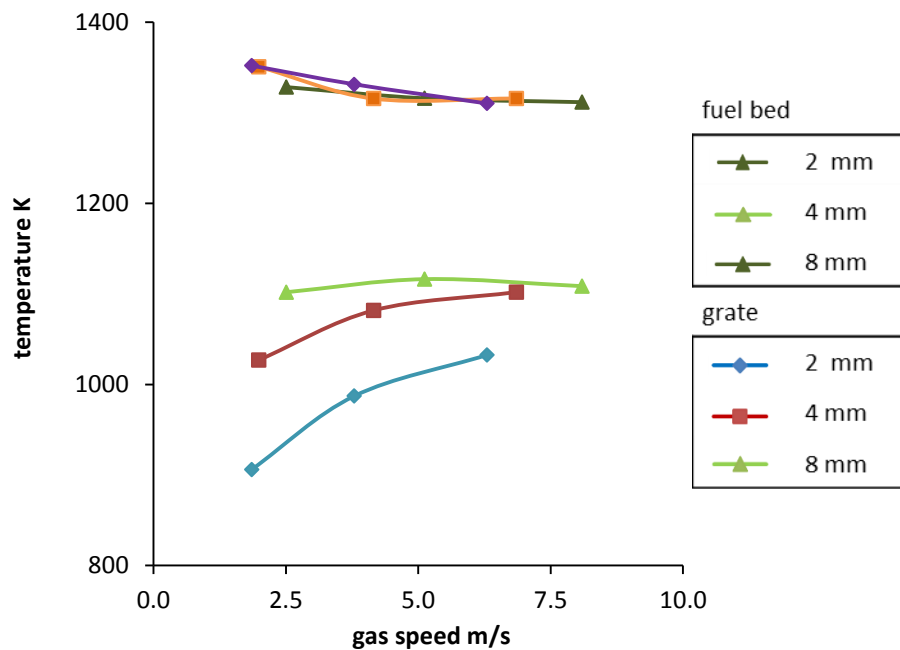


Figure 7.15 Ash covered grate: maximum temperatures as a function of peak gas speed entering the fuel bed for different passage sizes at an air flux of 0.2 $kg/m^2 s$.

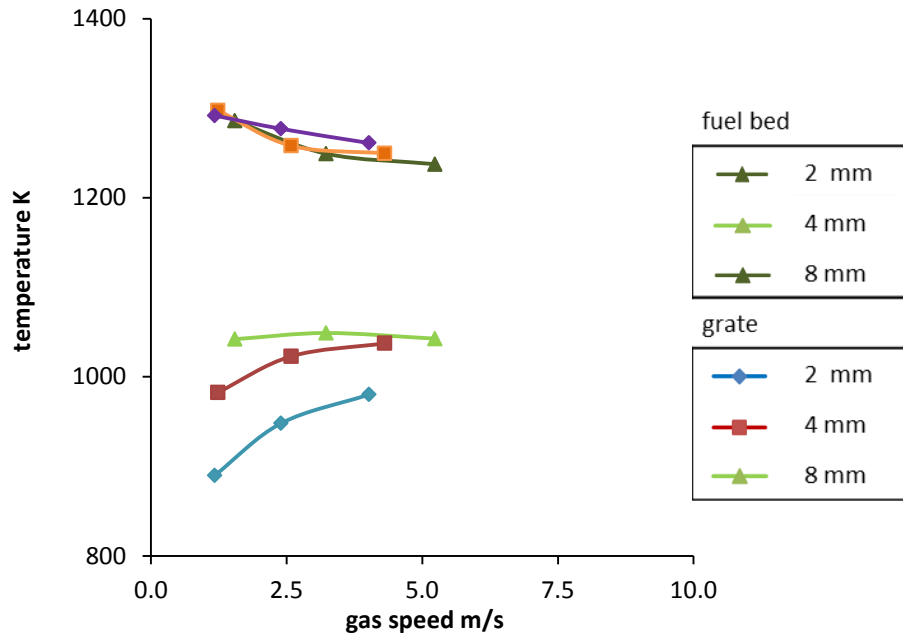


Figure 7.16 Ash covered grate: maximum temperatures as a function of peak gas speed entering the fuel bed for different passage sizes at an air flux of $0.125 \text{ kg/m}^2 \text{ s}$.

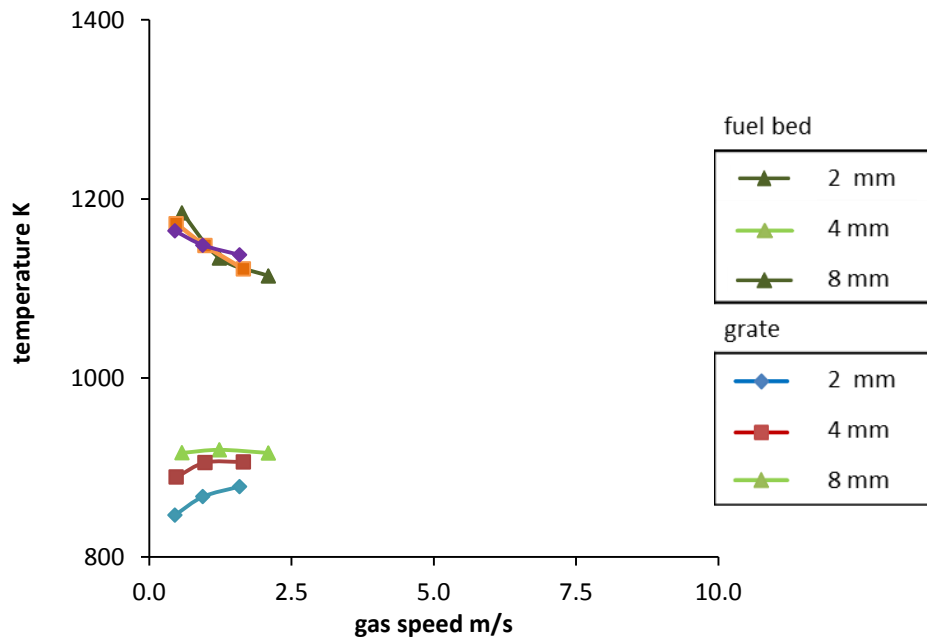


Figure 7.17 Ash covered grate: maximum temperatures as a function of peak gas speed entering the fuel bed for different passage sizes at an air flux of $0.05 \text{ kg/m}^2 \text{ s}$.

Although the presence of the ash layer has a negligible effect on the peak temperatures, its influence on the mean conversion yield along the grate surface is significant, as illustrated in *Figure 7.18*, *Figure 7.19*, and *Figure 7.20* for inlet fluxes of 0.2, 0.125, and 0.05 kg/m^2s , respectively. It is worth noting that the same trend is predicted as the cases without the initial ash layer, namely that the mean conversion yield decreases as the distance between passages increases (see section 7.7.1.1); however, the conversion yield is now substantially higher in all cases. This is due to the influence of the ash layer on the diffusion of oxygen across the surface of the grate. In the absence of any ash, all available oxygen is rapidly consumed in the immediate vicinity of the passage exit. The presence of even a thin layer of ash extends the distance the oxygen can flow across the grate surface before being consumed. This highlights the importance of maintaining a thin layer of ash on the grate throughout operation.

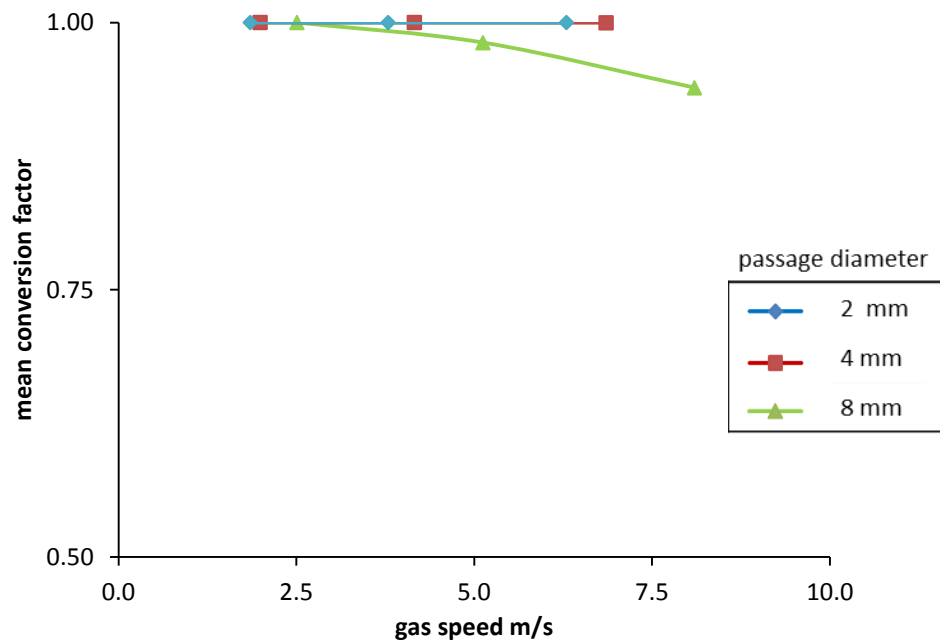


Figure 7.18 Ash covered grate: mean conversion yield at the surface of the grate as a function of peak gas speed entering the fuel bed for different passage sizes at an air flux of 0.2 $kg/m^2 s$.

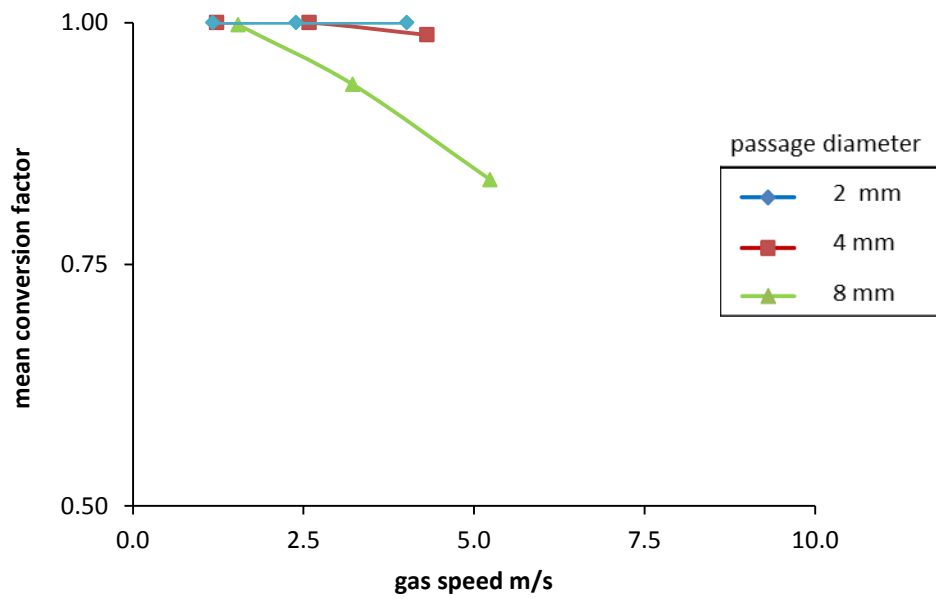


Figure 7.19 Ash covered grate: mean conversion yield at the surface of the grates as a function of peak gas speed entering the fuel bed for different passage sizes at an air flux of $0.125 \text{ kg/m}^2 \text{ s}$.

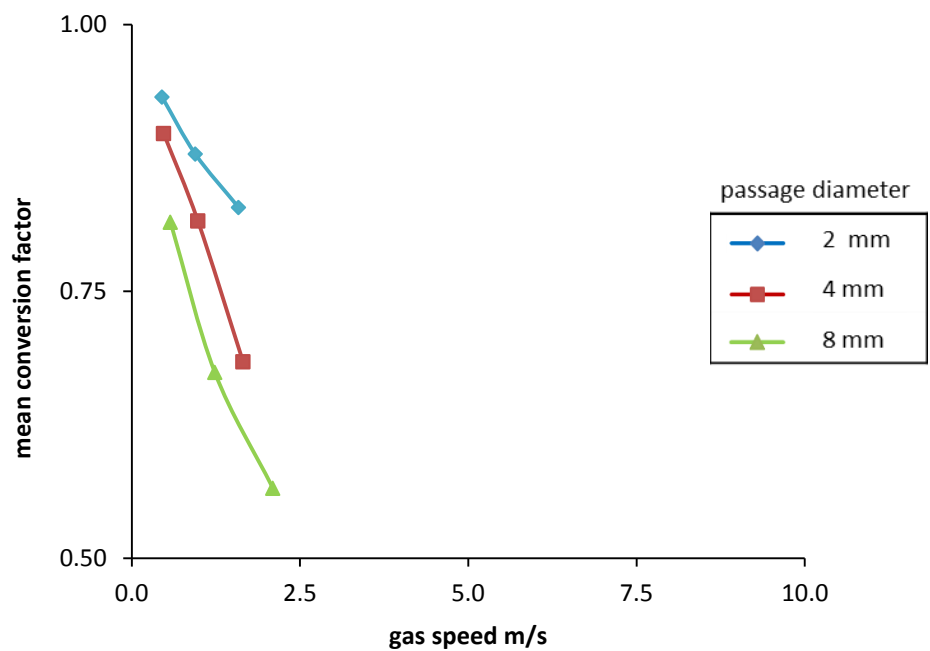


Figure 7.20 Ash covered grate: mean conversion yield at the surface of the grates as a function of peak gas speed entering the fuel bed for different passage sizes at an air flux of $0.05 \text{ kg/m}^2 \text{ s}$.

7.7.2 Carburisation

To examine the potential carburisation of the grate material, the minimum oxygen concentration on the surface of the grate was investigated.

7.7.2.1 Bare grate – no ash layer

The effect of increasing the distance between passages on the minimum volume fraction of oxygen on the surface of the grate is shown in *Figure 7.21* for an inlet flux of $0.2 \text{ kg/m}^2 \text{ s}$. The distance between passages is here presented as the distance between the passage centrelines. *Figure 7.21* clearly depicts the impact of the distance between passages on the oxygen content, which drops off rapidly as the distance is increased. The point of interest is when the volume fraction of oxygen approaches zero, as this may lead to conditions favouring carburisation, see section 7.2. Without an initial ash layer on the grate, this occurs when the distance between the passage centrelines is about 30 mm. The influence of the passage diameter seems minimal, although larger passages do appear to aid the diffusion of oxygen; note the small difference between the 2 mm and 4 mm passages when the distance is 8 mm, and similarly, between the 4 mm and 8 mm passages when the distance is 16 mm.

The air flow rate also has an effect on the minimum concentration of oxygen at the grate surface, as demonstrated in *Figure 7.22* and *Figure 7.23*. Although the oxygen concentration declines as the inlet flux is decreased, the distance at which it approaches zero remains relatively unchanged. This indicates that the inlet flow rate, within the range of the fluxes investigated, has a negligible effect on the propensity of carburisation to occur.

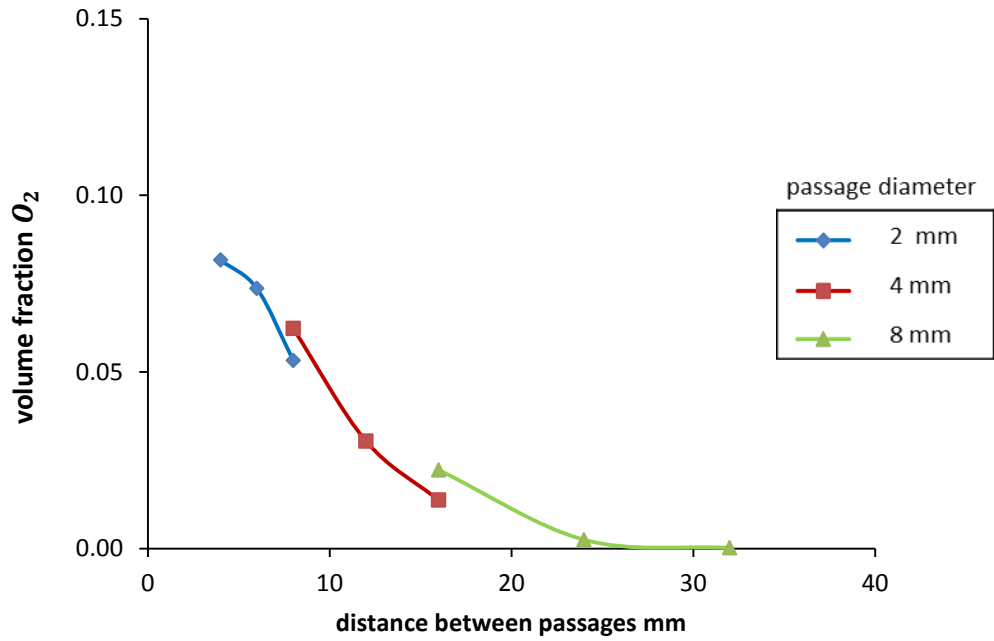


Figure 7.21 Bare grate – no ash layer: minimum oxygen concentration at the surface of the grate for different passage sizes at an inlet flux of $0.2 \text{ kg/m}^2 \text{ s}$.

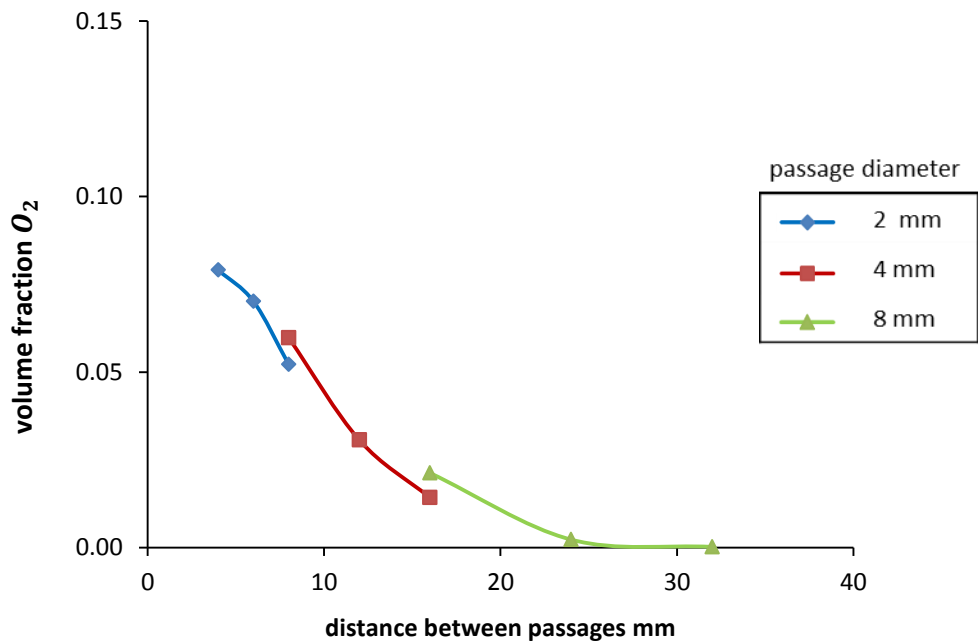


Figure 7.22 Bare grate – no ash layer: minimum oxygen concentration at the surface of the grate for different passage sizes at an inlet flux of $0.125 \text{ kg/m}^2 \text{ s}$.

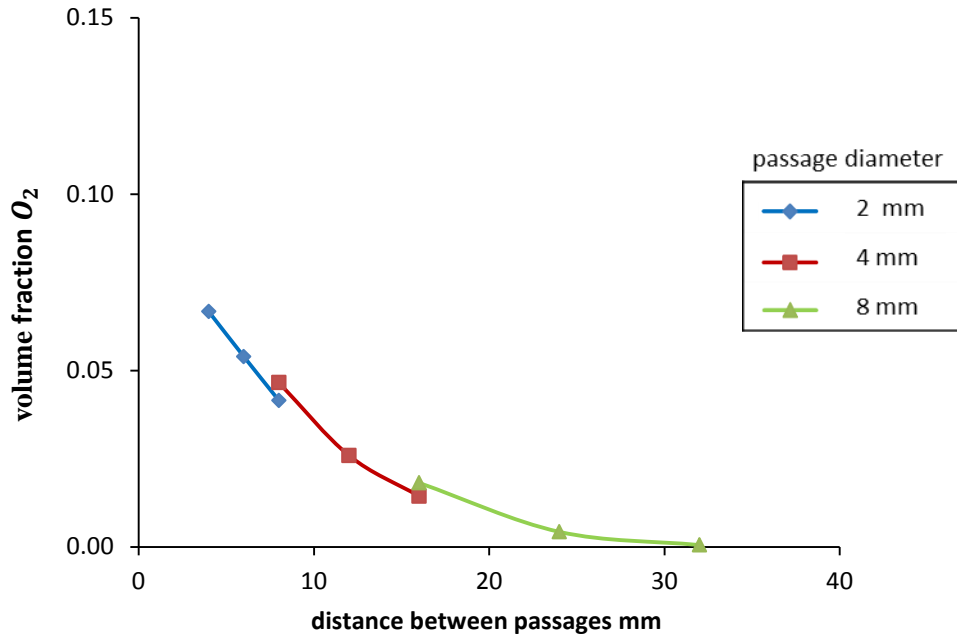


Figure 7.23 Bare grate – no ash layer: minimum oxygen concentration at the surface of the grate for different passage sizes at an inlet flux of $0.05 \text{ kg/m}^2 \text{ s}$.

7.7.2.2 The effects of a thin ash layer

Figure 7.24 shows the minimum volume fraction of oxygen as the distance between passages increases, for an inlet flux of $0.2 \text{ kg/m}^2 \text{ s}$. Comparing the case with a 2 mm ash layer, **Figure 7.24**, with the same case without the ash layer, **Figure 7.21**, the influence of the ash layer is apparent. The inclusion of a 2 mm ash layer significantly increases the minimum concentration of oxygen across the grate surface. In this case, the oxygen content does not drop to zero for any of the distances investigated; however, based on the curve, it appears as if this would occur when the distance between passages is approximately 35 – 40 mm, which is roughly 20 – 30% further than without the ash layer.

The same trend is noted for inlet fluxes of 0.05 and $0.125 \text{ kg/m}^2 \text{ s}$, illustrated in **Figure 7.25** and **Figure 7.26** respectively. This trend is expected since the ash layer enables the oxygen to disperse across the grate surface before being consumed; a similar effect was noted on the mean concentration yield at the grate surface (section 0). The exact effect of an ash layer is difficult to quantify owing to the large number

of factors that influence both the diffusion and consumption of oxygen near the grate, such as: the diameter of the ash particles, the porosity in the ash layer, and the presence of combustible gases. It is also worth noting that in an operational furnace, it is unlikely that a uniform layer of ash is formed. Nonetheless, these results highlight the importance of considering the thickness of the ash layer that forms during furnace operation, since even a thin ash layer has a beneficial influence on the conditions next to the grate.

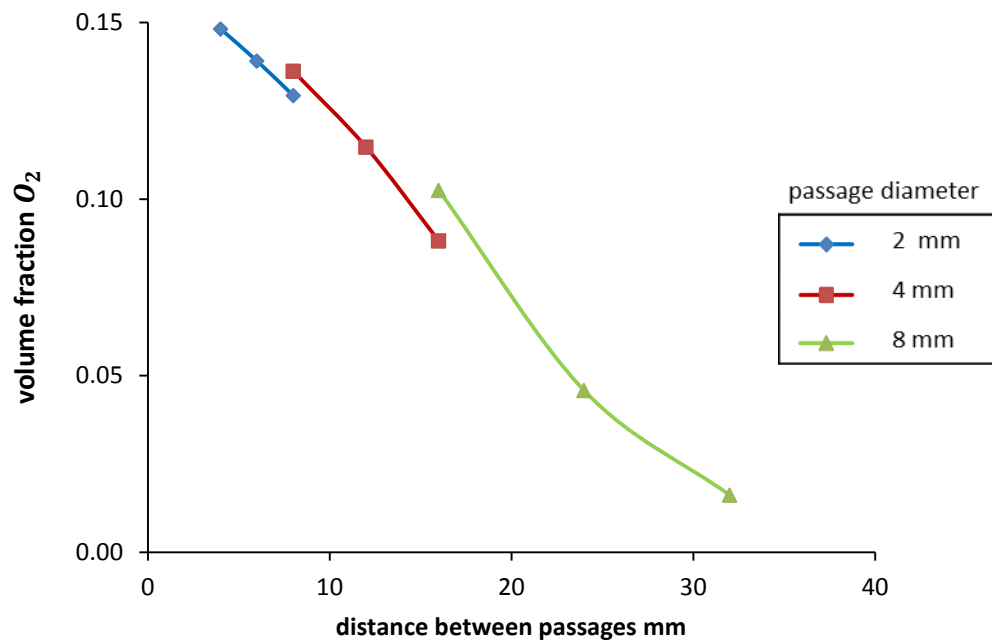


Figure 7.24 Ash covered grate: minimum oxygen concentration at the surface of the grate for different passage sizes at an inlet flux of $0.2 \text{ kg/m}^2 \text{ s}$.

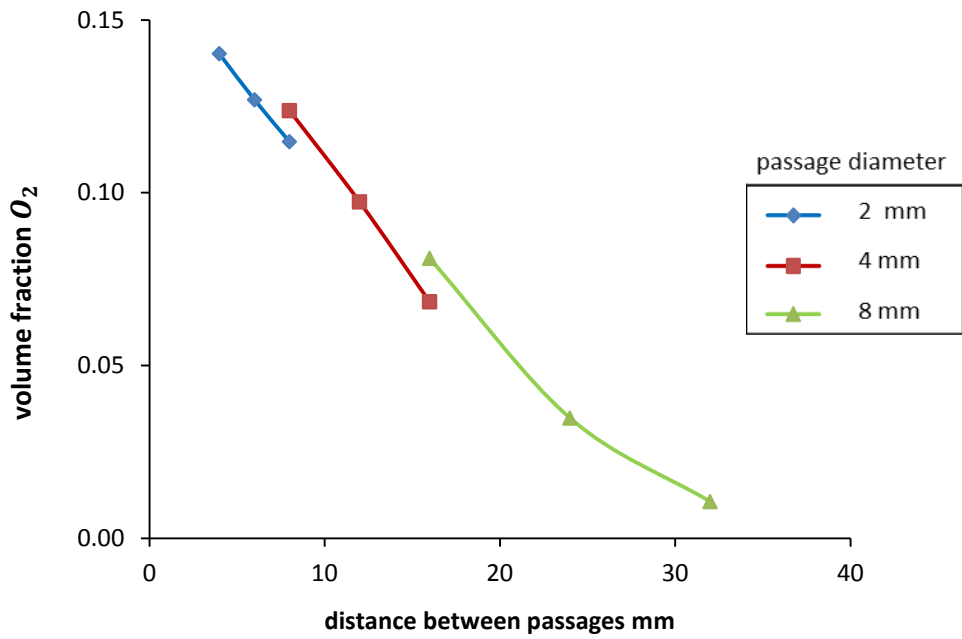


Figure 7.25 Ash covered grate: minimum oxygen concentration at the surface of the grate for different passage sizes at an inlet flux of $0.125 \text{ kg/m}^2 \text{ s}$.

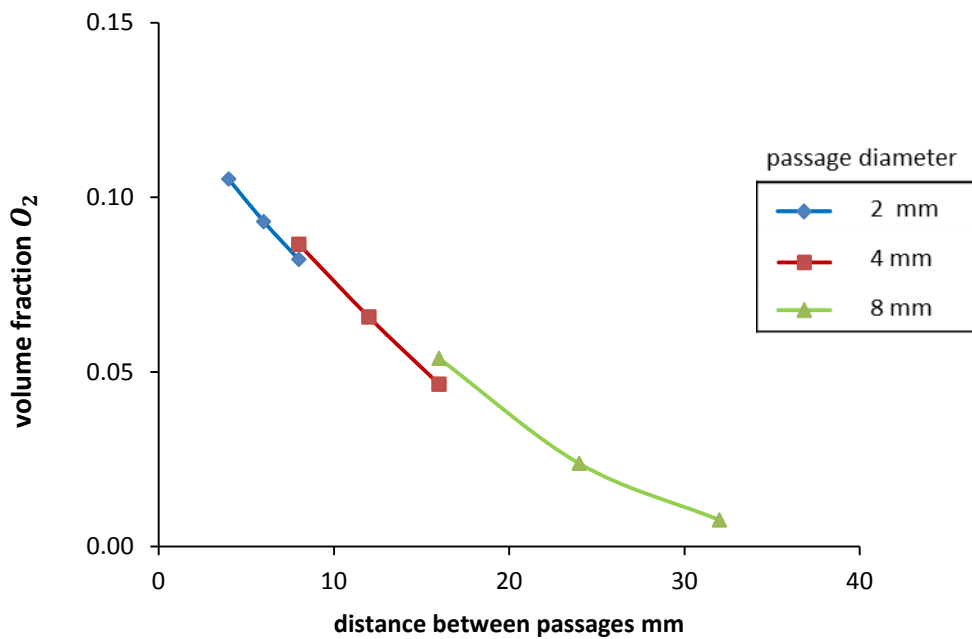


Figure 7.26 Ash covered grate: minimum oxygen concentration at the surface of the grate for different passage sizes at an inlet flux of $0.05 \text{ kg/m}^2 \text{ s}$.

7.8 Discussion

A 3D model was applied to investigate the effect of the shape of the grate and the inlet flow rate on factors that might lead to excessive grate wear; these included the peak temperature of the grate and the minimum oxygen content at the surface of the grate. The investigation was performed on a simplified grate design, consisting of square passages through the grate, in order to isolate the effects of the passage size and the spacing between passages. The inclusion of an initial ash layer, which is typically observed in operational furnaces [143], was also examined to ascertain its effect.

Before discussing the effects of the grate's shape, the reader is first reminded of the results from the 2D and 3D investigations into channelling in fixed beds, Chapters 5 and 6 respectively. These indicated that a high resistance to flow through the grate reduced the channelling effect, thus increasing furnace performance. The grate resistance is of course determined by the shape of the grate, in particular, the size of the passages and the distance between them. Specifically, the resistance to flow is increased by reducing the hydraulic diameter of the passages, and increasing the spacing between them, *i.e.* reducing the overall porosity of the grate.

Predictions indicate that decreasing the size of the passages significantly reduced the peak temperature of the grate for all cases investigated. Since decreasing the passage size also increases the resistance to flow through the grate, smaller passages appear to be beneficial in terms both of furnace performance and also of grate longevity. However, decreasing the size of the passages can lead to ash clogging. The minimum passage size should, therefore, only be limited by the ash clogging propensity for the desired application.

Predictions also imply that increasing the spacing between passages, *i.e.* reducing the grate porosity, raises two potential issues. First, reducing the porosity of the grate increases the peak temperatures experienced by the grate, although this effect declines as the passages become larger. Although the temperatures predicted do

not exceed the metallurgical limits of typical grate steels, the erosion rate of the steel is a factor, as shown by Deuis *et al.* [197] for two nickel chromium steels. The erosion rate exhibited a power law relationship with temperature, and increased sharply at temperatures above 1075 K; this is contrary to the common conception that the wear rate is not significantly affected until the temperature exceeds circa 1275 K. At high flow rates and low grate porosity, the peak grate temperatures predicted in the present study approach the critical temperature noted by Deuis *et al.*

Second, increasing the distance between passages decreases the minimum oxygen content at the surface of the grate. As described in section 7.2, reducing conditions, *i.e.* very low oxygen concentration, at the grate surface can lead to carburisation. Predictions indicated that this occurred when the distance between passages exceeded approximately 30 mm; this value should be considered a worst-case scenario.

These trends agree with observations from operational furnaces [3]. As mentioned, high resistance to flow through the grate improves the performance of the furnace. This has been implemented in operational furnaces either by plugging passages in the existing grate or by installing a redesigned grate, effectively increasing the distance between passages/reducing the porosity of the grate. However, these measures have caused an increase in the wear of the grate; this ties in with our predictions. A trade-off must therefore be made between improving the performance of the furnace and minimising the grate wear. An alternative is to employ more complicated grate designs that can increase the resistance to flow without affecting the size and distribution of the passages at the base of the fuel bed.

Including a thin layer of ash has a significant effect on the distribution of oxygen, since it has more time to diffuse across the surface of the grate before being consumed. In this case, a 2 mm ash layer enabled the spacing between passages to be approximately 20 – 30% greater before the grate experienced reducing, *i.e.*

potentially carburising, conditions, although quantitative comparisons come with a caveat. The ash layer did not, however, have a significant effect on the maximum temperature experienced by the grate. This indicates that if a layer of ash is visible on the grate, then any excessive grate wear is most likely due to high temperatures, rather than due to the carburisation of the steel.

Conduction between the grate and the particulate phase has been neglected here under the assumption of point contact. In reality, some heat conduction will occur between the particles and the grate. As part of future work, a more detailed description of heat conduction, accounting for particle shape and compression, could be included. Although this would result in slightly higher grate temperatures, the same trends are expected.

As described, chlorination of metal surfaces is a major cause of corrosion in biomass furnaces. Since the current model ignores trace elements such as chlorine, it is, therefore, unable to predict the effect of the grate design on chlorination, and also sulfidation. Suggestions for future work include extending the model's capabilities to account for these processes.

The representation of the grate's shape in this study is admittedly fairly simple; a detailed description of a typical grate bar, such as that of Martin and Saltiel [198], could be used in conjunction with our bed model as part of future work.

8. CONCLUSIONS AND RECOMMENDATIONS

8.1 Conclusions Regarding Channelling in Grate Furnaces

8.1.1 2D model developed

To investigate factors that influence channelling in fixed-bed combustion, an unsteady, 2D numerical model capable of predicting biomass combustion under fixed-bed conditions has been designed, developed, and described. This new computational model includes drying, pyrolysis, and heterogeneous char reactions, and incorporates bed shrinkage processes comprised of both continuous shrinkage and abrupt collapses. It is also capable of representing potentially important non-uniformities which may arise throughout a bed, such as irregular packing and non-homogeneous fuel composition.

8.1.2 Model validation

The overall model has been validated by means of two different data sources: one for ignition rates, and a second for species profiles through a biomass fuel bed.

8.1.3 2D investigation of channelling

The validated model was applied to investigate factors affecting channelling in a randomly-packed bed containing a high-porosity passage. The influence of flow resistance through the grate and bed height were compared with previous observations. Additional factors investigated here, which have not formerly been investigated, include flue gas recirculation and initial moisture content of the fuel. The results show that, as expected, increased grate resistance reduces, but does not eradicate, channelling. A higher grate resistance improved the gas distribution because it impeded flow from deviating towards the passage. For deeper beds, however, the effectiveness of grate resistance was diminished because the gas then had more residence time within the bed to track towards the high porosity passage. These predictions tallied with observations from several operational furnaces [5]. Increasing the initial moisture content from 0 to 30 % had a weak influence;

nonetheless, valley growth increased with moisture content, showing a propensity for wetter fuels to amplify channelling. The impact of flue gas recirculation appeared to be insignificant, although its benefits, such as reduced peak temperature, were apparent.

8.1.4 3D model developed

To capture 3D features of a burning fuel bed, the 2D method was extended to three dimensions. This is the first 3D model to examine the channelling phenomena and includes the same detailed shrinkage mechanism as the 2D model.

8.1.5 3D model parallelised

The 3D model was parallelised, enabling simulations to be carried out in parallel across generic high performance computers or clusters.

8.1.6 3D investigation of channelling

The 3D model was applied to reinvestigate the effect of the grate resistance on channelling in a randomly-packed bed containing a high-porosity passage. As expected, and in line with the 2D predictions, results showed that increasing the resistance to flow through the grate reduces channelling. Since similar trends were predicted in both the 2D and the 3D investigations, a 2D analysis appears sufficient to capture trends within an actual randomly-packed bed. However, disparities between the two differently shaped 3D passages, which cannot be differentiated in a 2D approximation, highlighted that a 2D representation of the fuel bed is incapable of capturing the details of a 3D process, such as channelling.

8.2 Conclusions Regarding Grate Design

8.2.1 Size of the grate passages

Predictions indicated that decreasing the size of the grate passages reduced the peak temperature of the grate for all scenarios examined. The minimum passage size

should therefore be limited only by the ash-clogging propensity of the target application.

8.2.2 Grate porosity/spacing between passages

Increasing the spacing between passages, *i.e.* reducing the porosity of the grate, caused the temperature of the grate to increase; however, this effect diminished as the passages became larger. Furthermore, reducing conditions were identified when the distance between the passages exceeded 30 mm, which increases the likelihood of carburisation occurring; the mean conversion yield at the surface of the grate also dropped off as passages were placed further apart.

8.2.3 Inlet air flux

Reducing the inlet air flux caused the peak temperature of the grate to fall in all cases, although there was no discernible effect on the critical distance between passages with respect to reducing conditions.

8.2.4 Ash layer

The presence of a thin ash layer had a beneficial effect; it increased the mean conversion yield next to the grate, and also prevented the onset of reducing conditions for the cases investigated.

8.2.5 Recommendations for grate design

- Smaller passages increase the resistance to flow through the grate, and reduce the peak temperatures experienced by the grate. This measure is expected to improve furnace performance in all scenarios, although ash clogging should be considered.
- Reducing the porosity of the grate increases the resistance to flow through the grate; however, it may lead to an increase in the grate temperature and also potentially carburising conditions. An alternative approach of increasing the grate resistance is recommended.

- A distance of 30 mm or more between passages can lead to reducing conditions at the surface of the grate. Although this reflects a worst-case scenario, it is recommended as a guideline distance.
- A layer of ash should be maintained on the grate at all times.

9. RECOMMENDATIONS FOR FUTURE WORK

9.1 Applying the Current Model

9.1.1 Fully-coupled fuel bed and freeboard simulation

ANSYS Fluent is commonly used to simulate the gas-phase reactions in the freeboard region (see *Figure 1.12*) of a grate furnace, because the submodels required are available within the code as standard. Since our bed model employs Fluent as the compute engine, it can be readily incorporated into a simulation of an entire grate furnace by extending the computational domain to include the region over the fuel bed (*i.e.* the freeboard). In this manner, the fuel bed and freeboard are automatically fully coupled during the solution process.

It is worth noting, however, that the current model cannot simulate the continuous progression of the fuel *along* a moving grate; methods to achieve this will be discussed in section 9.2.2.

9.1.2 Separate fuel bed and freeboard simulation

As an alternative to the fully-coupled fuel bed and freeboard simulation described in section 9.1.1, our bed model can be run separately in order to determine the inlet boundary conditions for a freeboard-only model, as outlined in section 1.6.1.

For a moving grate furnace this approach also avoids the need to simulate the continuous progression of the solid fuel along the grate. Instead, the properties of the gas leaving the fuel bed (composition, velocity, temperature, etc.) are exported at regular intervals throughout the duration of the simulation. These time-dependent results can then be extrapolated to a position on a moving grate by multiplying the simulated time by the horizontal speed of the grate. The gas conditions at the surface of the fuel bed, *i.e.* the inlet boundary conditions for the corresponding freeboard simulation, along the entire length of a grate can therefore be determined. Moreover, if the freeboard is the primary focus and several simulations are required, the computational cost is significantly lower than running

a fully-coupled bed and freeboard simulation each time, since the separate bed model needs only to be run once to acquire the inlet boundary conditions for the freeboard.

The gas composition entering the freeboard can be predicted for many different scenarios by simply altering the setup of the bed simulation, *i.e.* the inlet boundary conditions, or the properties and reaction constants for different fuels.

Furthermore, in an actual furnace the inlet air conditions (mass flux, air preheating, FGR, etc.) may vary along the length of the grate, as illustrated in *Figure 9.1*. These position-dependent inlet conditions in an actual furnace can be represented in our bed model by means of time-dependent boundary conditions for the inlet, which correspond to a position on the actual moving grate.

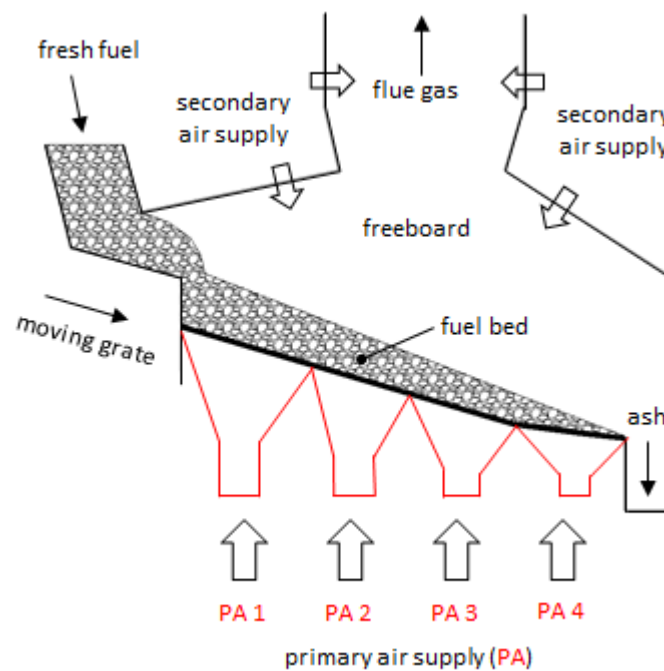


Figure 9.1 Schematic of a fixed-bed furnace showing how the primary air may be varied along the length of the grate

9.1.3 Length of the grate

The length of the grate is an important factor when designing a grate furnace; too short and fuel will not be completely burned before it reaches the end of the grate,

too long and the furnace will be larger and thus more expensive than necessary. Our model can be used to predict the burnout time (*i.e.* the time required to completely combust all fuel) for different furnaces by adjusting the initial bed height, the fuel properties and reaction constants, and the inlet conditions. The burnout time can then be used to calculate the length of the grate required by multiplying it by the expected horizontal speed of the grate. As noted in section 9.1.2, the influence of position-dependent inlet conditions can also be incorporated.

9.1.4 Detailed grate shape

The representation of the grate's shape in this study is admittedly fairly simple; a detailed description of a typical grate bar

9.2 Model Extensions

9.2.1 NO_x emissions

The formation of nitrogen oxides during combustion is a well-known issue. With respect to grate furnaces, measures to reduce NO_x emissions have primarily dealt with optimising the gas-phase reactions in the freeboard above the fuel bed [21]. Our bed model could be extended to predict NO_x formation within the fuel bed itself.

9.2.2 Walking column approach

The present study focused on an isolated region of the overall bed; this region is effectively treated as a batch combustion process. However, the walking column approach, see section 2.2.4, could be applied to the developed bed model to represent the progression of fuel along the grate.

This further development is readily achievable with our existing model since the fuel bed is initially discretised using quadrilateral (2D) or cubic (3D) cells to create columns of cells, a prerequisite for the shrinkage routine. Moreover, a user-defined coordinate system is already in place to identify the relative position of each cell, which can be utilised to find the corresponding cell in the adjacent column for a

walking column approach. The variables stored in each cell (cell height, solid density, temperature, etc.) can then be transferred to the adjacent cell to simulate the progression of fuel along the grate, $cell(x, y) \rightarrow cell(x + 1, y)$ if the grate is moving in the positive x-direction. This particular extension to the existing model would enable the entire fuel bed in a continuously operating grate furnace to be simulated.

9.2.3 Conduction between the fuel particles and the grate

As noted in section 7.8, conduction between the grate and the particulate-phase has been neglected here under the assumption of point contact. A detailed description of heat conduction, accounting for particle shape and compression, would be more representative.

9.2.4 Corrosion

The existing model ignores trace elements such as chlorine, potassium, and sulphur. These elements can have a variety of detrimental effects; for instance, chlorination of metal surfaces is a major cause of corrosion in biomass furnaces. Extending the model's capabilities to account for the presence of elements such as chlorine and sulphur is a prerequisite for including the corresponding corrosion submodels.

9.2.5 Deposition

Deposition on furnace surfaces is predominantly caused by alkali salts such as KCl, which may condense on furnace surfaces, and silica-rich ash particles, which may stick to the surface [133]. Deposition is a widespread issue in biomass furnaces and may significantly reduce the effectiveness of heat transfer surfaces over time [21]. The inclusion of a deposition submodel would enable deposition-prone surfaces to be identified, and mitigating measures to be investigated.

APPENDIX A
PARALLELISATION

Appendix A PARALLELISATION

A.1 Overview

Parallelisation involves running a simulation across multiple computer cores (termed compute nodes by ANSYS). In ANSYS Fluent, this is realised by splitting the computational domain into a number of sections, or partitions. Each partition is then assigned to a corresponding compute node, see *Figure A.1*. All the compute nodes then simultaneously execute the same program on their own partition. Fluent virtually connects these compute nodes by means of a message-passing library, which can send and receive arrays, synchronise the compute nodes, and perform global calculations. This message-passing library can be exercised in UDFs to pass solver variables, *i.e.* face and cell values which would not otherwise be available, from one compute node to another. It is worth noting that the parallelisation method outlined above, *i.e.* partitions and message-passing libraries, is not the only method of parallelisation, but merely that exercised by Fluent.

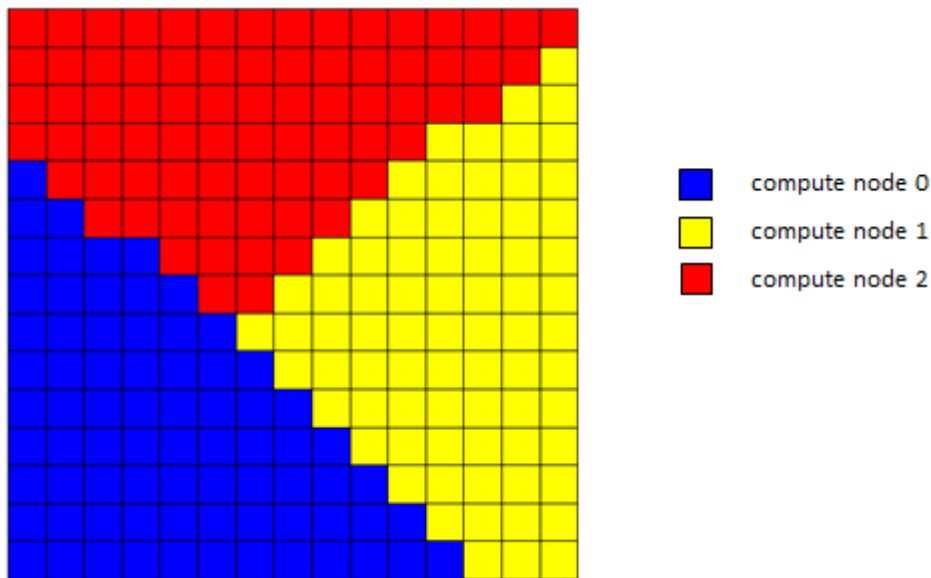


Figure A.1 Mesh partitioned across three compute nodes

A.1.1 Internal and external cells

Fluent uses a single layer of overlapping cells along partition boundaries to provide communication and continuity across the boundaries [199]. The overlapping cells are duplicated on compute nodes that are assigned adjacent partitions. However, a cell can only “belong” to one partition, and is termed an internal cell on the corresponding compute node. The same, *i.e.* duplicated, cell is termed an external cell on any other compute node, as shown in *Figure A.2*. By default, any cell which has a face on the partition boundary is included in this overlapping layer. When performing mesh manipulations, however, it is recommended to extend this overlapping layer to also include any cells which have a node on the partition boundary [199]. This “extended neighbourhood” is shown in *Figure A.3*.

It is worth noting that although the parallel communicator ensures the continuity of solver variables in the overlapping cells, this does not include user-defined memory values. These must be manually maintained to ensure that the values are the same in duplicated cells.

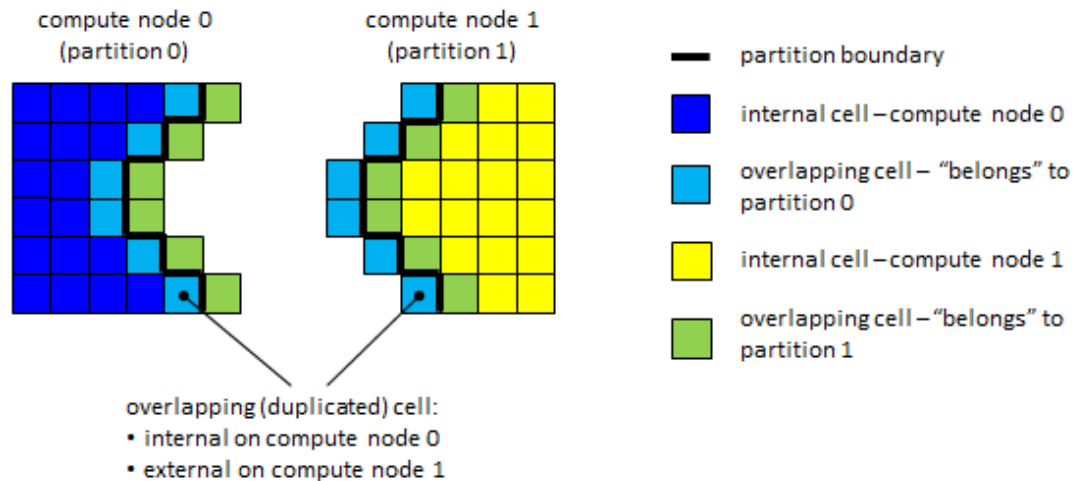


Figure A.2 Partitioned mesh showing cells overlapping on two compute nodes

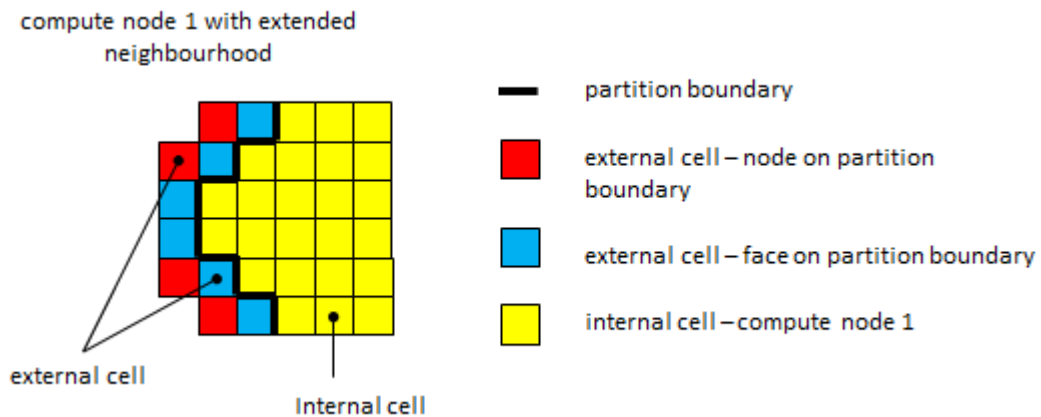


Figure A.3 Mesh partition showing extended external cells

A.1.2 Cell access

The majority of UDFs in our model are either called on a cell-by-cell basis or require macros to loop through all the cells. In parallel runs, special considerations are required to ensure that operations are only performed on the appropriate cells, whether internal, external, or both internal and external (see section A.1.1). To this end, Fluent provides macros to differentiate between internal and external cells, for more information see [199]. Hereinafter, any cell loop, or individual cell operation, refers to both internal and external cells unless otherwise stated.

A.1.3 Generating an array using values from multiple compute nodes

Certain operations in our model are dependent on values from multiple cells, which may be spread across multiple compute nodes. As mentioned in section A.1, a compute node does not have access to cell variables from other compute nodes. These variables can, however, be passed between compute nodes by means of array passing macros in user-defined functions. In some cases, it is necessary to generate an array of values from every internal cell in the domain. The procedure to do this is as follows:

- (1) On each compute node, generate an array that contains the desired variable values for every internal cell in that compute node.

- (2) All compute nodes, bar compute node 0, then send their array to compute node 0.
- (3) Compute node 0 receives the array from every other compute node in turn, and then accumulates each array to generate a complete array that contains the UDM values for every internal cell in the domain.
- (4) Compute node 0 then sends the complete array to every other compute node.
- (5) All compute nodes, bar compute node 0, then receive the complete array from compute node 0.

This approach, illustrated in *Figure A.4*, can be used to generate a complete array containing internal cell values only, external cell values only, or internal and external cell values, as required.

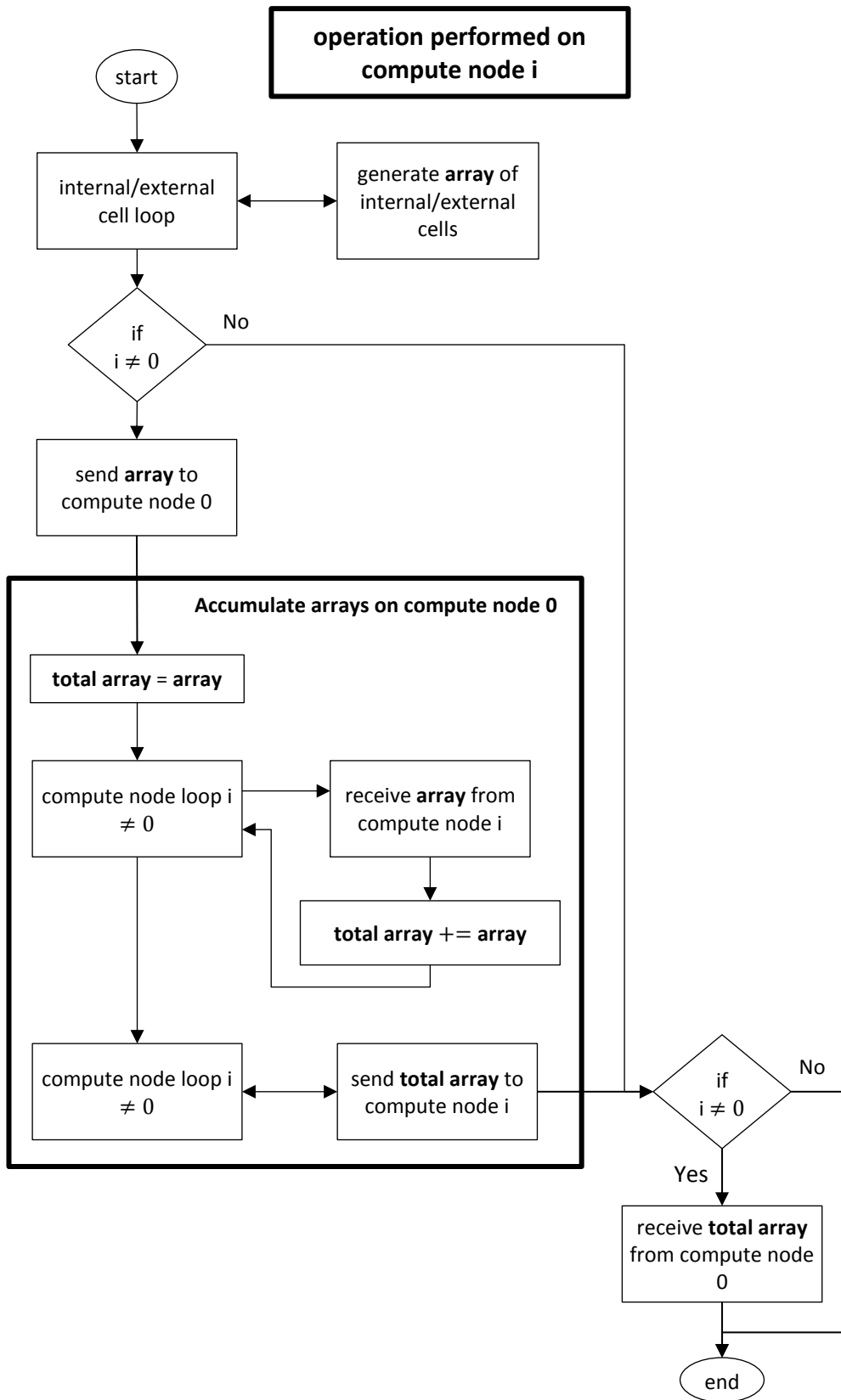


Figure A.4 Creating an array containing values from every cell in the domain

A.2 User-Defined Memory (UDM) Values

In our model, user-defined memory (UDM), which refers to user-controllable cell based memory locations, is used extensively for calculating and storing variables. Therefore, if UDM values in duplicated cells are not identical, a numerical error will result. There are two scenarios in our model where this can arise: initialisation of UDM values, and updating the UDM values during the simulation.

A.2.1 Initialisation

If random non-uniformities are introduced throughout the bed, the random UDM value assigned to an internal cell on one compute node may not match the random UDM value assigned to the corresponding external cell on a different compute node. This is addressed by applying the random function to all internal cells in the compute node. Complete arrays containing the randomly generated value and the corresponding user-defined coordinates (*i.e.* two coordinate arrays in 2D) for every internal cell in the domain are then generated, as described in section A.1.3. It is worth noting that overlapping (duplicated) cells will have the same user-defined coordinates. Therefore, by comparing the coordinates of each external cell with the complete coordinate arrays, the corresponding internal cell can be located, and the “random” UDM value can be matched.

A.2.2 Updating values

If the UDM value in an external cell is not altered in the exact same manner as the UDM value in the corresponding internal cell, then a difference will result. All UDM modifications must not, therefore, be performed on both internal and external cells. It is worth noting that all source terms, property updates, etc., must also be applied to both internal and external cells.

A.3 Mesh Deformation (Bed Shrinkage)

As described in section 3.5, mesh deformation is implemented by moving individual nodes. Recapping the major features of the deformation routine:

- Each cell only controls a single node; it therefore relies on the surrounding cells to move the other nodes.
- Owing to the “sliding” effect, the total displacement of a node is not determined just by the cell which controls it, but also by the combined displacement of all the cells which lie directly beneath.

A.3.1 Issues with parallel mesh deformation

These features pose two challenges to parallelisation. Consider the nodes of $cell(n, m)$ in *Figure A.5*; only internal cells are shown for clarity:

$$\text{Node 1: Total displacement} = f \left\{ \overbrace{cell(n, m)}^{\text{shrinkage}} + \overbrace{cell(n, m-1) + \dots + cell(n, 1)}^{\text{sliding}} \right\}.$$

Node 2: Duplicated on compute nodes A and B. Controlled by $cell(n, m-1)$ which is an internal cell on (*i.e.* “belongs to”) compute node B, and an external cell on compute node A.

Node 3: Similar to node 2, but controlled by $cell(n-1, m)$.

Node 4: Similar to node 2, but controlled by $cell(n-1, m-1)$.

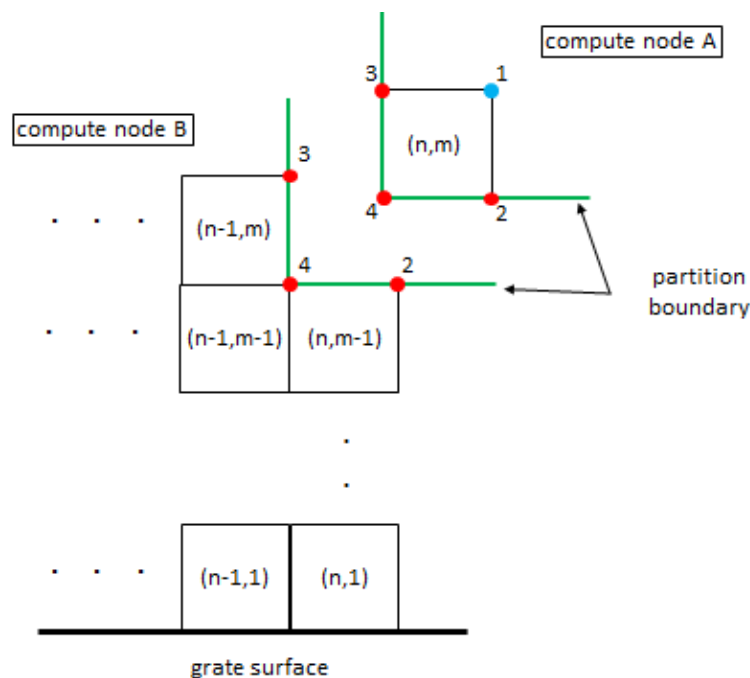


Figure A.5 Cell/node links in a partitioned mesh

In serial runs, the “sliding” effect is implemented by searching for all cells directly above the shrinking cell, each of which are then moved, in turn, by the same amount as the shrinking cell; see section 3.5.3.2 and *Figure 3.10*. This may not be possible in parallel, since a compute node cannot access, *i.e.* perform mesh manipulations on, any cell in a different compute node.

An alternative strategy to account for “sliding” is to calculate the total displacement of each cell; this includes the shrinkage of the cell itself, plus the combined shrinkage of all the cells directly below. The total displacement can, therefore, be implemented using a single manipulation per cell, thus access to other compute nodes is not necessary. However, if any of the cells directly below lie in a different compute node, their shrinkage information must be passed between the compute nodes, or the node does not “slide” by the full amount, see node 1 in *Figure A.6*.

The duplicated nodes (2, 3, and 4 in *Figure A.5*) must be moved by the same amount on each compute node, compute nodes A and B in this case. However, because the deformation routine is only applied to internal cells²⁵, duplicated nodes are only moved on the compute node to which their default “controlling” cell belongs. This eventually causes the duplicated nodes to separate, resulting in mesh failure, as illustrated in *Figure A.6*, with node 3 highlighted for clarity.

²⁵ The mesh deformation routine was initially run on both internal and external cells in an attempt to ensure that duplicated nodes were moved by the same amount on each compute node. However, for reasons unknown, performing mesh manipulations on external cells caused unpredictable results, and was therefore ruled out as a possible solution.

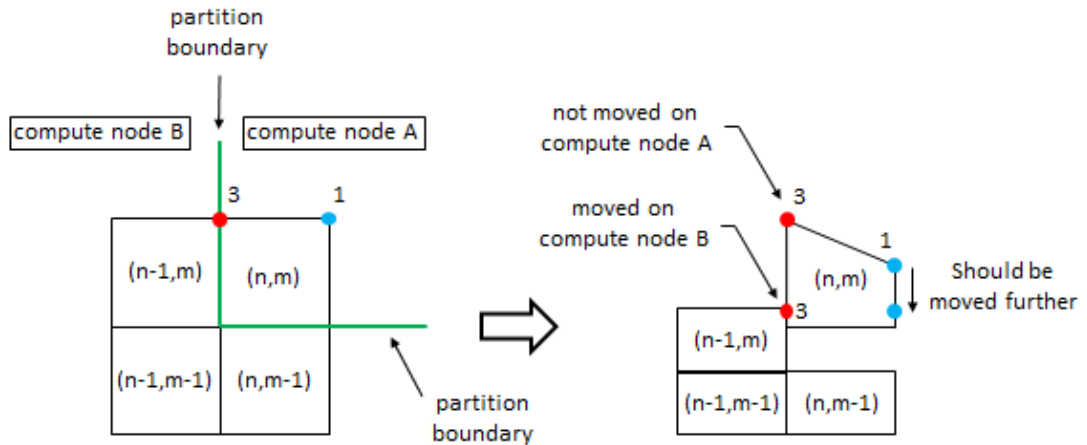


Figure A.6 Mesh deformation without parallel considerations

A.3.2 Solution overview

To determine the total displacement of each internal cell on a compute node, complete arrays containing the shrinkage and the corresponding user-defined coordinates of every internal cell in the domain are generated, as described in section A.1.3. The total displacement of every cell, which includes the shrinkage of the cell itself and the combined shrinkage of every cell beneath (*i.e.* sliding distance), is then calculated as shown in *Figure A.7*.

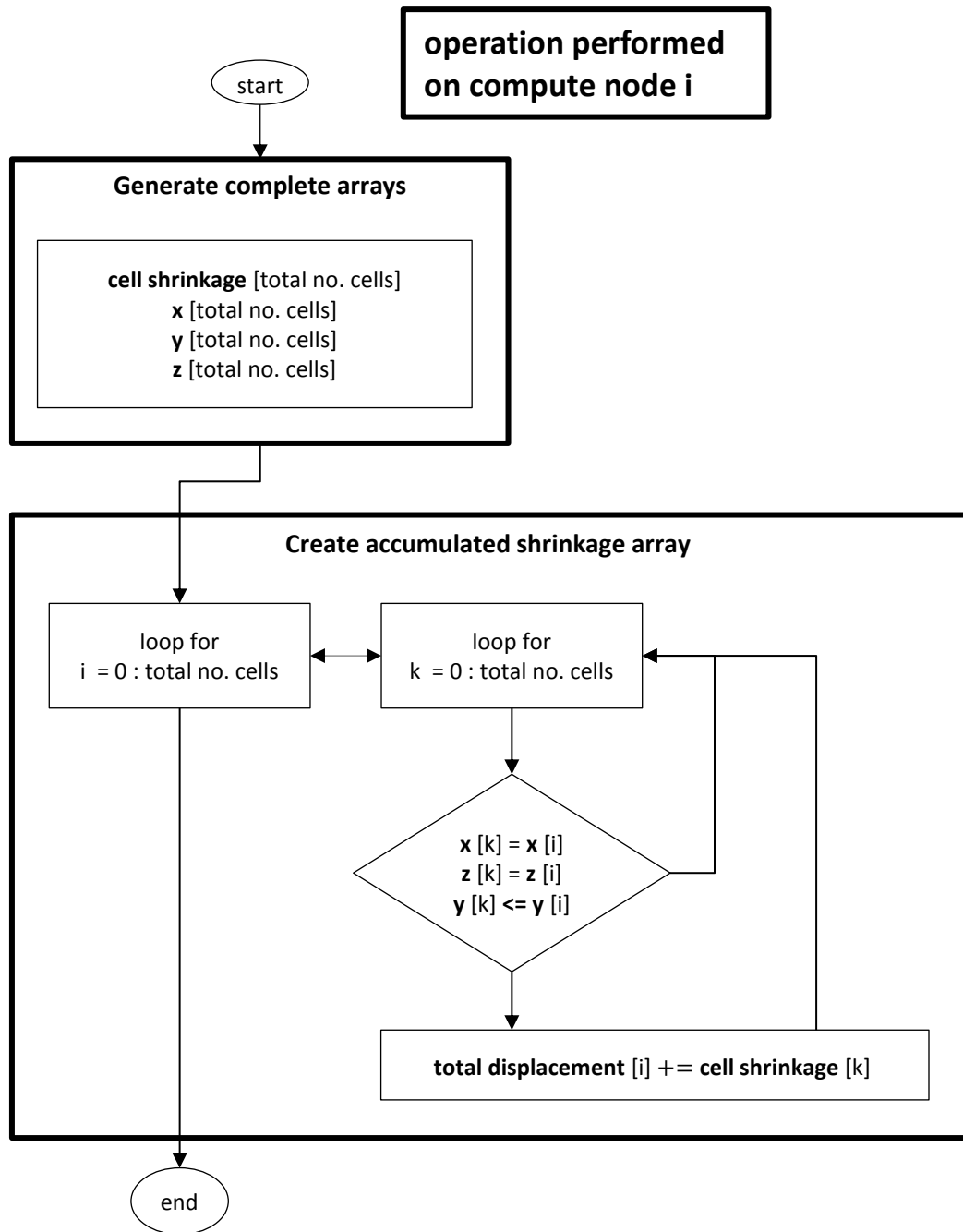


Figure A.7 Accumulated cell shrinkage

Controlling duplicated nodes

Duplicated nodes must be moved by the same amount on all compute nodes. Therefore, any cell that contains a duplicated node, which is not controlled by any other internal cell on that compute node, is identified. For example, in *Figure A.5*, *cell(n,m)* contains the duplicated nodes 2, 3, and 4; these are not controlled by any

internal cell in compute node A (recall that each cell only controls its upper right node in 2D). The identified cells, hereinafter termed outlying cells, are then given control of that particular outlying node (*i.e.* in this case, $cell(n,m)$ is allowed to move nodes 2, 3, and 4 on compute node A).

A.3.3 Identifying outlying cells

As with an internal node, a duplicated node may be common to multiple cells, as shown in *Figure A.8*. However, the node should only be controlled by a single cell; otherwise a manipulation may be repeated multiple times. A sorting system is therefore used to identify which cells are outlying cells, and more importantly, which particular node they may move. The sorting is performed during initialisation, at which point, the outlying cells and the node that they control are marked by means of UDM. This enables the outlying cells to be efficiently identified during the simulation.

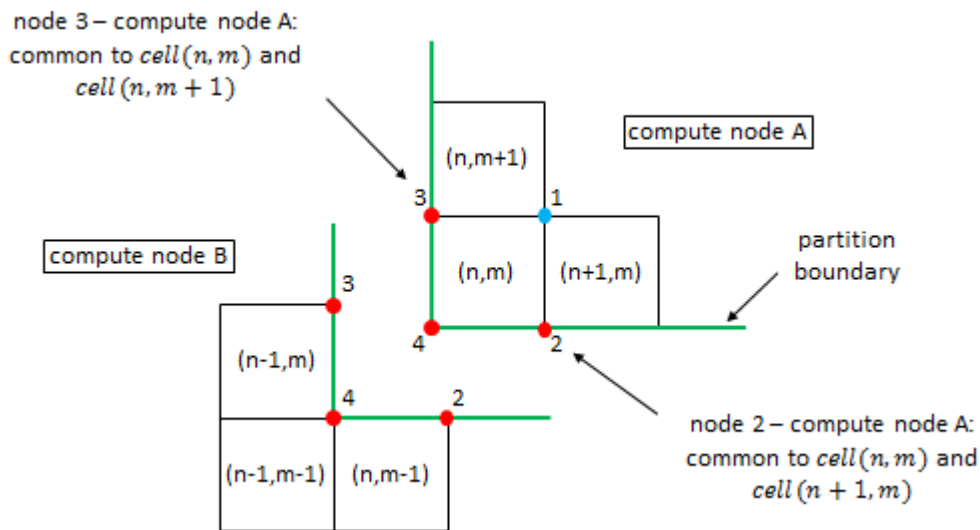


Figure A.8 Common duplicated nodes

2D sorting

Recall that each cell controls its upper right node by default, but relies on the surrounding cells to move the lower right node, upper left node, and lower left node. A cell is deemed an outlying cell if there is no internal cell on its compute node that can move these nodes, labelled 2 – 4 respectively in *Figure A.9*. For

sorting purposes, the cell nodes are prioritised; this enables a set of conditions to be applied to establish which cell gains controls (Note: these are and conditions – all must be satisfied to be true):

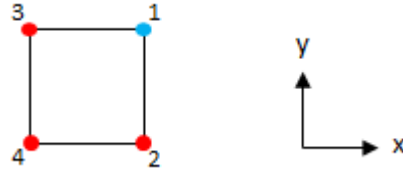


Figure A.9 Node priority in 2D

- (1) node 1 is controlled by default; see *Figure A.10* (a).
- (2) if there is no cell beneath (*i.e.* to move node 2, according to condition (1)), mark primary cell as an outlying cell with control of node 2, see *Figure A.10* (b).
- (3) if there are no cells to the left (1) and top left (because if there is no cell to the left, the bottom right node of the top left cell takes priority according to (2)), mark primary cell as an outlying cell with control of node 3, *Figure A.10* (c).
- (4) if there are no cells to the bottom left (1), left (2), and beneath (3), mark primary cell as an outlying cell with control of node 4, *Figure A.10* (d).

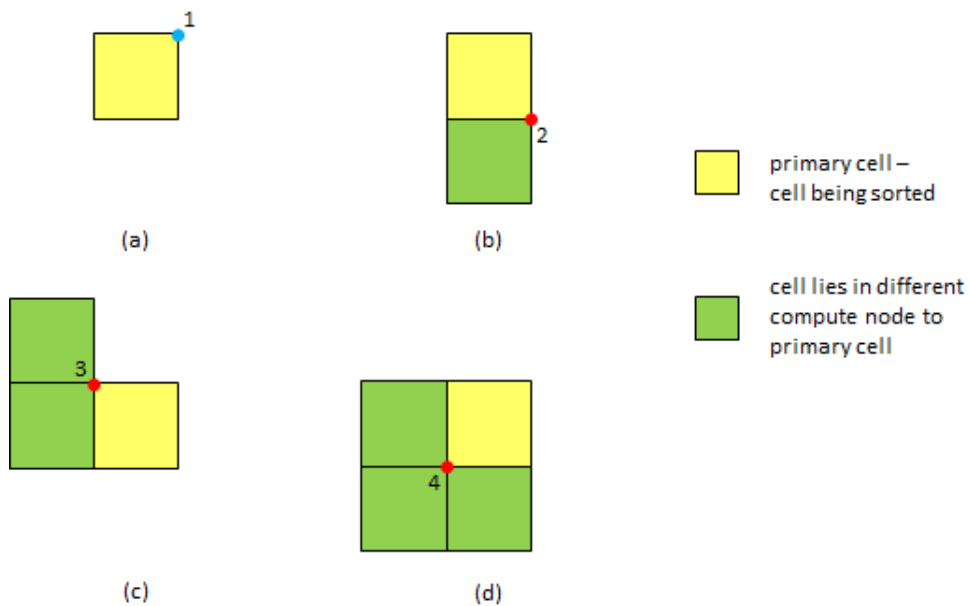


Figure A.10 Identifying outlying cells for nodes 1 – 4 in 2D

3D sorting

The same logic is applied to identify outlying cells in 3D. Recall that the front upper right node is moved in 3D, with seven ancillary nodes labelled 2 – 8 in order of priority in *Figure A.11*.

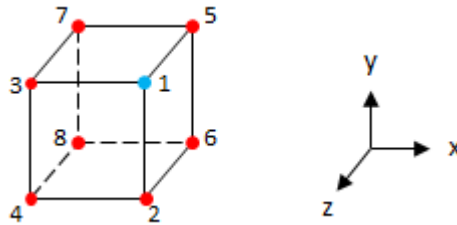


Figure A.11 Node priority in 3D

It is worth noting that in 3D, the conditions applied to sort nodes 1 – 4 are identical to 2D. The additional conditions required to sort nodes 5 – 8 on the back face of the 3D cell are:

- (5) if there are no cells behind (1), behind top (2), behind right (3), and behind top right (4), mark primary cell as an outlying cell with control of node 5, see *Figure A.12* (a).
- (6) if there are no cells behind bottom (1), behind (2), behind bottom right (3), behind right (4), and beneath (5), mark primary cell as an outlying cell with control of node 6, see *Figure A.12* (b).
- (7) if there are no cells behind left (1), behind top left (2), behind (3), behind top (4), left (5), and top left (6), mark primary cell as an outlying cell with control of node 7, see *Figure A.12* (c).
- (8) if there are no cells behind bottom left (1), behind left (2), behind bottom (3), behind (4), bottom left (5), left (6) and beneath (7), mark primary cell as an outlying cell with control of node 8, see *Figure A.12* (d).

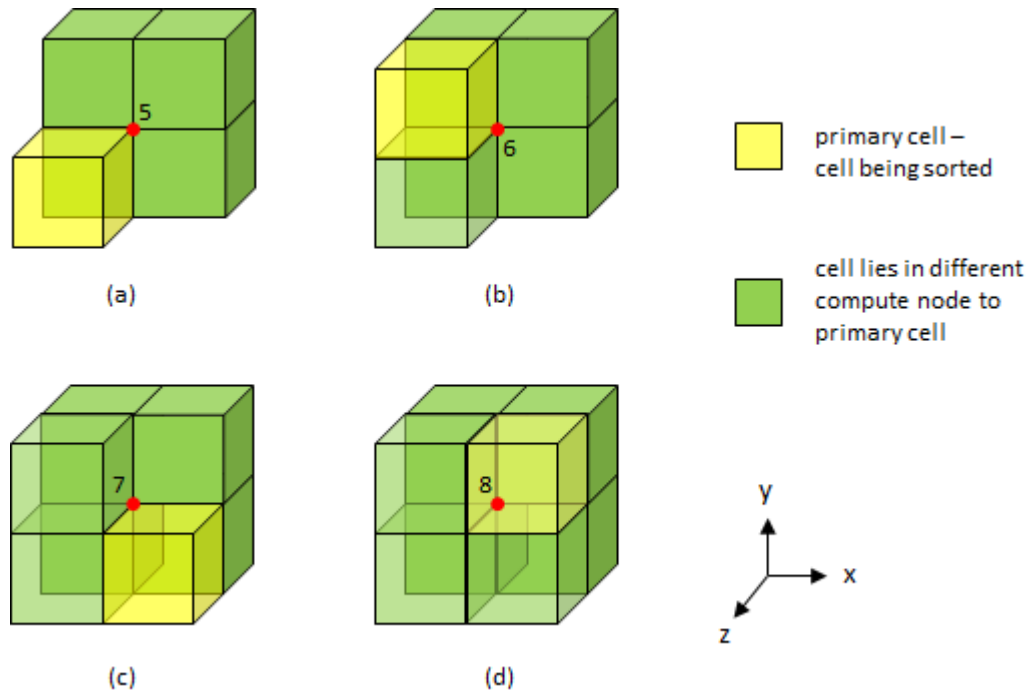


Figure A.12 Identifying outlying cells for nodes 5 – 8 in 3D

A.3.4 Moving nodes in outlying cells

The outlying cells are assigned control of nodes that are duplicated on their partition; however, they do not determine the displacement of these nodes. To ensure that the duplicated nodes are moved by the same amount on every compute node, the displacement is always determined by the default cell associated with that node, as shown in *Figure A.13*. An outlying cell must, therefore, search for the default cell associated with each duplicated node that it controls, in order to determine the shrinkage of that node, see *Figure A.14*.

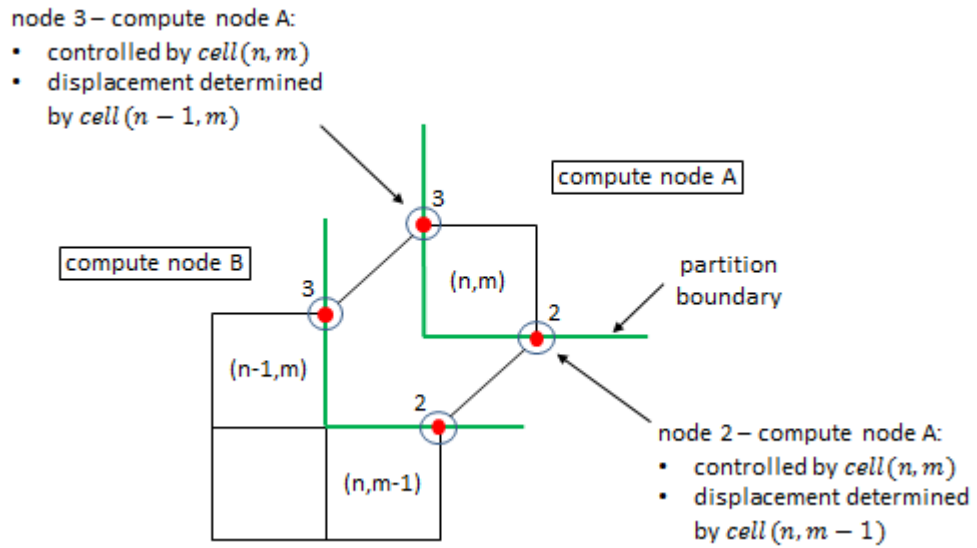


Figure A.13 Default cell determines the displacement of any duplicated nodes

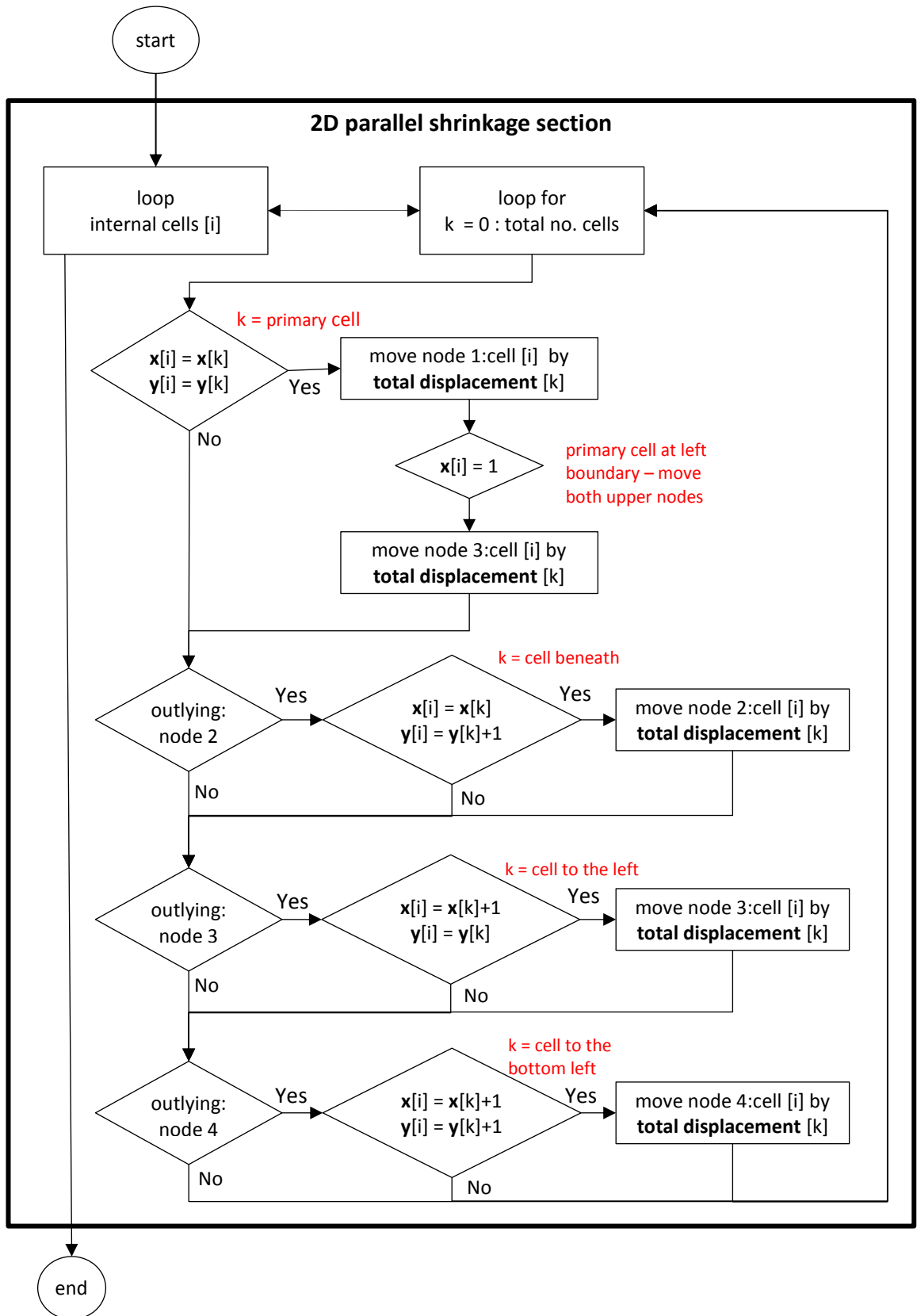


Figure A.14 Procedure to ensure that duplicated cells are moved by the same amount

A.4 Parallel Verification

To ensure that the parallelisation measures worked as expected in a complete fixed-bed simulation, an identical case was run first serial mode, and then in parallel across multiple cores; this results in a partitioned mesh as shown in *Figure A.15* for three compute nodes.

Figure A.16 shows spatial variation of gas speed after 600 s for both the serial and parallel runs. The results from each case are very similar. The minor discrepancies are due to stochastic differences resulting from the random porosity routine, which was called separately on each compute node. Bearing this in mind, the agreement between both runs is satisfactory. However, it is important to note that in order to directly compare several simulations, any stochastic differences should be precluded. This was achieved by means of an identically partitioned mesh for any cases to be compared. Since the random porosity routine is seeded, this prevents any random differences from arising.

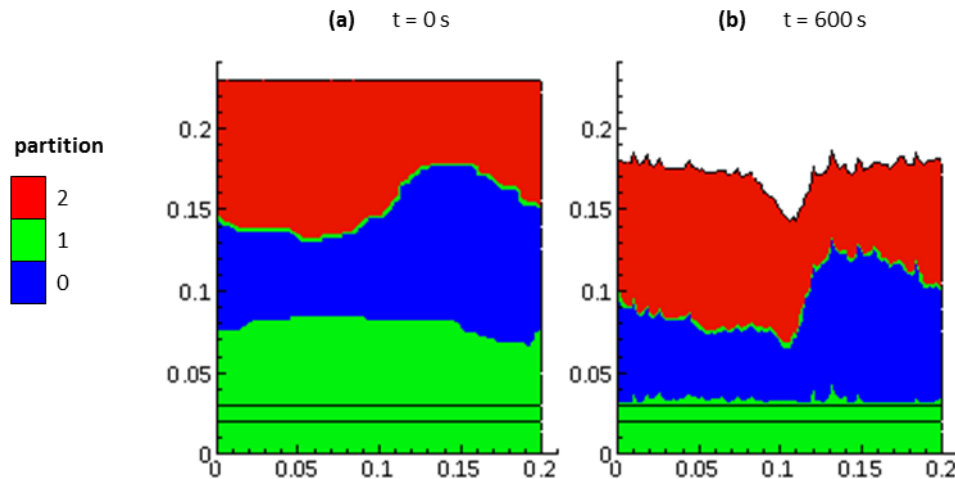


Figure A.15 Mesh partition in parallel run at time t

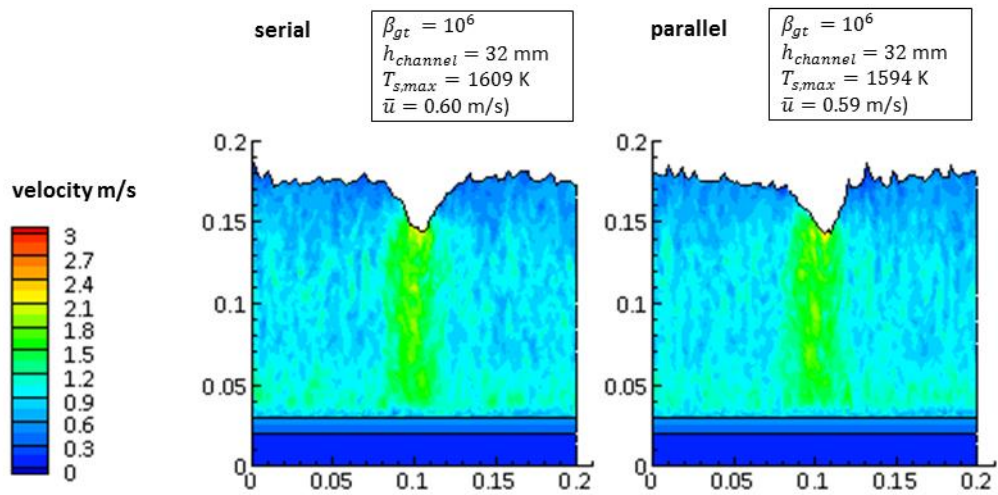


Figure A.16 Comparing an identical case run in serial and parallel

APPENDIX B
MESH SPACING PLOTS

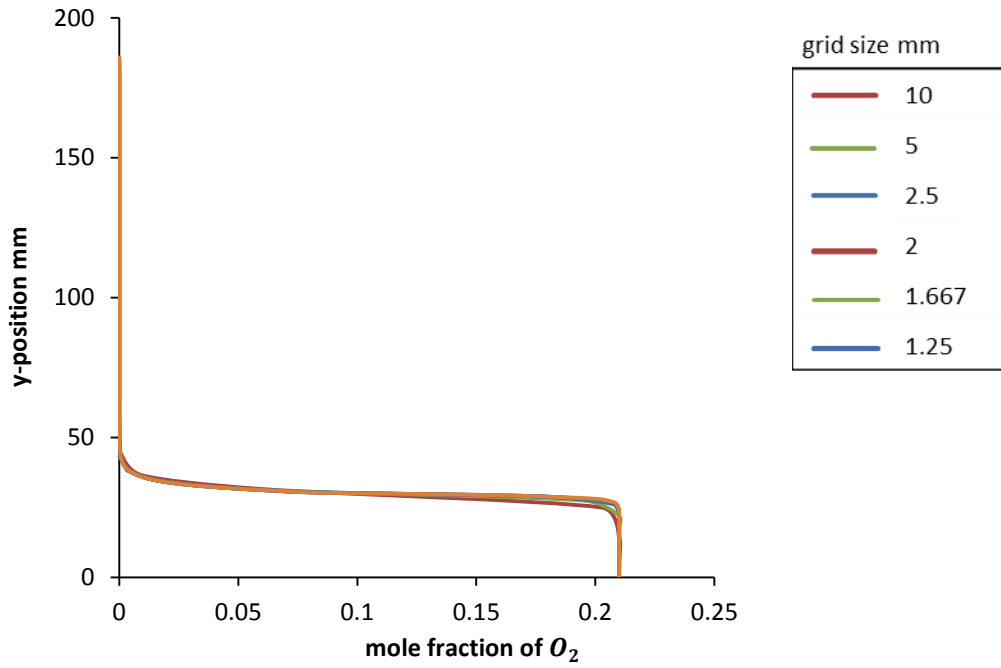


Figure B.1 Comparing mole fraction of O_2 for different grid sizes

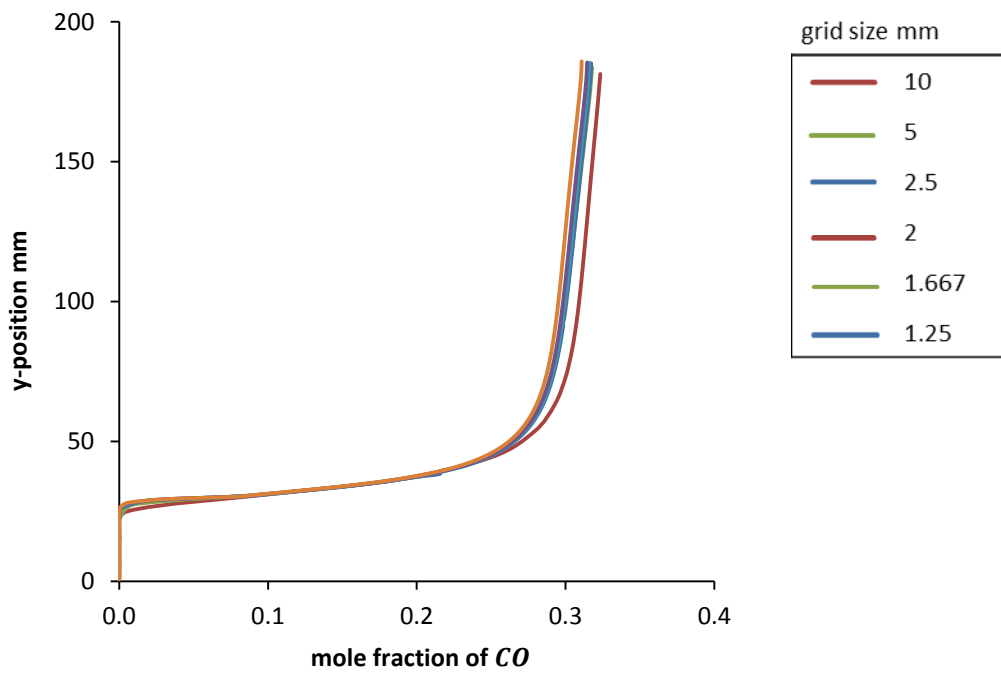


Figure B.2 Comparing mole fraction of CO for different grid sizes

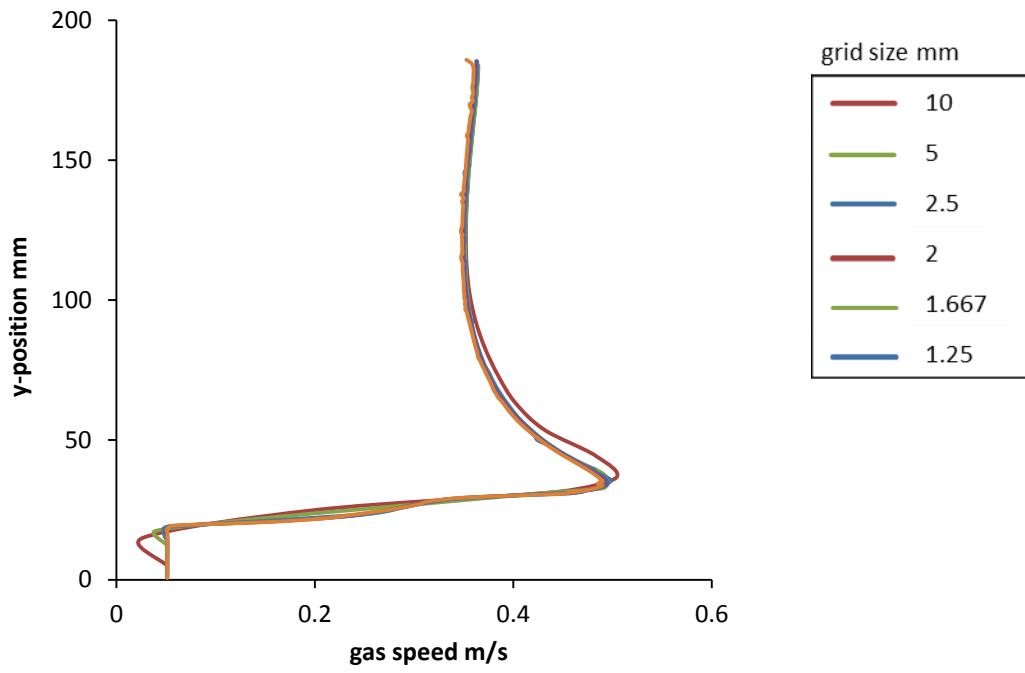


Figure B.3 Comparing gas speed for different grid sizes

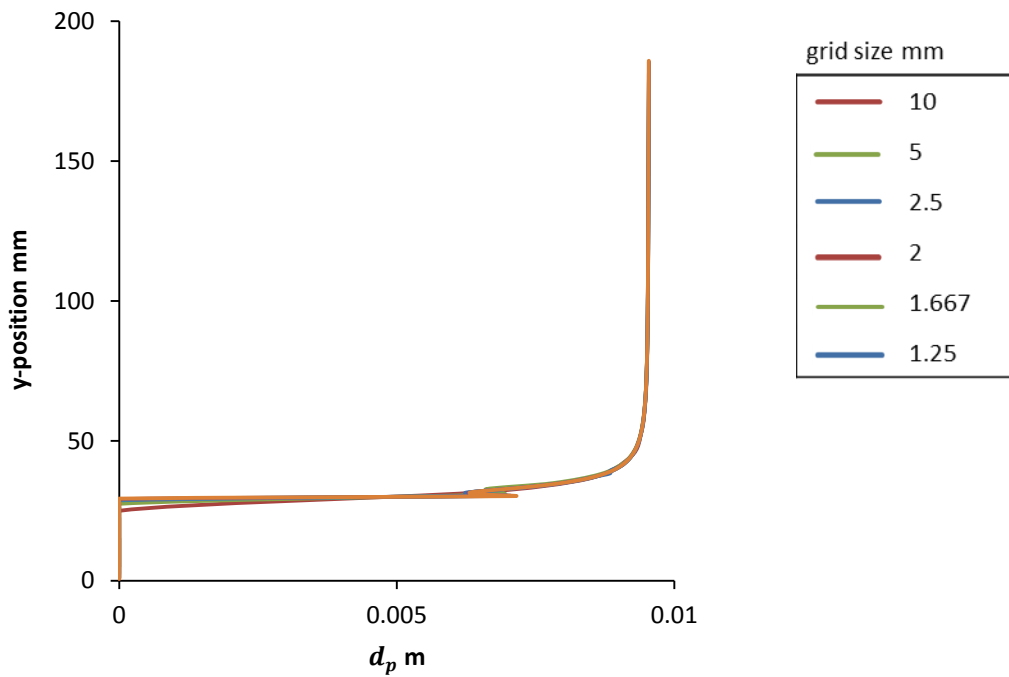


Figure B.4 Comparing particle diameter for different grid sizes

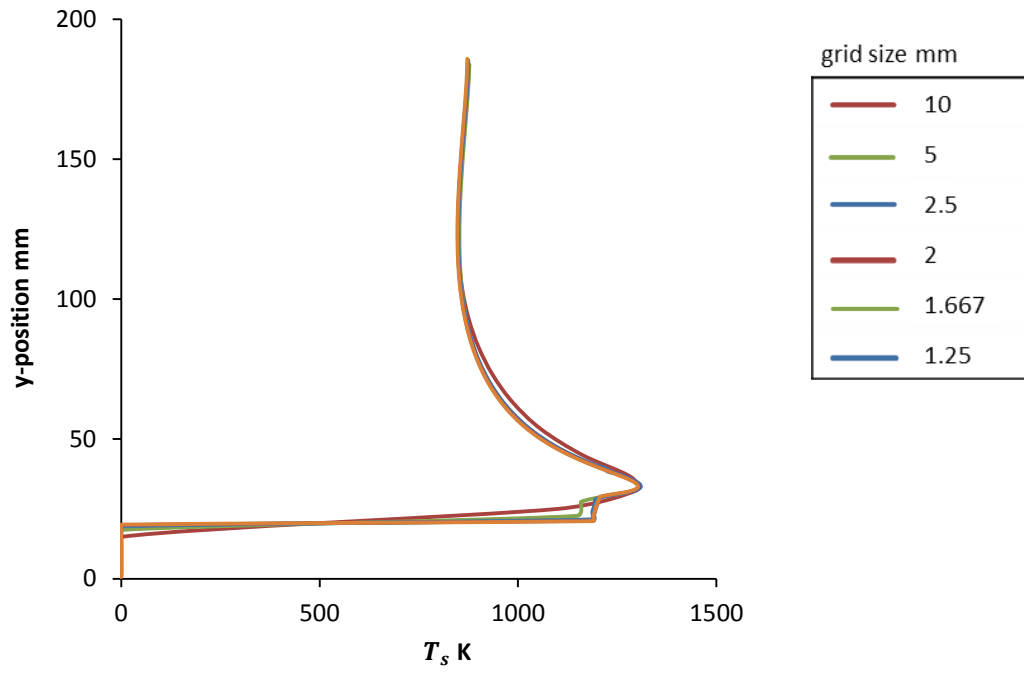


Figure B.5 Comparing solid phase temperature for different grid sizes

APPENDIX C
COLLATED EQUATIONS

Table C.1 Conservation equations

Mass	$\frac{\partial}{\partial t}(\varepsilon\rho_g) + \frac{\partial}{\partial x_i}(\varepsilon\rho_g u_i) = S_m$
Momentum	$\frac{\partial}{\partial t}(\varepsilon\rho_g u_i) + \frac{\partial}{\partial x_j}(\varepsilon\rho_g u_i u_j) = -\varepsilon \frac{\partial P}{\partial x_i} + \frac{\partial}{\partial x_j}(\varepsilon\tau_{ij}) + \varepsilon\rho_g g + S_{p,i}$
Species	$\frac{\partial}{\partial t}(\varepsilon Y_k \rho_g) + \frac{\partial}{\partial x_i}(\varepsilon Y_k \rho_g u_i) = \frac{\partial}{\partial x_i}(\varepsilon\rho_g D_{eff,k} \frac{\partial Y_k}{\partial x_i}) + S_{M,k} + S_{V,k} + S_{C,k} + S_{g,k}$
Energy (gas)	$\frac{\partial}{\partial t}(\varepsilon\rho_g c_{p,g} T_g) + \frac{\partial}{\partial x_i}(\varepsilon\rho_g u_i c_{p,g} T_g) = \frac{\partial}{\partial x_i}(\varepsilon\lambda_{g,eff} \frac{\partial T_g}{\partial x_i}) + S_{Q,ht} + S_{Q,gr} + S_{Q,sr2}$
Energy (solid)	$\frac{\partial}{\partial t}((1-\varepsilon)\rho_s c_{p,s} T_s) = \frac{\partial}{\partial x_i}((1-\varepsilon)\lambda_{s,eff} \frac{\partial T_s}{\partial x_i}) - S_{Q,ht} + S_{Q,sr1} - S_{Q,sr2}$
Turbulent energy	$\frac{\partial}{\partial t}(\varepsilon\rho_g k) + \frac{\partial}{\partial x_i}(\varepsilon\rho_g u_i k) = \frac{\partial}{\partial x_i}(\varepsilon(\mu + \frac{\mu_t}{\sigma_k}) \frac{\partial k}{\partial x_i}) + G_k + G_b - \rho_g \varepsilon_d + S_k$
Turbulent dissipation	$\frac{\partial}{\partial t}(\varepsilon\rho_g \varepsilon) + \frac{\partial}{\partial x_i}(\varepsilon\rho_g u_i \varepsilon) = \frac{\partial}{\partial x_i}(\varepsilon(\mu + \frac{\mu_t}{\sigma_\varepsilon}) \frac{\partial \varepsilon}{\partial x_i}) + C_1 \frac{\varepsilon}{\kappa} (G_k + C_3 G_b) - C_2 \rho_g \frac{\varepsilon^2}{\kappa} + S_\varepsilon$
	where
	$C_1 = 1.44, C_2 = 1.92, C_3 = 0.09, \sigma_k = 1.0, \sigma_\varepsilon = 1.3$

Table C.2 Gas phase packed bed relations

Thermal dispersion	$\lambda_{g,eff} = 0.8 \lambda_g + 0.5 c_{p,g} \rho_g u_g d_p$	[92]
Diffusivity	$D_{eff,k} = 0.8 D_{eff,AB,k} + 0.5 u_g d_p$	[92]
	$D_{eff,AB,k} = D_{AB,ref,k} \left(\frac{T_g}{T_{ref}} \right)^{1.75}$	[166]
Resistance to flow	$S_{p,i} = - \left(\frac{\mu}{\alpha} u_i + \beta \rho_g u u_i \right)$	[88]
	$\alpha = \frac{\varepsilon^3 d_p^2}{180(1-\varepsilon)^2}$	[167]
	$\beta = \frac{4(1-\varepsilon)}{\varepsilon^3 d_p}$	
Turbulent energy	$S_k = \frac{1.75(1-\varepsilon)}{\varepsilon d_p} u_g ^3$	[168]
Turbulent dissipation	$S_\varepsilon = \frac{4.55 c_2 (1-\varepsilon)^2}{\varepsilon^2 d_p^2} u_g ^4$	[168]
Gas mixing rates	$k_{mix} = \frac{1.2(1-\varepsilon)^{1/3} u_g}{d_p \varepsilon^{4/3}} \cdot \min \left(\frac{C_i}{\Omega_i} \right)$	[169]
	$k_{mix} = 0.63 \left(\frac{1.75(1-\varepsilon) u_g}{d_p \varepsilon} \right) \cdot \min \left(\frac{C_i}{\Omega_i} \right)$	[90]
	$k_{mix} = 0.5 \rho_g \left(\frac{150(1-\varepsilon)^{2/3} D_{eff}}{d_p^2 \varepsilon} + \frac{1.75(1-\varepsilon)^{1/3} u_g}{d_p \varepsilon} \right) \cdot \min \left(\frac{C_i}{\Omega_i} \right)$	[135]
	where $\min \left(\frac{C_i}{\Omega_i} \right) = \min \left(\frac{C_{react}}{\Omega_{react}}, \frac{C_{O_2}}{\Omega_{O_2}} \right)$	

EDM mixing rate

$$k_{mix,i} = A \frac{\epsilon}{k} \cdot \min\left(\frac{C_i}{\Omega_i}\right) \quad [88]$$

$$k_{mix,j} = AB \frac{\epsilon}{k} \cdot \left(\frac{\sum Y_j}{\sum \Omega_j M_j}\right)$$

$$k_{mix} = \min(k_{mix,i}, k_{mix,j})$$

Chemical reaction rate

$$k_{kin} = A_i T_g^b \exp(-E_i/RT_g) \sum [C_i]^v \quad (\text{only forward rate considered here}) \quad [88]$$

where v is a rate exponent

Effective reaction rate

$$k_{eff} = \min(k_{mix}, k_{kin}) \quad [88]$$

where i = reactant species, j = product species

Table C.3 Heat and mass transfer

Heat transfer coefficient	$h_{ht} = \frac{\lambda_{g,eff} Nu}{L_{char}}$		[92]
<i>particle</i>	$Nu = 2 + 1.1 Pr^{1/3} Re^{0.6}$		$L_{char} = d_p$ [92]
<i>grate surface</i>	$Nu = 0.332 Pr^{1/3} Re^{0.5}$	$Re < 10^5$	$L_{char} = 0.01$ (approximation) [172]
	$Nu = 0.0288 Pr^{1/3} Re^{0.8}$	$Re > 10^6$	[172]
<i>grate passages</i>	$Nu = 1.86 \left(\frac{Pr Re D_h}{h_{grate}} \right)^{1/3}$	$Re < 10^4$	$L_{char} = D_h$ [172]
	$Nu = 0.23 Pr^{0.4} Re^{0.8}$	$Re \geq 10^4$	[172]
	$S_{Q,ht} = A_{spec} h_{ht} (T_s - T_g)$		
Mass transfer coefficient	$h_{m,k} = \frac{D_{eff,k} Sh}{d_p}$		[92]
	$Sh = 2 + 1.1 Sc^{1/3} Re^{0.6}$		[92]
<i>with ash</i>	$h_{m,k,eff} = \left(\frac{1}{h_{m,k}} + \frac{1}{h_{m,A,k}} \right)^{-1}$		[91]
	$D_{eff,A,k} = \varepsilon_A^2 D_{eff,AB,k}$		[146]
	$h_{m,A,k} = \frac{D_{eff,A,k}}{\delta_A}$		[196]

Table C.4 Solid phase properties

Effective thermal conductivity	$\lambda_{s,eff} = \lambda_s + \lambda_{rad}$	[11]
---------------------------------------	---	------

Solid conductivity

Mass weighted method

$$\lambda_s = \varepsilon_p \lambda_g + \sum_k Y_k \lambda_k$$

Interpolation method

$$\lambda_s = \varepsilon_p \lambda_g + \eta_\lambda \lambda_w + (1 - \eta_\lambda) \lambda_c + \lambda_{p,rad} \quad [48]$$

$$\eta_\lambda = \frac{\rho_s - \rho_{c\infty}}{\rho_{SD,0} - \rho_{c\infty}} \quad \text{for single-step pyrolysis}$$

$$\eta_\lambda = \frac{\rho_s}{\rho_{SD,0}} \quad \text{for parallel reaction pyrolysis}$$

Wood fibres method

$$\lambda_s = \xi \lambda_{par} + (1 - \xi) \lambda_{ser} \quad [11]$$

$$\lambda_{par} = \varepsilon_p (\lambda_g + \lambda_{p,rad}) + \varepsilon_{p,M} \lambda_m + (1 - \varepsilon_p - \varepsilon_{p,M}) \lambda_{fiber,||}$$

$$\lambda_{ser} = \left(\frac{\varepsilon_{p,g}}{\lambda_g + \lambda_{p,rad}} + \frac{\varepsilon_{p,m}}{\lambda_m} + \frac{\varepsilon_{p,s}}{\lambda_{fiber,\perp}} \right)^{-1}$$

$$\varepsilon_p = 1 - \frac{\rho_s}{\rho_{th}}$$

$\varepsilon_{p,M}$ is the volume fraction of bound and free water

$\lambda_{p,rad}$ is the radiation within the particles (effectively same models as λ_{rad})

With ash (char only)

$$\lambda_s = \frac{d_{p,char}}{2} \left(\frac{d_{c,char}/2}{\varepsilon_c \lambda_g + \sum_k Y_{k,0} \lambda_k} + \frac{\delta_A}{\varepsilon_A \lambda_g + (1 - \varepsilon_A) \lambda_A} \right)^{-1}$$

Radiative contribution

$$\lambda_{rad} = 4\varepsilon\sigma_b\omega d_p T_s^3 \quad [175]$$

$$\lambda_{rad} = \frac{13.5\sigma_b d_p T_s^3}{\varepsilon\omega} \quad [35]$$

$$\lambda_{rad} = \frac{4\varepsilon\sigma_b\omega d_p T_s^3}{1 - \varepsilon} \quad [11]$$

Specific heat capacity

$$c_{p,s} = \sum_k Y_k \overline{c_{p,k}} \quad [104]$$

$$\overline{c_{p,k}} = \frac{\int_0^{T_s} c_{p,k} dT_s}{T_s}$$

Table C.5 Particle and bed shrinkage

Particle shrinkage

single-step pyrolysis

$$V_p = V_{p,0} \left(1 - \delta_{p,M} \left(1 - \frac{m_M}{m_{M,0}} \right) - \delta_{p,sd} \left(1 - \frac{m_{sd}}{m_{sd,0}} \right) - \delta_{p,C} \left(\frac{m_{C,burned}}{m_{C,\infty}} \right) \right) \quad [90]$$

$$\delta_{p,M} = \varphi_M X_{m,0}$$

$$\delta_{p,sd} = \varphi_{sd} (1 - \delta_{p,M})$$

$$\delta_{p,A} = \frac{X_{m,0} \rho_{s,0}}{(1 - \varepsilon_A) \rho_A}$$

$$\delta_{p,C} = 1 - \delta_{p,M} - \delta_{p,sd} - \delta_{p,A}$$

Parallel reaction pyrolysis

$$V_p = V_{p,0} \left(\frac{m_{sd}}{m_{sd,0}} + \varphi_C \frac{m_C}{m_{C,0}} \right) \quad [48]$$

Bed shrinkage

$$\frac{\partial V}{\partial t} = \frac{1}{(1 - \varepsilon_0)} \frac{\partial V_s}{\partial t} \quad [91]$$

$$\frac{\partial y}{\partial t} = \frac{1}{\Delta x \Delta z} \frac{\partial V}{\partial t}$$

$$\frac{\partial V}{\partial t_{shr}} = \delta_{shr} \frac{\partial V}{\partial t}$$

$$\Delta V_{col} = (1 - \delta_{shr}) \Delta V_{shr,acc}$$

Table C.6 Conversion equations – most common

Drying

Kinetic method

$$\frac{d\rho_M}{dt} = -k_M \rho_M \quad [35]$$

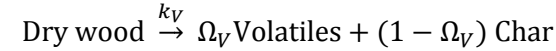
$$k_M = A_M e^{-E_M/RT}$$

Constant temperature method

$$\frac{d\rho_M}{dt} = \begin{cases} -0.5 \frac{(T_s - T_{evap}) \rho_s c_{p,s}}{\Delta H_M \Delta t}, & \text{if } T_s \geq T_{evap} \\ 0, & \text{if } T_s < T_{evap} \end{cases} \quad [31]$$

Pyrolysis

single-step pyrolysis



$$\frac{d\rho_{sd}}{dt} = -k_V \rho_V = -k_V \Omega_V \rho_{sd}$$

$$k_V = A_V e^{-E_V/RT}$$

$$\Omega_V \text{Volatiles} = \sum_i \Omega_{V,i} \text{Volatile}_i$$

Parallel reaction pyrolysis



$$k_{V,i} = A_{V,i} e^{-E_{V,i}/RT}$$

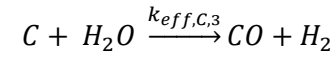
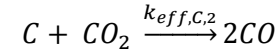
$$\frac{d\rho_{sd}}{dt} = -\rho_{sd} \sum_{i=1}^3 k_{V,i}$$

Char reactions



$$\Omega_C = \frac{2(1 + CO/CO_2)}{2 + CO/CO_2} \quad [174]$$

$$\frac{CO}{CO_2} = A e^{-E/RT} \quad [174]$$



$$\frac{d\rho_{c,j}}{dt} = -f_b A_{spec} M_C \Omega_C k_{eff,j}$$

$$k_{eff,j} = \frac{k_{C,j} h_{m,k}}{k_{C,j} + h_{m,k}} C_k$$

$$f_b = 1 - \frac{\rho_{sd}}{\rho_{sd,0}} \quad 0 < f_b < 1$$

Global model

$$k_{C,j} = A_{C,j} e^{-E_{C,j}/RT} \quad [90]$$

Intrinsic model

$$k_{C,j} = \eta \gamma \rho_{sd} A_g k_{int} \quad [89]$$

$$\eta = \frac{3}{\Phi} \left(\frac{1}{\tanh \Phi} - \frac{1}{\Phi} \right) \quad [82]$$

$$\Phi = \frac{d_p}{2} \left(\frac{k'_{int}}{\Omega D_{e,pore}} \right)^{1/2} \quad [82]$$

$$k'_{int} = \rho_{sd} A_g k_{int} \quad [82]$$

$$D_{e,pore} = \frac{D_{eff} \varepsilon_{char}}{\tau} \quad [82]$$

APPENDIX D
LIST OF UDFS AND FUNCTIONS

Appendix D

LIST OF UDFS AND FUNCTIONS

Name	Type	Description
(1) Volatile_composition	Function	Determines the stoichiometric ratio of species produced during pyrolysis – calls several standard matrix functions not mention here
(2) Specific_energy_wood	Function	Calculates the integral of wood energy for the Volatile composition calculation
(3) Normal_distribution	Function	Generates the value of the random porosity
(4) Porosity_central_channel	Function	Adjusts the random porosity to create a high-porosity passage (2D or 3D) in the centre of the domain
(5) Porosity_wall_channel	Function	Generates a wall bound relatively porous passage
(6) Average_porosity	Function	Calculates the average porosity along vertical traverses
(7) htc	Function	Determines the heat transfer coefficient between the gas and the fuel bed
(9) Mass_transfer_coefficient	Function	Determines the mass transfer coefficient between the gas and the fuel bed
(10) Particle_dimensions	Function	Calculates the shape of a shrinking 1D cylinder
(11) Pressure_drop_fuel_bed	Function	Calculates the permeability and Forchheimer constants for the fuel bed
(12) Pyrolysis_rates	Function	Determines the pyrolysis rates – contains switch for different pyrolysis submodels
(13) Heterogeneous_reaction_rate	Function	Determines the heterogeneous reaction rate for each reactant passed to it – contains switch for different heterogeneous reaction models

(14)	Gas_specific_energy	Function	Calculates the integral for the gas energy transfer that accompanies any mass transfer
(15)	Average_specific_heat	Function	Calculates the average specific heat capacity of the solid phase
(16)	My_gas_mixing_rate	Function	Calculates the gas mixing rate – contains switch for different models
(17)	DEFINE_INIT(Init)	UDF	Initialised the domain – <u>substantial</u> section of the overall code
(18)	DEFINE_EXECUTE_AT_END(end)	UDF	Updates solid phase properties at the end of a timestep
(19)	DEFINE_PROFILE (permeability)	UDF	Hooks the permeability (11) into Fluent
(20)	DEFINE_PROFILE (inertia)	UDF	Hooks the inertia (11) into Fluent
(21)	DEFINE_PROFILE (porosity)	UDF	Hooks the porosity calculated in (18) into Fluent
(22)	DEFINE_PROFILE (ht_surface_fluid)	UDF	Heat transfer <u>to</u> the fluid: convection from top and bottom surfaces of grate – same correlation used
(23)	DEFINE_PROFILE (ht_bottom_grate)	UDF	Heat transfer <u>from</u> the grate: convection to cold gas, radiation to windbox
(24)	DEFINE_PROFILE (ht_top_grate)	UDF	Heat transfer <u>to</u> the grate: convection from hot gas, radiation from fuel bed
(25)	DEFINE_PROFILE (ht_top_grate)	UDF	Heat transfer <u>from</u> the fuel bed: radiation to the grate
(26)	DEFINE_PROFILE (ht_passage_fluid)	UDF	Heat transfer <u>to</u> the fluid: convection from the grate
(27)	DEFINE_PROFILE (ht_passage_grate)	UDF	Heat transfer <u>from</u> the grate: convection to the fluid
(28)	DEFINE_PROFILE (o2_backflow)	UDF	Determined boundary condition for O_2 at the outlet in the event of backflow – based on the cell adjacent to the outlet
(29)	DEFINE_PROFILE (co2_backflow)	UDF	CO_2 : same as O_2 above

(30)	DEFINE_PROFILE (co_backflow)	UDF	CO : same as O_2 above
(31)	DEFINE_PROFILE (h2o_backflow)	UDF	H_2O : same as O_2 above
(32)	DEFINE_PROFILE (h2_backflow)	UDF	H_2 : same as O_2 above
(34)	DEFINE_PROFILE (tar_backflow)	UDF	tar : same as O_2 above
(35)	DEFINE_PROFILE (ch4_backflow)	UDF	CH_4 : same as O_2 above
(36)	DEFINE_PROFILE (n2_backflow)	UDF	N_2 : same as O_2 above
(37)	DEFINE_PROFILE (temp_backflow)	UDF	Gas temperature: same as O_2 above
(38)	DEFINE_PROFILE (turb_energy_backflow)	UDF	Turbulent energy: same as O_2 above
(39)	DEFINE_PROFILE (turb_diss_backflow)	UDF	Turbulent dissipation: same as O_2 above
(40)	DEFINE_SOURCE (drying)	UDF	Hooks water vapour source to gas phase into Fluent
(41)	DEFINE_SOURCE (ch4)	UDF	Hooks CH_4 source from pyrolysis to gas phase into Fluent
(42)	DEFINE_SOURCE (co2)	UDF	Hooks CO_2 source from pyrolysis to gas phase into Fluent
(43)	DEFINE_SOURCE (co)	UDF	Hooks CO source from pyrolysis to gas phase into Fluent
(44)	DEFINE_SOURCE (h2o)	UDF	Hooks H_2O source from pyrolysis to gas phase into Fluent
(45)	DEFINE_SOURCE (tar)	UDF	Hooks tar source from pyrolysis to gas phase into Fluent
(46)	DEFINE_SOURCE (h2)	UDF	Hooks H_2 source from pyrolysis to gas phase into Fluent
(47)	DEFINE_SOURCE (o2_comb)	UDF	Hooks O_2 sink from char combustion to gas phase into Fluent

(48)	DEFINE_SOURCE (co2_comb)	UDF	Hooks CO_2 source from char combustion to gas phase into Fluent
(49)	DEFINE_SOURCE (co_comb)	UDF	Hooks CO source from char combustion to gas phase into Fluent
(50)	DEFINE_SOURCE (co2_gas)	UDF	Hooks CO_2 sink from CO_2 char gasification to gas phase into Fluent
(51)	DEFINE_SOURCE (co_gas_co2)	UDF	Hooks CO source from CO_2 char combustion to gas phase into Fluent
(52)	DEFINE_SOURCE (h2o_gas)	UDF	Hooks H_2O sink from H_2O char gasification to gas phase into Fluent
(53)	DEFINE_SOURCE (co_gas_h2o)	UDF	Hooks CO source from H_2O char combustion to gas phase into Fluent
(54)	DEFINE_SOURCE (h2_gas_h2o)	UDF	Hooks H_2 source from H_2O char combustion to gas phase into Fluent
(55)	DEFINE_SOURCE (total)	UDF	Hooks total mass source from all solid reaction to gas phase into Fluent
(56)	DEFINE_SOURCE (turb_energy)	UDF	Hooks turbulent energy source term into Fluent
(57)	DEFINE_SOURCE (turb_diss)	UDF	Hooks turbulent energy source term into Fluent
(58)	DEFINE_SOURCE (gas_energy_bed)	UDF	Hooks total heat source/sink to the gas phase in the bed (convection with solid phase)
(59)	DEFINE_SOURCE (solid_energy_bed)	UDF	Hooks total heat source/sink to the solid phase including heat of solid phase reactions
(60)	DEFINE_SOURCE (gas_energy_grate)	UDF	Hooks total heat source/sink to the gas phase when the grate was represented as a porous medium
(61)	DEFINE_SOURCE (solid_energy_grate)	UDF	Hooks total heat source/sink to the solid phase when the grate was represented as a porous medium
(62)	DEFINE_PROPERTY (gas_cond)	UDF	Hooks the effective thermal conductivity of the gas phase due to the presence of the packed bed

(63)	DEFINE_PROPERTY (mass_diff)	UDF	Hooks the effective diffusion coefficient for <u>each</u> species in the gas phase due to the presence of the packed bed
(64)	DEFINE_DIFFUSIVITY(diff_all)	UDF	Hooks the diffusion coefficient for all user-defined scalars (UDS) into Fluent; in this case, it refers to the solid energy equation
(65)	DEFINE_UDS_UNSTEADY(first_order)	UDF	Hooks the transient term of the solid phase energy equation into Fluent (UDS)
(66)	DEFINE_DIFFUSIVITY(diff_all)	UDF	Hooks the diffusion coefficient for all user-defined scalars (UDS) into Fluent; in this case, it refers to the solid energy equation
(67)	DEFINE_DIFFUSIVITY(diff_all)	UDF	Hooks the diffusion coefficient for all user-defined scalars (UDS) into Fluent; in this case, it refers to the solid energy equation
(68)	DEFINE_VR_RATE(gas_react)	UDF	Hooked the overall gas reaction rate into Fluent – accounted for gas mixing rate due to the presence of the packed bed. Necessary if source terms for k and ϵ and not used in conjunction with standard EDM
(69)	DEFINE_GRID_MOTION.bed)	UDF	Manipulates the nodes positions throughout the bed – <u>substantial</u> section of the code

REFERENCES

- [1] KARA Energy Systems. Available: <http://www.kara-greenenergy.com>, Accessed on: 11/12/2012
- [2] Y. B. Yang, C. Ryu, J. Goodfellow, V. N. Sharifi, and J. Swithenbank, "Modelling Waste Combustion in Grate Furnaces," *Process Safety and Environmental Protection*, vol. 82, pp. 208-222, 2004.
- [3] S. Hermansson, "Detecting, Modelling and Measuring Disturbances in Fixed-Bed Combustion," PhD, Energy and Environment, Chalmers University of Technology, Göteborg, 2010.
- [4] C. Yin, L. Rosendahl, S. K. Kær, S. Clausen, S. L. Hvid, and T. Hiller, "Mathematical modeling and experimental study of biomass combustion in a thermal 108 MW grate-fired boiler," *Energy and Fuels*, vol. 22, pp. 1380-1390, 2008.
- [5] S. Hermansson, C. Olausson, H. Thunman, M. Rönnbäck, and B. Leckner, "Combustion Disturbances in the Fuel Bed of Grate Furnaces," in *7th European Conference on Industrial Furnaces and Boilers*, Porto, Portugal, 2006.
- [6] International Energy Agency. Key World Energy Statistics 2012 [Online]. Available: <http://www.iea.org/publications/freepublications/publication/name,31287,en.html>, Accessed on: 11/12/2012
- [7] International Energy Agency, *World Energy Outlook 2012*: OECD Publishing, 2012.
- [8] U. S. Energy Information Administration. International Energy Outlook 2011 [Online]. Available: <http://www.eia.gov/oiaf/ieo/index.html>, Accessed on: 11/12/2012
- [9] E. Rehfuss, "Fuel for life: household energy and health," WHO, 2006.
- [10] EPSSU, "Energy in Ireland - Key Statistics 2009," Sustainable Energy Ireland 2009.
- [11] M. G. Gronli, "A theoretical and experimental study of the thermal degradation of biomass," Engineering Ph.D. Thesis, Norwegian University of Science and Technology, Norway, Trondheim, 1996.
- [12] B. G. Miller and D. A. Tillman, *Combustion Engineering Issues for Solid Fuel Systems*: Academic Press, Elsevier, 2008.
- [13] M. Bellais, "Modelling of the pyrolysis of large wood particles," Engineering Ph.D. Thesis, KTH, Sweden, Stockholm, 2007.
- [14] K. W. Ragland, D. J. Aerts, and A. J. Baker, "Properties of wood for combustion analysis," *Bioresource Technology*, vol. 37, pp. 161-168, 1991.
- [15] S. Van Loo and J. Koppejan, *The Handbook of Biomass Combustion and Co-firing* Earthscan, 2008.
- [16] Forest Products Laboratory, "Wood Handbook: Wood as an Engineering Material," ed: U.S. Department of Agriculture, 2010.
- [17] G. Wiltsee, "Lessons Learned from Existing Biomass Power Plants," U. S. D. o. E. Laboratory, Ed., ed: National Renewable Energy Laboratory, 2000.
- [18] Drax Power Limited. Available: <http://www.draxpower.com>, Accessed on: 11/12/2012
- [19] J. Rezaian and N. P. Cheremisinoff, *Gasification Technologies: A Primer for Engineers and Scientist*: Boca Raton: Taylor & Francis Group, 2005.
- [20] R. P. van der Lans, L. T. Pedersen, A. Jensen, P. Glarborg, and K. Dam-Johansen, "Modelling and experiments of straw combustion in a grate furnace," *Biomass and Bioenergy*, vol. 19, pp. 199-208, 2000.
- [21] C. Yin, L. A. Rosendahl, and S. K. Kær, "Grate-firing of biomass for heat and power production," *Progress in Energy and Combustion Science*, vol. 34, pp. 725-754, 2008.

- [22] T. Nussbaumer, "Combustion and Co-combustion of Biomass: Fundamentals, Technologies, and Primary Measures for Emission Reduction," *Energy Fuels*, vol. 17, pp. 1510-1521, 2003.
- [23] Y. Niu, H. Tan, L. Ma, M. Pourkashanian, Z. Liu, Y. Liu, X. Wang, H. Liu, and T. Xu, "Slagging Characteristics on the Superheaters of a 12 MW Biomass-Fired Boiler," *Energy & Fuels*, vol. 24, pp. 5222-5227, 2010.
- [24] H. Zhou, P. A. Jensen, and F. J. Frandsen, "Dynamic mechanistic model of superheater deposit growth and shedding in a biomass fired grate boiler," *Fuel*, vol. 86, pp. 1519-1533, 2007.
- [25] C. Mueller, M. Selenius, M. Theis, B. J. Skrifvars, R. Backman, M. Hupa, H. Tran, and I. Naruse, "Deposition behaviour of molten alkali-rich fly ashes - Development of a submodel for CFD applications," Chicago, IL, 2005, pp. 2991-2998.
- [26] A. Phongphiphat, C. Ryu, Y. B. Yang, K. N. Finney, A. Leyland, V. N. Sharifi, and J. Swithenbank, "Investigation into high-temperature corrosion in a large-scale municipal waste-to-energy plant," *Corrosion Science*, vol. 52, pp. 3861-3874, 2010.
- [27] M. Theis, B.-J. Skrifvars, M. Hupa, and H. Tran, "Fouling tendency of ash resulting from burning mixtures of biofuels. Part 1: Deposition rates," *Fuel*, vol. 85, pp. 1125-1130, 2006.
- [28] Y. B. Yang, J. Goodfellow, Y. R. Goh, V. Nasserzadeh, and J. Swithenbank, "Investigation of channel formation due to random packing in a burning waste bed," *Process Safety and Environmental Protection*, vol. 79, pp. 267-277, 2001.
- [29] Neil T. M. Duffy and John A. Eaton, "Investigation of factors affecting channelling in fixed-bed solid fuel combustion using CFD," *Combustion and Flame*, vol. 160, pp. 2204-2220, 2013.
- [30] M. G. Gronli and M. C. Melaaen, "Mathematical model for wood pyrolysis-comparison of experimental measurements with model predictions," *Energy and Fuels*, vol. 14, pp. 791-800, 2000.
- [31] B. Peters and C. Bruch, "Drying and pyrolysis of wood particles: Experiments and simulation," *Journal of Analytical and Applied Pyrolysis*, vol. 70, pp. 233-250, 2003.
- [32] K. M. Bryden, K. W. Ragland, and C. J. Rutland, "Modeling thermally thick pyrolysis of wood," *Biomass and Bioenergy*, vol. 22, pp. 41-53, 2002.
- [33] Y. B. Yang, V. N. Sharifi, J. Swithenbank, L. Ma, L. I. Darvell, J. M. Jones, M. Pourkashanian, and A. Williams, "Combustion of a single particle of biomass," *Energy and Fuels*, vol. 22, pp. 306-316, 2008.
- [34] J. Collazo, J. Porteiro, D. Patiño, and E. Granada, "Numerical modeling of the combustion of densified wood under fixed-bed conditions," *Fuel*, vol. 93, pp. 149-159, 2012.
- [35] W.-C. R. Chan, M. Kelbon, and B. B. Krieger, "Modelling and experimental verification of physical and chemical processes during pyrolysis of a large biomass particle," *Fuel*, vol. 64, pp. 1505-1513, 1985.
- [36] K. K. Kuo, *Principles of Combustion*: John Wiley & Sons, 1986.
- [37] S. S. Alves and J. L. Figueiredo, "A model for pyrolysis of wet wood," *Chemical Engineering Science*, vol. 44, pp. 2861-2869, 1989.
- [38] N. Ouelhazi, G. Arnaud, and J. P. Fohr, "A two-dimensional study of wood plank drying. The effect of gaseous pressure below boiling point," *Transport in Porous Media*, vol. 7, pp. 39-61, 1992.
- [39] *ANSYS CFX-Solver Theory Guide*, Southpointe, 275 Technology Drive, Canonsburg, USA: ANSYS Inc., 2009.
- [40] J. Saastamoinen and J. R. Richard, "Simultaneous drying and pyrolysis of solid fuel particles," *Combustion and Flame*, vol. 106, pp. 288-300, 1996.
- [41] C. Di Blasi, "Modeling and simulation of combustion processes of charring and non-charring solid fuels," *Progress in Energy and Combustion Science*, vol. 19, pp. 71-104, 1993.

- [42] A. M. Eaton, L. D. Smoot, S. C. Hill, and C. N. Eatough, "Components, formulations, solutions, evaluation, and application of comprehensive combustion models," *Progress in Energy and Combustion Science*, vol. 25, pp. 387-436, 1999.
- [43] A. Arenillas, F. Rubiera, C. Pevida, and J. J. Pis, "A comparison of different methods for predicting coal devolatilisation kinetics," *Journal of Analytical and Applied Pyrolysis*, vol. 58-59, pp. 685-701, 2001.
- [44] H. Kobayashi, J. B. Howard, and A. F. Sarofim, "Coal devolatilization at high temperatures," pp. 411-425, 1976.
- [45] F. Shafizadeh and S. Chin Peter P, "Thermal Deterioration of Wood," in *Wood Technology: Chemical Aspects*. vol. 43, ed: American Chemical Society, 1977, pp. 57-81.
- [46] R. H. Hurt and J. M. Calo, "Semi-global intrinsic kinetics for char combustion modeling," *Combustion and Flame*, vol. 125, pp. 1138-1149, 2001.
- [47] F. Thurner and U. Mann, "Kinetic investigation of wood pyrolysis," *Industrial & Engineering Chemistry Process Design and Development*, vol. 20, pp. 482-488, 1981.
- [48] C. Di Blasi, "Heat, momentum and mass transport through a shrinking biomass particle exposed to thermal radiation," *Chemical Engineering Science*, vol. 51, pp. 1121-1132, 1996.
- [49] A. G. Liden, F. Berruti, and D. S. Scott, " A kinetic model for the production of liquids from the flash pyrolysis of biomass," *Chemical Engineering Communications*, vol. 65, pp. 207-221, 1988/03/01 1988.
- [50] A. A. Rostami, M. R. Hajaligol, and S. E. Wrenn, "A biomass pyrolysis sub-model for CFD applications," *Fuel*, vol. 83, pp. 1519-1525, 2004.
- [51] M. L. de Souza-Santos, *Solid Fuels Combustion and Gasification: Modeling, Simulation and Equipment Operation*: Marcel Dekker, Inc., 2004.
- [52] K. Miura, "A new and simple method to estimate $f(E)$ and $k_0(E)$ in the distributed activation energy model from three sets of experimental data," *Energy & Fuels*, vol. 9, pp. 302-307, 1995.
- [53] M. J. Antal, E. G. Plett, and T. P. Chung, "Recent progress in kinetic models for coal pyrolysis," *Am Chem Soc Div Fuel Chem Prepr*, vol. 22, pp. 137-148, 1977.
- [54] C. P. Please, M. J. McGuinness, and D. L. S. McElwain, "Approximations to the distributed activation energy model for the pyrolysis of coal," *Combustion and Flame*, vol. 133, pp. 107-117, 2003.
- [55] G. Várhegyi, P. Szabó, and M. J. Antal Jr, "Kinetics of charcoal devolatilization," *Energy and Fuels*, vol. 16, pp. 724-731, 2002.
- [56] D. Ferdous, A. K. Dalai, S. K. Bej, and R. W. Thring, "Pyrolysis of lignins: Experimental and kinetics studies," *Energy and Fuels*, vol. 16, pp. 1405-1412, 2002.
- [57] A. K. Burnham, M. S. Oh, R. W. Crawford, and A. M. Samoun, "Pyrolysis of Argonne premium coals: activation energy distributions and related chemistry," *Energy & Fuels*, vol. 3, pp. 42-55, 1989.
- [58] A. K. Burnham, "Global kinetic analysis of complex materials," *Energy and Fuels*, vol. 13, pp. 1-22, 1999.
- [59] T. Maki, A. Takatsuno, and K. Miura, "Analysis of pyrolysis reactions of various coals including argonne premium coals using a new distributed activation energy model," *Energy and Fuels*, vol. 11, pp. 972-977, 1997.
- [60] K. Miura and T. Maki, "A simple method for estimating $f(E)$ and $k_0(E)$ in the distributed activation energy model," *Energy and Fuels*, vol. 12, pp. 864-869, 1998.
- [61] J. Yu and M. Zhang, "A simple method for predicting the rate constant of pulverized-coal pyrolysis at higher heating rate," *Energy and Fuels*, vol. 17, pp. 1085-1090, 2003.

- [62] J. Cai and R. Liu, "New distributed activation energy model: Numerical solution and application to pyrolysis kinetics of some types of biomass," *Bioresource Technology*, vol. 99, pp. 2795-2799, 2008.
- [63] C. C. Lakshmanan and N. White, "A new distributed activation energy model using Weibull distribution for the representation of complex kinetics," *Energy & Fuels*, vol. 8, pp. 1158-1167, 1994.
- [64] P. R. Solomon, D. G. Hamblen, R. M. Carangelo, M. A. Serio, and G. V. Deshpande, "General model of coal devolatilization," *Energy and Fuels*, vol. 2, pp. 405-422, 1988.
- [65] D. M. Grant, R. J. Pugmire, T. H. Fletcher, and A. R. Kerstein, "Chemical model of coal devolatilization using percolation lattice statistics," *Energy & Fuels*, vol. 3, pp. 175-186, 1989.
- [66] S. Niksa and A. R. Kerstein, "FLASHCHAIN theory for rapid coal devolatilization kinetics. 1. Formulation," *Energy & Fuels*, vol. 5, pp. 647-665, 1991.
- [67] Y. Chen, S. Charpenay, A. Jensen, M. A. Wójtowicz, and M. A. Serio, "Modeling of biomass pyrolysis kinetics," *Symposium (International) on Combustion*, vol. 27, pp. 1327-1334, 1998.
- [68] Y. Chen, S. Charpenay, A. Jensen, M. A. Wójtowicz, and M. A. Serio, "Extension of a coal pyrolysis model to biomass feedstocks," in *9th International Conference on Coal Science*, Hamburg, Germany, 1997, pp. 561-564.
- [69] S. Niksa, "Predicting the rapid devolatilization of diverse forms of biomass with bio-FLASHCHAIN," *Symposium (International) on Combustion*, vol. 28, pp. 2727-2733, 2000.
- [70] Advanced Fuel Research Inc. *FG-DVC Model*. Available: <http://www.afrinc.com/products/fgdvc/>, Accessed on 11/12/2012.
- [71] S. Niksa and A. R. Kerstein, "The distributed-energy chain model for rapid coal devolatilization kinetics. Part I: Formulation," *Combustion and Flame*, vol. 66, pp. 95-109, 1986.
- [72] S. Niksa, "The distributed-energy chain model for rapid coal devolatilization kinetics. Part II: Transient weight loss correlations," *Combustion and Flame*, vol. 66, pp. 111-119, 1986.
- [73] S. Niksa, "Flashchain theory for rapid coal devolatilization kinetics. 7. Predicting the release of oxygen species from various coals," *Energy and Fuels*, vol. 10, pp. 173-187, 1996.
- [74] S. Niksa, "FLASHCHAIN theory for rapid coal devolatilization kinetics. 6. Predicting the evolution of fuel nitrogen from various coals," *Energy & Fuels*, vol. 9, pp. 467-478, 1995.
- [75] S. Niksa, "FLASHCHAIN theory for rapid coal devolatilization kinetics. 5. Interpreting rates of devolatilization for various coal types and operating conditions," *Energy & Fuels*, vol. 8, pp. 671-679, 1994.
- [76] S. Niksa, "FLASHCHAIN theory for rapid coal devolatilization kinetics. 4. Predicting ultimate yields from ultimate analyses alone," *Energy & Fuels*, vol. 8, pp. 659-670, 1994.
- [77] S. Niksa, "FLASHCHAIN theory for rapid coal devolatilization kinetics. 3. Modeling the behavior of various coals," *Energy & Fuels*, vol. 5, pp. 673-683, 1991.
- [78] S. Niksa, "FLASHCHAIN theory for rapid coal devolatilization kinetics. 2. Impact of operating conditions," *Energy & Fuels*, vol. 5, pp. 665-673, 1991.
- [79] J. Rath, M. G. Wolfinger, G. Steiner, G. Krammer, F. Barontini, and V. Cozzani, "Heat of wood pyrolysis," *Fuel*, vol. 82, pp. 81-91, 2003.
- [80] A. Williams, R. Backreedy, R. Habib, J. M. Jones, and M. Pourkashanian, "Modelling coal combustion: The current position," *Fuel*, vol. 81, pp. 605-618, 2002.

- [81] J. M. Jones, M. Pourkashanian, A. Williams, and D. Hainsworth, "A comprehensive biomass combustion model," *Renewable Energy*, vol. 19, pp. 229-234, 2000.
- [82] N. M. Laurendeau, "Heterogeneous kinetics of coal char gasification and combustion," *Progress in Energy and Combustion Science*, vol. 4, pp. 221-270, 1978.
- [83] H. Zhou, A. D. Jensen, P. Glarborg, P. A. Jensen, and A. Kavaliauskas, "Numerical modeling of straw combustion in a fixed bed," *Fuel*, vol. 84, pp. 389-403, 2005.
- [84] I. Glassman, *Combustion*, 3rd ed.: Academic Press, 1997.
- [85] A. Williams, M. Pourkashanian, and J. M. Jones, "Combustion of pulverised coal and biomass," *Progress in Energy and Combustion Science*, vol. 27, pp. 587-610, 2001.
- [86] M. M. Baum and P. J. Street, "Predicting the Combustion Behaviour of Coal Particles," *Combustion Science and Technology*, vol. 3, pp. 231 - 243, 1971.
- [87] A. Williams, M. Pourkashanian, and J. M. Jones, "The combustion of coal and some other solid fuels," *Symposium (International) on Combustion*, vol. 28, pp. 2141-2161, 2000.
- [88] *ANSYS Fluent Theory Guide*, Southpointe, 275 Technology Drive, Canonsburg, USA: ANSYS Inc., in *Release 14.0*, 2011.
- [89] I. W. Smith, "The combustion rates of coal chars: A review," *Symposium (International) on Combustion*, vol. 19, pp. 1045-1065, 1982.
- [90] R. Johansson, H. Thunman, and B. Leckner, "Sensitivity analysis of a fixed bed combustion model," *Energy and Fuels*, vol. 21, pp. 1493-1503, 2007.
- [91] S. Hermansson and H. Thunman, "CFD modelling of bed shrinkage and channelling in fixed-bed combustion," *Combustion and Flame*, 2011.
- [92] N. Wakao and S. Kageui, *Heat and Mass Transfer in Packed Beds*. London, UK: Gordon and Breach Science, 1982.
- [93] R. H. Essenhigh and A. M. Mescher, "Influence of pressure on the combustion rate of carbon," *Symposium (International) on Combustion*, vol. 26, pp. 3085-3094, 1996.
- [94] R. H. Essenhigh, "An integration path for the carbon-oxygen reaction with internal reaction," *Symposium (International) on Combustion*, vol. 22, pp. 89-96, 1989.
- [95] A. Elfakhany, T. Klason, and X. S. Bai, "Modelling of pulverised wood combustion using a functional group model," *Combustion Theory and Modelling*, vol. 12, pp. 883-904, 2008.
- [96] R. E. Mitchell, "On the products of the heterogeneous oxidation reaction at the surfaces of burning coal char particles," *Symposium (International) on Combustion*, vol. 22, pp. 69-78, 1989.
- [97] C. Di Blasi, "Modeling wood gasification in a countercurrent fixed-bed reactor," *AIChE Journal*, vol. 50, pp. 2306-2319, 2004.
- [98] S. K. Bhatia and D. D. Perlmutter, "Random pore model for fluid-solid reactions - 2. Diffusion and Transport effects " *AIChE Journal*, vol. 27, pp. 247-254, 1981.
- [99] S. K. Bhatia and D. D. Perlmutter, "A random pore model for fluid-solid reactions: I. Isothermal, kinetic control," *AIChE Journal*, vol. 26, pp. 379-386, 1980.
- [100] S. K. Bhatia and B. J. Vartak, "Reaction of microporous solids: The discrete random pore model," *Carbon*, vol. 34, pp. 1383-1391, 1996.
- [101] G. A. Simons, "The pore tree structure of porous char," *Symposium (International) on Combustion*, vol. 19, pp. 1067-1076, 1982.
- [102] H. Thunman, F. Niklasson, F. Johnsson, and B. Leckner, "Composition of Volatile Gases and Thermochemical Properties of Wood for Modeling of Fixed or Fluidized Beds," *Energy & Fuels*, vol. 15, pp. 1488-1497, 2001.
- [103] K. M. Bryden, "Computation Modeling of Wood Combustion," PhD PhD, Mechanical Engineering, University of Wisconsin-Madison, Wisconsin, 1998.

- [104] J. Cooper and W. L. H. Hallett, "A numerical model for packed-bed combustion of char particles," *Chemical Engineering Science*, vol. 55, pp. 4451-4460, 2000.
- [105] B. Peters, *Thermal Conversion of Solid Fuels*. Southampton, UK: WIT Press, 2003.
- [106] D. Shin and S. Choi, "The combustion of simulated waste particles in a fixed bed," *Combustion and Flame*, vol. 121, pp. 167-180, 2000.
- [107] M. Fatehi and M. Kaviany, "Adiabatic reverse combustion in a packed bed," *Combustion and Flame*, vol. 99, pp. 1-17, 1994.
- [108] J. J. Saastamoinen, M. Horttanainen, and P. Sarkomaa, "Ignition wave propagation and release of volatiles in beds of wood particles," *Combustion Science and Technology*, vol. 165, pp. 41-60, 2001.
- [109] K. M. Bryden and K. W. Ragland, "Numerical modeling of a deep, fixed bed combustor," *Energy and Fuels*, vol. 10, pp. 269-275, 1996.
- [110] S. K. Kær, "Numerical modelling of a straw-fired grate boiler," *Fuel*, vol. 83, pp. 1183-1190, 2004.
- [111] B. Peters, E. Schröder, C. Bruch, and T. Nussbaumer, "Measurements and particle resolved modelling of heat-up and drying of a packed bed," *Biomass and Bioenergy*, vol. 23, pp. 291-306, 2002.
- [112] B. Peters, "Measurements and application of a discrete particle model (DPM) to simulate combustion of a packed bed of individual fuel particles," *Combustion and Flame*, vol. 131, pp. 132-146, 2002.
- [113] C. Bruch, B. Peters, and T. Nussbaumer, "Modelling wood combustion under fixed bed conditions," *Fuel*, vol. 82, pp. 729-738, 2003.
- [114] Y. R. Goh, R. G. Siddall, V. Nasserzadeh, R. Zakaria, J. Swithenbank, D. Lawrence, N. Garrod, and B. Jones, *Mathematical modelling of the burning bed of a waste incinerator* vol. 71. London, Royaume-Uni: Institute of Energy, 1998.
- [115] Y. R. Goh, C. N. Lim, R. Zakaria, K. H. Chan, G. Reynolds, Y. B. Yang, R. G. Siddall, V. Nasserzadeh, and J. Swithenbank, "Mixing, Modelling and Measurements of Incinerator Bed Combustion," *Process Safety and Environmental Protection*, vol. 78, pp. 21-32, 2000.
- [116] Y. R. Goh, Y. B. Yang, R. Zakaria, R. G. Siddall, V. Nasserzadeh, and J. Swithenbank, "Development of an incinerator bed model for municipal solid waste incineration," *Combustion Science and Technology*, vol. 162, pp. 37-58, 2001.
- [117] M. Beckmann and R. Scholz, "Simplified mathematical model of combustion in stoker systems," in *3rd European Conference on Industrial Furnaces and Boilers*, Lisbon, Portugal, 1995, pp. 61-70.
- [118] NETL, "MFIx," Available: <https://mfix.netl.doe.gov>, Accessed on: 11/12/2012.
- [119] OpenCFD, "OpenFOAM," Available: <http://www.openfoam.com>, Accessed on: 11/12/2012
- [120] J. J. Saastamoinen, R. Taipale, M. Horttanainen, and P. Sarkomaa, "Propagation of the ignition front in beds of wood particles," *Combustion and Flame*, vol. 123, pp. 214-226, 2000.
- [121] Y. R. Goh, R. Zakaria, Y. B. Yang, V. Nasserzadeh, and J. Swithenbank, "Reduction of NO_x during incineration of municipal solid waste by a fundamental combustion technique," *Journal of the Institute of Energy*, vol. 76, pp. 72-79, 2003.
- [122] Y. B. Yang, H. Yamauchi, V. N. Sharifi, and J. Swithenbank, "Effect of moisture content of fuel on the combustion behaviour of biomass and municipal solid waste in a packed bed," *Journal of the Institute of Energy*, vol. 76, pp. 105-115, 2003.
- [123] Y. B. Yang, H. Yamauchi, V. Nasserzadeh, and J. Swithenbank, "Effects of fuel devolatilisation on the combustion of wood chips and incineration of simulated municipal solid wastes in a packed bed," *Fuel*, vol. 82, pp. 2205-2221, 2003.
- [124] Y. B. Yang, C. Ryu, A. Khor, N. E. Yates, V. N. Sharifi, and J. Swithenbank, "Effect of fuel properties on biomass combustion. Part II. Modelling approach - Identification of the controlling factors," *Fuel*, vol. 84, pp. 2116-2130, 2005.

- [125] Y. B. Yang, V. N. Sharifi, and J. Swithenbank, "Effect of air flow rate and fuel moisture on the burning behaviours of biomass and simulated municipal solid wastes in packed beds," *Fuel*, vol. 83, pp. 1553-1562, 2004.
- [126] Y. B. Yang, J. Goodfellow, V. Nasserzadeh, and J. Swithenbank, "Study on the transient process of waste fuel incineration in a full-scale moving-bed furnace," *Combustion Science and Technology*, vol. 177, pp. 127-150, 2005.
- [127] Y. B. Yang, A. N. Phan, C. Ryu, V. Sharifi, and J. Swithenbank, "Mathematical modelling of slow pyrolysis of segregated solid wastes in a packed-bed pyrolyser," *Fuel*, vol. 86, pp. 169-180, 2007.
- [128] H. Zhou, A. D. Jensen, P. Glarborg, and A. Kavaliauskas, "Formation and reduction of nitric oxide in fixed-bed combustion of straw," *Fuel*, vol. 85, pp. 705-716, 2006.
- [129] J. S. Ryan and W. L. H. Hallett, "Packed bed combustion of char particles: Experiments and an ash model," *Chemical Engineering Science*, vol. 57, pp. 3873-3882, 2002.
- [130] E. Girgis and W. L. H. Hallett, "Wood combustion in an overfeed packed bed, including detailed measurements within the bed," *Energy and Fuels*, vol. 24, pp. 1584-1591, 2010.
- [131] C. Ryu, D. Shin, and S. Choi, "Combined simulation of combustion and gas flow in a grate-type incinerator," *J Air Waste Manag Assoc*, vol. 52, pp. 189-97, Feb 2002.
- [132] S. K. Kær, "Straw combustion on slow-moving grates - A comparison of model predictions with experimental data," *Biomass and Bioenergy*, vol. 28, pp. 307-320, 2005.
- [133] S. K. Kær, L. A. Rosendahl, and L. L. Baxter, "Towards a CFD-based mechanistic deposit formation model for straw-fired boilers," *Fuel*, vol. 85, pp. 833-848, 2006.
- [134] B. Miljković, I. Pešenjanski, and M. Vičević, "Mathematical modelling of straw combustion in a moving bed combustor: A two dimensional approach," *Fuel*, 2012.
- [135] Y. B. Yang, Y. R. Goh, R. Zakaria, V. Nasserzadeh, and J. Swithenbank, "Mathematical modelling of MSW incineration on a travelling bed," *Waste Management*, vol. 22, pp. 369-380, 2002.
- [136] Y. B. Yang, V. Nasserzadeh, J. Goodfellow, Y. R. Goh, and J. Swithenbank, "Parameter study on the incineration of municipal solid waste fuels in packed beds," *Journal of the Institute of Energy*, vol. 75, pp. 66-80, 2002.
- [137] Y. B. Yang, R. Newman, V. Sharifi, J. Swithenbank, and J. Ariss, "Mathematical modelling of straw combustion in a 38 MWe power plant furnace and effect of operating conditions," *Fuel*, vol. 86, pp. 129-142, 2007.
- [138] Y. B. Yang, V. N. Sharifi, and J. Swithenbank, "Substoichiometric conversion of biomass and solid wastes to energy in packed beds," *AIChE Journal*, vol. 52, pp. 809-817, 2006.
- [139] Y. B. Yang, V. N. Sharifi, and J. Swithenbank, "Converting moving-grate incineration from combustion to gasification - Numerical simulation of the burning characteristics," *Waste Management*, vol. 27, pp. 645-655, 2007.
- [140] Y. B. Yang, V. N. Sharifi, and J. Swithenbank, "Numerical simulation of the burning characteristics of thermally-thick biomass fuels in packed-beds," *Process Safety and Environmental Protection*, vol. 83, pp. 549-558, 2005.
- [141] Y. B. Yang, C. K. Ryu, V. N. Sharifi, and J. Swithenbank, "Effect of model and operating parameters on air gasification of char," *Energy and Fuels*, vol. 20, pp. 1698-1708, 2006.
- [142] Y. B. Yang, V. Sharifi, and J. Swithenbank, "Mathematical modelling of sewage sludge incineration in a bubbling fluidised bed with special consideration for thermally-thick fuel particles," *Waste Management*, vol. 28, pp. 2245-2258, 2008.
- [143] S. Hermansson and H. Thunman, "Measures to reduce grate material wear in fixed-bed combustion," *Energy and Fuels*, vol. 25, pp. 1387-1395, 2011.

- [144] J. Collazo, J. Porteiro, J. L. Míguez, E. Granada, and M. A. Gómez, "Numerical simulation of a small-scale biomass boiler," *Energy Conversion and Management*, vol. 64, pp. 87-96, 2012.
- [145] R. Mehrabian, R. Scharler, A. Weissinger, and I. Obernberger, "Optimisation of Biomass Grate Furnaces with a New 3D Packed Bed Combustion Model - On Example of a Small-Scale Underfeed Stoker Furnace," in *18th European Biomass Conference & Exhibition*, Lyon, France, 2010.
- [146] R. Mehrabian, S. Stangl, R. Scharler, I. Obernberger, and A. Weissinger, "CFD simulation of biomass grate furnaces with a comprehensive 3D packed bed model," in *25th German Flame Day*, Karlsruhe, Germany, 2011.
- [147] R. Buczyński, R. Weber, A. Szlek, and R. Nosek, "Time-dependent combustion of solid fuels in a fixed-bed: Measurements and mathematical modeling," *Energy and Fuels*, vol. 26, pp. 4767-4774, 2012.
- [148] D. Kurz, U. Schnell, and G. Scheffknecht, "CFD simulation of wood chip combustion on a grate using an Euler-Euler approach," *Combustion Theory and Modelling*, vol. 16, pp. 251-273, 2012.
- [149] J. C. Wurzenberger, S. Wallner, H. Raupenstrauch, and J. G. Khinast, "Thermal conversion of biomass: Comprehensive reactor and particle modeling," *AIChE Journal*, vol. 48, pp. 2398-2411, 2002.
- [150] H. Thunman, B. Leckner, F. Niklasson, and F. Johnsson, "Combustion of wood particles - A particle model for Eulerian calculations," *Combustion and Flame*, vol. 129, pp. 30-46, 2002.
- [151] H. Thunman and B. Leckner, "Modeling of the combustion front in a countercurrent fuel converter," 2002, pp. 511-518.
- [152] H. Thunman and B. Leckner, "Co-current and counter-current fixed bed combustion of biofuel - A comparison," *Fuel*, vol. 82, pp. 275-283, 2003.
- [153] J. Porteiro, J. L. Míguez, E. Granada, and J. C. Moran, "Mathematical modelling of the combustion of a single wood particle," *Fuel Processing Technology*, vol. 87, pp. 169-175, 2006.
- [154] J. Porteiro, E. Granada, J. Collazo, D. Patiño, and J. C. Morán, "A model for the combustion of large particles of densified wood," *Energy and Fuels*, vol. 21, pp. 3151-3159, 2007.
- [155] J. Porteiro, J. Collazo, D. Patiño, E. Granada, J. C. M. Gonzalez, and J. L. Míguez, "Numerical modeling of a biomass pellet domestic boiler," *Energy and Fuels*, vol. 23, pp. 1067-1075, 2009.
- [156] R. Johansson, H. Thunman, and B. Leckner, "Influence of intraparticle gradients in modeling of fixed bed combustion," *Combustion and Flame*, vol. 149, pp. 49-62, 2007.
- [157] Y. B. Yang, C. N. Lim, J. Goodfellow, V. N. Sharifi, and J. Swithenbank, "A diffusion model for particle mixing in a packed bed of burning solids," *Fuel*, vol. 84, pp. 213-225, 2005.
- [158] B. Peters, A. Džiugys, H. Hunsinger, and L. Krebs, "An approach to qualify the intensity of mixing on a forward acting grate," *Chemical Engineering Science*, vol. 60, pp. 1649-1659, 2005.
- [159] H. Kruggel-Emden, E. Simsek, S. Wirtz, and V. Scherer, "A Comparative Numerical Study of Particle Mixing on Different Grate Designs Through the Discrete Element Method," *Journal of Pressure Vessel Technology*, vol. 129, pp. 593-600, 2007.
- [160] E. Simsek, B. Brosch, S. Wirtz, V. Scherer, and F. Krüll, "Numerical simulation of grate firing systems using a coupled CFD/discrete element method (DEM)," *Powder Technology*, vol. 193, pp. 266-273, 2009.
- [161] F. Sudbrock, E. Simsek, S. Wirtz, and V. Scherer, "An experimental analysis on mixing and stoking of monodisperse spheres on a grate," *Powder Technology*, vol. 198, pp. 29-37, 2010.

- [162] F. Sudbrock, E. Simsek, S. Rickelt, S. Wirtz, and V. Scherer, "Discrete element analysis of experiments on mixing and stoking of monodisperse spheres on a grate," *Powder Technology*, vol. 208, pp. 111-120, 2011.
- [163] H. Kruggel-Emden, S. Wirtz, and V. Scherer, "An experimental investigation of mixing of wood pellets on a forward acting grate in discontinuous operation," *Powder Technology*, vol. 233, pp. 261-277, 2013.
- [164] J. Dai, H. Cui, and J. R. Grace, "Biomass feeding for thermochemical reactors," *Progress in Energy and Combustion Science*, vol. 38, pp. 716-736, 2012.
- [165] Y. B. Yang, V. Nasserzadeh, J. Goodfellow, and J. Swithenbank, "Simulation of Channel Growth in a Burning Bed of Solids," *Chemical Engineering Research and Design*, vol. 81, pp. 221-232, 2003.
- [166] W. J. Massman, "A review of the molecular diffusivities of H₂O, CO₂, CH₄, CO, O₃, SO₂, NH₃, N₂O, NO, and NO₂ in air, O₂ and N₂ near STP," *Atmospheric Environment*, vol. 32, pp. 1111-1127, 1998.
- [167] F. A. L. Dullien, *Porous media fluid transport and pore structure*, 2nd ed. San Diego: Academic Press, Inc, 1992.
- [168] A. Nakayama and F. Kuwahara, "A General Macroscopic Turbulence Model for Flows in Packed Beds, Channels, Pipes, and Rod Bundles," *Journal of Fluids Engineering*, vol. 130, pp. 101205-7, 2008.
- [169] S. Frigerio, H. Thunman, B. Leckner, and S. Hermansson, "Estimation of gas phase mixing in packed beds," *Combustion and Flame*, vol. 153, pp. 137-148, 2008.
- [170] C. K. Westbrook and F. L. Dryer, "Chemical kinetic modeling of hydrocarbon combustion," *Progress in Energy and Combustion Science*, vol. 10, pp. 1-57, 1984.
- [171] J. B. Howard, G. C. Williams, and D. H. Fine, "Kinetics of carbon monoxide oxidation in postflame gases," *Symposium (International) on Combustion*, vol. 14, pp. 975-986, 1973.
- [172] F. P. Incropera, D. P. Dewitt, T. L. Bergman, and A. S. Lavine, *Fundamentals of Heat and Mass Transfer*, 6 ed. NJ, USA: John Wiley and Sons, Inc., 2007.
- [173] J. Porteiro, D. Patiño, J. Moran, and E. Granada, "Study of a fixed-bed biomass combustor: Influential parameters on ignition front propagation using parametric analysis," *Energy and Fuels*, vol. 24, pp. 3890-3897, 2010.
- [174] D. D. Evans and H. W. Emmons, "Combustion of wood charcoal," *Fire Safety Journal*, vol. 1, pp. 57-66, 1977.
- [175] M. J. Hage and K. M. Bryden, "Modeling the impact of shrinkage on the pyrolysis of dry biomass," *Chemical Engineering Science*, vol. 57, pp. 2811-2823, 2002.
- [176] B. M. Suleiman, J. Larfeldt, B. Leckner, and M. Gustavsson, "Thermal conductivity and diffusivity of wood," *Wood Science and Technology*, vol. 33, pp. 465-473, 1999.
- [177] J. Porteiro, D. Patiño, J. Collazo, E. Granada, J. Moran, and J. L. Miguez, "Experimental analysis of the ignition front propagation of several biomass fuels in a fixed-bed combustor," *Fuel*, vol. 89, pp. 26-35, 2010.
- [178] J. Porteiro, D. Patiño, J. L. Miguez, E. Granada, J. Moran, and J. Collazo, "Study of the reaction front thickness in a counter-current fixed-bed combustor of a pelletised biomass," *Combustion and Flame*, vol. 159, pp. 1296-1302, 2012.
- [179] H. Thunman and B. Leckner, "Ignition and propagation of a reaction front in cross-current bed combustion of wet biofuels," *Fuel*, vol. 80, pp. 473-481, 2001.
- [180] R. Bauer, M. Gölles, T. Brunner, N. Dourdoumas, and I. Obernberger, "Modelling of grate combustion in a medium scale biomass furnace for control purposes," *Biomass and Bioenergy*, vol. 34, pp. 417-427, 2010.
- [181] M. Gölles, R. Bauer, T. Brunner, N. Dourdoumas, and I. Obernberger, "Model based control of a biomass grate furnace," in *9th European Conference on Industrial Furnace and Boilers*, Estoril, Portugal, 2011.
- [182] A. Montillet and L. Le Coq, "Characteristics of fixed beds packed with anisotropic particles - Use of image analysis," *Powder Technology*, vol. 121, pp. 138-148, 2001.

- [183] D. B. Thomas, W. Luk, P. H. W. Leong, and J. D. Villasenor, "Gaussian random number generators," *ACM Comput. Surv.*, vol. 39, p. 11, 2007.
- [184] E. Houshfar, R. A. Khalil, T. Løvås, and Ø. Skreiberg, "Enhanced NO_x reduction by combined staged air and flue gas recirculation in biomass grate combustion," *Energy and Fuels*, vol. 26, pp. 3003-3011, 2012.
- [185] H. Thunman and B. Leckner, "Thermal conductivity of wood - Models for different stages of combustion," *Biomass and Bioenergy*, vol. 23, pp. 47-54, 2002.
- [186] D. Merrick, "Mathematical models of the thermal decomposition of coal. 2. Specific heats and heats of reaction," *Fuel*, vol. 62, pp. 540-546, 1983.
- [187] ICHEC. Available: <http://www.ichec.ie/infrastructure/stokes.php>, Accessed on: 11/12/2012
- [188] G. Sorell, "Picking nickel-base alloys to resist heat and corrosion," *Chemical Processing*, vol. 61, 1998.
- [189] F. J. Frandsen, "Ash research from Palm Coast, Florida to Banff, Canada: Entry of biomass in modern power boilers," *Energy and Fuels*, vol. 23, pp. 3347-3378, 2009.
- [190] A. Williams, J. M. Jones, L. Ma, and M. Pourkashanian, "Pollutants from the combustion of solid biomass fuels," *Progress in Energy and Combustion Science*, vol. 38, pp. 113-137, 2012.
- [191] H. Asteman and M. Spiegel, "Investigation of the HCl (g) attack on pre-oxidized pure Fe, Cr, Ni and commercial 304 steel at 400 °C," *Corrosion Science*, vol. 49, pp. 3626-3637, 2007.
- [192] I. M. Allam and Z. M. Gasem, "High temperature corrosion of alloy Haynes 556 in carburizing/oxidizing environments," *Materials and Corrosion*, vol. 58, pp. 245-253, 2007.
- [193] H. J. Grabke, "A case of nitridation, carburization and oxidation on a stainless steel," *Materials and Corrosion*, vol. 56, pp. 384-388, 2005.
- [194] M. Hänsel, C. A. Boddington, and D. J. Young, "Internal oxidation and carburisation of heat-resistant alloys," *Corrosion Science*, vol. 45, pp. 967-981, 2003.
- [195] T. Gheno, D. Monceau, J. Zhang, and D. J. Young, "Carburisation of ferritic Fe-Cr alloys by low carbon activity gases," *Corrosion Science*, vol. 53, pp. 2767-2777, 2011.
- [196] H. Zhang, J. Yan, M. Ni, and K. Cen, "The research on gas diffusion through the coal ash layer during the coal combustion process," *Combustion Science and Technology*, vol. 174, pp. 55-73, 2002/10/01 2002.
- [197] R. L. Deuis, A. M. Brown, and S. Petrone, "Hot erosion wear and carburization in petrochemical furnaces," *Materials and Corrosion*, vol. 57, pp. 135-146, 2006.
- [198] A. R. Martin and C. Saltiel, "Three-dimensional fluid flow and heat transfer analysis of grate blocks in a waste-to-energy power plant," *Numerical Heat Transfer, Part A: Applications*, vol. 29, pp. 795-808, 1996/06/01 1996.
- [199] *ANSYS FLUENT UDF Manual*. Southpointe, 275 Technology Drive, Canonsburg, USA: ANSYS Inc., 2011.